TOPICS IN THE THEORY OF CORE-COLLAPSE SUPERNOVAE

by

Todd Alan Thompson

A Dissertation Submitted to the Faculty of the

Department of Physics

In Partial Fulfillment of the Requirements
For the Degree of

Doctor of Philosophy

In the Graduate College

The University of Arizona

2 0 0 2

Get the official approval page
from the Graduate College
before your final defense.

Statement by Author

Dedication

For my parents, Barbara and Terry, and for my brother, Brian.

Acknowledgments

From the physics department, I would like to extend special thanks to Robert McCroskey, Mike Fromerth, Tom Burch, and Jason Hamm. Each has been a good friend to me. I would also like to thank Chris Wiggins for his encouragement and example in my first year in Tucson. In addition, I thank Professor Doug Toussaint, who in his classes and in conversation has inspired me to be a better teacher and physicist.

From the Astronomy Department, I would like to thank David Sudarsky, Jennifer Scott, and Audra Baleisis for friendship, good conversations, and their perpetually open door. Without their office to walk into, my time at Steward Observatory would have been considerably different and, I suspect, much less fun. I thank Professors Michael Meyer and Daniel Eisenstein for helping me traverse the postdoc-hunting minefield. Professor Phil Pinto also contributed to my stability in this regard and was always helpful in answering my questions on numerics. I also thank Jeff Fookson, who has administered the computers necessary for the calculations contained in this thesis.

Both here and abroad I have benefited from association with a number of first-rate researchers, including Professors Hans-Thomas Janka, Stan Woosley, Chris Fryer, George Fuller, Eli Livne, Itamar Lichtenstadt, Jorge Horvath, and Brad Meyer. My education in all areas of theoretical astrophysics has been increased in my many conversations with each and I appreciate their encouragement to do and learn more.

There is not sufficient space here to describe fully the debt I owe to my advisor, Professor Adam Burrows. Much, if not the whole, of my scientific eduction is due to him. I could not have hoped for a more focused, engaged, and knowledgeable mentor. He has consistently sparked my interest in physics, suggested good problems and projects, and steered me just enough in coming to completion. He has emphasized the science foremost and I take his example with me in moving on from Arizona. His never-ending supply of fine chocolates and quotes from the romantics will be sorely missed.

I thank my family for their guidance, belief in me, encouragement, and enthusiasm.

Finally, I thank Katy Byram, who with love and endless patience has carried me through these last five years.

Table of Contents

Table of Contents—*Continued*

Table of Contents—*Continued*

List of Figures

List of Figures—*Continued*

List of Tables

Abstract

We study the physics of core-collapse supernovae and the neutron stars they create. We study the microphysics of neutrino interactions and demonstrate the importance of two processes previously ignored in full supernova simulations: inelastic neutrino-nucleon scattering and nucleon-nucleon bremsstrahlung. We show that these processes dominate neutrino-electron scattering and electron-positron annihilation as thermalization and production mechanisms, respectively, for mu- and tau-neutrinos in regimes vital to emergent spectrum formation.

In addition, we solve the general-relativistic steady-state eigenvalue problem of neutrino-driven protoneutron star winds, which immediately follow core-collapse supernova explosions. We provide velocity, density, temperature, and composition profiles and explore the systematics and structures generic to such a wind for a variety of protoneutron star characteristics. Furthermore, we derive the entropy, dynamical timescale, and compositions essential in assessing this site as a candidate for r-process nucleosynthesis.

Finally, we construct dynamical models of core-collapse supernovae. We employ a full solution to the transport equation for each neutrino species, a realistic high-density nuclear equation of state, and explicit hydrodynamics. We present results from a set of different supernova progenitors. We vary the microphysics and nuclear equation of state and compare our results to those of other groups. We examine the electron-neutrino breakout phenomenon and address the importance of nucleon-nucleon bremsstrahlung and inelastic neutrino-electron scattering in μ and τ neutrino spectrum formation. We convolve the emergent spectra obtained in these models with terrestrial neutrino detectors and find that the electron-neutrino breakout burst can likely be observed and identified uniquely.

TOPICS IN THE THEORY OF CORE-COLLAPSE SUPERNOVAE

Todd Alan Thompson, Ph.D.
The University of Arizona, 2002

Director: Adam Burrows and Doug Toussaint

We study the physics of core-collapse supernovae and the neutron stars they create. We study the microphysics of neutrino interactions and demonstrate the importance of two processes previously ignored in full supernova simulations: inelastic neutrino-nucleon scattering and nucleon-nucleon bremsstrahlung. We show that these processes dominate neutrino-electron scattering and electron-positron annihilation as thermalization and production mechanisms, respectively, for mu- and tau-neutrinos in regimes vital to emergent spectrum formation.

In addition, we solve the general-relativistic steady-state eigenvalue problem of neutrino-driven protoneutron star winds, which immediately follow core-collapse supernova explosions. We provide velocity, density, temperature, and composition profiles and explore the systematics and structures generic to such a wind for a variety of protoneutron star characteristics. Furthermore, we derive the entropy, dynamical timescale, and compositions essential in assessing this site as a candidate for r-process nucleosynthesis.

Finally, we construct dynamical models of core-collapse supernovae. We employ a full solution to the transport equation for each neutrino species, a realistic high-density nuclear equation of state, and explicit hydrodynamics. We present results from a set of different supernova progenitors. We vary the microphysics and nuclear equation of state and compare our results to those of other groups. We examine the electron-neutrino breakout phenomenon and address the importance of nucleon-nucleon bremsstrahlung and inelastic neutrino-electron scattering in μ and τ neutrino spectrum formation. We convolve the emergent spectra obtained in these models with

terrestrial neutrino detectors and find that the electron-neutrino breakout burst can likely be observed and identified uniquely.

Chapter 1
Introduction

Core-collapse supernovae are among the most energetic phenomena in the universe. Although the luminous energy radiated during such an event is sizable ($\sim 10^{49}$ erg), the total energy emitted in neutrinos is a prodigious $\sim 3 \times 10^{53}$ erg. In fact, for a fraction of a second during neutrinosphere breakout, the neutrino luminosity from a supernova is greater than the luminosity in photons from the rest of the visible universe. This copious neutrino emission originates in the cores of supernovae where temperatures surpass 10^{11} Kelvin and mass densities reach $2-3$ times those of nuclei. From the perspective of fundamental physics, the conditions attending collapse and explosion make supernovae a laboratory for the study of weak and high-density nuclear interactions. From a broader astrophysical standpoint, core-collapse supernovae are essential as a primary source of energy and elements in the interstellar medium, affecting galactic morphology and chemical evolution. Despite the importance of such phenomena, the supernova problem is unsolved and a comprehensive theory of core-collapse remains elusive.

1.1 The Supernova Story

In the early 1930's Chandrasekhar (see e.g., Chandrasekhar 1967 and references therein) derived the maximum stable mass for a white dwarf, a compact object with radius of order thousands of kilometers, supported against gravity by electron degeneracy pressure. Chandrasekhar showed that above a certain mass the configuration was dynamically unstable and that an object that reached such a mass would collapse inexorably. Modern stellar evolution calculations show that stars with mass greater than ~ 8 solar masses ($M_\odot$) develop inner cores much like degenerate white dwarfs, which become dynamically unstable to collapse in the manner predicted by Chandrasekhar when their mass approaches $\sim 1.4\,\mathrm{M}_\odot$. Although the massive star considered may have lived quietly for millions of years, the collapse proceeds on timescales of less than a second. In 1934, just two years after Chadwick discovered the neutron, Baade & Zwicky proposed with considerable prescience that supernovae represent the transition between normal massive stars and neutron stars, ultra-compact objects composed predominantly of neutrons. It was thought that the implosion caused by Chandrasekhar's dynamical instability might reverse at nuclear densities and that the shock wave created might be sufficient to tear apart the outer parts of the massive star, littering the galaxy with nucleosynthetic products and leaving behind both a spectacular remnant of the explosion and a newly-born neutron star.

As beautiful and intuitive as it might be, the idea that this shock, having been generated by the preceding implosion, continues promptly from the core and becomes the supernova is incorrect. In the early 1980's it was shown that the shock must stall due to neutrino losses and the photodissociation of nuclei (e.g. Mazurek 1982; Burrows & Lattimer 1985; Bruenn 1985). A robust conclusion of these calculations is that the shock formed at bounce stalls into an accretion shock after having traveled of order only 100 kilometers (km). How this shock might be revived via neutrino heating or some other mechanism is the focus of modern supernova theory.

1.2 The Physical Conditions

Although the details change with the given model assumptions and with the initial progenitor, the basic numbers are the following. A 'standard' Type-II supernova progenitor might have a total mass of $\sim 15\,\mathrm{M}_\odot$, have lived for a multiple of 10^7 years, and be classified as a red supergiant with a radius of some several $\times 10^{13}$ centimeters (cm). It has an onion-skin structure with an extended hydrogen envelope, a layer of helium below, and a core of oxygen, magnesium, and silicon, which dumps the ashes of nuclear burning onto a core of iron several thousands of kilometers in radius, roughly the size of the Earth or a white dwarf. Figure (1.1) shows a schematic of this initial configuration in the upper left-hand corner. This part of the diagram is meant to illustrate a blue supergiant progenitor, with a smaller hydrogen envelope and so the radius of the object is labeled as 3×10^{12} cm. The inner core is supported by the degeneracy pressure of relativistic electrons and becomes dynamically unstable when the mass grows to $\mathrm{M} \sim 1.45(Y_e/0.5)^2\,\mathrm{M}_\odot$, where $Y_e[= (n_{e^-} - n_{e^+})/n_b]$ is the electron fraction, and n_{e^-}, n_{e^+}, and n_b are the number densities of electrons, positrons, and baryons, respectively. Perhaps more precisely stated, the Chandrasekhar instability is encountered when the average adiabatic index ($\Gamma_s[= d\ln P/d\ln\rho|_s]$) of the self-gravitating core dips below 4/3.

Collapse: At the moment collapse ensues the core temperature may be $\sim 1\,\mathrm{MeV}$ and the mass density may be $\lesssim 10^{10}$ g cm^{-3}. The core collapses on a dynamical timescale $\tau \sim (G\bar{\rho})^{-1/2} \sim 0.1$ seconds, where G is the gravitational constant and $\bar{\rho}$ is the average density of the core material. During infall and bounce, peak negative velocities approach a fourth of the speed of light. This collapse epoch is illustrated in the lower left-hand corner of Fig. (1.1). The core density rises to nuclear densities ($\rho_{\rm nuc} \sim 2 - 3 \times 10^{14}$ g cm^{-3}) and the temperature to $\sim 10\,\mathrm{MeV}$. Owing to the thermo-static effects engendered by the existence of many excited states of nuclei in a realistic nuclear equation of state, up until these densities and temperatures, the neutrons and protons are still locked in massive nuclei. In fact, just before the phase transition from nuclei to free nucleons, the atomic mass (A) of a representative heavy nucleus in the core may approach several hundred. Until central densities of $\sim 5 \times 10^{12}$ g cm^{-3} are reached, the process of electron capture on free protons ($e^- + p \rightarrow n + \nu_e$) depletes the total electron fraction in the core as the final-state electron neutrinos (ν_es) escape to infinity, thereby aiding collapse by removing electron pressure support. In essence, it is this process with its final-state neutron, which creates the *neutron* star left behind by core-collapse. Above these densities, the timescale for electron neutrino diffusion from the core becomes much longer than that for the hydrodynamical evolution and the neutrinos are trapped. As a result, equilibrium is established between $e^- + p \rightarrow n + \nu_e$ and its inverse.

Bounce and Breakout: At $\rho_{\rm nuc}$ the nuclei dissolve into free nucleons. At this point the nucleons contribute significantly to the pressure and the equation of state stiffens ($d\ln P/d\ln\rho|_s \rightarrow 2-3$). As a result, the collapse halts and a strong sound wave is formed at the center of the object. As the wave propagates down the density gradient of the infalling material it steepens into a shock as it encounters the supersonically collapsing outer core [1]. The shock forms at a radius of just $10-20$ km with a maximum positive velocity of $\sim 3\times 10^9$ cm s^{-1} (see the lower right-hand snapshot in Fig. 1.1). As the shock liberates free protons, the process $e^- + p \rightarrow n + \nu_e$ generates a huge local luminosity (L_{ν_e}) of electron neutrinos just behind the shock. This region is opaque to the final-state electron neutrinos and they are effectively trapped, their diffusion timescale being much longer than that for shock evolution. As a result, L_{ν_e} can reach $1-2\times 10^{54}$ erg s^{-1}. As the shock moves out in radius, it eventually encounters lower mass densities and the previously trapped electron neutrinos decouple from this more optically thin region and propagate ahead of the shock. This pulse of electron neutrinos arrives at infinity with $L_{\nu_e}(\infty) \sim 2-3\times 10^{53}$ erg s^{-1}. This electron-neutrino breakout signals collapse and bounce and, as Chapter 4 shows, may be detected unambiguously from the next galactic supernova in modern neutrino detectors such as SuperKamiokande and the Sudbury Neutrino Observatory. The electron neutrino breakout pulse is virtually simultaneous with the turn-on of the other neutrino species. Anti-electron neutrinos ($\bar{\nu}_e$s), suppressed until now by the very small positron number density caused by the very large chemical potential of the electrons throughout the core, are generated predominantly in the hot post-bounce environment by $e^+ + n \rightarrow p + \bar{\nu}_e$. Mu- and tau-neutrinos are also produced in this epoch

[1] A shock is a non-linear phenomenon admitted by the equations of hydrodynamics. It is evidenced by discontinuities in the fluid variables such as velocity, temperature, and density.

by electron-positron annihilation ($e^+e^- \rightarrow \nu_\mu\bar{\nu}_\mu$), nucleon-nucleon bremsstrahlung (e.g. $np \rightarrow np\nu_\mu\bar{\nu}_\mu$), and neutrino/anti-neutrino annihilation ($\nu_e\bar{\nu}_e \rightarrow \nu_\mu\bar{\nu}_\mu$; Buras et al. 2002). Although each of these processes also contributes for ν_e and $\bar{\nu}_e$ neutrinos, the charged-current processes $e^+ + n \rightarrow p + \bar{\nu}_e$ and $e^- + p \rightarrow n + \nu_e$ dominate.

At just $\sim 75\,\mathrm{km}$ the shock stalls as a result of two effects. First, as the shock begins moving outward it dissociates the infalling iron-peak nuclei into free nucleons, thus giving up $\sim 8.8\,\mathrm{MeV}$ per baryon in binding energy. Second, and most importantly, as the shock dissociates nuclei into free nucleons, electrons capture on the newly liberated protons to produce electron-neutrinos in the reaction $e^- + p \rightarrow n + \nu_e$. The electron-neutrino breakout phenomenon and subsequent neutrino losses are thus responsible for the inability of the bounce shock to promptly become the supernova.

Equilibrium: Only $2-3$ milliseconds after the shock was created it has succumbed and a quasi-hydrostatic equilibrium is maintained between the newly-born 'proto'neutron star (with radius of $\sim 50-80\,\mathrm{km}$) and the stalled accretion shock. This phase in the evolution is illustrated in the upper right-hand snapshot of Fig. (1.1), which shows the hot, extended protoneutron star, the accompanying neutrino radiation, and the mass-flux of the infalling material ($\dot{M}$). Although the shock stalls at $75-100\,\mathrm{km}$, it may move slowly over hundreds of milliseconds to larger radius ($\sim 200\,\mathrm{km}$) as the composition of the infalling material changes and because neutrino heating and cooling affect the dynamics. The matter from the star itself continues falling onto the shock on near-free-fall timescales. The core of the protoneutron star is hot and dense, producing neutrinos of all species. The neutrinos diffuse in the dense inner core, but at some radius decouple from the matter and free-stream to infinity. The radius of decoupling, called the neutrinosphere (R_ν), is roughly defined as the point at which the mean-free path for neutrino interaction approaches the characteristic length scale of the object as a whole (perhaps $50-100\,\mathrm{km}$). Owing to the fact that neutrino-matter cross sections are generally proportional to the neutrino energy squared (ε_ν^2), the neutrinosphere is very energy dependent and not sharply defined.

The primary processes driving neutrino heating (H) and cooling (C) in and around the neutrinospheres are $e^- + p \rightarrow n + \nu_e$ (C), $e^+ + n \rightarrow p + \bar{\nu}_e$ (C), $\nu_e + n \rightarrow e^- + p$ (H), and $\bar{\nu}_e + p \rightarrow e^+ + n$ (H). Importantly, a robust conclusion of detailed numerical models is that directly above the electron neutrinosphere ($R_{\nu_e} \sim 60\,\mathrm{km}$) is a region of net neutrino cooling. At what is called the gain radius (R_g), heating balances cooling ($R_g \sim 100\,\mathrm{km}$). Treating the problem stationarily, R_g must also correspond with a peak in the matter entropy because $Tv\,ds/dr|_{R_g} \simeq H - C = 0$, where s is the specific entropy and T and v are the postshock temperature and velocity, respectively (e.g. Burrows, Hayes, & Fryxell 1995). Between R_g and the radius of the shock ($R_s \sim 200\,\mathrm{km}$) is a region of net neutrino heating.

The Neutrino-Driven Mechanism: The radial extent of the heating region, as well as the magnitude of the net energy deposition depend crucially on the neutrino energy density and flux in this semi-transparent regime. Because this regime is marginally optically thin to neutrinos, the transport equation must be solved accurately for all neutrino species. Fundamentally, the neutrino-driven mechanism succeeds when the hot protoneutron star transfers enough energy to the region just behind the shock via neutrino interactions. Note that the kinetic energy associated with the mass motions of observed supernovae is $\sim 10^{51}$ erg. In contrast, the amount of gravitational binding energy released in going from a degenerate progenitor iron core with a radius of several thousand kilometers to a neutron star with a radius of order ten kilometers is approximately $E \sim GM^2/R$. Taking $M = 1.4\mathrm{M}_\odot$ and $R = 10$ kilometers implies $E \sim 3 \times 10^{53}$ erg. Virtually all of that energy is released in the form of neutrinos, only a small fraction ($\sim 1\%$) of which must couple to the mantle above the protoneutron star that is ejected as the supernova.

All one-dimensional models that do not employ ad hoc neutrino luminosity boost mechanisms fail in one spatial dimension. However, models of supernovae in two dimensions yielded explosions as a result of the larger gain region caused by convection behind the shock (Herant et al. 1994; Burrows, Hayes, & Fryxell 1995). These models, however, suffered from crude treatments of the neutrino transport in the semi-transparent gain region and, hence, cannot be regarded as a solution to the supernova problem. For a more complete analysis of the requirements for the neutrino-driven mechanism, the reader is referred to Bethe & Wilson (1985), Burrows & Goshy (1993), and Janka (2001).

Explosion and Protoneutron Star Cooling: Assuming that some combination of neutrino heating and multi-dimensional convective effects are sufficient to drive explosion, the protoneutron star is left to cool and contract (see the central drawing in Fig. 1.1). This cooling phase may last tens of seconds and most of the gravitational binding energy will be released in neutrinos as the protoneutron star contracts from $\sim 50\,\mathrm{km}$ to of order $10\,\mathrm{km}$. In the successful two-dimensional simulation of Burrows, Hayes, & Fryxell (1995) the shock, newly-revived, moves outward in radius at a velocity of ~ 20000 km s^{-1}. The region behind the shock and above the neutrinosphere becomes more tenuous as the shock moves out. A portion of the neutrino radiation coming from the cooling neutron star may drive a wind via energy deposition into this evacuating region (Janka & Müller 1996; Burrows, Hayes, & Fryxell 1995).

1.3 This Thesis in Context

Microphysics: At the temperatures and densities achieved in core-collapse supernovae, neutrinos are produced in profusion via charged- and neutral-current weak interactions. The emission and absorption mechanisms, combined with opacity sources such as neutrino-electron and neutrino-nucleon scattering, couple the neutrinos to the ambient matter, affecting energy transport from the dense inner core to the more tenuous outer layers, where the neutrinos free-stream. This coupling may be sufficient to drive Type-II supernovae. Essential in answering the question of whether the neutrino mechanism succeeds generically is a precise understanding of neutrino transport in this context. In turn, this analysis relies on detailed knowledge of the role and importance of each relevant weak interaction. Full supernova models are often difficult to diagnose in this regard. Simple test problems often shed light on the role of particular processes. In Chapter 2 we analyze the importance of several neutrino interactions in an easily manipulated theoretical framework. Particularly, we focus on the role of inelastic neutrino-nucleon scattering as an energy exchange process and nucleon-nucleon bremsstrahlung as a production process in models of supernovae. For more than 20 years theorists have neglected these processes. Chapter 2 shows unequivocally that they cannot be ignored; an accurate prediction of the emergent neutrino spectrum from a galactic core-collapse supernova relies on their inclusion. Motivated by the work of Hannestad & Raffelt (1998) and Burrows & Sawyer (1998), we compare neutrino-nucleon scattering and bremsstrahlung with processes previously thought to dominate in the supernova problem.

Although supernova theorists had neglected the inelasticity of neutrino-nucleon scattering, they included the neutrino-electron energy redistribution kernel in their solution to the neutrino Boltzmann equation. Chapter 2 compares the neutrino-nucleon and neutrino-electron scattering thermalization rates for all relevant neutrino energies, at a variety of temperatures, densities, and compositions. Our results contradict the accepted approximation and show clearly that above neutrino energies of ~ 15 MeV, neutrino-nucleon scattering is comparable with or dominates neutrino-electron scattering as a thermalization mechanism. Similarly, the supernova community considered electron/positron annihilation as the dominant production process for μ and τ neutrino/anti-neutrino pairs. Again, in contrast to the standard thinking on neutrino processes, we discovered that nucleon-nucleon bremsstrahlung dominates production in regimes vital to spectrum formation. In addition, as part of this study we derived for the first time the emissivity due to nucleon-nucleon bremsstrahlung at arbitrary nucleon degeneracy.

Dynamical Models and Neutrino Signals: Fundamental to an understanding of supernovae is a precise prediction of the neutrino signature from such an event.

Modern terrestrial neutrino detectors can expect to observe thousands of neutrinos from the next galactic supernova. The best direct observation that can be made of supernovae, the one most capable of revealing the details of the inner core structure, is that of the neutrino signature of core collapse. Comparing the emergent spectrum and its time evolution from models of supernovae with the neutrino signature observed in underground detectors is the acid test for any complete theory of core collapse. In addition, the observed spectral evolution can put significant constraints on the physics of neutrino oscillations, including the mass hierarchy, and the high-density nuclear equation of state. It can also unambiguously indicate black hole formation. Although much work has been done on the mechanism itself, comparatively little attention has been paid to the detailed systematic changes in the detected neutrino spectra as a function of progenitor, high-density nuclear equation of state, and neutrino microphysics. The basics of the modern supernova paradigm including shock breakout, shock stall, accretion onto the core, and subsequent explosion will all be borne out in the neutrino signature. For these reasons, precise models of supernovae should be constructed, their neutrino signatures diagnosed, and these signals folded with the sensitivities and characteristics of modern detectors. We have done exactly that. Chapter 4 gives the details of our models of supernovae, predictions for the time evolution of the neutrino spectra for all species, and our predictions for the signals observed in several neutrino detectors in the first ~ 250 milliseconds after collapse. Large variations in actual detected signals from future supernovae can only represent new and interesting, previously ignored or perhaps even unknown physics. The work of Chapter 4 is part of a new and small class of tools that address the core-collapse problem with previously unattained precision in one spatial dimension. Comparable to this work is only that of Rampp & Janka (2002) and Mezzacappa et al. (2001) and Liebendörfer (2000).

Protoneutron Star Winds and the r-Process: Although predicting the neutrino signature of collapse and explosion is absolutely crucial to a complete theory of supernovae, we are only afforded a potential glimpse of such an event once every ~50 years. Next to electromagnetic observations of supernovae and their remnants, one might also hope to learn something about the mechanism of supernovae from their nucleosynthetic ejecta.

A complete and self-consistent theory of the origin of the elements has been the grand program of nuclear astrophysics since the field's inception. The rapid(r) neutron-capture process is responsible for $\sim 50\%$ of nuclei with atomic mass greater than 60. Recent abundance observations of ultra-metal-poor halo stars by the Hubble Space Telescope (e.g. Cowan et al. 1999; Sneden et al. 1998) show remarkable agreement with solar values for $A > 135$ – suggesting a universal r-process site that acts early in the chemical enrichment history of the galaxy. While the relevant nuclear physics is fairly well understood, the site in Nature where the r-process occurs, producing abundance peaks at $A \sim 80$, 130, and 195, is one of the outstanding unknowns in astrophysics.

Some multiple of 10^{53} erg will be lost via neutrino radiation by the protoneutron star as it cools after the preceding supernova explosion. A small fraction of that energy will be deposited in the surface layers of the nascent neutron star, heating and driving material from its surface in a hydrodynamical wind. As a consequence of the charged-current electron and anti-electron neutrino interactions, the wind is expected to be neutron-rich. The large neutron excess, coupled with high matter entropy, is thought to be conducive to a robust r-process. Although considerable research on protoneutron star winds has been conducted, only Woosley et al. (1994) calculated the nucleosynthetic yield from winds obtained in self-consistent core-collapse calculations. Other investigators (e.g. Burrows et al. 1995) obtained winds after successful explosions, but were unable to evolve the wind to late times due to timestep limitations caused by their explicit hydrodynamics. Woosley et al. (1994) obtained significant r-process yields tens of seconds after explosion, but the very high entropy and long dynamical timescale realized in their calculations have never been independently reproduced. Indeed, several groups have concluded that such entropies cannot be achieved in transonic winds and that they are not likely to be obtained during the cooling phase of protoneutron star evolution (e.g. Takahashi et al. 1994; Qian and Woosley 1996). Moreover, fully self-consistent steady-state models in general relativity had not previously been constructed. Chapter 3 fills these gaps in our understanding of this phenomenon.

In Chapter 3 we solve the eigenvalue problem of steady-state transonic neutrino-driven winds in general relativity. For given protoneutron star masses, radii, and neutrino spectral characteristics, we compute the mass outflow rate using the appropriate hydrodynamical wind equations. We obtain velocity, temperature, density, and composition profiles and compute the asymptotic entropy, dynamical timescale, and electron fraction – each essential in assessing this site as a candidate for r-process nucleosynthesis. We include a detailed analysis of the important power laws governing this system and map the entire relevant parameter space. We then post-process our wind profiles for their nucleosynthetic yield. For the first time, we derive the relationship between the entropy and dynamical timescale and the associated mass outflow rate. We derive significant constraints on the epochs of wind evolution when the r-process is likely to occur. Before this work, many assumed that the wind would naturally evolve to high entropy (~ 400 k$_B$ baryon^{-1}) and relatively long dynamical timescales (hundreds of milliseconds). Thus, generation of r-process nuclei would proceed at late times, many seconds after the supernova explosion. This work rules out such a scenario. It shows that although the wind evolves to high entropy at late times (as the neutrino luminosity decays) it fails to enter a regime where a robust r-process can take place. We also show that even if r-processing could occur at these late times, the mass loss rate is too small (less than $\sim 10^{-9}$ M$_\odot$ s^{-1}) to contribute significantly to the total r-process budget of the galaxy.

We show that a robust r-process can only be achieved in winds from very massive protoneutron stars with high neutrino luminosities that contract rapidly after the preceding supernova. Although we were able to achieve nucleosynthesis up to the platinum peak, the protoneutron star characteristics required to generate such spherical transonic winds are unrealistic. Our results indicate that although nuclei with mass numbers up to ~ 135 may be produced generically in this environment, a full r-process, producing elements up to the actinides, is unlikely. Finally, we also show that shocks engendered by the interaction of the newly formed wind with the preceding supernova shock may have important dynamical and nucleosynthetic consequences.

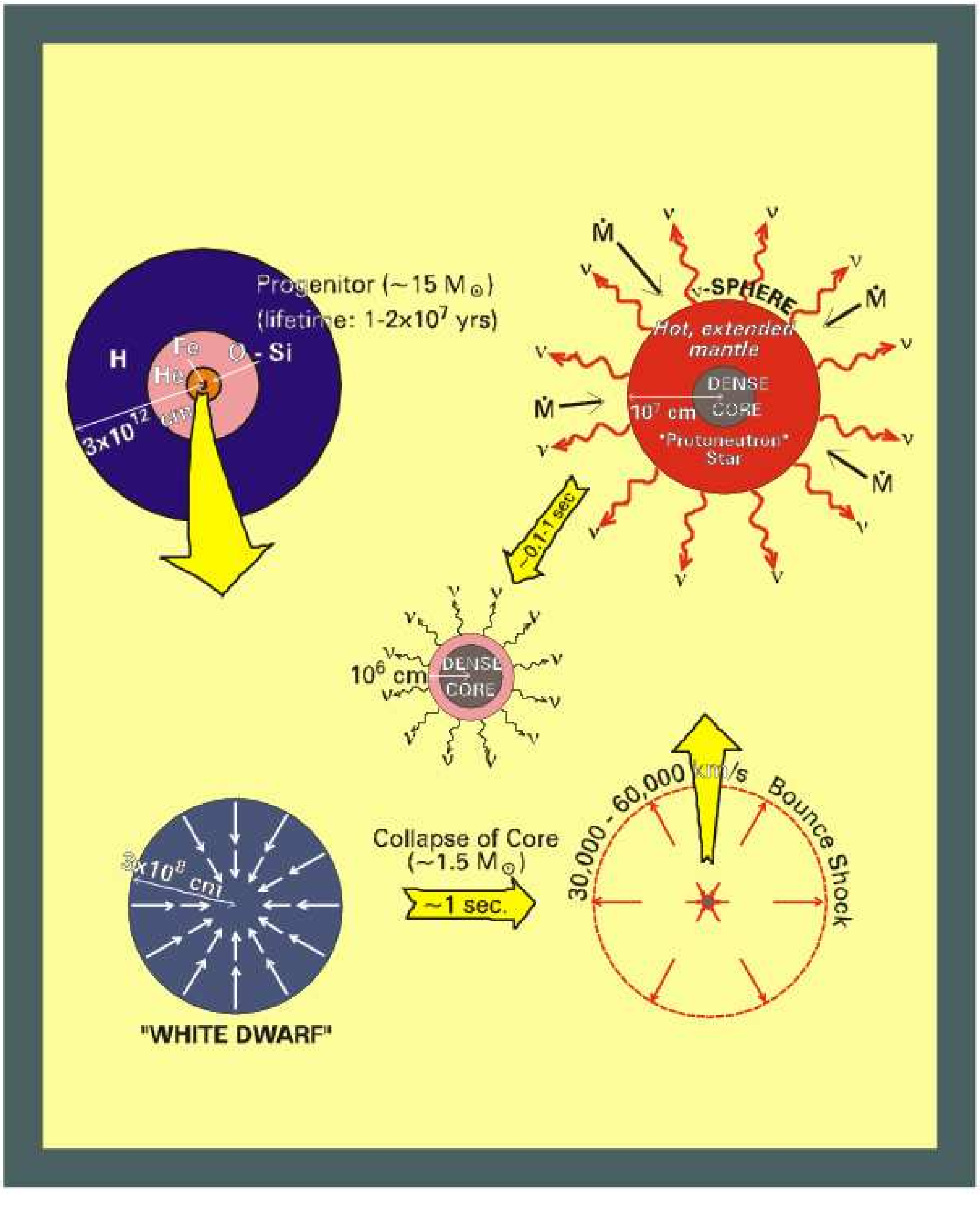

FIGURE 1.1. A cartoon of the basic stages in a supernova for a $15\,\mathrm{M}_\odot$ progenitor. The initial 'onion-skin' configuration is shown in the upper left-hand corner. The $\sim 1.5\,\mathrm{M}_\odot$ iron-core collapses dynamically (lower left-hand corner). The nuclear EOS stiffens during collapse and drives a prompt 'Bounce' shock into the supersonic outer core (lower right-hand corner). The shock stalls due to neutrino emission and dissociation losses (upper right-hand corner). Assuming a successful supernova explosion, the newly-formed protoneutron star is left to cool and contract (center).

Chapter 2

Thermalization and Production

2.1 Introduction

The cores of protoneutron stars and core-collapse supernovae are characterized by mass densities of order $\sim 10^{10} - 10^{14}$ g cm^{-3} and temperatures that range from ~ 1 to 50 MeV. The matter is composed predominantly of nucleons, electrons, positrons, and neutrinos of all species. For ν_μ and ν_τ types (collectively 'ν_μs'), which carry away 50−60% of the $\sim 2-3\times10^{53}$ ergs liberated during collapse and explosion, the prevailing opacity and production processes are ν_μ-electron scattering, ν_μ-nucleon scattering, electron-positron annihilation ($e^+e^- \leftrightarrow \nu_\mu\bar{\nu}_\mu$), and nucleon-nucleon bremsstrahlung. While all of these processes contribute for the electron types (ν_es and $\bar{\nu}_e$s), the charged-current absorption processes $\nu_e n \leftrightarrow pe^-$ and $\bar{\nu}_e p \leftrightarrow ne^+$ dominate their opacity so completely that in this paper we address only ν_μ production and thermalization.

Supernova theorists had long held (Lamb & Pethick 1976) that ν_μ-nucleon scattering was unimportant as a mechanism for neutrino equilibration. While this process was included as a source of opacity (Bruenn 1985; Burrows, Hayes, & Fryxell 1995), it served only to redistribute the neutrinos in space, not in energy. In contrast, ν_μ-electron scattering was thought to dominate ν_μ neutrino thermalization. In addition, the only $\nu_\mu\bar{\nu}_\mu$ pair production mechanisms employed in full supernova calculations were $e^+e^- \leftrightarrow \nu_\mu\bar{\nu}_\mu$ and plasmon decay ($\gamma_{pl} \leftrightarrow \nu_\mu\bar{\nu}_\mu$) (Bruenn 1985); nucleon-nucleon bremsstrahlung was neglected as a source. Recent developments, however, call both these practices into question and motivate a re-evaluation of these opacities in the supernova context. Analytic formulae have recently been derived (Reddy, Prakash, & Lattimer 1998; Burrows & Sawyer 1998, 1999), which include the full nucleon kinematics and Pauli blocking in the final state at arbitrary nucleon degeneracy. These efforts reveal that the average rate of energy transfer in ν_μ-nucleon scattering may surpass previous estimates by an order of magnitude (Burrows & Sawyer 1998; Hannestad & Raffelt 1998; Keil, Janka, & Raffelt 1999; Janka et al. 1996; Raffelt & Seckel 1998; Sigl 1997). Hence, this process may compete with ν_μ-electron scattering as an equilibration mechanism. Similarly, estimates for the total nucleon-nucleon bremsstrahlung rate have been obtained (Hannestad & Raffelt 1998; Burrows et al. 1999; Friman & Maxwell 1979; Flowers, Sutherland, & Bond 1975), which indicate that this process might compete with e^+e^- annihilation.

These results suggest that the time is ripe for a technical study of the relative importance of each process for production or thermalization. To conduct such a study, we consider ν_μ neutrinos in an isotropic homogeneous thermal bath of scatterers and absorbers. In this system, the full transport problem is reduced to an evolution of the neutrino distribution function (f_ν) in energy space alone. Although this is a simplification of the true problem, it provides a theoretical laboratory in which to analyze the rates both for equilibration of an initial neutrino distribution function with dense nuclear matter and for production of the neutrinos themselves. From these rates we determine the importance and particular character of each process, and discover in which energy, temperature, or density regime each dominates. We employ a general prescription for solving the Boltzmann equation in this system with the full energy redistribution collision term. We compare quantitatively, via direct numerical evolution of an arbitrary neutrino distribution function, the rates for thermalization and production by each process, at all neutrino energies. Furthermore, we present the total nucleon-nucleon bremsstrahlung rate for arbitrary nucleon degeneracy and derive the single ν_μ and $\bar{\nu}_\mu$ production spectra. This facilitates a more comprehensive evaluation of its relative importance in neutrino production than has previously been possible.

In §2.2, we discuss the general form of the Boltzmann equation and our use of it to study ν_μ equilibration and production rates. In §2.3, we provide formulae for each of the four processes we consider: ν_μ-nucleon scattering, ν_μ-electron scattering, and $\nu_\mu\bar{\nu}_\mu$ pair production via both nucleon-nucleon bremsstrahlung and e^+e^- annihilation. In §2.4, we present the results of our equilibration calculations, showing the time evolution of ν_μ distribution functions as influenced by each of these processes individually. We include plots of thermalization and production rates for each process as a function of neutrino energy and time. For the scattering interactions we include figures of the time evolution of the net energy transfer to the medium as a function of incident neutrino energy. We repeat this analysis at points in temperature, density, and composition space relevant to supernovae and protoneutron stars, taken from snapshots of a stellar profile during a realistic collapse calculation (Burrows, Hayes, & Fryxell 1995). Using these results, we discuss the relative importance of each process in shaping the emergent ν_μ spectrum. In §2.5, we recapitulate our findings and conclusions.

2.2 The Boltzmann Equation

The static (velocity$=$ 0) Boltzmann equation for the evolution of the neutrino distribution function (f_ν), including Pauli blocking in the final state, and for a spherical geometry, is

$$\left(\frac{1}{c}\frac{\partial}{\partial t}+\mu\frac{\partial}{\partial r}+\frac{1-\mu^2}{r}\frac{\partial}{\partial \mu}\right)f_\nu=(1-f_\nu)j_\nu-f_\nu\chi_\nu, \tag{2.1}$$

where t is the time, r is the radial coordinate, and $\mu(=\cos\theta)$ is the cosine of the zenith angle. j_ν and χ_ν are the total *source* and *sink*, respectively. For emission and absorption, j_ν is the emissivity and χ_ν is the extinction coefficient. For scattering, both j_ν and χ_ν are energy redistribution integrals which couple one neutrino energy bin with all the others. The matrix element and associated phase-space integrations which comprise j_ν and χ_ν for electron and nucleon scattering yield the probability that a given collision will scatter a particle into any angle or energy bin. A full transport calculation couples energy and angular bins to each other through the right hand side of eq. (2.1).

In a homogeneous, isotropic thermal bath of scatterers and absorbers no spatial or angular gradients exist. Consequently, the Boltzmann equation becomes

$$\frac{1}{c}\frac{\partial f_\nu}{\partial t} = (1 - f_\nu)j_\nu - f_\nu \chi_\nu . \tag{2.2}$$

By dealing with this system, the transport problem reduces to an evolution of f_ν in just energy and time. Note that for scattering processes, both j_ν and χ_ν require an integral over the scattered neutrino distribution function f'_ν. Similarly, in evolving f_ν via the production and absorption processes, j_ν and χ_ν involve an integration over the anti-neutrino distribution function $f_{\bar{\nu}}$. Therefore, $f_{\bar{\nu}}$ must be evolved simultaneously with f_ν. While j_ν and χ_ν may be fairly complicated integrals over phase-space, the numerical solution of eq. (2.2) is straightforward.

Given an arbitrary initial f_ν, we divide the relevant neutrino energy (ε_ν) range into n energy bins (typically 200 bins with $0 \leq \varepsilon_\nu$ (MeV) ≤ 100). We then solve eq. (2.2) for each bin individually and explicitly:

$$f^i_{\nu,\,k+1} = f^i_{\nu,\,k} + c(\Delta t)_k \left[(1 - f^i_{\nu,k})\, j_{\nu,k} - f^i_{\nu,k}\, \chi_{\nu,k} \right] ,$$

where i denotes the neutrino energy bin and k denotes the timestep. Angular integrals over scattering cosines which appear in the ν_μ-nucleon and ν_μ-electron scattering formalism, as well as the electron energy integration needed for e^+e^- annihilation, are carried out with a 4-point Gauss-Legendre integration scheme. The double integral over dimensionless nucleon momentum variables needed to obtain the contribution from nucleon-nucleon bremsstrahlung is computed using nested 16-point Gauss-Laguerre quadratures.

2.2.1 Rates for f_ν Evolution and Energy Transfer

Scattering, emission, and absorption processes, at a given neutrino energy (ε_ν), produce and remove neutrinos from the phase-space density at that energy. The former achieves this by transferring energy to the matter during scattering, the latter two by emitting or absorbing directly from that bin. The Boltzmann equation can then be written in terms of an *in* and an *out* channel, the former a *source* and the latter a *sink*:

$$\frac{\partial f_\nu}{\partial t} = \left.\frac{\partial f_\nu}{\partial t}\right|_{in} - \left.\frac{\partial f_\nu}{\partial t}\right|_{out} . \tag{2.3}$$

Consequently, for any interaction, there are two rates to consider: the rate for scattering or production into a given energy bin (Γ_{in}) and the inverse rate for scattering or absorption out of that bin (Γ_{out}). The rates cj_ν and $c\chi_\nu$ yield timescales for an interaction to occur, but fail, in the case of the former, to fold in Pauli blocking in the final state. Equation (2.3) includes these effects and provides natural timescales for f_ν evolution:

$$\Gamma_{in} = \frac{1}{f_\nu}\left.\frac{\partial f_\nu}{\partial t}\right|_{in} = \frac{(1-f_\nu)}{f_\nu} cj_\nu \tag{2.4}$$

and

$$\Gamma_{out} = \frac{1}{f_\nu}\left.\frac{\partial f_\nu}{\partial t}\right|_{out} = c\chi_\nu . \tag{2.5}$$

Note that although eq. (2.5) does not explicitly contain a Pauli blocking term, χ_ν contains an integral over $(1 - f'_\nu)$, in the case of scattering, and an appropriate final-state blocking term, in the case of absorption. At a given ε_ν, then, Γ_{in} incorporates information about the ν_μ phase-space density at that energy. Conversely, at that same ε_ν, Γ_{out} contains information about the phase-space at all other energies. Regardless of the initial distribution, $\partial f_\nu/\partial t = 0$ in equilibrium. This implies $\Gamma_{in} = \Gamma_{out}$ in equilibrium and, hence, we build in a test for the degree to which the system has thermalized.

Just as there are distinct rates for the *in* and *out* channels of the Boltzmann equation during equilibration, so too are there distinct scattering energy transfers. For ν_μ scattering with a scatterer s (electron or nucleon), at a specific ε_ν, two thermal average energy transfers can be defined;

$$\langle\omega\rangle_{in} = \frac{\int d^3p'_\nu\, \omega\, f'_\nu\, \mathcal{I}^{in}\left[\nu_\mu s \leftarrow \nu'_\mu s'\right]}{\int d^3p'_\nu\, f'_\nu\, \mathcal{I}^{in}\left[\nu_\mu s \leftarrow \nu'_\mu s'\right]} \tag{2.6}$$

and

$$\langle\omega\rangle_{out} = \frac{\int d^3p'_\nu\, \omega\, (1-f'_\nu)\, \mathcal{I}^{out}\left[\nu_\mu s \rightarrow \nu'_\mu s'\right]}{\int d^3p'_\nu\, (1-f'_\nu)\, \mathcal{I}^{out}\left[\nu_\mu s \rightarrow \nu'_\mu s'\right]}, \tag{2.7}$$

where primes denote the scattered neutrino, $\omega(=\varepsilon_\nu - \varepsilon'_\nu)$ is the energy transfer, and $\mathcal{I}^{in}$ and $\mathcal{I}^{out}$ are the kernels for scattering into and out of a given energy bin, respectively. As a consequence of detailed balance between the *in* and *out* channels of the Boltzmann equation, $\mathcal{I}^{in} = e^{-\beta\omega}\mathcal{I}^{out}$, where $\beta = 1/k_BT$ and T is the matter temperature. (The scattering kernels are discussed in detail in §2.3 for both scattering processes.) Note that the denominators in eqs. (2.6) and (2.7), up to constants which divide out in the definitions of $\langle\omega\rangle_{in}$ and $\langle\omega\rangle_{out}$, are just j_ν and χ_ν, respectively.

In an effort to provide more than one measure of the timescale for f_ν equilibration due to scattering and to make contact with previous neutrino thermalization studies (Tubbs 1978; Tubbs 1979; Tubbs et al. 1980) we also define a set of timescales in terms of $\langle\omega\rangle_{out}$ and the higher ω-moment, $\langle\omega^2\rangle_{out}$;

$$\Gamma_D = c\chi_\nu \left|\frac{\langle\omega\rangle_{out}}{\varepsilon_\nu}\right| \tag{2.8}$$

and

$$\Gamma_E = c\chi_\nu \frac{\langle\omega^2\rangle_{out}}{\varepsilon_\nu^2}. \tag{2.9}$$

Γ_D is the rate for shifting the centroid of a given distribution and Γ_E is the rate for spreading an initial distribution (Tubbs 1979). In contrast with the work of Tubbs (1978), Tubbs (1979), and Tubbs et al. (1980), we include the full effects of Pauli blocking in the final state, allowing us to deal consistently with cases in which the ν_μs are partially degenerate.

2.3 Individual Interactions

This section details the source and sink terms necessary to solve the Boltzmann equation for the time-evolution of f_ν. Sections §2.3.1 and §2.3.2 are dedicated to the presentation and discussion of the collision terms for ν_μ-nucleon and ν_μ-electron scattering, respectively. Section §2.3.3 describes the Legendre series expansion approximation and the use of it to compute the contribution to the Boltzmann equation, the pair emissivity, and the single ν_μ spectrum due to $e^+e^- \leftrightarrow \nu_\mu\bar{\nu}_\mu$. Our derivations of j_ν and χ_ν, as well as the single and pair spectra from nucleon-nucleon bremsstrahlung at arbitrary nucleon degeneracy and in the non-degenerate limit, are presented in §2.3.4. In what follows, we take $G^2 \simeq 1.55 \times 10^{-33}$ cm^3 MeV^{-2} s^{-1}, $\sin^2\theta_W \simeq 0.231$, and employ natural units in which $\hbar = c = k_B = 1$.

2.3.1 Nucleon Scattering: $\nu_\mu n \leftrightarrow \nu_\mu n$ and $\nu_\mu p \leftrightarrow \nu_\mu p$

Researchers working on supernova and protoneutron star evolution have recently re-evaluated the issue of energy transfer via ν_μ-nucleon scattering (Burrows & Sawyer 1998; Hannestad & Raffelt 1998; Keil et al. 1995; Janka et al. 1996; Raffelt & Seckel 1998). Originally, the assumption was made that the nucleons were stationary (Lamb & Pethick 1976). If a neutron of mass m_n is at rest with respect to an incoming neutrino of energy ε_ν, one finds that the energy transfer ($\bar{\omega}$) is $\sim -\varepsilon_\nu^2/m_n$. For $\varepsilon_\nu =$ 10 MeV, $\bar{\omega} \sim -0.1$ MeV, a fractional energy lost of 1%. Using these simple kinematic arguments and disregarding neutrino and nucleon Pauli blocking, one finds that the thermalization rate for ν_μ-electron scattering should be approximately a factor of 20 larger than that for ν_μ-nucleon scattering. In the context of interest, however, at temperatures of order 10 MeV and mass densities of order 10^{13} g cm^{-3}, free nucleons are not stationary, but have thermal velocities. The fractional energy exchange per collision, in the case of ν_μ-neutron scattering, is then $\sim p_n/m_n c$ (Burrows & Sawyer 1998). For $T \sim 10$ MeV this gives a $\sim$10$-$20% change in ε_ν per collision. This calls the naive estimate of the relative importance of ν_μ-nucleon scattering as a thermalization process into question and a more complete exploration of the relative importance of the two scattering processes is necessary.

Recently, analytic formulae have been derived which include the full kinematics of ν_μ-nucleon scattering at arbitrary nucleon degeneracy (Reddy, Praksh, & Lattimer 1998; Burrows & Sawyer 1998, 1999). At the temperatures and densities encountered in the supernova context non-interacting nucleons are not relativistic. Due to nucleon-nucleon interactions, however, at and around nuclear density ($\sim 2.68 \times 10^{14}$ g cm^{-3}), the nucleon's effective mass drops and is expected to be comparable with its Fermi momentum (Reddy, Praksh, & Lattimer 1998). In such a circumstance, a relativistic description of the ν_μ-nucleon scattering interaction is warranted. In addition, spin and density correlation effects engendered by these nucleon-nucleon interactions have been found to suppress the ν_μ-nucleon interaction rate by as much as a factor of $\sim 2-3$ (Burrows & Sawyer 1998; Raffelt & Seckel 1998; Sigl 1997).

In this study, we focus on ν_μ equilibration rates at densities $\lesssim 1\times10^{14}$ g cm^{-3} where it is still unclear if nucleon-nucleon interactions will play an important role. This ambiguity is due in part to uncertainties both in the nuclear equation of state and the nucleon-nucleon interaction itself. For this reason, in considering neutrino-nucleon scattering, we choose to treat the nucleons as non-relativistic and non-interacting, thereby ignoring collective effects which might enhance or reduce the ν_μ-nucleon scattering rate. Particularly, in calculating this scattering rate, we ignore the effect of inelastic nucleon-nucleon scattering (*e.g.* $\nu_\mu nn \leftrightarrow \nu_\mu nn$) (Hannestad & Raffelt 1998). Making these assumptions, we find that j_ν and χ_ν in eq. (2.2) are given by

$$j_\nu = \frac{G^2}{(2\pi)^3}\int d^3\vec{p}_\nu^{\,\prime}\,\mathcal{I}_{\rm NC}\,f_\nu^\prime\,e^{-\beta\omega} \tag{2.10}$$

and

$$\chi_\nu = \frac{G^2}{(2\pi)^3}\int d^3\vec{p}_\nu^{\,\prime}\,\mathcal{I}_{\rm NC}\,[1-f_\nu^\prime], \tag{2.11}$$

where $\beta = 1/T$, $\vec{p}_\nu^{\,\prime}$ is the final state neutrino momentum, and ω is the energy transfer.

In eqs. (2.10) and (2.11), the neutral-current scattering kernel is given by

$$\mathcal{I}_{\rm NC} = S(q,\omega)\,[(1+\mu)V^2 + (3-\mu)A^2], \tag{2.12}$$

where $\mu(=\cos\theta)$ is the cosine of the scattering angle between incident and final state neutrinos and $S(q,\omega)$ is the dynamic structure function. In eq. (2.12), V and A are the appropriate vector and axial-vector coupling constants; for ν_μ-neutron scattering, $V=-1/2$ and $A=-1.26/2$. The dynamic structure function is

$$\begin{aligned} S(q,\omega) &= 2\int \frac{d^3\vec{p}}{(2\pi)^3}\, f\,(1-f')\,(2\pi)\delta(\omega+\varepsilon-\varepsilon') \\ &= 2\,{\rm Im}\Pi^{(0)}(q,\omega)\,(1-e^{-\beta\omega})^{-1} \end{aligned} \tag{2.13}$$

where $q = |p_\nu - p_\nu'| = [\varepsilon_\nu^2 + \varepsilon_\nu'^2 - 2\varepsilon_\nu\varepsilon_\nu'\mu]^{1/2}$ is the magnitude of the momentum transfer, and f and f' are the incident and scattered nucleon distribution functions, respectively. In eq. (2.13), $\vec{p}$ is the incident nucleon momentum, ε is the incident nucleon energy, and ε' is the scattered nucleon energy. The imaginary part of the free polarization is given by (Burrows & Sawyer 1998; Fetter & Walecka 1971)

$${\rm Im}\Pi^{(0)}(q,\omega) = \frac{m^2}{2\pi\beta q}{\rm ln}\left[\frac{1+e^{-Q^2+\eta}}{1+e^{-Q^2+\eta-\beta\omega}}\right], \tag{2.14}$$

where

$$Q = \left(\frac{m\beta}{2}\right)^{1/2}\left(-\frac{\omega}{q}+\frac{q}{2m}\right), \tag{2.15}$$

η is the nucleon degeneracy (μ/T), and m is the nucleon mass. The factor $e^{-\beta\omega}$ which appears in eq. (2.10) is a consequence of the fact that $S(q,-\omega) = e^{-\beta\omega}S(q,\omega)$, itself a consequence of detailed balance between the *in* and *out* channels of the Boltzmann equation. The dynamic structure function can be thought of as a correlation function which connects ε_ν and ε_ν'.

The ϕ angular integrations implicit in eqs. (2.10) and (2.11) can be computed trivially assuming the isotropy of f_ν. Furthermore, defining the coordinate system with the momentum vector of the incident neutrino, the scattering angle and the direction cosine are equivalent. Combining these two equations in the Boltzmann equation for the evolution of f_ν due to neutral-current ν_μ-nucleon scattering, we obtain

$$\frac{\partial f_\nu}{\partial t} = \frac{G^2}{(2\pi)^2}\int_0^\infty d\varepsilon'_\nu \varepsilon'^2_\nu \int_{-1}^{1} d\mu\, \mathcal{I}_{\rm NC}\left\{[1-f_\nu]\, f'_\nu e^{-\beta\omega} - f_\nu[1-f'_\nu]\right\}. \tag{2.16}$$

2.3.2 Electron Scattering: $\nu_\mu e^- \leftrightarrow \nu_\mu e^-$

At the temperatures and densities encountered in supernovae and protoneutron stars, electrons are highly relativistic. A formalism analogous to that used for ν_μ-nucleon scattering is desired in order to include the full electron kinematics at arbitrary electron degeneracy. Reddy, Prakash, & Lattimer (1998) have developed a relativistic generalization of the structure function formalism described in §2.3.1. They obtain a set of polarization functions which characterize the relativistic medium's response to a neutrino probe in terms of polylogarithmic functions. In analogy with eq. (2.16), we can write the Boltzmann equation for the evolution of f_ν due to ν_μ-electron scattering, as

$$\frac{\partial f_\nu}{\partial t} = \frac{G^2}{(4\pi)^3}\int d^3p'_\nu\, \mathcal{I}^r_{\rm NC}\left\{[1-f_\nu]\, f'_\nu e^{-\beta\omega} - f_\nu[1-f'_\nu]\right\}, \tag{2.17}$$

where $\mathcal{I}^r_{\rm NC}$ is the relativistic neutral-current scattering kernel for ν_μs, analogous to $\mathcal{I}_{\rm NC}$ in eq. (2.12). All the physics of the interaction is contained in $\mathcal{I}^r_{NC}$, which can be written as

$$\mathcal{I}^r_{\rm NC} = \frac{q^2_\mu}{\varepsilon_\nu\varepsilon'_\nu}{\rm Im}\{\Lambda^{\alpha\beta}\Pi^R_{\alpha\beta}\}(1-e^{-\beta\omega})^{-1}, \tag{2.18}$$

where q_μ $(=(\omega,\vec{q}))$ is the four-momentum transfer. As in the non-relativistic case, $\mathcal{I}^r_{\rm NC}$ is composed of the lepton tensor,

$$\Lambda^{\alpha\beta} = 8[2k^\alpha k^\beta + (k\cdot q)g^{\alpha\beta} - (k^\alpha q^\beta + q^\alpha k^\beta) - i\epsilon^{\alpha\beta\mu\nu}k^\mu q^\nu], \tag{2.19}$$

which is just the squared and spin-summed matrix element for the scattering process written in terms of k_α, the incident ν_μ four-momentum. The scattering kernel also contains the retarded polarization tensor, $\Pi^R_{\alpha\beta}$, which is directly analogous to the free polarization in the non-relativistic case given in eq. (2.13). The retarded polarization tensor is related to the causal polarization by

$$\mathrm{Im}\,\Pi^R_{\alpha\beta} = \tanh\left(-\frac{1}{2}\beta\omega\right)\mathrm{Im}\,\Pi_{\alpha\beta} \tag{2.20}$$

and

$$\Pi_{\alpha\beta} = -i\int\frac{d^4p}{(2\pi)^4}\mathrm{Tr}[G_e(p)J_\alpha G'_e(p+q)J_\beta]. \tag{2.21}$$

In eq. (2.21), p_α is the electron four-momentum and J_α is the current operator. The electron Green's functions (G_e and G'_e), explicit in the free polarization, connect points in electron energy space and characterize the effect of the interaction on relativistic electrons. The polarization tensor can be written in terms of a vector part, an axial-vector part, and a mixed part, so that

$$\Pi_{\alpha\beta} = V^2\Pi^V_{\alpha\beta} + A^2\Pi^A_{\alpha\beta} - 2VA\,\Pi^{VA}_{\alpha\beta}. \tag{2.22}$$

In turn, the vector part of the polarization tensor can be written in terms of two independent components, Π_T and Π_L. In contrast with eq. (2.12), since $v/c \sim 1$ for the electrons, the angular terms which were dropped from the matrix element in the non-relativistic case, leading to a single structure function, must now be retained. $\mathcal{I}^r_{\mathrm{NC}}$ can then be written as a set of three structure functions (Reddy, Prakash, & Lattimer 1998):

$$\mathcal{I}^r_{\mathrm{NC}} = 8\frac{q^2_\mu}{\varepsilon_\nu\varepsilon'_\nu}[A\mathcal{S}_1(q,\omega) + \mathcal{S}_2(q,\omega) + B\mathcal{S}_3(q,\omega)](1-e^{-\beta\omega})^{-1}, \tag{2.23}$$

where $A = (4\varepsilon_\nu\varepsilon'_\nu + q^2_\alpha)/2q^2$ and $B = \varepsilon_\nu + \varepsilon'_\nu$. These structure functions can be written in terms of the vector parts of the retarded polarization tensor (Π^R_T and Π^R_L), the axial part (Π^R_A), and the mixed part (Π^R_{VA}):

$$\mathcal{S}_1(q,\omega) = (V^2 + A^2)\ \left[\mathrm{Im}\Pi^R_L(q,\omega) + \mathrm{Im}\Pi^R_T(q,\omega)\right], \tag{2.24}$$

$$\mathcal{S}_2(q,\omega) = (V^2 + A^2)\ \mathrm{Im}\Pi^R_T(q,\omega) - A^2\mathrm{Im}\Pi^R_A(q,\omega), \tag{2.25}$$

and

$$\mathcal{S}_3(q,\omega) \;=\; 2VA\ \mathrm{Im}\Pi^R_{VA}(q,\omega). \tag{2.26}$$

The retarded polarization functions, in terms of differences between polylogarithmic integrals, can be found in Appendix B.3.1.

2.3.3 Electron-Positron Annihilation: $e^+e^- \leftrightarrow \nu_\mu\bar{\nu}_\mu$

Fermi's Golden Rule for the total volumetric emission rate for the production of ν_μs via electron-positron annihilation can be written as

$$\begin{aligned} Q \;&=\; \int \frac{d^3\vec{p}}{(2\pi)^3 2\varepsilon}\frac{d^3\vec{p}'}{(2\pi)^3 2\varepsilon'}\frac{d^3\vec{q}_\nu}{(2\pi)^3 2\varepsilon_\nu}\frac{d^3\vec{q}_{\bar{\nu}}}{(2\pi)^3 2\varepsilon_{\bar{\nu}}}\,\varepsilon_\nu \\ &\times \left(\frac{1}{4}\sum_s |\mathcal{M}^2|\right)(2\pi)^4\delta^4(\mathrm{P})\,\Xi[f], \end{aligned} \tag{2.27}$$

where

$$\Xi[f] = (1-f_\nu)(1-f_{\bar{\nu}})f_{e^-}f_{e^+}, \tag{2.28}$$

and $\delta^4(\mathrm{P})$ conserves four-momentum. f_{e^-} and f_{e^+} are the electron and positron distribution functions. In eq. (2.27), $p_\alpha(=(\varepsilon,\vec{p}))$ and $p'_\alpha(=(\varepsilon',\vec{p}'))$ are the four-momenta of the electron and positron, respectively, and $q^\alpha_\nu(=(\varepsilon_\nu,\vec{q_\nu}))$ and $q^\alpha_{\bar{\nu}}(=(\varepsilon_{\bar{\nu}},\vec{q_{\bar{\nu}}}))$ are the four-momenta of the ν_μ and $\bar{\nu}_\mu$, respectively. The process of electron-positron annihilation into a neutrino/anti-neutrino pairs is related to neutrino-electron scattering considered in §2.3.2 via a crossing symmetry. In order to make the problem tractable, we follow the standard procedure (Bruenn 1985) of expanding the production kernel in a Legendre series in the scattering angle to first order (see Appendix B.1.4). Near the neutrinospheres, at densities which render neutrino transport diffusive this approximation holds. In a full neutrino transport algorithm, however, which must handle both the diffusion and free-streaming limits, the second-order term, with proper closure relations, must be used in the semi-transparent regime between the neutrinospheres and the shock (Pons, Miralles, & Ibáñez 1998). Having made this approximation, including only the zeroth- and first-order terms, the single ν_μ spectrum is

$$\frac{dQ}{d\varepsilon_\nu} = (1 - f_\nu)\,\frac{\varepsilon_\nu^3}{8\pi^4}\int_0^\infty d\varepsilon_{\bar{\nu}}\,\varepsilon_{\bar{\nu}}^2\;\Phi_0^p(\varepsilon_\nu,\varepsilon_{\bar{\nu}})\,(1 - f_{\bar{\nu}}), \tag{2.29}$$

where $\Phi_0^p(\varepsilon_\nu,\varepsilon_{\bar{\nu}})$ is the zeroth-order production kernel expansion coefficient, an integral over the electron energy (see Appendix B.1.4) (Bruenn 1985). With the differential spectrum or emissivity ($dQ/d\varepsilon_\nu$) in hand, it is a simple matter to extract the contribution to the Boltzmann equation due to e^+e^- annihilation. As eq. (2.29) already contains the ν_μ blocking factor, the contribution to the Boltzmann equation, the *in* channel explicit in eq. (2.3), can be written as (Bruenn 1985)

$$\left.\frac{\partial f_\nu}{\partial t}\right|_{in} = \frac{1}{4\pi}\frac{(2\pi)^3}{\varepsilon_\nu^3}\frac{dQ}{d\varepsilon_\nu}. \tag{2.30}$$

In order to obtain the *out* channel for absorption due to e^+e^- annihilation, we need only replace $\mathcal{F}_{e^-}\mathcal{F}_{e^+}$ in eq. (2.28) with an electron/positron blocking term, $(1 - \mathcal{F}_{e^-})(1 - \mathcal{F}_{e^+})$, and replace the ν_μ and $\bar{\nu}_\mu$ blocking terms in eq. (2.29) with $\mathcal{F}_\nu\mathcal{F}_{\bar{\nu}}$. Finally, the Boltzmann equation for the evolution of f_ν in time due to $e^+e^- \leftrightarrow \nu_\mu\bar{\nu}_\mu$ can be written as

$$\frac{\partial f_\nu}{\partial t} = \frac{2G^2}{(2\pi)^3}\int_0^\infty d\varepsilon_{\bar{\nu}}\,\varepsilon_{\bar{\nu}}^2\int_0^\epsilon d\varepsilon\,H_o(\varepsilon_\nu,\varepsilon_{\bar{\nu}},\varepsilon)\;\{\Xi[f] - \Xi'[f]\}, \tag{2.31}$$

where

$$\Xi'[f] = f_\nu f_{\bar{\nu}}(1 - f_{e^-})(1 - f_{e^+}), \tag{2.32}$$

$\epsilon = \varepsilon_\nu + \varepsilon_{\bar{\nu}}$, and $H_o(\varepsilon_\nu,\varepsilon_{\bar{\nu}},\varepsilon)$ is given in eq. (B.21). In solving eq. (2.31), $f_{\bar{\nu}}$ must be evolved simultaneously with f_ν. To do so, in addition to making the appropriate changes to the vector and axial-vector coupling constants, V and A, one needs to integrate over ε_ν instead of $\varepsilon_{\bar{\nu}}$. Note that the electron and positron distribution functions appear explicitly in eq. (2.31). We take these distributions to be Fermi-Dirac at temperature T and with η_e determined by T, ρ, and Y_e.

Equation (2.27) may also be used to find the total volumetric $\nu_\mu\bar{\nu}_\mu$ pair spectrum by replacing ε_ν in the numerator with ϵ. Ignoring neutrino blocking in the final state one can show that (Dicus 1975)

$$Q_{\nu_\mu\bar{\nu}_\mu} \simeq 2.09\times 10^{24}\left(\frac{T}{\mathrm{MeV}}\right)^9 f(\eta_e) \quad \mathrm{ergs\ \ cm^{-3}\ \ s^{-1}}, \tag{2.33}$$

where

$$f(\eta_e) = \frac{F_4(\eta_e)F_3(-\eta_e)+F_4(-\eta_e)F_3(\eta_e)}{2F_4(0)F_3(0)}, \tag{2.34}$$

and

$$F_n(y) = \int_0^\infty \frac{x^n}{e^{x-y}+1}\,dx \tag{2.35}$$

are the Fermi integrals.

2.3.4 Nucleon-Nucleon Bremsstrahlung

The importance of nucleon-nucleon bremsstrahlung in late-time neutron star cooling has been acknowledged for some time (Friman & Maxwell 1979; Flowers, Sutherland, & Bond 1975). Recently, however, this process has received more attention as a contributor of $\nu_\mu\bar{\nu}_\mu$ pairs and as an energy transport mechanism in both core-collapse supernova and nascent neutron star evolution (Hannestad & Raffelt 1998; Burrows et al. 1999; Brinkmann & Turner 1988; Suzuki 1993). The contribution from nucleon-nucleon bremsstrahlung is a composite of neutron-neutron (nn), proton-proton (pp), and neutron-proton (np) bremsstrahlung. Fermi's Golden Rule for the total volumetric emissivity of single ν_μs due to nn, pp, or np bremsstrahlung, including ν_μ and $\bar{\nu}_\mu$ blocking in the final state, is given by

$$Q = \int\left[\prod_{i=1}^{4}\frac{d^3\vec{p}_i}{(2\pi)^3}\right]\frac{d^3\vec{q}_\nu}{(2\pi)^3 2\varepsilon_\nu}\frac{d^3\vec{q}_{\bar{\nu}}}{(2\pi)^3 2\varepsilon_{\bar{\nu}}}\,\varepsilon_\nu\left(s\sum|\mathcal{M}|^2\right)(2\pi)^4\delta^4(\mathrm{P})\,\Xi[f] \tag{2.36}$$

where

$$\Xi[f] = f_1 f_2(1-f_3)(1-f_4)(1-f_\nu)(1-f_{\bar{\nu}}). \tag{2.37}$$

The product of differential phase space factors in eq. (2.36) includes a term for each of the four nucleons involved in the process; 1 and 2 denote initial-state nucleons whereas 3 and 4 denote final-state nucleons. In eq. (2.36), s is a symmetry factor for identical initial-state fermions, $\vec{q}_\nu$ is the neutrino three-momentum, ε_ν is the neutrino energy, and the four-momentum conserving delta function is explicit. In a one-pion exchange model for the nucleon-nucleon interaction, the spin-summed matrix element can be approximated by (Friman & Maxwell 1979; Brinkmann & Turner 1988)

$$\sum_s |\mathcal{M}|^2 \simeq 64 G^2 g_A^2 \left(\frac{f}{m_\pi}\right)^4 \left[\left(\frac{k^2}{k^2+m_\pi^2}\right)^2 + \ldots\right] \epsilon^{-2}(\varepsilon_\nu \varepsilon_{\bar{\nu}} - \vec{q}_\nu \cdot \hat{k}\, \vec{q}_{\bar{\nu}} \cdot \hat{k}) \tag{2.38}$$

where $\epsilon = \varepsilon_\nu + \varepsilon_{\bar{\nu}}$, k is the magnitude of the nucleon momentum transfer, $g_A \simeq -1.26$, $f \sim 1$ is the pion-nucleon coupling, and m_π is the mass of the pion. In order to make the 18-dimensional phase-space integration in eq. (2.36) tractable we assume the quantity in square brackets to be of order unity, but possibly as low as 0.1 (Burrows et al. 1999). To acknowledge our ignorance, we introduce the factor, ζ, and assume these momentum terms are constant. Recently, Hanhart, Phillips, & Reddy (2001) have addressed these momentum terms in the context of axion emission and $\nu_\mu \bar{\nu}_\mu$ production in supernovae. In an effort to make contact with the approximation to the matrix element we present here, they plot ζ as a function of average relative thermal nucleon momentum ($\bar{p}$; Phillips, private communication). The function peaks for $\zeta(\bar{p})$ between $150 - 200$ MeV at $\zeta \simeq 0.47$. At $\bar{p} = 50$ MeV $\zeta \simeq 0.08$ and at $\bar{p} = 500$ MeV $\zeta \simeq 0.27$. We are most interested in the region around the ν_μ neutrinospheres, where the emergent spectrum might be most affected by nucleon-nucleon bremsstrahlung. Mass densities and temperatures in this region might be $10^{12} - 10^{13}$ g cm^{-3} and $5-10$ MeV, respectively. We estimate $\bar{p}$ in this regime to be ~ 175 MeV and take $\zeta = 0.5$ for all thermodynamical points in this Chapter. Furthermore, we neglect the momentum of the neutrinos relative to the momentum of the nucleons. We are left with a simple, but general, form for the bremsstrahlung matrix element:

$$\sum |\mathcal{M}|^2 \simeq A\zeta \frac{\varepsilon_\nu \varepsilon_{\bar{\nu}}}{\epsilon^2}, \tag{2.39}$$

where $A = 64G^2 g_A^2 f^4/m_\pi^4$. In the case of nn or pp bremsstrahlung, as appropriate for identical particles in the initial state, the symmetry factor (s) in eq. (2.36) is 1/4. Such a symmetry factor does not enter for the mixed-nucleon process, np, which is still further enhanced by the fact that a charged pion mediates the nucleon exchange (Brinkmann & Turner 1988). This increases the matrix element in eq. (2.39) by a factor of 7/3 in the degenerate nucleon limit and $\sim 5/2$ in the non-degenerate limit (Brinkmann & Turner 1988). Considering the already substantial simplifications made by choosing not to handle the momentum terms directly, we will adopt the more conservative $4 \times (7/3)$ enhancement for the np matrix element. The total volumetric emission rate combining all processes is just $Q_{tot} = Q_{nn} + Q_{pp} + Q_{np}$. What remains is to reduce eq. (2.36) to a useful expression in asymmetric matter and at arbitrary neutron and proton degeneracy.

Following Brinkmann & Turner (1988), we define new momenta, $p_\pm = (p_1 \pm p_2)/2$ and $p_{3c,4c} = p_{3,4} - p_+$, new direction cosines, $\gamma_1 = p_+ \cdot p_-/|p_+||p_-|$ and $\gamma_c = p_+ \cdot p_{3c}/|p_+||p_{3c}|$, and let $u_i = p_i^2/2mT$. Furthermore, we note that $d^3p_1 d^3p_2 = 8d^3p_+ d^3p_-$. Using the three-momentum conserving delta function, we can do the $d^3\vec{p}_4$ integral trivially. Rewriting eq. (2.36) with these definitions, we find that

$$\begin{aligned} Q &= 2As\zeta(2mT)^{9/2}(2\pi)^{-9} \int d\varepsilon_\nu\, \varepsilon_\nu^3 \int d\varepsilon_{\bar{\nu}}\, du_-\, du_+\, du_{3c}\, d\gamma_1\, d\gamma_c \\ &\times\ (\varepsilon_{\bar{\nu}}/\epsilon)^2\, (u_- u_+ u_{3c})^{1/2}\, \delta(E)\; \Xi[f], \end{aligned} \tag{2.40}$$

where

$$\delta(E) = \delta(\sum_{i=1}^{4} \varepsilon_i - \epsilon) = \delta(2T(u_- - u_{3c} - \epsilon/2T)). \tag{2.41}$$

The nucleon distribution functions in the term $\Xi[f]$ in eq. (2.40) have been rewritten in terms of the new direction cosines, the dimensionless momenta (u_i), and the initial-state nucleon degeneracy factors $\eta_{1,2} = \mu_{1,2}/T$:

$$f_1 = \frac{e^{-(a_1'+b'\gamma_1)}}{2\cosh(a_1'+b'\gamma_1)} \qquad \text{and} \qquad f_2 = \frac{e^{-(a_2'-b'\gamma_1)}}{2\cosh(a_2'-b'\gamma_1)}, \tag{2.42}$$

where $a'_{1,2} = a_{1,2}/2 = \frac{1}{2}(u_+ + u_- - \eta_{1,2})$ and $b' = b/2 = (u_+u_-)^{1/2}$. Furthermore,

$$(1-f_3) = \frac{e^{(c_1'+d'\gamma_c)}}{2\cosh(c_1'+d'\gamma_c)} \qquad \text{and} \qquad (1-f_4) = \frac{e^{(c_2'-d'\gamma_c)}}{2\cosh(c_2'-d'\gamma_c)}, \tag{2.43}$$

where $c'_{1,2} = c_{1,2}/2 = \frac{1}{2}(u_+ + u_{3c} - \eta_{1,2})$ and $d' = d/2 = (u_+u_{3c})^{1/2}$. f_ν and $f_{\bar{\nu}}$, in contrast with the nucleon distribution functions, are independent of angle; for a given set of thermodynamic conditions, they remain functions of energy alone. While non-trivial, the integrations over γ_1 and γ_c can be performed. For example, the result for the γ_1 integration is of the form

$$\frac{1}{2\sqrt{B(B+1)}} \ln\left[(B-(1+2B)\xi^2 + 2\xi\sqrt{B}(B+1)(\xi^2-1)\right], \tag{2.44}$$

where $B = \sinh^2 a'$ and $\xi = \cosh b'\gamma_1$. With a proper evaluation of the integration limits and some algebra one can rewrite this result as

$$\frac{1}{2\sinh a' \cosh a'} \ln\left[\frac{(1+\cosh a\, \cosh b + \sinh a\, \sinh b)}{(1+\cosh a\, \cosh b - \sinh a\, \sinh b)}\right]. \tag{2.45}$$

Similar operations yield a result for the γ_c integral in terms of c and d. In addition, eq. (2.41) can be used to eliminate the integral over u_-. Collectively, these manipulations reveal that the differential ν_μ bremsstrahlung emissivity at arbitrary neutron and proton degeneracy is simply a three-dimensional integral over u_+, u_{3c}, and $\varepsilon_{\bar{\nu}}$:

$$\begin{aligned} \frac{dQ}{d\varepsilon_\nu} &= Ks\zeta\,(1-f_\nu)\,\varepsilon_\nu^3 \int d\varepsilon_{\bar{\nu}}\, du_+\, du_{3c}\, (\varepsilon_{\bar{\nu}}/\epsilon)^2\, u_+^{-1/2} e^{-\beta\epsilon/2} \\ &\times \Phi(\epsilon, u_+, u_{3c})\,(1-f_{\bar{\nu}}), \end{aligned} \tag{2.46}$$

where

$$K = 2G^2 \left(\frac{m}{2\pi^2}\right)^{9/2} \left(\frac{f}{m_\pi}\right)^4 g_A^2\, T^{7/2}, \tag{2.47}$$

$$\begin{aligned}\Phi(\epsilon,u_+,u_{3c}) &= \sinh^{-1}(f)\ln\left[\left(\frac{1+\cosh(e_+)}{1+\cosh(e_-)}\right)\left(\frac{\cosh(f)+\cosh(g_+)}{\cosh(f)+\cosh(g_-)}\right)\right] \\ &\times \sinh^{-1}(j)\ln\left[\left(\frac{1+\cosh(h_+)}{1+\cosh(h_-)}\right)\left(\frac{\cosh(j)+\cosh(k_+)}{\cosh(j)+\cosh(k_-)}\right)\right], \qquad (2.48)\end{aligned}$$

and

$$\begin{aligned} e_\pm &= (u_+^{1/2} \pm u_-^{1/2})^2 - \eta_2 \\ f &= u_+ + u_- - \eta_1/2 - \eta_2/2 \\ g_\pm &= \pm 2(u_+u_-)^{1/2} - \eta_1/2 + \eta_2/2 \\ h_\pm &= (u_+^{1/2} \pm u_{3c}^{1/2})^2 - \eta_2 \\ j &= u_+ + u_{3c} - \eta_1/2 - \eta_2/2 \\ k_\pm &= \pm 2(u_+u_{3c})^{1/2} - \eta_1/2 + \eta_2/2 \quad . \qquad (2.49)\end{aligned}$$

Though u_- has been integrated out via the energy-conserving delta function, it appears here in an attempt to make this expression more compact and should be read as $u_- = u_{3c} + \epsilon/2T$. Importantly, if $\eta_1 = \eta_2$ the right-hand term within both logarithmic terms in $\Phi(\epsilon, u_+, u_{3c})$ becomes unity.

Using eq. (2.30), we can easily obtain the contribution to the Boltzmann equation due to nucleon-nucleon bremsstrahlung for arbitrary nucleon degeneracy, in asymmetric matter, and including the full nucleon and neutrino Pauli blocking terms. We find that

$$j_\nu = K's\zeta \int d\varepsilon_{\bar{\nu}}\, du_+\, du_{3c}\, (\varepsilon_{\bar{\nu}}/\epsilon)^2\, u_+^{-1/2} e^{-\beta\epsilon/2}\, \Phi(\epsilon, u_+, u_{3c})\, (1 - f_{\bar{\nu}}) \qquad (2.50)$$

where $K' = [(2\pi)^3/4\pi]K$. The nucleon phase-space integrations above are identical in form for the $\nu_\mu\bar{\nu}_\mu$ absorption process, $\nu_\mu\bar{\nu}_\mu nn \to nn$. In this case, then, the primed energies are now associated with nucleons 1 and 2 in the above manipulations and the incident nucleons (3 and 4) have unprimed energies. If we take the form derived above for the nucleon phase-space terms, the absorption channel (χ_ν) must then contain a factor of $e^{\beta\epsilon}$. In addition, the blocking term, $(1 - f_{\bar{\nu}})$, becomes $f_{\bar{\nu}}$. The Boltzmann equation for the evolution of f_ν in time is then,

$$\frac{1}{c}\frac{\partial f_\nu}{\partial t} = K' s \zeta \int d\varepsilon_{\bar{\nu}}\, du_+\, du_{3c}\, (\varepsilon_{\bar{\nu}}/\epsilon)^2\, u_+^{-1/2} e^{-\beta\epsilon/2}\ \Phi(\epsilon, u_+, u_{3c})\, \Xi[f], \tag{2.51}$$

where

$$\Xi[f] = (1 - f_\nu)(1 - f_{\bar{\nu}}) - f_\nu f_{\bar{\nu}}\, e^{\beta\epsilon}. \tag{2.52}$$

For the neutron-neutron (nn) or proton-proton (pp) bremsstrahlung contribution, we simply set $s = 1/4$ in eq. (2.51) and use $\eta_1 = \eta_2 = \eta_n$ or $\eta_1 = \eta_2 = \eta_p$, respectively. For the mixed nucleon (np) bremsstrahlung we set $s = 1$, multiply eq. (2.51) by 7/3, and set $\eta_1 = \eta_n$ and $\eta_2 = \eta_p$. While eqs. (2.46) and (2.51) may not appear symmetric in η_1 and η_2 the logarithmic terms conspire to ensure that the rates for both np and pn bremsstrahlung are identical, as they should be. That is, it makes no difference whether we set η_n or η_p equal to η_1 or η_2.

Just as in §2.3.3, in considering $e^+e^- \leftrightarrow \nu_\mu\bar{\nu}_\mu$, $f_{\bar{\nu}}$ must be evolved simultaneously with f_ν. In this case, however, the situation is simpler. Suppose we wish to compare electron-positron annihilation with nucleon-nucleon bremsstrahlung by starting at $t = 0$ with $f_{\bar{\nu}} = f_\nu = 0$ over all energies. We then solve eq. (2.31) and its $f_{\bar{\nu}}$ counterpart at each timestep and at each energy. For e^+e^- annihilation, f_ν and $f_{\bar{\nu}}$ will evolve differently; they will be visibly different at each timestep, because of the weighting of the vector and axial-vector coupling constants which appear in the matrix element. In contrast, eq. (2.51) for bremsstrahlung must be solved only once. Since there is no difference in weighting between ν_μ and $\bar{\nu}_\mu$, we can set $f_{\bar{\nu}} = f_\nu$ at every energy, at every timestep, as long as $f_{\bar{\nu}} = f_\nu$ at $t = 0$. Of course, if we wish to consider $f_{\bar{\nu}} \neq f_\nu$ initially, the two distributions would need to be evolved separately and simultaneously, coupled through the blocking and source terms on the right-hand side of the Boltzmann equation.

Equation (2.36) can also be used to find the total volumetric $\nu_\mu\bar{\nu}_\mu$ pair emissivity. To facilitate this we replace ε_ν with ϵ and insert $\int \delta(\epsilon - (\varepsilon_\nu + \varepsilon_{\bar{\nu}}))d\epsilon$. Assuming the neutrinos are radiated isotropically, we can use this delta function to do the integral over $d^3\vec{q}_{\bar{\nu}}$ and leave the total rate in terms of an integral over ε_ν from zero to ϵ and another over ϵ from zero to infinity. Momentarily ignoring neutrino blocking in the final state, the former can be integrated easily. Making the same momentum, angle, and nucleon distribution function substitutions we used in deriving the single ν_μ spectrum we can reduce the pair spectrum to an integral over u_+, u_{3c}, and $q = \epsilon/2T$. We find that

$$Q_{\nu_\mu\bar{\nu}_\mu} = Ds\zeta T^{8.5}\int dq\, du_{3c}\, du_+\, q^4 e^{-q}\, u_+^{-1/2}\, \Phi(\epsilon, u_+, u_{3c}), \tag{2.53}$$

where

$$D = \frac{8}{15}\frac{G^2 g_A^2}{\sqrt{2}\,\pi^9}\left(\frac{f}{m_\pi}\right)^4 m^{9/2}, \tag{2.54}$$

and $\Phi(\epsilon, u_+, u_{3c})$ is defined in eq. (2.48). Note that eq. (2.53) allows us to easily calculate the pair differential volumetric emissivity $(dQ_{\nu_\mu\bar{\nu}_\mu}/d\epsilon)$. For $Q^{nn}_{\nu_\mu\bar{\nu}_\mu}$ and $Q^{pp}_{\nu_\mu\bar{\nu}_\mu}$, $s = 1/4$. As with the single ν_μ spectrum, for $Q^{np}_{\nu_\mu\bar{\nu}_\mu}$ multiply eq. (2.53) by 7/3 and set $s = 1$. Finally, $Q^{tot}_{\nu_\mu\bar{\nu}_\mu}$=$Q^{nn}_{\nu_\mu\bar{\nu}_\mu}$+ $Q^{pp}_{\nu_\mu\bar{\nu}_\mu}$+$Q^{np}_{\nu_\mu\bar{\nu}_\mu}$.

The Non-Degenerate Nucleon Limit In the non-degenerate nucleon limit, the term $f_1 f_2(1-f_3)(1-f_4)$ reduces to $e^{\eta_1}e^{\eta_2}e^{-2(u_+ + u_-)}$ (Burrows et al. 1999), which is independent of angle. This tremendous simplification allows for easy integration over u_+ and u_{3c} in eqs. (2.46), (2.51), and (2.53). The total volumetric emissivity of a single $\nu_\mu\bar{\nu}_\mu$ pair in this limit, ignoring ν_μ and $\bar{\nu}_\mu$ blocking in the final state, is (Burrows et al. 1999)

$$Q_{\nu_\mu\bar{\nu}_\mu} \simeq 1.04 \times 10^{30}\zeta(X\rho_{14})^2\left(\frac{T}{\mathrm{MeV}}\right)^{5.5}\ \mathrm{ergs\,cm^{-3}\,s^{-1}}. \tag{2.55}$$

For nn and pp bremsstrahlung, X is the number fraction of neutrons (X_n) or protons (X_p), respectively. For the mixed-nucleon process (np), X^2 becomes $(28/3)X_nX_p$. Figure 2.1 compares the non-degenerate nucleon limit (eq. 2.55) with the arbitrary nucleon degeneracy generalization (eq. 2.53) in the case of neutron-neutron (nn) bremsstrahlung, as a function of the neutron degeneracy $\eta_n = \mu_n/T$. The filled square shows the degenerate limit obtained by Flowers, Sutherland, and Bond (1975). Note that at $\eta_n \simeq 0$, the fractional difference between the two is just $\sim 12\%$. At realistic neutron degeneracies within the core ($\eta_n \sim 2$), this difference approaches 30%.

The single differential ν_μ emissivity can be written in terms of the pair emissivity (Burrows et al. 1999):

$$\begin{aligned}\frac{dQ}{d\varepsilon_\nu} &= C\left(\frac{Q_{\nu_\mu\bar{\nu}_\mu}}{T^4}\right)\varepsilon_\nu^3\int_1^\infty \frac{e^{-2q_\nu x}}{x^3}(x^2-x)^{1/2}dx \\ &= C\left(\frac{Q_{\nu_\mu\bar{\nu}_\mu}}{T^4}\right)\varepsilon_\nu^3\int_{q_\nu}^\infty \frac{e^{-q}}{q}K_1(q)(q-q_\nu)^2\,dq\ ,\end{aligned} \tag{2.56}$$

where $C = 2310/2048 \simeq 1.128$, $q_\nu = \varepsilon_\nu/2T$, $q = \epsilon/2T$, and K_1 is the standard modified Bessel function of imaginary argument. A useful fit to eq. (2.56), good to better than 3% over the full range of relevant neutrino energies is (Burrows et al. 1999)

$$\frac{dQ}{d\varepsilon_\nu} \sim 0.234\ \frac{Q_{\nu_\mu\bar{\nu}_\mu}}{T}\left(\frac{\varepsilon_\nu}{T}\right)^{2.4} e^{-1.1\varepsilon_\nu/T}. \tag{2.57}$$

Using eq. (2.30), we obtain the contribution to the Boltzmann equation including Pauli blocking of ν_μ and $\bar{\nu}_\mu$ neutrinos in the final state:

$$\frac{\partial f_\nu}{\partial t} = \mathcal{C}s\zeta\int_0^\infty d\varepsilon_{\bar{\nu}}\,(\varepsilon_{\bar{\nu}}^2/\epsilon)K_1\left(\frac{\beta\epsilon}{2}\right)e^{-\beta\epsilon/2}\left\{(1-f_\nu)(1-f_{\bar{\nu}}) - f_\nu f_{\bar{\nu}}e^{\beta\epsilon}\right\}. \tag{2.58}$$

where

$$\mathcal{C} = \frac{G^2 m^{4.5}}{\pi^{6.5}}\left(\frac{f}{m_\pi}\right)^4 g_A^2\,T^{2.5}\,e^{\eta_1}\,e^{\eta_2} \simeq \frac{2G^2g_A^2}{\pi^{3.5}}\left(\frac{f}{m_\pi}\right)^4\frac{m^{1.5}}{T^{.5}}\,n_1 n_2\,. \tag{2.59}$$

In obtaining eq. (2.59), we have used the thermodynamic identity in the non-degenerate limit,

$$e^{\eta_i} = \left(\frac{2\pi}{mT}\right)^{3/2}\frac{n_i}{2}, \tag{2.60}$$

where n is the number density of nucleons considered and i is 1 or 2 for neutrons or protons, depending on which nucleon bremsstrahlung process is considered.

2.4 Results

The numerical algorithm we have developed accepts arbitrary initial ν_μ and $\bar{\nu}_\mu$ phase-space distributions. Using the scattering formalism developed in the previous section, we evolve two initial distribution functions: (1) a broad Gaussian in energy centered at 40 MeV with a maximum of $f_\nu = 0.80$ and a full-width at half-maximum of $\sim$28.6 MeV, and (2) a Fermi-Dirac distribution at a temperature $2\times$ the temperature of the surrounding matter and with zero chemical potential. While the former is unphysical in the context of supernova calculations, it illustrates the effects of blocking on both the average energy transfer and the rates for each scattering process. Furthermore, its evolution is more dynamic than the Fermi-Dirac distribution. As a result, the way in which the distribution is spread and shifted in time is more apparent. The essential differences between the two processes are then more easily gleaned. The latter initial distribution is motivated by consideration of the environment within the core of a supernova. The ν_μ and $\bar{\nu}_\mu$ distribution functions, having been generated as pairs via $e^+e^- \leftrightarrow \nu_\mu\bar{\nu}_\mu$ and nucleon-nucleon bremsstrahlung should have approximately zero chemical potential. Furthermore, even in the dense core, the ν_μs will diffuse outward in radius and, hence, from higher to lower temperatures. By starting with a Fermi-Dirac distribution at twice the temperature of the matter at that radius, we learn more about how equilibration might effect the emergent ν_μ spectrum in an actual collapse or protoneutron star cooling calculation.

For the production and emission processes, we start with zero neutrino occupancy and let each build to an equilibrium distribution of ν_μs and $\bar{\nu}_\mu$s. As a check to the calculation, the asymptotic distribution should be Fermi-Dirac at the temperature of the ambient matter with zero neutrino chemical potential. Throughout these simulations, we take the factor ζ in eq. (2.51) for nucleon-nucleon bremsstrahlung to be 0.5 (see §2.3.4).

We repeat these calculations for four temperature, density, and composition points (StarA, StarB, StarC, and StarD) taken from the one-dimensional collapse calculation profile, *Star* (Burrows, Hayes, & Fryxell 1995), corresponding to four radii below the shock ($\sim$ 80 km). Roughly, these points have densities 10^{14}, 10^{13}, 10^{12}, and 10^{11} g cm^{-3}. The actual numbers are shown in Table 2.1.

2.4.1 Scattering

Figures 2.2 and 2.3 show the evolution of a Gaussian distribution at $t = 0$ to an equilibrium Fermi-Dirac distribution at the temperature of the surrounding matter due to ν_μ-neutron ($\nu_\mu n$) and ν_μ-electron ($\nu_\mu e^-$) scattering, respectively. The equilibrium distribution has a non-zero neutrino chemical potential set by the initial total number of ν_μs, which is conserved to better than .001% throughout the calculation. Multiple curves on each plot show snapshots of f_ν in time from $t = 0$ to 1000 microseconds (μs). Both calculations were carried out at the thermodynamic point StarB whose characteristics are shown in Table 2.1. StarB is indicative of the core of a supernova, a region of moderate to high temperatures ($T \sim 15$ MeV) and densities of $\sim 10^{13}$ g cm^{-3}. These two figures illustrate the fundamental differences between $\nu_\mu e^-$ and $\nu_\mu n$ scattering as thermalization processes. Curve A in Fig. 2.2 and curve C in Fig. 2.3 indicate that at high ν_μ energies ($\varepsilon_\nu \gtrsim 30$ MeV) $\nu_\mu n$ scattering is a much more effective thermalization mechanism. At $\varepsilon_\nu \simeq 40$ MeV both curves show the distribution is within $\sim$30% of equilibrium. Importantly, however, curve A is at 0.33 μs for $\nu_\mu n$ scattering whereas curve C is at 3.30 μs for $\nu_\mu e^-$ scattering. Curve C, in Fig. 2.2 for $\nu_\mu n$ scattering, also at $t = 3.30$ μs, shows that above $\sim$25 MeV the distribution has almost equilibrated. For $\nu_\mu e^-$ scattering, similar evolution at high neutrino energies takes approximately 25 μs. These simple estimates reveal that $\nu_\mu n$ scattering is about 10 times faster than $\nu_\mu e^-$ scattering at equilibrating ν_μs with energies greater than approximately 25 MeV.

This situation is reversed at low ε_νs. Comparing curve E at $t = 33.0$ μs in both Fig. 2.2 and Fig. 2.3, we can see that at $\sim$ 10 MeV both distributions have filled to approximately the same percentage of the asymptotic, equilibrium f_ν. However, below $\varepsilon_\nu \sim$8 MeV, $\nu_\mu n$ scattering has not filled f_ν to the extent $\nu_\mu e^-$ scattering has. In fact, the rate at which these low-energy states are filled by $\nu_\mu n$ scattering is very low; the energy transfer (ω) is much smaller than the incident ν_μ energy. In this regime, the Fokker-Planck approximation for the time evolution of f_ν in energy space may be applicable. In marked contrast, Fig. 2.3 indicates how effective $\nu_\mu e^-$ scattering is at filling the lowest ε_ν states. Curves F from Figs. 2.2 and 2.3, taken at 1000 μs, show that though the distribution has reached equilibrium via $\nu_\mu e^-$ scattering, for $\nu_\mu n$ scattering the very lowest energy states remain unfilled. For each of the four points in the *Star* profile we consider, $\nu_\mu n$ scattering dominates at high energies ($\gtrsim$ 20 MeV), whereas $\nu_\mu e^-$ scattering dominates at low ν_μ energies ($\lesssim$ 10 MeV) and particularly for $\varepsilon_\nu \lesssim 3$ MeV.

Figures 2.4 and 2.5 depict the evolution of f_ν via $\nu_\mu n$ and $\nu_\mu e^-$ scattering, respectively, for an initial Fermi-Dirac distribution at 2$\times$ the temperature of the surrounding neutrons and electrons and with zero neutrino chemical potential. This calculation was carried out at StarC (see Table 2.1), which is representative of the outer core, in the semi-transparent regime, where the neutrinos begin to decouple from the matter (near the neutrinosphere). The same systematics highlighted in the discussion of the evolution of the initial Gaussian distribution for StarB are borne out in these figures. Curves A and B on both plots, denoting 0.10 and 0.33 milliseconds (ms) of elapsed time, respectively, confirm that above $\varepsilon_\nu \sim 15$ MeV $\nu_\mu n$ scattering dominates thermalization.

Figures 2.6 and 2.7 show $\langle\omega\rangle_{in}$ and $\langle\omega\rangle_{out}$, as defined in eqs. (2.6) and (2.7), for $\nu_\mu n$ scattering and $\nu_\mu e^-$ scattering, respectively. The separate curves portray the evolution in time of the thermal average energy transfers as the distributions evolve to equilibrium (cf. Figs. 2.4 and 2.5). As one would expect from kinematic arguments, the magnitudes of both $\langle\omega\rangle_{in}$ and $\langle\omega\rangle_{out}$ for $\nu_\mu n$ scattering are much less than those for $\nu_\mu e^-$ scattering. Though the energy transfers are much smaller, even at the highest energies, $\nu_\mu n$ scattering still dominates $\nu_\mu e^-$ scattering in thermalizing the ν_μ distribution because the rate for scattering is so much larger. At low neutrino energies, however, both average energy transfers for neutron scattering go to zero, whereas they approach large negative values (~ -20 MeV) for electron scattering.

At these low energies, the fact that the rate for $\nu_\mu n$ scattering is larger than for $\nu_\mu e^-$ scattering fails to compensate for the vanishing energy transfer. For example, at $\varepsilon_\nu = 3$ MeV and $t = 33$ ms, the energy transfer for $\nu_\mu e^-$ scattering is more than 100 times that for $\nu_\mu n$ scattering.

In order to fold in information about both the rate of scattering and the average thermal energy transfer, we plot Γ_D and Γ_E (eqs. 2.8 and 2.9) in Fig. 2.8 for all four points considered in the *Star* profile. We show here a snapshot of the rates for both scattering processes for a Fermi-Dirac distribution initially at twice the local matter temperature, with zero neutrino chemical potential. Note that the spikes in Γ_D indicate the neutrino energy at which $\langle\omega\rangle_{out} = 0$ (cf. Figs. 2.6 and 2.7). In general, we find that as $\varepsilon_\nu \to 0$, Γ_D and Γ_E go to zero for ν_μ-neutron scattering, whereas Γ_D approaches a constant and Γ_E gets very large for $\nu_\mu e^-$ scattering (Tubbs 1979). This is a consequence of the fact that, regardless of f_ν, $\langle\omega\rangle_{out} \to 0$ for $\nu_\mu n$ scattering as $\varepsilon_\nu \to 0$, as shown in Fig. 2.6. For $\nu_\mu e^-$ scattering the situation is different. As Fig. 2.7 reveals, $\langle\omega\rangle_{out}$ approaches ~ -20 MeV at $\varepsilon_\nu = 0$. As expected from our analysis of the evolution of f_ν in Figs. 2.4 and 2.5, at approximately 40 MeV the thermalization rate for $\nu_\mu n$ scattering for StarB is about an order of magnitude greater than that for $\nu_\mu e^-$ scattering. Specifically, the Γ_D's cross at $\sim$15 MeV, whereas the Γ_E's cross at $\sim$20 MeV. Below these energies, both $\nu_\mu n$ rates drop off precipitously as a consequence of the fact that $\langle\omega\rangle_{out} \to 0$. Below $\varepsilon_\nu \sim 5$ MeV, the thermalization rate for $\nu_\mu e^-$ scattering dominates by 2-5 orders of magnitude. As evidenced by the other panels in Fig. 2.8, this same trend holds in the other regions of the stellar profile. In general, the rates drop over the whole energy range for both processes as the density and temperature decrease, but the same systematics hold. In fact, for StarA, StarC, and StarD the Γ_E and Γ_D crossing points for both processes are lower than those for StarB. As a result of the higher temperature at this radius ($T \simeq 14.5$ MeV) $\nu_\mu e^-$ scattering is important in thermalizing slightly higher energy neutrinos than at the other radii. For StarC and StarD, specifically, both rates cross at neutrino energies less than 12 MeV.

These results demonstrate that ν_μ-nucleon scattering is an important thermalization process from the dense core through the semi-transparent regime for ν_μs with energies greater than approximately 15 MeV. The addition of this energy transfer mechanism implies that the ν_μs stay energetically coupled to the surrounding matter longer than has been previously estimated (Burrows & Mazurek 1982). We can approximate the radius at which the ν_μs energetically decouple from the matter (the E_μ-sphere) (Burrows & Mazurek 1982) by observing when the diffusion timescale is approximately equal to the equilibration timescale given by $\Gamma_D^{-1} = \tau_D$, as defined in eq. (2.8). Using this crude approximation we find that by including ν_μ-nucleon energy transfer the E_μ-sphere is pushed outward in radius by approximately 3 kilometers. This difference in radius corresponds to a 1-2 MeV drop in the matter temperature in the model *Star*. The average energy of the emergent spectrum is roughly correlated with the local matter temperature of the E_μ-sphere. Therefore, we conclude that ν_μ-nucleon energy transfer in full transport calculations will likely soften the emergent ν_μ spectrum.

2.4.2 Emission and Absorption

Figure 2.9 shows the total integrated volumetric emissivity as a function of radius in the model *Star* for nucleon-nucleon bremsstrahlung in the non-degenerate nucleon limit (eq. 2.55), its generalization for arbitrary nucleon degeneracy (eq. 2.53), and the emissivity for e^+e^- annihilation (eq. 2.33). Note that not one of these expressions contains neutrino blocking terms and that the general bremsstrahlung rate crosses that for e^+e^- annihilation at $\sim$ 23 kilometers where $\rho \simeq 6 \times 10^{12}$ g cm^{-3}, $T \simeq 11$ MeV, and $Y_e \simeq 0.13$. While this plot gives a general idea of where e^+e^- annihilation should begin to compete with nucleon-nucleon bremsstrahlung, it fails to include the differential nature of the production in energy. In addition, it does not include absorption or blocking effects, which quantitatively alter the relative strength of the emission.

To begin to understand the import of these terms and the character of each pair production process, we include Figs. 2.10 and 2.11, which show the time evolution of f_ν via nucleon-nucleon bremsstrahlung and electron-positron annihilation, respectively, for the point StarC, initialized with zero ν_μ and $\bar{\nu}_\mu$ phase-space occupancies. The final equilibrium distribution is Fermi-Dirac at the temperature of the surrounding matter, with zero neutrino chemical potential. Comparing curve C on both graphs, which marks 10.0 milliseconds (ms) of elapsed time, one can see that bremsstrahlung dominates production below ~ 15 MeV. Indeed, bremsstrahlung overshoots its equilibrium distribution at energies below 10 MeV before finally filling the higher ε_ν states. In contrast, electron-positron annihilation fills the higher states first and moves slowly toward the low-lying neutrino energies, taking a factor of 10 more time at this thermodynamic point to reach equilibrium.

In Figs. 2.12 and 2.13, we plot Γ_{in} and Γ_{out}, as defined in eqs. (2.4) and (2.5), for both production processes at the point StarB. As one would predict from our simple observations of the time evolution of f_ν, the bremsstrahlung rates are much faster ($\sim$2 orders of magnitude) than the e^+e^- annihilation rates at low neutrino energies. At StarC, e^+e^- annihilation competes with bremsstrahlung above $\varepsilon_\nu \sim 15$ MeV. For StarB, however, at a matter density an order of magnitude greater than that for StarC, the energy at which nucleon-nucleon bremsstrahlung becomes more important than e^+e^- annihilation is ~ 60 MeV. In this regime, where $T \sim 12-14$ MeV and $\rho \sim 10^{13}$ g cm^{-3}, we find that bremsstrahlung dominates neutrino pair-production via electron-positron annihilation. A close look at the evolution of the total thermal average neutrino energy ($\langle\varepsilon_\nu\rangle$) reveals that f_ν reaches its asymptotic equilibrium distribution via nucleon-nucleon bremsstrahlung in ~ 1 ms. Electron-positron annihilation takes ~ 50 ms to fill all but the very lowest energy states. This trend continues as the matter becomes more dense. For StarA, well beneath the neutrinospheres at $\rho \sim 10^{14}$

g cm^{-3}, the rates for bremsstrahlung and electron-positron annihilation never cross. In fact, the former produces an equilibrium Fermi sea of ν_μ's in $\sim$ 50 μs, whereas the latter takes $\sim 10^3$ seconds. This difference of 8 orders of magnitude in timescale, however, is a bit misleading. Similar to $\nu_\mu n$ scattering, e^+e^- annihilation has trouble filling only the very lowest neutrino energy states. In actuality, at the highest energies, both Γ_{in} and Γ_{out} for e^+e^- annihilation come within 3-4 orders of magnitude of the rates for bremsstrahlung at the same energy. Still, the difference is striking. As the temperature drops from StarB (14 MeV) to StarA (10 MeV) and the density increases by an order of magnitude, η_e goes from 3.79 to 15.75. Consequently, Pauli blocking of electrons in the final state suppresses the process $\nu_\mu\bar{\nu}_\mu \to e^+e^-$, and the phase-space density of positrons is depleted to such an extent that $e^+e^- \to \nu_\mu\bar{\nu}_\mu$ is suppressed as well. We conclude that beneath the neutrinospheres and specifically for $\rho \sim 10^{13}$ g cm^{-3}, nucleon-nucleon bremsstrahlung is the primary and dominant $\nu_\mu\bar{\nu}_\mu$ source. Near the neutrinosphere, within the gain region and behind the shock, between 30 km and 60 km at $\rho \sim 10^{12}$ g cm^{-3} and $T \sim 6 - 8$ MeV, bremsstrahlung competes with e^+e^- annihilation at all neutrino energies and is the primary production process for the low-lying ε_ν and $\varepsilon_{\bar{\nu}}$ states.

The addition of nucleon-nucleon bremsstrahlung will have quantitative implications for the ν_μ and ν_τ emergent spectra. Specifically, they should be softer and brighter. Burrows et al. (2000) confirm this with their study of static supernova and protoneutron star atmospheres, having included nucleon-nucleon bremsstrahlung in the non-degenerate limit. In addition to observing a systematic softening, they also find that the ν_μ spectrum is a factor of 2 more luminous at $\varepsilon_\nu = 10$ MeV.

2.5 Summary and Conclusions

Our results for equilibration via ν_μ-electron scattering and ν_μ-nucleon scattering indicate that the latter competes with or dominates the former as a thermalizer for neutrino energies $\gtrsim$ 10 MeV for $\rho \gtrsim 1 \times 10^{11}$ g cm^{-3} at all temperatures. At neutrino energies $\gtrsim$ 30 MeV the difference at all densities and temperatures is approximately an order of magnitude. For the production and absorption processes, we find that nucleon-nucleon bremsstrahlung, at the average energy of an equilibrium Fermi-Dirac distribution at the local temperature, is 5 and 2 orders of magnitude faster than e^+e^- annihilation at StarA ($T \sim 10$ MeV, $\rho \sim 10^{14}$ g cm^{-3}) and StarB ($T \sim 15$ MeV, $\rho \sim 10^{13}$ g cm^{-3}), respectively. Only for $\rho \sim 10^{12}$ g cm^{-3} and $T \sim 6$ MeV does $e^+e^- \leftrightarrow \nu_\mu\bar{\nu}_\mu$ begin to compete with bremsstrahlung at all energies. We conclude from this study that the emergent ν_μ and ν_τ spectrum is (1) brighter and (2) softer than previously estimated. The former results from the inclusion of the new pair emission process, nucleon-nucleon bremsstrahlung. The latter is a consequence of both the increased energy coupling between the nuclear and neutrino fluids through ν_μ-nucleon scattering and the fact that bremsstrahlung dominates e^+e^- annihilation near the neutrinospheres at the lowest neutrino energies. While the full transport problem, including ν_μ-nucleon scattering energy redistribution and nucleon-nucleon bremsstrahlung, must be solved in order to delineate precisely what consequences these processes have for the emergent ν_μ spectrum, these calculations demonstrate that they should not be omitted.

TABLE 2.1. Star Model Parameters

Label	R (km)	ρ (g cm^{-3})	T (MeV)	Y_e	η_n	η_p	η_e
StarA	10.75	1.281×10^{14}	10.56	0.2752	2.37	0.70	15.75
StarB	18.75	1.023×10^{13}	14.51	0.2021	-1.62	-3.04	3.79
StarC	34.75	1.082×10^{12}	6.139	0.0907	-2.48	-4.81	3.03
StarD	49.75	1.071×10^{11}	4.527	0.1671	-4.45	-6.06	1.93

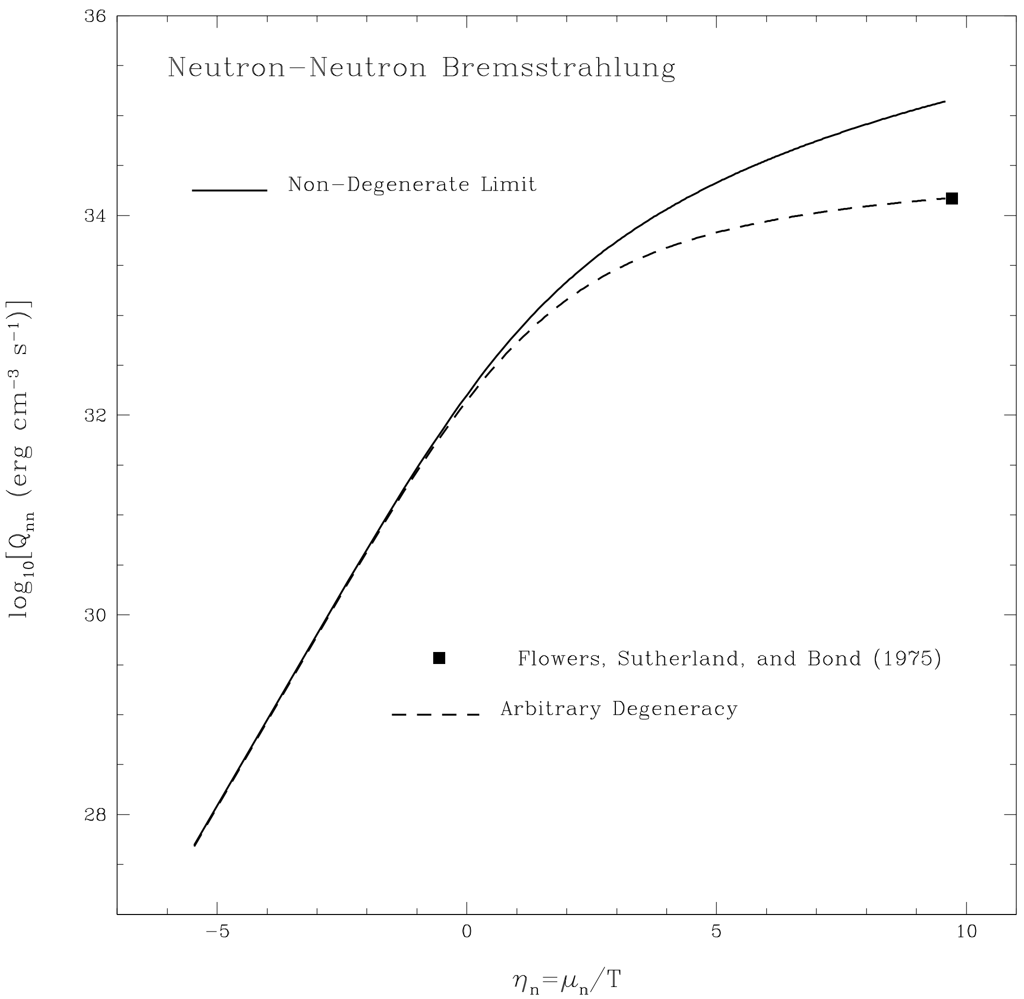

FIGURE 2.1. The total volumetric emissivity due to neutron-neutron bremsstrahlung (Q_{nn}) in ergs cm^{-3} s^{-1} in the non-degenerate neutron limit (solid line, eq. 2.55) and at arbitrary nucleon degeneracy (dashed line, eq. 2.53) for T = 6 MeV, Y_e = 0.0, and for a range of densities from 5×10^{10} g cm^{-3} to nuclear density ($\sim 2.68 \times 10^{14}$ g cm^{-3}). The filled box denotes the degenerate neutron limit obtained by Flowers, Sutherland, and Bond (1975).

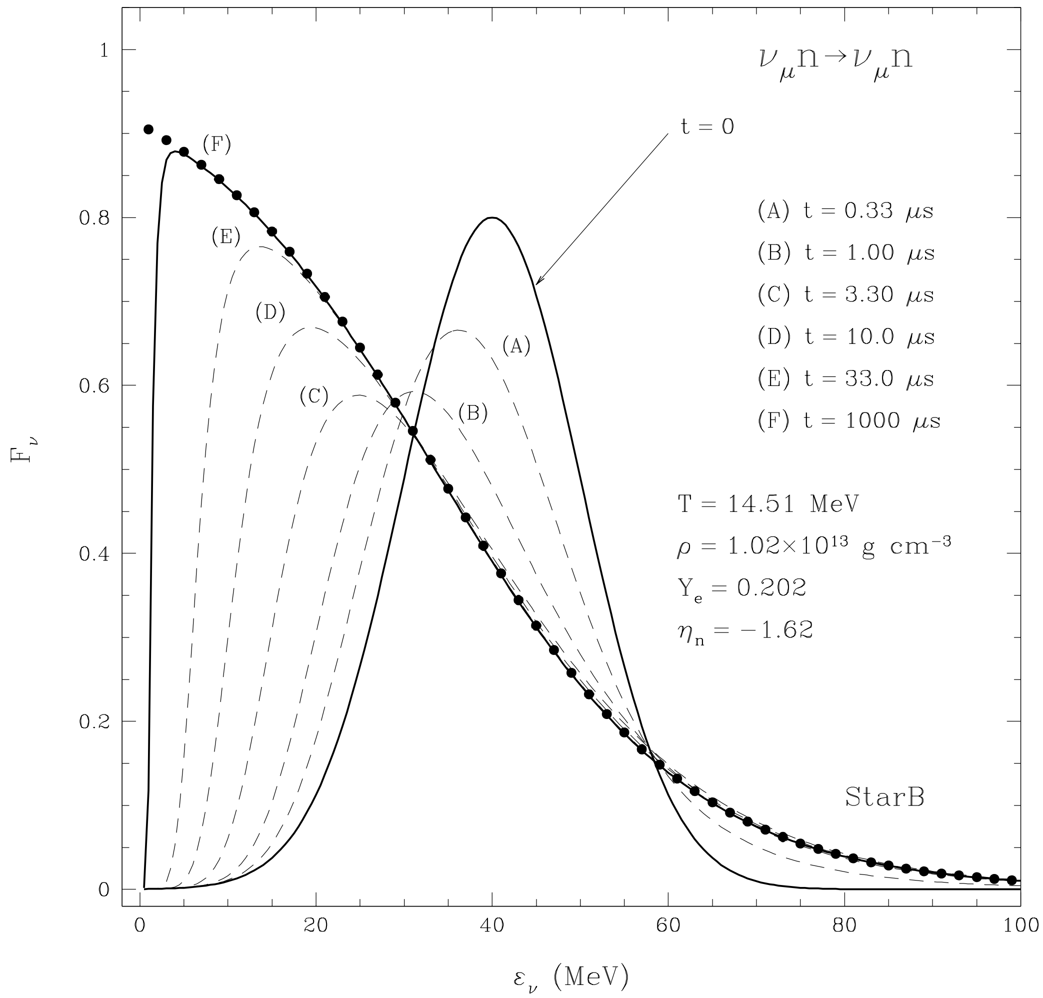

FIGURE 2.2. The time evolution via ν_μ-neutron scattering of the neutrino distribution function (f_ν) for an initial Gaussian distribution centered on 40 MeV, for the thermodynamic characteristics specified by StarB in Table 2.1. The curves show the distribution at snapshots in time: (A) $t = 0.33\,\mu$s, (B) $t = 1.00\,\mu$s, (C) $t = 3.30\,\mu$s, (D) $t = 10.0\,\mu$s, (E) $t = 33.0\,\mu$s, and (F) $t = 1000\,\mu$s. The solid dots denote an equilibrium Fermi-Dirac distribution at the temperature of the surrounding thermal bath with a neutrino chemical potential $\mu_\nu \simeq 2.32T$ set by the initial ν_μ neutrino number density.

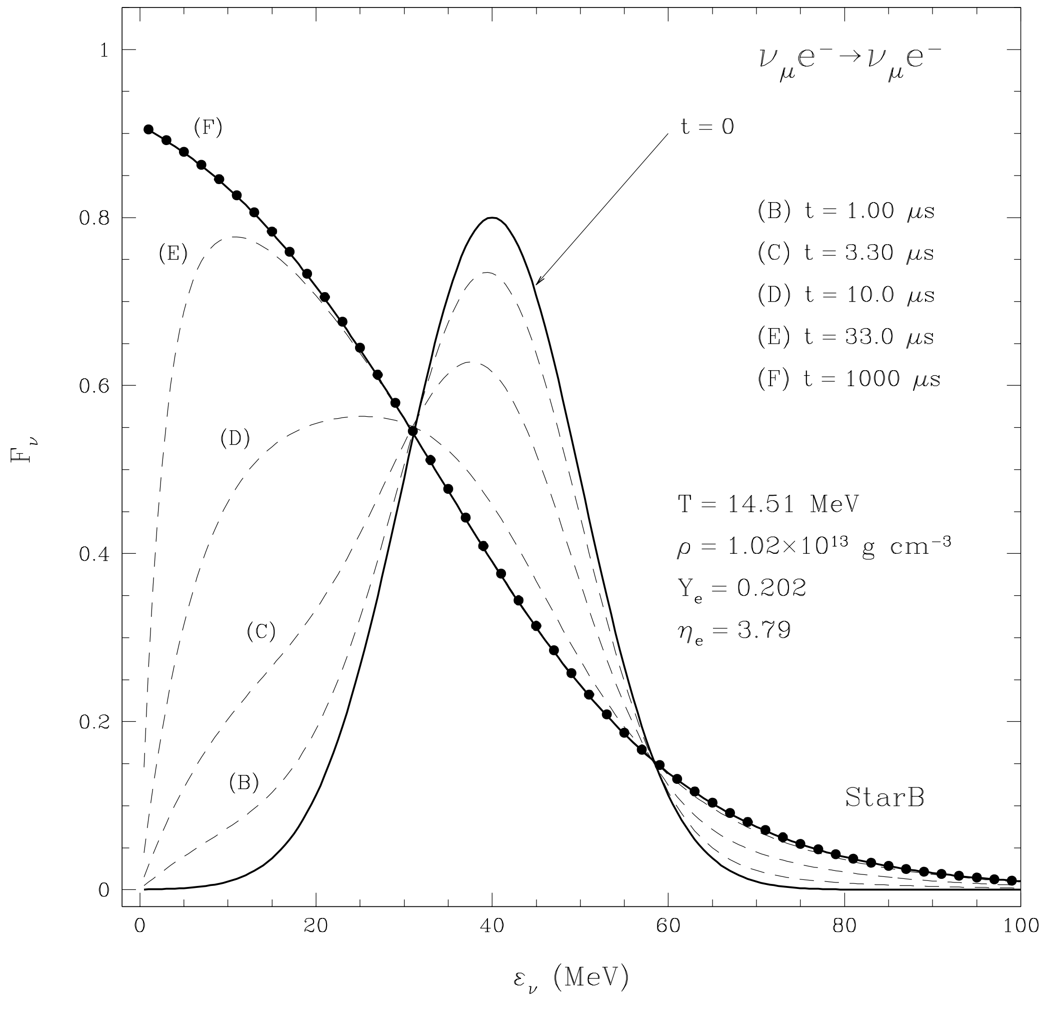

FIGURE 2.3. The same as Fig. 2.2, but for ν_μ-electron scattering.

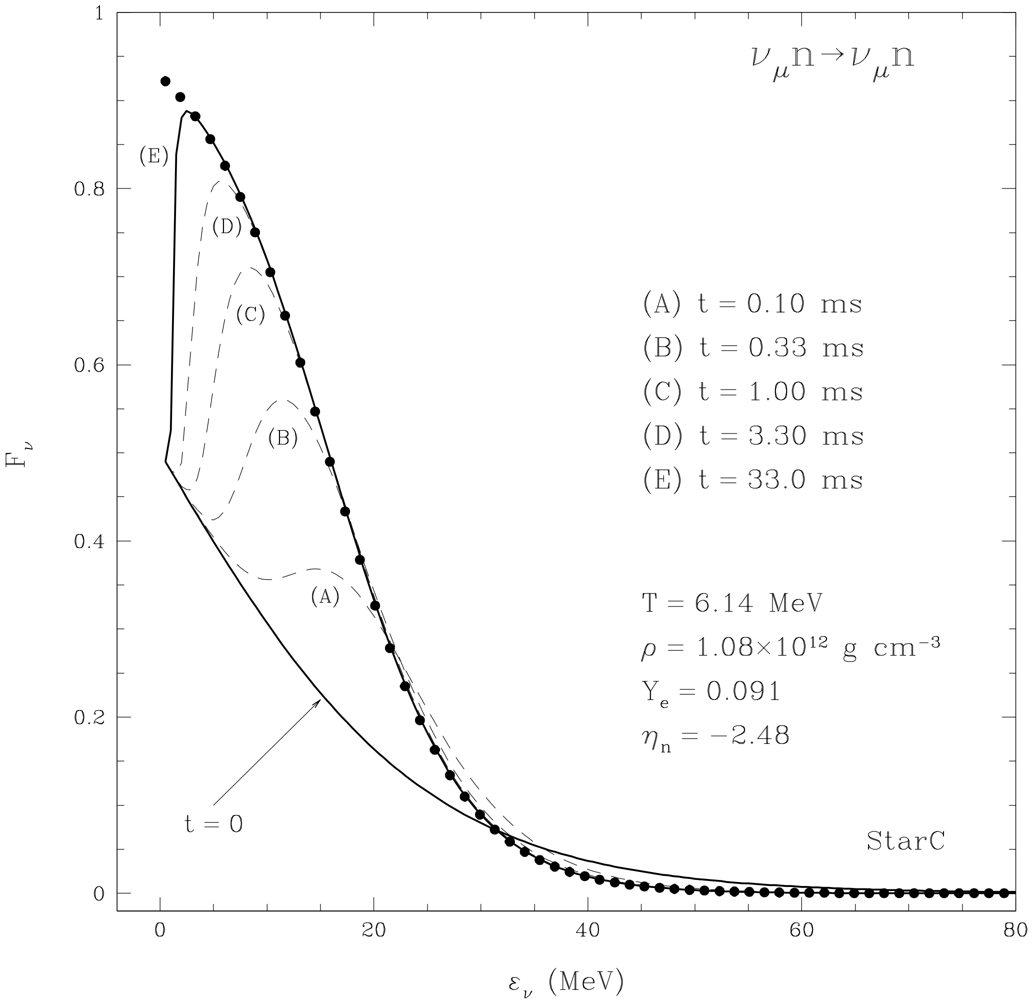

FIGURE 2.4. The time evolution via ν_μ-neutron scattering of the neutrino distribution function (f_ν) for an initial Fermi-Dirac distribution at 2× the ambient temperature, for the thermodynamic characteristics specified by StarC in Table 2.1. The curves show the distribution at snapshots in time: (A) $t = 0.10$ milliseconds (ms), (B) $t = 0.33$ ms, (C) $t = 1.0$ ms, (D) $t = 3.3$ ms, and (E) $t = 33.0$ ms. The solid dots denote an equilibrium Fermi-Dirac distribution at the temperature of the surrounding thermal bath with a neutrino chemical potential $\mu_\nu \simeq 2.55T$ set by the initial ν_μ neutrino number density. Comparison of this plot with Fig. 2.5 shows that $\nu_\mu n$ scattering dominates thermalization above $\varepsilon_\nu \sim 10$ MeV.

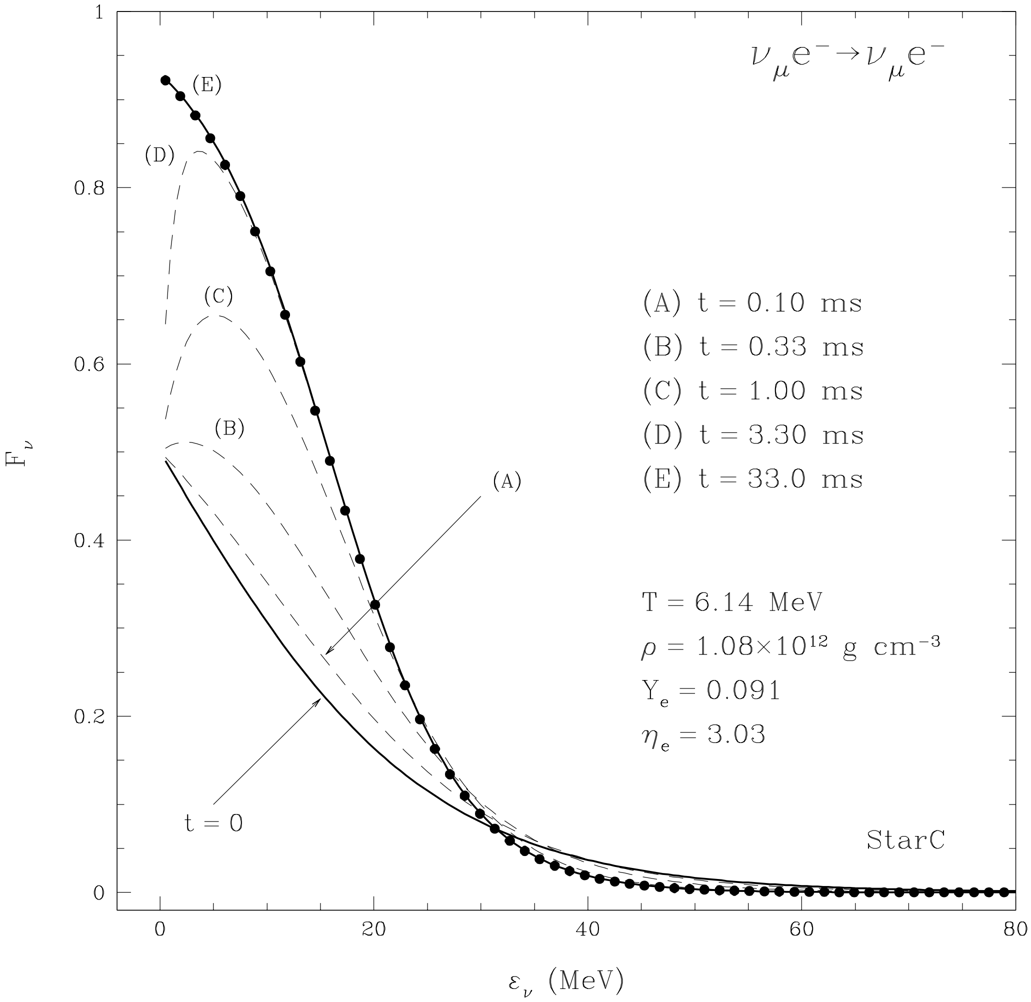

FIGURE 2.5. The same as Fig. 2.4, but for ν_μ-electron scattering. Comparison of this plot with Fig. 2.4 shows that ν_μ-electron scattering dominates thermalization below $\varepsilon_\nu \sim 10$ MeV.

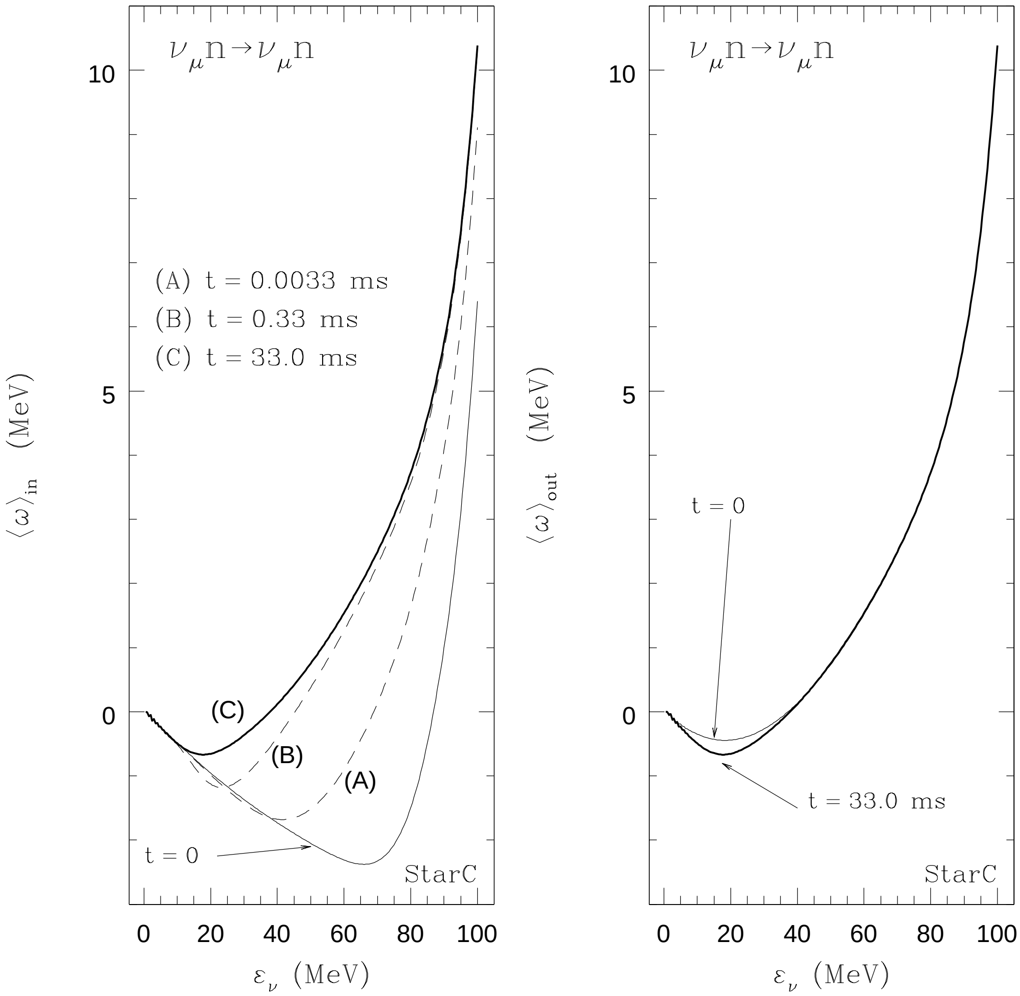

FIGURE 2.6. The thermal average energy transfers, $\langle\omega\rangle_{in}$ and $\langle\omega\rangle_{out}$, defined in eqs. (2.6) and (2.7), respectively, as a function of neutrino energy (ε_ν) for ν_μ-neutron scattering at the thermodynamic point StarC. The curves show snapshots of the average energy transfers in time as f_ν evolves (see Fig. 2.4). For $\langle\omega\rangle_{in}$, (A) $t = 0.0033$ milliseconds (ms), (B) $t = 0.33$ ms, and (C) $t = 33.0$ ms. We show $\langle\omega\rangle_{out}$ at $t = 0$ (thin line) and $t = 33.0$ ms (thick line). Note that in equilibrium ($t \sim 33.0$ ms) $\langle\omega\rangle_{in} = \langle\omega\rangle_{out}$.

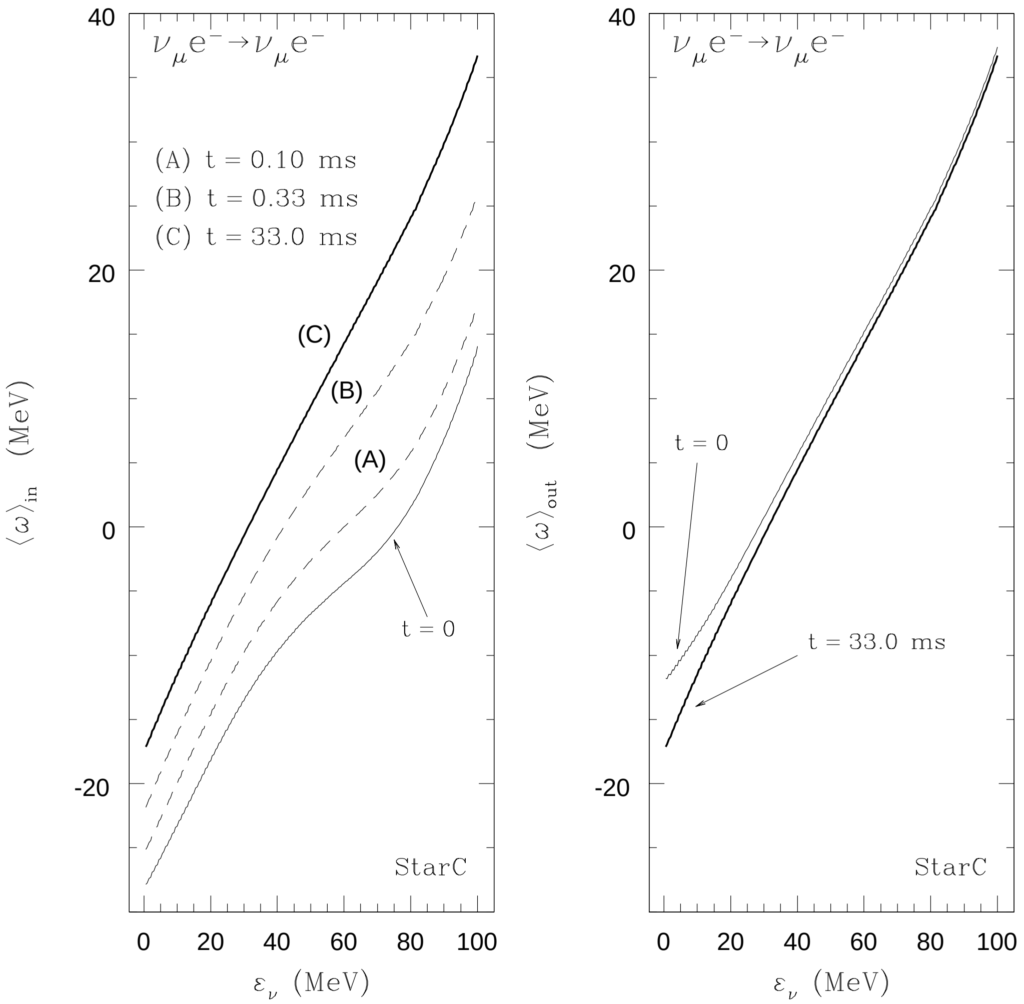

FIGURE 2.7. The same as Fig. 2.6, but for ν_μ-electron scattering. For $\langle\omega\rangle_{in}$, (A) $t = 0.10$ milliseconds (ms), (B) $t = 0.33$ ms, and (C) $t = 33.0$ ms.

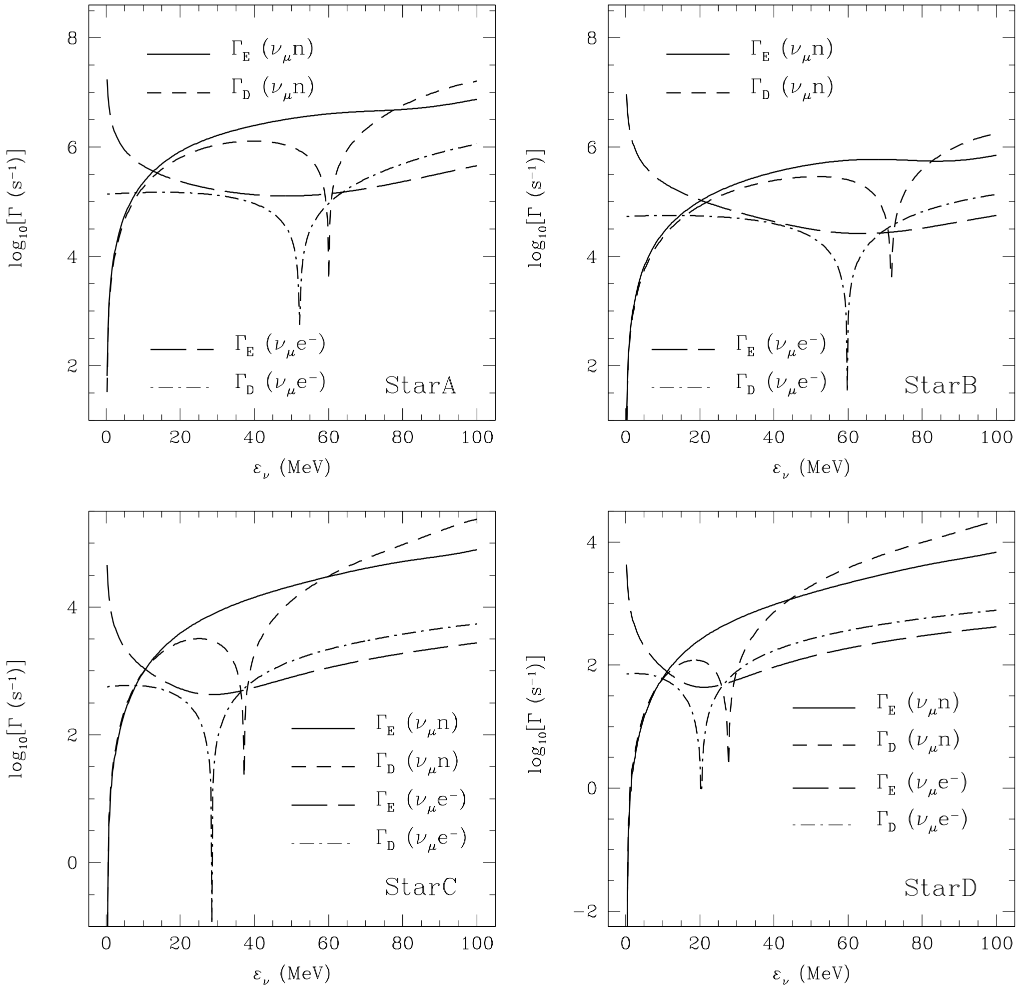

FIGURE 2.8. Γ_D and Γ_E as defined in eqs. (2.8) and (2.9), respectively, for both $\nu_\mu n$ and $\nu_\mu e^-$ scattering for an initial Fermi-Dirac distribution at StarA, StarB, StarC, and StarD (see Table 2.1) at a snapshot in time. The spikes in the Γ_D curves are a consequence of the fact that $\langle\omega\rangle_{out} \to 0$ at those neutrino energies (compare the plot above for StarA with Figs. 2.6 and 2.7). The solid and the short-dashed lines in all four plots are Γ_E and Γ_D, respectively, for $\nu_\mu n$ scattering. The long-dashed and long-short-dashed lines are Γ_E and Γ_D, respectively, for $\nu_\mu e^-$ scattering. At all four points in the stellar profile *Star*, $\nu_\mu n$ scattering dominates $\nu_\mu e^-$ scattering at energies above 10−20 MeV by approximately an order of magnitude. For StarA, the points where the rates for ν_μ-electron and ν_μ-neutron scattering cross are at ~ 8 and ~ 13 MeV. For StarB, they lie higher, at ~ 15 and ~ 20 MeV, due predominantly to the higher temperature at that radius. For both StarC and StarD, the rates cross at between 7 and 12 MeV.

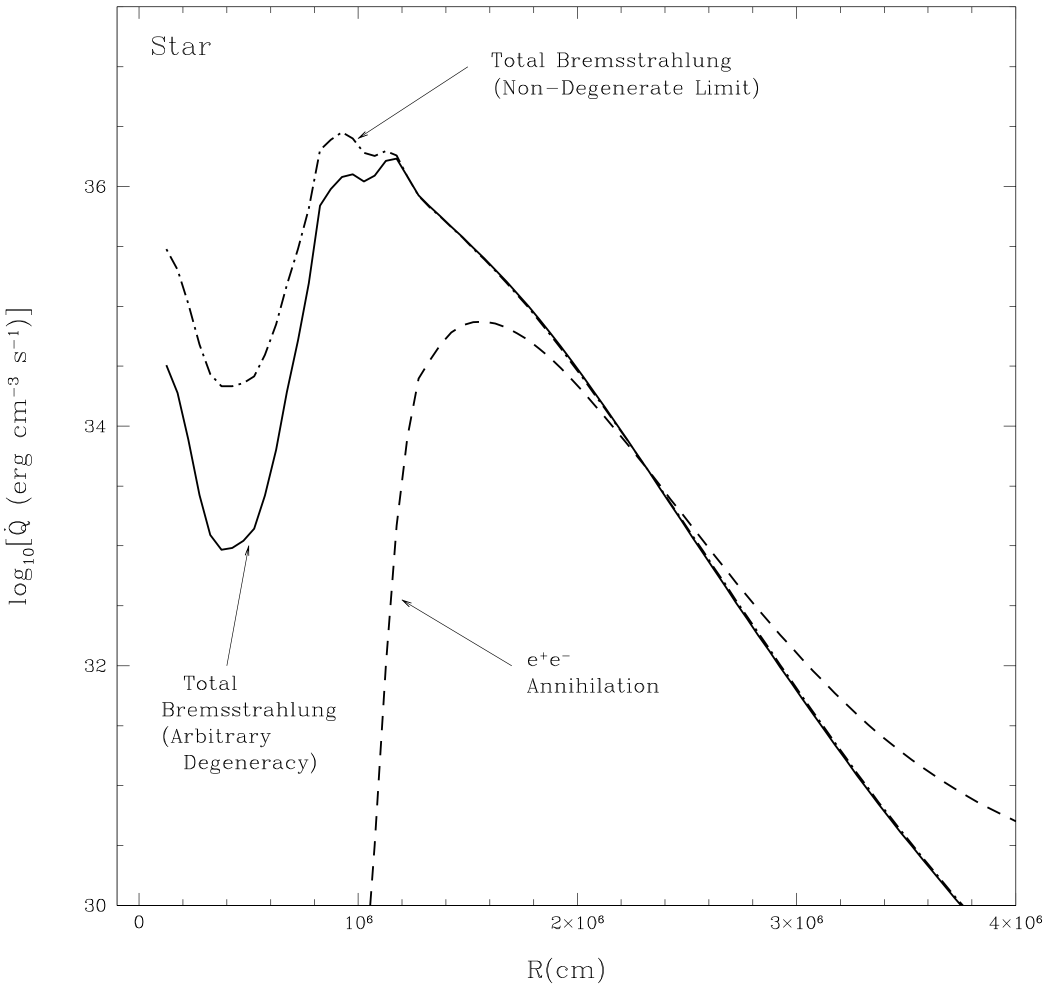

FIGURE 2.9. The integrated total volumetric emissivity in ergs cm^{-3} s^{-1} for e^+e^- annihilation and nucleon-nucleon bremsstrahlung in the non-degenerate limit (Eq. 2.55) and at arbitrary degeneracy (Eq. 2.46) as a function of radius in the stellar collapse profile, *Star*. Note that the total bremsstrahlung and e^+e^- annihilation emissivities cross at $R \sim 23$ kilometers where $\rho \simeq 6 \times 10^{12}$ g cm^{-3} and $T \simeq 11$ MeV. Above this radius, e^+e^- dominates.

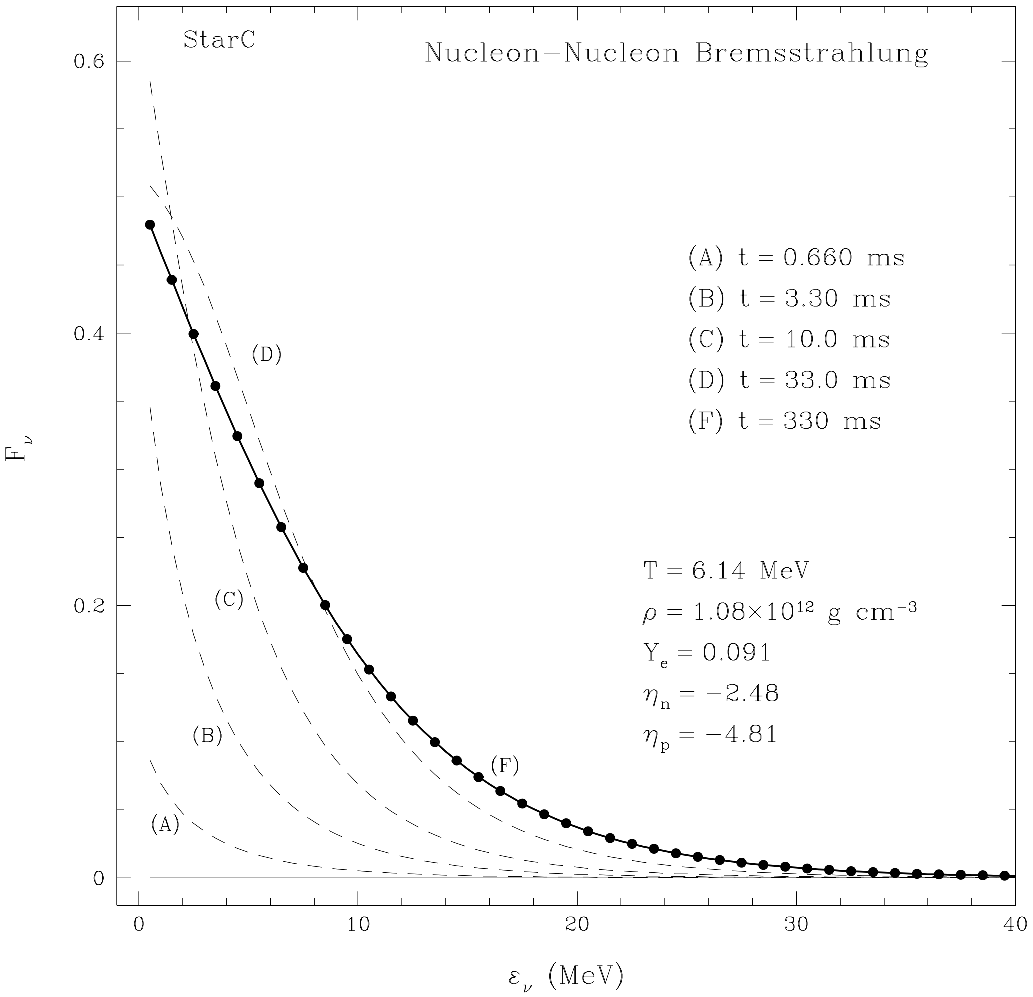

FIGURE 2.10. The time evolution of f_ν due to nucleon-nucleon bremsstrahlung via eq. (2.51) for the point StarC described in Table 2.1 starting with $f_\nu = f_{\bar{\nu}} = 0$ at all energies. Curves show snapshots of the evolution of f_ν with time: (A) $t = 0.66$ milliseconds (ms), (B) $t = 3.30$ ms, (C) $t = 10.0$ ms, (D) $t = 33.0$ ms, and (F) $t = 330$ ms. The solid dots denote an equilibrium Fermi-Dirac distribution at the temperature of the surrounding thermal bath with zero neutrino chemical potential.

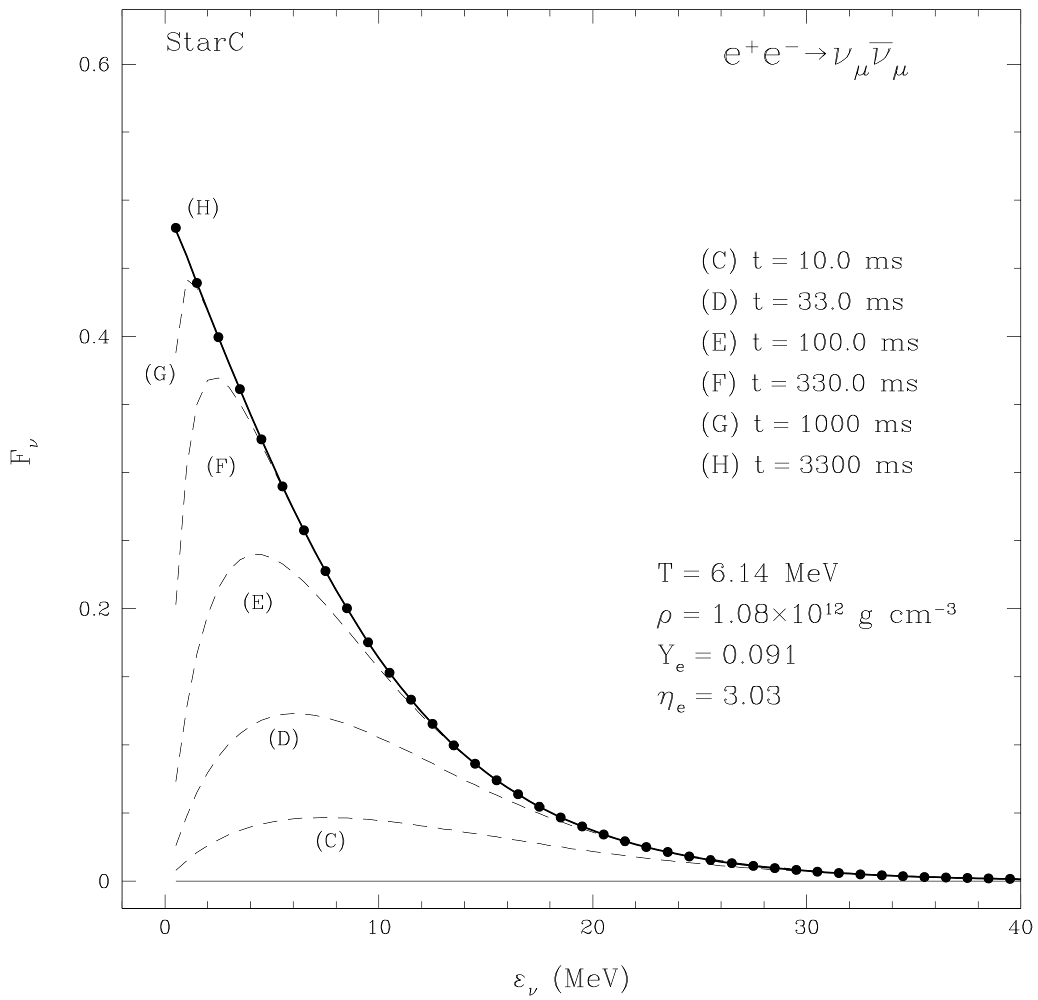

FIGURE 2.11. The same as Fig. 2.10, but for e^+e^- annihilation via eq. (2.31). Curves show snapshots of the evolution of f_ν with time: (C) $t = 10.0$ milliseconds (ms), (D) $t = 33.0$ ms, (E) $t = 100.0$ ms, (F) $t = 330.0$ ms, (G) $t = 1000$ ms, and (H) $t = 3300$ ms.

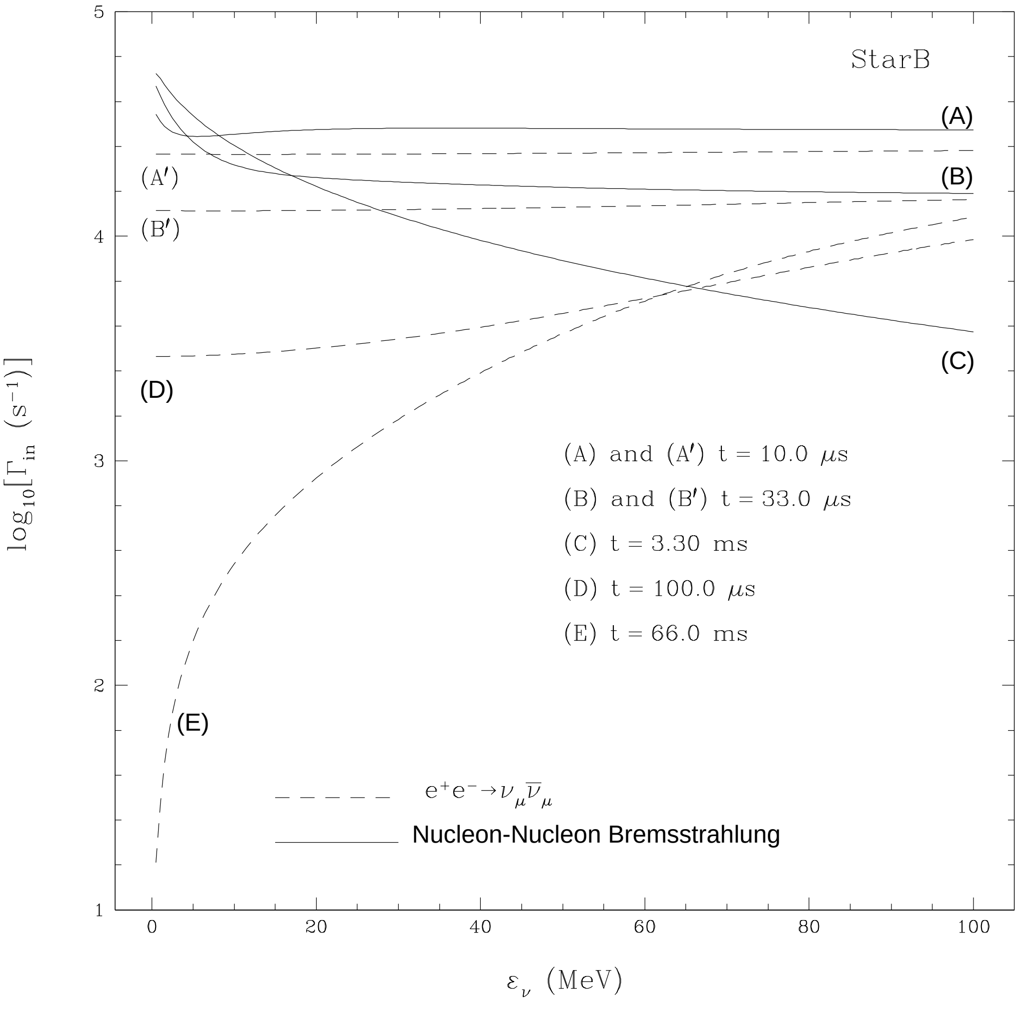

FIGURE 2.12. Γ_{in} as defined in eq. (2.4) for nucleon-nucleon bremsstrahlung (solid lines) and e^+e^- annihilation (dashed lines), for the point StarB. Each curve shows a snapshot of Γ_{in} as f_ν builds from zero phase-space occupancy at $t = 0$: for (A) and (A′) $t = 10.0$ μs. (B) and (B′) denote $t = 33.0$ μs. (C) marks the equilibrium rate for bremsstrahlung at $t = 3.3$ milliseconds. Curves (D) and (E) mark 100.0 μs and 66.0 milliseconds, respectively, for e^+e^- annihilation. The latter, marks the e^+e^- equilibrium rate. Note that the equilibrium rates cross at $\varepsilon_\nu \sim 65$ MeV.

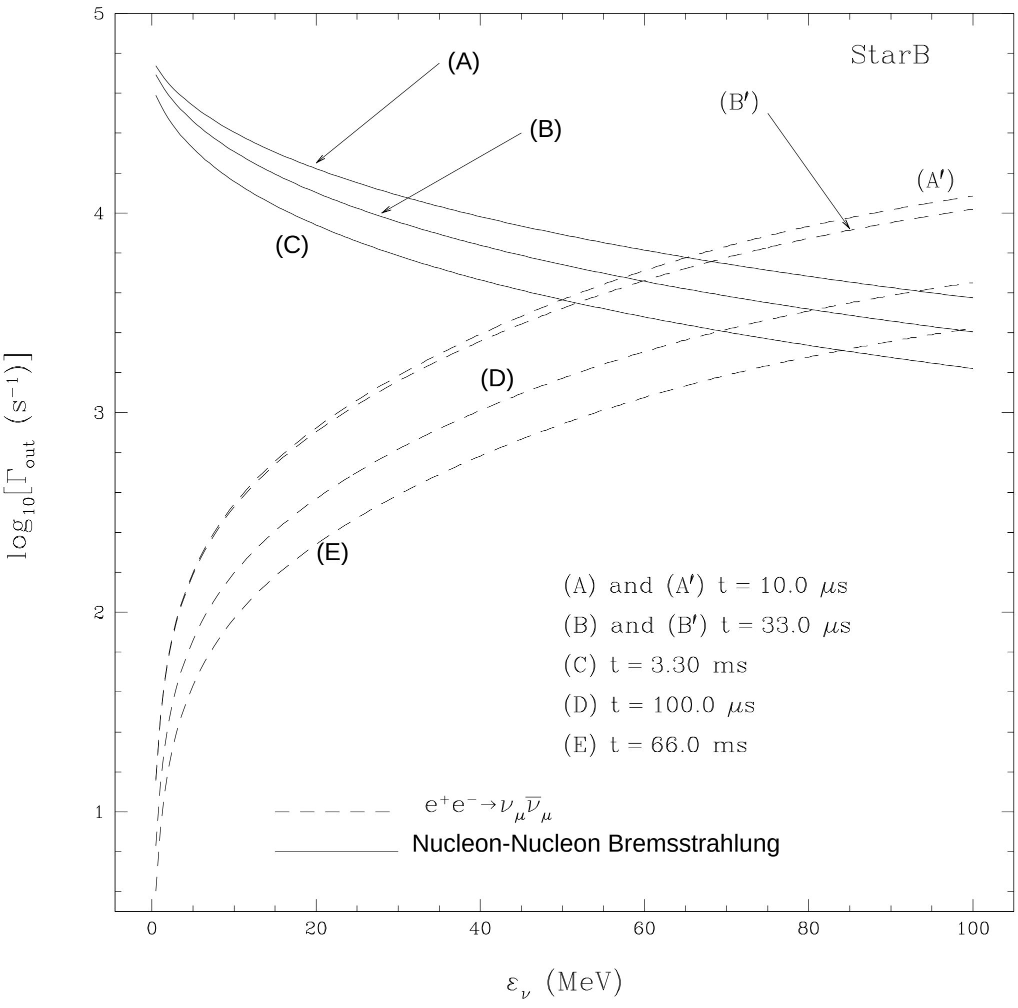

FIGURE 2.13. The same as Fig. 2.12, for the same times, but for Γ_{out} as defined in eq. (2.5).

Chapter 3

Protoneutron Star Winds

3.1 Introduction

The successful two-dimensional Type-II supernova simulation of Burrows, Hayes, and Fryxell (1995) shows clearly a post-explosion neutrino-driven wind, emerging approximately 150 milliseconds (ms) after bounce. The convective plumes and fingers due to Rayleigh-Taylor instabilities that accompany shock re-ignition in the gain region are pushed out and cleared from the area closest to the neutron star by the pressure of the neutrino-driven wind. The last 50 ms of the simulation show that a nearly spherically symmetric wind has established itself as the protoneutron star, newly born, begins its Kelvin-Helmholtz cooling phase.[1] Although these simulations employed only crude neutrino transport, did not address the issue of fallback, and did not study the wind as a function of progenitor mass and structure, they are suggestive of a general phenomenon that might naturally accompany many core-collapse supernovae.

Some multiple of 10^{53} erg will be lost via neutrino radiation by the protoneutron star as it cools. A small fraction of that energy will be deposited in the surface layers of the nascent neutron star, heating and driving material from its surface. Although the wind is interesting in its own right, hydrodynamically and as a phenomenon that attends both the supernova and the Kelvin-Helmholtz cooling phase, perhaps its most important ramification is the potential production of $\sim$50% of all the nuclides above the iron group in rapid(r) neutron-capture nucleosynthesis.

In the r-process, rapid interaction of neutrons with heavy, neutron-rich, seed nuclei allows a neutron capture-disintegration equilibrium to establish itself among the isotopes of each element. Beta decays occur on a longer timescale and increase the

[1] See 2D simulations at http://www.astrophysics.arizona.edu/movies.html.

nuclear charge. For sufficiently large neutron-to-seed ratio, the 'nuclear flow' proceeds to the heaviest nuclei, forming abundance peaks at $A \sim 80$, 130, and 195 (Burbidge et al. 1957; Wallerstein et al. 1997). The neutron-to-seed ratio itself is largely set by the dynamical timescale (τ_ρ; see eq. 3.36), entropy (s), and neutron richness in the earlier phase of the expansion (Hoffman, Woosley, and Qian 1997; Meyer and Brown 1997; Freiburghaus et al. 1999). While the nuclear physics is fairly well understood, the astrophysical site has not been unambiguously established. Currently, neutron star mergers (Freiburghaus, Rosswog, and Thielemann 1999, and references therein; Rosswog et al.1999) and protoneutron star winds (Meyer et al. 1992; Woosley and Hoffman 1992; Woosley et al. 1994; Qian and Woosley 1996; Hoffman, Woosley, and Qian 1997; Otsuki et al. 2000) are considered the most viable candidates.

In addition to attaining the requisite neutron-to-seed ratios, dynamical timescales, and temperatures, the astrophysical site must consistently reproduce the observed solar abundance pattern of r-process elements with $A \gtrsim 135$. Recent observations of neutron-capture elements in ultra-metal-poor halo stars (Burris et al. 2000; McWilliam et al. 1995a,b; Sneden et al. 1996; Cowan et al. 1996; Westin et al. 2000; Hill et al. 2001) show remarkable agreement with the solar r-process abundance pattern in this mass range. This suggests a universal mechanism for producing the second and third abundance peaks, which acts early in the chemical enrichment history of the galaxy. In this paper, beyond addressing the physical nature and systematics of the wind, we investigate its potential as a site for r-process nucleosynthesis up to and beyond the third abundance peak.

Duncan, Shapiro, & Wasserman (1986) were the first to address the physics of steady-state neutrino-driven neutron star winds. Although interested in the relative importance of the neutrino and photon luminosity in determining the wind dynamics, they also identified some of the basic systematics and scaling relations generic to the problem. More recent investigations have focused less on the general physics of the wind and more on its potential nucleosynthetic yield. Woosley et al. (1994) conducted the first such detailed study. They followed the nucleosynthesis in a protoneutron star wind that emerged in a one-dimensional post-supernova environment. Approximately 18 seconds after collapse and explosion, their model attained entropies of $\sim$400 (throughout, we quote entropy per k_B per baryon), long dynamical timescales, and electron fraction (Y_e) in the range $0.36 - 0.44$. However, in their model the supernova shock reached only 50,000 km at these late times. In turn, this external boundary caused the wind material to move slowly. It remained in the heating regime for an extended period, thus raising the entropy above what any simulation or analytical calculation has since obtained. Although the r-process proceeded to the third abundance peak in their calculation, nuclei in the mass range near $A \sim 90$ (particularly, ^{88}Sr, ^{89}Y, and ^{90}Zr) were overproduced by more than a factor of 100.

Takahashi, Witti, & Janka (1994) conducted a similar investigation, but did not attain the entropies of Woosley et al. (1994). In fact, they fell short by a factor of ~ 5. Later, Qian & Woosley (1996) showed that for reasonable protoneutron star characteristics, including post-Newtonian corrections, an entropy of 400 is unrealistic. Qian & Woosley (1996) also provided many analytical scaling relations that have since framed the discussion of neutrino-driven winds. Following this work, Hoffman, Woosley, & Qian (1997) conducted nucleosynthetic calculations in the wind models of Qian & Woosley (1996). They concluded that the standard wind models of Qian & Woosley (1996) did not produce third peak r-process nucleosynthesis. They also employed an adiabatic cooling prescription to survey the parameter space relevant to protoneutron star winds and noted several important systematics in the nucleosynthesis. Particularly, they identified a low entropy (~ 120), fast timescale ($\tau_\rho \sim 2$ ms), and *high* electron fraction ($Y_e \gtrsim 0.48$) window where third peak r-process could take place (see their Fig. 10).

Cardall & Fuller (1997) generalized some of the scaling relations presented in Qian & Woosley (1996) to include general relativity and found significant enhancements in the entropy and dynamical timescale of the wind in this framework. Recently, Otsuki et al. (2000) have sought to solve the general-relativistic wind equations and to conduct r-process calculations in the winds they obtained. They concluded that r-process nucleosynthesis can proceed to the third abundance peak at $A \sim 195$ for a protoneutron star with radius 10 km, a gravitational mass of 2 $M_\odot$, and total neutrino luminosity of 10^{52} erg s^{-1}. These conditions produce modest entropies ($s \sim 140$) and fast dynamical timescales ($\tau_\rho \sim 2-3$ ms). Although a significant parameter in protoneutron star winds, Y_e was fixed by hand in their calculations. Furthermore, they employed a simple equation of state and, in the context of the transonic wind problem, an unphysical external boundary condition.

These uncertainties and ambiguities in the conclusions of previous groups suggest that a re-evaluation is in order. Our goal in this paper is to solve the full eigenvalue problem of the steady-state transonic wind problem in general relativity, employing physical boundary conditions. Using this formalism, we survey the relevant parameter space, identify the major systematic trends, and explore some of the particulars of the general-relativistic treatment. We then use these steady-state solutions to model the whole of the Kelvin-Helmholtz cooling phase, including radial contraction of the protoneutron star, as well as the evolution of the neutrino luminosity and average neutrino energy. We estimate the total amount of material ejected during this cooling epoch, and put significant constraints on the range of entropies and dynamical timescales that might actually occur in Nature. In addition, for a subset of the models generated, we calculate the total nucleosynthetic yield as a function of atomic mass.

In §3.2, we present the fundamental equations for a time-independent neutrino-driven wind (general-relativistic and Newtonian, see Appendix A for a derivation), including the equation for the evolution of the electron fraction. In addition, we present the integrals of the motion and a discussion of the equation of state we employ. In §3.3, we describe our solution to the wind problem using an iterative relaxation procedure on an adjustable radial grid and the necessary boundary conditions. In §3.4, we present the neutrino heating rates used in this study, review the effects of general relativity, discuss potential modifications to the energy deposition rates, and explore (approximately) the effects of transport. In §3.5, we present our results for the wind problem itself. The wind structures and general characteristics as a function of neutron star mass, radius, and neutrino spectral character are explored. We cover the entire relevant parameter space and include some modifications to the power laws presented in Qian & Woosley (1996). In §3.6, we use our steady-state wind results to construct a sequence of such models that represent the time evolution of the wind during the protoneutron star cooling phase. We estimate the total mass ejected for a given evolutionary trajectory and put useful constraints on possible epochs of r-process nucleosynthesis. In §3.7, we present nucleosynthetic results from a subset of our wind trajectories. In §3.8, we discuss reasonable modifications to our wind models that might yield a successful r-process, including changes to the energy deposition function. Finally, in §3.9 we review our results, summarizing the constraints our calculations impose on the viability of the protoneutron star wind as the astrophysical site of the r-process. Furthermore, we speculate on the effects of progenitor structures and fallback, as well as hydrodynamical and transport considerations left to be addressed in future work.

3.2 The Steady-State Wind Equations

The time-independent hydrodynamical equations for flow in a Schwarzschild spacetime can be written in the form (Nobili, Turolla, and Zampieri 1991; Flammang 1982)

$$\frac{1}{vy}\frac{d(vy)}{dr} + \frac{1}{\rho}\frac{d\rho}{dr} + \frac{2}{r} = 0, \tag{3.1}$$

$$\frac{1}{y}\frac{dy}{dr} + \frac{1}{\varepsilon + P}\frac{dP}{dr} = 0, \tag{3.2}$$

and

$$\frac{d\varepsilon}{dr} - \frac{\varepsilon + P}{\rho}\frac{d\rho}{dr} + \rho\frac{\dot{q}}{vy} = 0, \tag{3.3}$$

where $u_r (= vy)$ is the radial component of the fluid four-velocity, v is the velocity of the matter measured by a stationary observer,

$$y = \left(\frac{1 - 2GM/rc^2}{1 - v^2/c^2} \right)^{1/2} , \tag{3.4}$$

$\varepsilon\,(= \rho c^2 + \rho\epsilon)$ is the total mass-energy density, ρ is the rest-mass density, P is the pressure, ϵ is the specific internal energy, and $\dot{q}$ is the energy deposition rate per unit mass. These equations assume that the mass of the wind is negligible. Although not readily apparent in the form above, eqs. (3.1)−(3.3) exhibit a critical point when v equals the local speed of sound. In order to make the solution to this system tractable and the critical point manifest we recast the equations as

$$\frac{\partial v}{\partial r} = \frac{v}{2r} \left[\frac{v_e^2}{y^2} \left(\frac{1 - c_s^2/c^2}{c_s^2 - v^2} \right) - 4c_s^2 \left(\frac{1 - v^2/c^2}{c_s^2 - v^2} \right) \right] + \frac{D}{C_V T} \frac{\dot{q}}{y} \left(\frac{1 - v^2/c^2}{c_s^2 - v^2} \right) , \tag{3.5}$$

$$\frac{\partial \rho}{\partial r} = \frac{2\rho}{r} \left(\frac{v^2 - v_e^2/4y^2}{c_s^2 - v^2} \right) - \frac{\rho}{(vy)} \frac{D}{C_V T} \frac{\dot{q}}{c_s^2 - v^2}, \tag{3.6}$$

and

$$\frac{\partial T}{\partial r} = \frac{2}{r\rho} \frac{D}{C_V} \frac{(P + \varepsilon)}{c^2} \left(\frac{v^2 - v_e^2/4y^2}{c_s^2 - v^2} \right) + \frac{\dot{q}}{C_V (vy)} \left(\frac{(1 - D/c^2) c_T^2 - v^2}{c_s^2 - v^2} \right) . \tag{3.7}$$

In the above expressions, C_V is the specific heat at constant volume, c_s is the local adiabatic sound speed, c_T is the isothermal sound speed, $v_e = (2GM/r)^{1/2}$, M is the protoneutron star gravitational mass, and

$$D = c^2 \frac{T}{\varepsilon + P} \left. \frac{\partial P}{\partial T} \right|_\rho . \tag{3.8}$$

Taking the limits $v/c \ll 1$ and $c_s/c \ll 1$ we recover the Newtonian wind equations in critical form;

$$\frac{\partial v}{\partial r} = \frac{v}{2r} \left(\frac{v_e^2 - 4c_s^2}{c_s^2 - v^2} \right) + \frac{D}{C_V T} \frac{\dot{q}}{c_s^2 - v^2}, \tag{3.9}$$

$$\frac{\partial \rho}{\partial r} = \frac{2\rho}{r} \left(\frac{v^2 - v_e^2/4}{c_s^2 - v^2} \right) - \frac{\rho}{v} \frac{D}{C_V T} \frac{\dot{q}}{c_s^2 - v^2} \tag{3.10}$$

and

$$\frac{\partial T}{\partial r}=\frac{2}{r}\frac{D}{C_V}\left(\frac{v^2-v_e^2/4}{c_s^2-v^2}\right)+\frac{\dot{q}}{C_V v}\left(\frac{c_T^2-v^2}{c_s^2-v^2}\right). \tag{3.11}$$

In this limit, D becomes $(T/\rho)\,\partial P/\partial T|_\rho$. (Please see a more detailed discussion and derivation in Appendix A) The differential wind equations, both Newtonian and general-relativistic, are solved in precisely the form above, as a two-point boundary value problem, using a relaxation algorithm described in §3.3. Note that direct integration of the continuity equation (eq. 3.1) yields the eigenvalue of the steady-state wind problem, the mass outflow rate $\dot{M}=4\pi r^2\rho v y$. In addition, for $\dot{q}=0$, eqs. (3.1)-(3.3) admit a second integral of the flow, the Bernoulli integral. We impose neither as a mathematical constraint in solving the system. Instead, we use the degree to which each is conserved to gauge the accuracy of our converged models. In the Newtonian case, the Bernoulli integral can be expressed by

$$\dot{M}\Delta\left(\epsilon+\frac{1}{2}v^2+\frac{P}{\rho}-\frac{GM}{r}\right)=\int_{R_\nu}^{r}d^3r'\,\rho\,\dot{q}=Q(r), \tag{3.12}$$

where R_ν is the coordinate radius of the protoneutron star surface. In general relativity, with $\dot{q}=0$, $\gamma h\sqrt{-g_{00}}$ is a constant. Here, γ is the Lorenz factor and h is the specific enthalpy. With a source term, the differential change in neutrino luminosity is given by

$$e^{-2\phi}\frac{\partial}{\partial\mu}(L_\nu e^{2\phi})=-\dot{q}, \tag{3.13}$$

where $d\mu/dr=4\pi r^2\rho\,e^\Lambda$ and $ds^2=-e^{2\phi}dt^2+e^{2\Lambda}dr^2+r^2d\Omega$ defines the metric. The total energy deposition rate is then,

$$Q=4\pi\int_{R_\nu}^{\infty}dr\,r^2\,\rho\,\dot{q}\,e^\Lambda\,e^{2\phi}. \tag{3.14}$$

Using these prescriptions for the Bernoulli integral and the equation for $\dot{M}$ and employing modest radial zoning (2000 points), we typically conserve both to better than 0.1%.

In our solution to the wind problem, we couple the three wind equations in critical form to the differential equation describing the evolution of the electron fraction, Y_e, due to the charged-current electron-type neutrino interactions with free nucleons: $\nu_e n \leftrightarrow e^- p$ and $\bar{\nu}_e p \leftrightarrow e^+ n$. This differential equation does not contain a critical point and can be written as

$$(vy)\frac{dY_e}{dr} = X_n[\Gamma_{\nu_e n} + \Gamma_{e^+ n}] - X_p[\Gamma_{\bar{\nu}_e p} + \Gamma_{e^- p}], \tag{3.15}$$

where X_n and X_p are the neutron and proton fraction, respectively. The Γ's are the number rates for emission and absorption, taken from the approximations of Qian & Woosley (1996). The number rate subscripts denote initial-state particles. The asymptotic value of the electron fraction (Y_e^a) is generally determined within ~10 km of the protoneutron star surface. Ignoring the details of transport and neutrino decoupling near the neutrinospheres, Y_e^a is determined by both the luminosity ratio $L_{\bar{\nu}_e}/L_{\nu_e}$ and the energy ratio $\langle\varepsilon_{\bar{\nu}_e}\rangle/\langle\varepsilon_{\nu_e}\rangle$, where $\langle\varepsilon_\nu\rangle = \langle E_\nu^2\rangle/\langle E_\nu\rangle$, and E_ν is the neutrino energy. To rough (but useful) approximation (Qian et al. 1993; Qian and Woosley 1996),

$$Y_e^a \simeq \frac{\Gamma_{\nu_e n}}{\Gamma_{\nu_e n} + \Gamma_{\bar{\nu}_e p}} \simeq \left[1 + \left(\frac{L_{\bar{\nu}_e}}{L_{\nu_e}}\right)\frac{\langle\varepsilon_{\bar{\nu}_e}\rangle - 2\Delta + 1.2\Delta^2/\langle\varepsilon_{\bar{\nu}_e}\rangle}{\langle\varepsilon_{\nu_e}\rangle + 2\Delta + 1.2\Delta^2/\langle\varepsilon_{\nu_e}\rangle}\right]^{-1}, \tag{3.16}$$

The energy threshold ($\Delta = m_n - m_p \simeq 1.293$ MeV) for the $\bar{\nu}_e$ neutrino absorption process, $\bar{\nu}_e p \to n e^+$, is manifest in eq. (3.16). Note the difference in sign on the 2Δ term between numerator and denominator. This implies that simply having $L_{\bar{\nu}_e}/L_{\nu_e} > 1$ and $\langle\varepsilon_{\bar{\nu}_e}\rangle/\langle\varepsilon_{\nu_e}\rangle > 1$ is not sufficient to guarantee $Y_e^a < 0.5$; the magnitudes of $\langle\varepsilon_{\bar{\nu}_e}\rangle$ and $\langle\varepsilon_{\nu_e}\rangle$ are also important. For example, taking $L_{\bar{\nu}_e}/L_{\nu_e} = 1.1$ and $\langle\varepsilon_{\bar{\nu}_e}\rangle/\langle\varepsilon_{\nu_e}\rangle = 13$ MeV/10 MeV gives $Y_e^a \simeq 0.52$ Hence, if $L_{\bar{\nu}_e}$ and L_{ν_e} are correlated with $\langle\varepsilon_{\bar{\nu}_e}\rangle$ and $\langle\varepsilon_{\nu_e}\rangle$, respectively, then even for constant $L_{\bar{\nu}_e}/L_{\nu_e}$ and $\langle\varepsilon_{\bar{\nu}_e}\rangle/\langle\varepsilon_{\nu_e}\rangle$, Y_e^a must increase as the total neutrino luminosity of the protoneutron star decays in time. This phenomenon, which we refer to as the *threshold effect*, is important for the viability of an r-process epoch in protoneutron star winds at late times and low $\langle\varepsilon_{\bar{\nu}_e}\rangle$ and $\langle\varepsilon_{\nu_e}\rangle$. Other possible effects that might bear materially on Y_e^a include the formation of alpha particles from free nucleons (the alpha effect) (Fuller and Meyer

1995; McLaughlin, Fuller, and Wilson 1996), the differential redshift of $\bar{\nu}_e$ neutrinos versus ν_e neutrinos, due to the physical separation of their respective neutrinospheres (Fuller and Qian 1996), and charge conjugation violation (Horowitz and Li 2000).

Coupled to the wind equations and the equation for Y_e evolution is a simple equation of state (EOS) well-suited to the conditions in the neutrino-driven wind ($T \lesssim 5$ MeV, $\rho \lesssim 10^{13}$ g cm^{-3}, and $0.0 \lesssim Y_e \lesssim 0.5$). Under these conditions, to good approximation, free neutrons, protons, and alpha particles may be treated as non-relativistic ideal gases. A fully general electron/positron equation of state is employed. Photons are also included. Past wind studies have approximated electrons and positrons as non-degenerate and relativistic. Although $\eta_e(=\mu_e/T)$ divided by π may approach $\sim$10 at the protoneutron surface, it drops steeply with the density so that in the main heating region the non-degenerate assumption is justified. In contrast, however, it is important to include the non-relativistic character of the electrons and positrons. For a broad range of protoneutron star characteristics, the temperature drops to ~ 0.5 MeV within $\sim 50-100$ km of the neutron star surface. The dynamics and asymptotic character of the wind, including mass outflow rate, asymptotic velocity, and composition can be significantly affected by assuming relativistic electrons and positrons throughout the wind profile. In addition, the important range of matter temperatures for r-process nucleosynthesis occurs for $T(r) \lesssim 0.5$ MeV. Sumiyoshi et al. (2000) have found that using a general electron/positron EOS can decrease the dynamical timescale in the nucleosynthetic region of the wind by as much as a factor of two, a potentially important modification when considering the viability of the neutrino-driven wind as a candidate site for the r-process.

3.3 Numerical Technique

Past numerical studies of steady-state protoneutron star winds have at times been hampered by unphysical boundary conditions and ill-defined numerics not generally suited to the solution of the protoneutron star wind problem.

The solution to the wind equations constitutes an eigenvalue problem. For a given set of protoneutron star characteristics and boundary conditions, there exists a unique mass outflow rate ($\dot{M} = 4\pi r^2 \rho v y$) and critical radius ($R_c$) where the matter velocity is equal to the local speed of sound ($v(R_c) = c_s$). Although eqs. (3.5)-(3.7) are ordinary differential equations, one cannot treat the wind as an initial value problem; the critical point necessitates a two-point boundary value prescription.

Even though shooting methods determine $\dot{M}$ precisely, R_c can remain uncertain (London and Flannery 1982). In addition, although Duncan, Shapiro, & Wasserman (1986) made effective use of this method, they were forced to employ two types of shooting: one for high $\dot{M}$ solutions and another for low $\dot{M}$ solutions. In an effort to circumvent these problems and to construct a robust algorithm with flexible boundary conditions, we solve both the Newtonian and general-relativistic wind equations as a two-point boundary value problem using a relaxation algorithm on an adaptive radial mesh, as described in London & Flannery (1982) (see also Kippenhahn, Weigert, and Hoffmeister 1968; Eggleton 1971; Press et al. 1992).

Both the general relativistic and Newtonian wind equations can be reduced to a set of ordinary differential equations, including the equation for the evolution of the electron fraction in radius. These equations take on the simple form,

$$\frac{d\mathbf{y}}{dx} = \mathbf{f}(x, \mathbf{y}), \tag{3.17}$$

and can be differenced as

$$\mathbf{y}_k - \mathbf{y}_{k-1} - (x_k - x_{k-1})\,\mathbf{f}\left[\frac{1}{2}(x_k + x_{k+1}), \frac{1}{2}(\mathbf{y}_k + \mathbf{y}_{k+1})\right] = \mathbf{E}_k = 0, \tag{3.18}$$

where k labels mesh points. This simple finite difference scheme couples pairs of points only. Following Press et al. (1992), the solution to the set of equations, given a guess for each $\mathbf{y}_k$, proceeds by iteration. Increments in each $\mathbf{y}_k$ are obtained by expanding the finite difference equations in a Taylor series;

$$\begin{aligned}\mathbf{E}_k(\mathbf{y}_k + \boldsymbol{\Delta}\mathbf{y}_k, \mathbf{y}_{k-1} + \boldsymbol{\Delta}\mathbf{y}_{k-1}) &\simeq \\ \mathbf{E}_k(\mathbf{y}_k, \mathbf{y}_{k-1}) &+ \sum_{n=1}^{N} \frac{\partial \mathbf{E}_k}{\partial y_{n,k-1}} \Delta y_{n,k-1} + \sum_{n=1}^{N} \frac{\partial \mathbf{E}_k}{\partial y_{n,k}} \Delta y_{n,k},\end{aligned}$$

where n labels dependent variables. The solution to the set of equations corresponds to the condition that $\mathbf{E}_k(\mathbf{y} + \boldsymbol{\Delta}\mathbf{y}) = 0$. Simple matrix manipulations give $\boldsymbol{\Delta}\mathbf{y}$ such that the solution is improved to within a specified tolerance. The set of equations to be solved is then,

$$\sum_{n=1}^{N} S_{j,n} \Delta y_{n,k-1} + \sum_{n=1}^{2N} S_{j,n} \Delta y_{n-N,k} = -E_{j,k}, \quad j = 1, 2, \ldots, N \tag{3.19}$$

where each $S_{j,n}$ is defined by (Press et al. 1992)

$$S_{j,n} = \frac{\partial E_{j,k}}{\partial y_{n,k-1}}, \quad S_{j,n+N} = \frac{\partial E_{j,k}}{\partial y_{n,k}}. \tag{3.20}$$

In practice, we take these partial derivatives numerically.

The relaxation algorithm, as outlined above, involves replacing the differential equations with algebraic difference equations at each point on the radial grid. Then, given an initial guess for each variable, at each point, the solution is obtained by iteration. However, because the condition $v(R_c) = c_s$ defines the outer boundary and this point is not known *a priori* - such knowledge would effectively constitute the solution - we follow the procedure of London & Flannery (1982) and introduce a new independent variable q that labels radial mesh points by integers ($q_1 \leq q \leq q_N$). The price paid is three more differential equations:

$$\frac{dr}{dq} = \frac{\psi}{\phi(r)},$$

$$\frac{dQ}{dq} = \psi,$$

and

$$\frac{d\psi}{dq} = 0. \tag{3.21}$$

In this scheme, r becomes a dependent variable, $Q(r)$ is a mesh spacing function (e.g., $Q(r) = \log r$), ψ is an intermediate variable, and $\phi(r)$ is proportional to the density of mesh points. The system is solved on the mesh of q values. Hence, the outer radial coordinate, at which the $v(R_c) = c_s$ boundary condition is to obtain, adjusts in a Newton-Raphson sense to simultaneously satisfy all boundary conditions. Typically, when we begin a calculation, we start with an initial guess that extends to a radius with Mach number of ~ 0.9. With each iteration, R_c is adjusted so that the Mach number goes to 1.

We now have three wind equations for $\rho(q)$, $T(q)$, and $v(q)$, three extra differential equations for the mesh algorithm, and the equation for $Y_e(q)$. Seven boundary conditions must then be imposed to close the system. The boundary conditions on the first two of eqs. (3.21) are simply $r(q_1) = R_\nu$ and $Q(q_1) = \log(R_\nu)$ (for log spacing), where R_ν is the protoneutron star radius. Two more boundary conditions obtain at the critical point. Taking q_N as the outer mesh point, we have that $v(q_N) = c_s$ and we have that the numerator of any of the differential equations for $\rho(r)$, $T(r)$, or $v(r)$ must simultaneously be zero to ensure continuity of the solution through the sonic point. Three additional boundary conditions are required to specify the problem completely. Although simply setting $Y_e(q_1)$, $\rho(q_1)$, and $T(q_1)$ at R_ν is sufficient, we do not use this prescription. Instead, we assume that the radius of neutrino decoupling coincides with the coordinate radius of the protoneutron star surface. In addition, we assume that this neutrinosphere (R_ν) is the same for all neutrino species: electron (ν_e), anti-electron ($\bar{\nu}_e$), and mu and tau neutrinos (collectively, ν_μ's). Indeed, as the protoneutron star cools we expect these neutrinospheres to be separated by just tenths of kilometers. As the ν_e neutrinos have the largest net opacity (κ_{ν_e}) of any species, we set an integral boundary condition on their optical depth (τ_{ν_e}):

$$\tau_{\nu_e}(R_\nu) = \int_{R_\nu}^{\infty} \kappa_{\nu_e} \rho \, dr = \frac{2}{3}. \tag{3.22}$$

Included in the ν_e opacity are contributions from scattering with free nucleons, scattering on electron/positron pairs, $\nu_e n \to pe^-$, and alpha scattering. As a second boundary condition, we assume that the net neutrino heating balances the net cooling at R_ν. That is, $\dot{q}(R_\nu) = 0$. Finally, our third boundary condition assumes that the charged-current processes are in equilibrium at the protoneutron star surface. Explicitly,

$$\left.\frac{dY_e}{dr}\right|_{R_\nu} = 0. \tag{3.23}$$

For a given protoneutron star mass and radius and a set of average neutrino energies and luminosities, we start with a guess for the mass density at the surface of the protoneutron star. We use a two-dimensional Newton-Raphson algorithm to simultaneously satisfy the conditions on $\dot{q}$ and dY_e/dr at R_ν. This determines $T(R_\nu)$ and $Y_e(R_\nu)$ for the first step. At each subsequent iterative step, the relaxation algorithm attempts to satisfy the integral boundary condition on τ_{ν_e}. Effectively, this procedure results in a new $T(R_\nu)$ and $Y_e(R_\nu)$. In this way, we satisfy all boundary conditions simultaneously. Given a good initial guess for the solution (i.e., maximum deviations from convergence in any variable of $\lesssim 20\%$) we obtain a solution in just 5−10 iterations. Once the profile for $R_\nu \leq r \leq R_c$ is obtained, we use l'Hospital's rule to bridge R_c and then integrate to larger radii as an initial value problem using a fourth-order Runga-Kutta scheme. Successfully converged models then serve as an initial guess for the next protoneutron star model with adjacent characteristics (i.e., in mass, radius, or neutrino spectral characteristics).

3.3.1 Tests of the Code

We do not impose $d\dot{\mathrm{M}}/dr = 0$ or the Bernoulli integral as mathematical constraints on the system. Instead, we use the degree to which these conditions obtain to gauge the precision of our method. Typically, both are conserved to better than 0.1% in both general-relativistic and Newtonian calculations. In addition, as we increase the number of mesh points, the error in both of these quantities decreases significantly.

One may argue that eq. (3.23) need not hold generally. In fact, we adjusted the code to accept a fixed $Y_e(R_\nu)$ boundary condition to make sure this has no effect on the asymptotic character of the wind. We find that the number rates are large enough at the surface that Y_e is forced from $Y_e(R_\nu)$ to a value such that $dY_e/dr \sim 0$ in the first radial zone with no appreciable effect on any aspect of the wind. For simplicity, then, we have chosen to enforce eq. (3.23).

Similarly, in a fully dynamical calculation, one would not expect $\dot{q}(R_\nu) = 0$, generally. While this may certainly be true, in our solution to the steady-state wind we encounter numerical instabilities that preclude solution of the equations with finite $\dot{q}(R_\nu)$. It is difficult to estimate the importance of such an assumption without employing the full machinery of radiation hydrodynamics.

3.4 The Neutrino Heating Function

The neutrino energy deposition rate ($\dot{q}$) is a sum of contributions from the charged-current ν_e and $\bar{\nu}_e$ neutrino absorption processes, neutrino-electron/positron scattering, neutrino-nucleon scattering, and the process $\nu\bar{\nu} \leftrightarrow e^+e^-$. We describe each in turn.

3.4.1 The Charged-Current Processes

At the entropies encountered in supernovae ($\lesssim 40$), the charged-current or beta processes ($\nu_e n \leftrightarrow e^- p$ and $\bar{\nu}_e p \leftrightarrow e^+ n$) dominate the opacity and energy exchange for the electron and anti-electron neutrinos. In the protoneutron star wind context, at much higher entropies, we expect these processes to compete with neutrino-electron/positron scattering in the net energy deposition. Ignoring final-state blocking and assuming relativistic electrons and positrons, the charged-current cooling function can be written as

$$C_{\rm cc} \simeq 2.0 \times 10^{18}\, T^6 \left[X_p \frac{F_5(\eta_e)}{F_5(0)} + X_n \frac{F_5(-\eta_e)}{F_5(0)} \right] \quad \text{erg g}^{-1}\ \text{s}^{-1}, \tag{3.24}$$

where

$$F_n(y) = \int_0^\infty \frac{x^n}{e^{x-y}+1}\, dx$$

are the Fermi integrals, X_n and X_p are the neutron and proton fractions, respectively, T is in MeV, and $\eta_e = \mu_e/T$. The heating rate due to neutrino captures on free nucleons can be written as

$$\begin{aligned} H_{\rm cc} \quad \simeq & \quad 9.3 \times 10^{18}\ R_{\nu 6}^{-2} \quad \text{erg g}^{-1}\ \text{s}^{-1} \\ & \times \ \left[X_n\, L_{\nu_e}^{51}\, \langle \varepsilon_{\nu_e}^2 \rangle + X_p\, L_{\bar\nu_e}^{51}\, \langle \varepsilon_{\bar\nu_e}^2 \rangle \right]\ \Phi^6\ \Xi(r), \end{aligned} \tag{3.25}$$

where $R_{\nu 6}$ is the neutrinosphere radius in units of 10^6 cm and both L_ν and $\langle\varepsilon_\nu\rangle$ are defined at R_ν. We separate L_ν and $\langle\varepsilon_\nu\rangle$ in this heating rate and those below. Although L_ν and $\langle\varepsilon_\nu\rangle$ are correlated, L_ν and the tail of the neutrino energy distribution are generally not. We retain L_ν and $\langle\varepsilon_\nu\rangle$ separately so we have the freedom to change them independently. With eqs. (3.24) and (3.25), the net energy deposition due to the charged-current processes is then $\dot q_{cc} = H_{cc} - C_{cc}$. In eq. (3.25),

$$\langle \varepsilon_\nu^2 \rangle = \int_{-1}^{1} d\mu \int d\varepsilon_\nu \varepsilon_\nu^5 f_\nu \cdot \left[\int_{-1}^{1} d\mu \int d\varepsilon_\nu \varepsilon_\nu^3 f_\nu \right]^{-1}, \tag{3.26}$$

where $\mu (= \cos\theta)$ is the cosine of the zenith angle and f_ν is the neutrino distribution function. Φ accounts for the gravitational redshift of neutrinos from the protoneutron star surface and is given by

$$\Phi = \left(\frac{1 - 2GM/R_\nu c^2}{1 - 2GM/rc^2} \right)^{1/2}. \tag{3.27}$$

Also present in eq. (3.25) is the spherical dilution function, $\Xi(r)$, which describes the radial dependence of the neutrino energy and number densities. In the vacuum approximation, assuming a sharp neutrinosphere,

$$\Xi(r) = 1 - \sqrt{1 - (R_\nu/r)^2/\Phi^2} \tag{3.28}$$

and is related to the flux factor $\langle\mu\rangle(= F_\nu/J_\nu)$ by $\langle\mu\rangle = R_\nu^2/2\Phi^2\Xi(r)r^2$, where F_ν and J_ν are the neutrino flux and energy density, respectively. In eq. (3.28), the factor Φ^2 accounts for the bending of null geodesics in a curved spacetime (Cardall and Fuller 1997; Salmonson and Wilson 1999). This effectively increases the neutrino number density a given mass element sees at any radius, thus augmenting the energy deposition. In contrast, since the heating rate for any neutrino interaction is proportional to positive powers of L_ν and $\langle\varepsilon_\nu\rangle$, the gravitational redshift terms which modify these quantities can only decrease the energy deposition rate at a given radius. As pointed out by Cardall & Fuller (1997), the augmentation of $\dot{q}$ by the bending of neutrino trajectories and the degradation of $\dot{q}$ by the gravitational redshift compete as M/R_ν increases, but the latter dominates.

Qian & Woosley (1996), Otsuki et al. (2000), and Wanajo et al. (2000) have employed eq. (3.28) or its Newtonian analog in their studies of neutrino-driven winds. In an effort to address neutrino decoupling more fully, we compared our wind solutions using this spherical dilution factor to those obtained with an effective $\Xi(r)$ derived from the Monte-Carlo transport results of Janka (1991) who connected $\langle\mu\rangle$ with the density gradient at 10^{10} g cm^{-3} and the curvature of the opacity profile at the radius of decoupling. The difference between the radial dependence of $\langle\mu\rangle$ using this approach and the effective flux factor obtained in a vacuum approximation is significant, as would be expected, only when the atmosphere is sufficiently extended. That is, as the density gradient just exterior to the neutrinosphere goes to infinity, so too should the Monte-Carlo results of Janka (1991) approach the vacuum approximation. Hence, significant deviations from the vacuum approximation only present themselves when the radius of the neutron star is large ($\sim 20 - 40$ km) and/or the total neutrino luminosity is very high (i.e., the temperature at R_ν is large). As the protoneutron star cools and the luminosity decreases for a given R_ν, the density gradient becomes steeper (see Fig. 3.2 below), thus making the vacuum approximation more appropriate. Over the range of models presented here, we have examined the effects of using the Janka (1991) $\langle\mu\rangle$ in order to characterize the spherical dilution of neutrinos for all of the relevant heating processes and find them negligible, particularly for the compact protoneutron star wind models most likely to be important for r-process nucleosynthesis.

We emphasize that this simple comparison is not a complete analysis of the transport effects that might be important in determining $\dot{q}(r)$. While this result suggests the vacuum approximation is appropriate in our scheme for handling the neutrinospheres and boundary conditions, it says nothing about actual transport effects in the decoupling region.

3.4.2 Neutrino-Electron/Positron Scattering

At high entropies, electron-positron pairs are produced in abundance. Therefore, neutrino-pair scattering is expected to contribute substantially to the total energy deposition in the protoneutron star wind. The energy transfer associated with a single neutrino-electron or positron scattering event is well approximated by $\omega_i \simeq (\varepsilon_{\nu_i} - 4T)/2$, where ω is the energy transfer, T is the matter temperature, and ε_{ν_i} is the neutrino energy of species i (Bahcall 1964). We have confirmed this approximation using the thermalization code described in Chapter 2, which employs the fully relativistic structure function formalism of Reddy, Prakash, & Lattimer (1998). The net heating rate due to the interaction of the neutrino fluid with the pair plasma can be approximated by $\dot{q} \simeq c n_e n_{\nu_i} \langle\sigma_{\nu_i e}\,\omega\rangle$, where n_e and n_{ν_i} are the number density of electrons and neutrinos, respectively, and $\sigma_{\nu_i e}$ is the cross section for scattering. We obtain

$$\dot{q}_{\nu_i e} = \int \omega\, c\, \sigma_{\nu_i e} \frac{dn_e}{d\varepsilon_e} d\varepsilon_e \frac{dn_{\nu_i}}{d\varepsilon_{\nu_i}} d\varepsilon_{\nu_i}, \tag{3.29}$$

where $\sigma_{\nu_i e}(=\kappa_i\, T\, \varepsilon_{\nu_i})$ is the cross-section for neutrino scattering on relativistic, non-degenerate electrons (Tubbs and Schramm 1975). $\kappa_i = \sigma_o \Lambda_i / 2m_e^2$ is a neutrino species dependent constant, where m_e is the mass of the electron in MeV, $\sigma_o \simeq 1.71 \times 10^{-44}$

cm^2, and

$$\Lambda_i = (c_V + c_A)^2 + \frac{1}{3}(c_V - c_A)^2. \tag{3.30}$$

c_V and c_A are the vector and axial-vector coupling constants for a given neutrino species. We find that the energy deposition rate can be expressed as

$$\begin{aligned} \dot{q}_{\nu_i e} \;&=\; \frac{c}{\rho}\left(\frac{T^3}{(\hbar c)^3}\frac{F_2(\eta_e)}{\pi^2}\right)\frac{L_\nu}{4\pi r^2 c\langle\varepsilon_\nu\rangle\langle\mu\rangle}\;\Phi^2\;\;\mathrm{erg\;\;g^{-1}\;\;s^{-1}} \\ &\times\;\left[\frac{\kappa}{2}\langle\varepsilon_\nu\rangle\frac{F_4(\eta_\nu)}{F_3(\eta_\nu)}T\left(\langle\varepsilon_\nu\rangle\Phi\frac{F_2(\eta_\nu)}{F_3(\eta_\nu)} - 4T\frac{F_3(\eta_e)}{F_4(\eta_e)}\right)\right]. \end{aligned} \tag{3.31}$$

We drop the subscript i here for brevity. Note that $\langle\mu\rangle(= R_\nu^2/2\Phi^2\Xi(r)r^2)$ contains two powers of the redshift. η_ν is an effective degeneracy parameter obtained from fitting the neutrino distribution function with a Fermi-Dirac distribution with an appropriate T_ν and η_ν (Janka and Hillebrandt 1989). Although we retain the general form here, in the wind calculations presented below we take $\eta_\nu = 0$ for all neutrino species. In eq. (3.31), the first term in parentheses is the number density of electrons, n_e. Alternatively, with the replacement $\eta_e \to -\eta_e$, it is the number density of positrons. The next term is the number density of neutrinos, a function of radius, which depends also on the flux factor, $\langle\mu\rangle$. The term in square brackets is the appropriately averaged product of the cross section for scattering and the energy transfer per scattering, $\langle\sigma_{\nu_i e}\,\omega\rangle$. We retain the form $\dot{q} = c n_e n_{\nu_i}\langle\sigma_{\nu_i e}\,\omega\rangle$ here for clarity. Note that, for $\eta_\nu = \eta_e = 0$, $\langle\varepsilon_\nu\rangle$ equals $3.15T_\nu$ and the second quantity in parentheses in eq. (3.31) is simply $(T_{\nu_i} - T)$; net heating occurs if $T_\nu > T(r)$ at any r. In order to obtain the contribution to the net heating from neutrino-positron scattering, in addition to the change in η_e, one must also make appropriate changes to Λ_i.

3.4.3 Neutrino-Nucleon Scattering

The energy transfer associated with a single neutrino-nucleon scattering event is much smaller than that for neutrino-electron scattering. The cross section, however, is much larger. Using our neutrino thermalization code, which solves the Boltzmann equation in an isotropic, homogeneous thermal bath of scatterers, including the full collision term, with Pauli blocking and explicit coupling between all energy bins (Chapter 2), we confirm that the average energy transfer for neutrino-nucleon scattering, in non-degenerate nuclear matter, for neutrino energies below ~40 MeV is well approximated by $\omega \simeq \varepsilon_\nu(\varepsilon_\nu - 6T)/m_N$, where m_N is the nucleon mass in MeV (Tubbs 1979). We derive the heating rate for neutrino-neutron scattering as

$$\dot{q}_{\nu_i n} = \frac{cn_n}{\rho}\frac{L_\nu}{4\pi r^2 c\langle\varepsilon_\nu\rangle\langle\mu\rangle}\ \Phi^4\ \ \mathrm{erg\ \ g^{-1}\ \ s^{-1}}$$

$$\times\left[\kappa\left(\frac{F_2(\eta_\nu)}{F_3(\eta_\nu)}\langle\varepsilon_\nu\rangle\right)^2\frac{\langle\varepsilon_\nu\rangle}{m_n}\frac{F_6(\eta_\nu)}{F_3(\eta_\nu)}\left(\langle\varepsilon_\nu\rangle\Phi\frac{F_2(\eta_\nu)}{F_3(\eta_\nu)} - 6T\frac{F_5(\eta_e)}{F_6(\eta_e)}\right)\right]. \tag{3.32}$$

$\kappa = \sigma_o/(16m_e^2)(1+3g_A^2)$ for neutron scattering and $\kappa = \sigma_o/(4m_e^2)[4\sin^4\theta_W - 2\sin^2\theta_W + (1+3g_A^2)/4]$ for neutrino-proton scattering, where $\sin^2\theta_W \simeq 0.231$ and $g_A(\simeq -1.26)$ is the axial-vector coupling constant.

3.4.4 $\nu_i\bar{\nu}_i \leftrightarrow e^+e^-$

Cooling due to e^+e^- annihilation, assuming relativistic electrons and positrons, and ignoring Pauli blocking in the final state, can be written as

$$C_{e^+e^-\to\nu\bar{\nu}} \simeq 1.4\times 10^{17}\,\frac{T^9}{\rho_8}\,f(\eta_e)\ \ \mathrm{ergs\ \ g^{-1}\ \ s^{-1}}, \tag{3.33}$$

where

$$f(\eta_e) = \frac{F_4(\eta_e)F_3(-\eta_e) + F_4(-\eta_e)F_3(\eta_e)}{2F_4(0)F_3(0)}. \tag{3.34}$$

ρ_8 is the mass density in units of 10^8 g cm^{-3} and T is in MeV. We employed eq. (3.33) with and without the η_e dependence and compared it to the results using the fit given in Itoh et al. (1996). Such a modification amounted to no more than a 1-2% change in the entropy, dynamical timescale, total energy deposition, or mass outflow rate.

Much more uncertain than eq. (3.33) is the heating due to $\nu\bar{\nu} \to e^+e^-$. The spherical dilution of this process from the neutrinospheres is complicated. For a given flux, the local energy density depends sensitively on $\langle\mu\rangle$, which can only be properly treated by solving the full transport problem. We save such an investigation for a later work. Instead, we compare two approaches. The first is based on the vacuum spherical dilution approximation, written simply as (Qian and Woosley 1996)

$$\begin{aligned} H &\simeq 1.6\times 10^{19}\frac{\Psi(x)}{\rho_8\, R_{\nu\,6}^4}\ \Phi^9\ \text{erg g}^{-1}\ \text{s}^{-1} \\ &\times\ \left[L^{51}_{\bar{\nu}_e}L^{51}_{\nu_e}(\langle\varepsilon_{\bar{\nu}_e}\rangle+\langle\varepsilon_{\nu_e}\rangle)+\frac{6}{7}(L^{51}_{\nu_\mu})^2\langle\varepsilon_{\nu_\mu}\rangle\right], \end{aligned} \tag{3.35}$$

where $\Psi(x)=(1-x)^4(x^2+4x+5)$, $x=(1-(R_\nu/r)^2/\Phi^2)^{1/2}$, $R_{\nu\,6}$ is the neutrinosphere radius in units of 10^6 cm, and $L^{51}_{\nu_i}$ is the neutrino luminosity in units of 10^{51} erg s^{-1}. The redshift term, Φ, appearing in x, accounts for the amplification of this process due to the bending of null geodesics in general relativity as in eq. (3.28) (Salmonson and Wilson 1999). We compared this approximation to the heating rate obtained by (77). Because of the extreme nature of the density gradient just exterior to the protoneutron star, we find that the vacuum approximation adequately characterizes the energy deposition. In addition, the fact that there is no obvious way to include the general relativistic effects in the parameterization of $\langle\mu\rangle$ by Janka (1991) led us to employ eq. (3.35) in the wind models we present here.

3.4.5 Other Possible Neutrino Processes

We were motivated to consider nucleon-nucleon bremsstrahlung, plasma, and photo-neutrino processes by the sensitivity of the dynamical timescale and asymptotic entropy to changes in the energy deposition profile (see §3.8.3 and Qian and Woosley 1996). We found that none of these processes contributed significantly. Qian and Fuller (1995a,b) have addressed the possibility that neutrino oscillations may effectively provide an extra energy source, at larger radii, beyond the point where the mass outflow rate is determined. In §3.8.3, we include an ad hoc energy source to test the sensitivity of our results to changes in $\dot{q}(r)$, but do not address the issue of neutrino oscillations directly.

3.5 Results: Fiducial Models

With a robust and efficient means by which to solve the wind problem, coupled with physical boundary conditions and a well-motivated neutrino heating algorithm we can now survey the protoneutron star wind parameter space.

Supernova and protoneutron star calculations, coupled with observations of neutron star binary systems and our knowledge of the high-density nuclear equation of state, place useful limits on the parameter space that protoneutron stars actually inhabit. Particularly, we are interested in a range of protoneutron star masses from 1.2 to 2.0 $M_\odot$, total neutrino luminosities from 4×10^{52} to 1×10^{51} erg s^{-1}, average neutrino energies as high as 35 MeV for ν_μ neutrinos and 15-20 MeV for ν_e and $\bar{\nu}_e$ neutrinos with $\langle \varepsilon_{\nu_e} \rangle < \langle \varepsilon_{\bar{\nu}_e} \rangle < \langle \varepsilon_{\nu_\mu} \rangle$, and a range of neutron star radii from 20 km to perhaps 9 km.

Our main goal in this section is to map the possible protoneutron star wind parameter space, taking as input the physical ranges specified above. In what follows, we present the basic structure of the wind and identify some of the systematics we can use to assess this site as a candidate for r-process nucleosynthesis. Particularly, we include a discussion of the dynamical timescale, the electron fraction, and the asymptotic entropy. In identifying some of the approximate power law relations which characterize the wind, we refer to *low* and *high* total neutrino luminosities, with *low* denoting $\lesssim 10^{52}$ erg s^{-1} and *high* meaning $\gtrsim 10^{52}$ erg s^{-1}. We write these power laws in terms of L_ν and $\langle \varepsilon_\nu \rangle$. These stand for a representative luminosity and a representative average energy, respectively. That is, we take $L_{\bar{\nu}_e}/L_{\nu_e}$, $L_{\bar{\nu}_e}/L_{\nu_\mu}$, $\langle \varepsilon_{\bar{\nu}_e} \rangle / \langle \varepsilon_{\nu_e} \rangle$, and $\langle \varepsilon_{\bar{\nu}_e} \rangle / \langle \varepsilon_{\nu_\mu} \rangle$ as constant.

We employ the notation L_ν^{51} to refer to luminosities in units of 10^{51} erg s^{-1}. All neutrino luminosities quoted throughout this paper are local quantities at the neutron star surface. The luminosity at infinity can be obtained from the luminosities quoted here by multiplying the local luminosity by two powers of the gravitational redshift (eq. 3.27). For example, taking $M = 1.4$ $M_\odot$ and $R_\nu = 10$ km, $\Phi^2 \simeq 0.58$. In order to keep track of our models, we use the $\bar{\nu}_e$ neutrino luminosity ($L_{\bar{\nu}_e}$) to label each individual model. The total luminosity can then be obtained from the ratios $L_{\bar{\nu}_e}/L_{\nu_e}$ and $L_{\bar{\nu}_e}/L_{\nu_\mu}$. Finally, in our expressions for $\dot{q}$ we included η_{ν_i} terms for completeness. In what follows, we take $\eta_{\nu_e} = \eta_{\bar{\nu}_e} = \eta_{\nu_\mu} = 0$. For an assessment of this assumption, see Janka & Hillebrandt (1989) and Myra & Burrows (1990).

3.5.1 The Structure of Neutrino-Driven Winds

Figures 3.1, 3.2, and 3.3 show the velocity, mass density, and temperature as a function of radius for eight different neutrino luminosities. For these models, R_ν is 10 km and the neutron star gravitational mass is 1.4 $M_\odot$. The average neutrino energies were set at $\langle\varepsilon_{\nu_e}\rangle = 11$ MeV, $\langle\varepsilon_{\bar{\nu}_e}\rangle = 14$ MeV, and $\langle\varepsilon_{\nu_\mu}\rangle = 23$ MeV for the highest luminosity. For each subsequent luminosity, the average energies were decreased according to $\langle\varepsilon_\nu\rangle \propto L_\nu^{1/4}$. The luminosities were held in the ratios $L_{\bar{\nu}_e}/L_{\nu_e} = 1.3$ and $L_{\bar{\nu}_e}/L_{\nu_\mu} = 1.4$. In these figures, critical points ($v = c_s$) are shown as dots. Table 3.1 lists the global properties of each of these models, including the integrated energy deposition rate, Q (eq. 3.14), and the mechanical luminosity or hydrodynamical power, $P_{\rm mech} = \dot{M}v_a^2/2$, where v_a is the asymptotic velocity. In addition, we include the asymptotic entropy s_a and dynamical timescale defined as the e-folding time of the density at $T = 0.5$ MeV:

$$\tau_\rho = \frac{1}{vy}\left|\frac{1}{\rho}\frac{\partial\rho}{\partial r}\right|^{-1}. \tag{3.36}$$

Figure 3.1 shows clearly that even relatively close to the neutron star ($r \sim 400$ km) the flow is not homologous (i.e., v is not proportional to r). At much smaller radii, however, in the heating region ($r \lesssim 60$ km, compare with Fig. 3.4) the flow is homologous with $v \propto L_\nu r$. We have found that simple parameterizations of $v(r)$, particularly for low neutrino luminosities, are not straightforward. Although not readily apparent, the asymptotic velocity (v_a) is a power law in L_ν. For high $L_\nu^{\rm tot}$, $v_a \propto L_\nu^{0.3}$. For low L_ν, the index is ~ 0.46. The critical radius (R_c) also increases as a power of luminosity for low L_ν. For $M = 1.4$ M$_\odot$, the index is ~ 0.95, while for $M = 2.0$ M$_\odot$ $R_c \propto L_\nu^{-0.85}$. Note that if the protoneutron star cools as $L_\nu \propto t^{-0.9}$ then we should expect R_c to grow linearly with time, implying that at late times the velocity of the critical point away from the neutron star is approximately constant.

The stiff nature of the wind equations is manifest in Fig. 3.2. The inset shows that ρ drops by more than four orders of magnitude in just 1-3 km, before the neutrino heating rate reaches a maximum. Figure 3.4 shows the total specific heating rate for each of the eight fiducial wind models. Note that the maximum in $\dot{q}$ occurs very close to the protoneutron star surface and that the position of this maximum is not a function of L_ν. At $r \sim 12$ km the density gradient changes dramatically, as the slow moving material in this inner atmosphere accelerates to infinity. Concomitant with this change in $\rho(r)$ and the peak in $\dot{q}$ is a rise in T and most of the entropy production. Figure 3.5 shows the entropy as a function of radius. Note that the entropy quickly comes to within a few percent of its asymptotic value (s_a). We find that s_a is proportional to $L_\nu^{-0.24}$ for all luminosities, for 1.4 M$_\odot$. For $M = 2.0$ M$_\odot$, s_a is proportional to $L_\nu^{-0.25}$. As L_ν decreases, the gradients in ρ, T, and the entropy near R_ν become larger. Inspection of Fig. 3.3 shows that the 0.1 MeV $\lesssim T \lesssim$ 0.5 MeV region where the r-process (and preceding α-process) might take place, lies between 50 km and 500 km for $L^{51}_{\bar{\nu}_e} = 8.0$ and between 25 km and 150 km for $L^{51}_{\bar{\nu}_e} = 1.0$. Importantly, Fig. 3.1 shows that the wind is still accelerating significantly at these radii. This calls into question the assumption of a constant velocity outflow used by many r-process modelers (e.g., Meyer and Brown 1997).

Figure 3.6 shows a breakdown of the total energy deposition into its separate components for the $L^{51}_{\bar{\nu}_e} = 8.0$ fiducial model. All of the heating processes conspire to give $\dot{q}(R_\nu) = 0$, in accordance with our boundary condition. At the surface, the charged-current heating rate ($\dot{q}_{cc}$) provides net cooling, which balances heating from neutrino-nucleon scattering ($\dot{q}_{\nu N}$). $\dot{q}_{cc}$ generally dominates the other heating processes in the models we consider here. Note that heating due to neutrino-electron/positron scattering ($\dot{q}_{\nu e}$) does not contribute as significantly as is indicated by Qian & Woosley (1996) and Otsuki et al. (2000), because of their simplifying assumption that the energy transfer per scattering is $\sim \varepsilon_\nu/2$ instead of $\sim (\varepsilon_\nu - 4T)/2$ (§3.4.2). Comparing Fig. 3.6 with Fig. 3.7, we can see that the drop in $\dot{q}_{cc}$ at $r \simeq 35$ km is due to the formation of α particles. As the luminosity decreases this transition region moves in, so that for $L^{51}_{\bar{\nu}_e} = 0.60$, $\dot{q}_{cc} \to 0$ near $r \sim 22$ km. As the ratio of M/R_ν increases, the heating rate due to $\nu_i\bar{\nu}_i \to e^+e^-$ ($\dot{q}_{\nu\bar{\nu}}$) increases substantially relative to both $\dot{q}_{\nu e}$ and $\dot{q}_{cc}$. In fact, for $M/R_\nu = 2.0\,\mathrm{M}_\odot/10$ km, the peak in $\dot{q}_{\nu\bar{\nu}}$ is actually slightly higher than that for $\dot{q}_{\nu e}$. However, $\dot{q}_{cc}$ still dominates heating at the peak in $\dot{q}_{\rm tot}$ by a factor of ~ 1.5. Note that an increase in L_{ν_μ} or $\langle\varepsilon_{\nu_\mu}\rangle$ increases the importance of $\dot{q}_{\nu e}$ and $\dot{q}_{\nu\bar{\nu}}$ relative to $\dot{q}_{cc}$. In particular, this increases the energy deposition at larger radii. We explore some of these effects on the asymptotic character of the wind in §3.8.3.

Qian & Woosley (1996) found that $\dot{M} \propto L_\nu^{2.5} M^{-2}$ for Newtonian gravity. We find that the index of this power law in L_ν is slightly decreased in general relativity to 2.4−2.5, but that the dependence on M is stronger; $\dot{M}$ is approximately proportional to $M^{-3.1}$ for high luminosities. The index decreases to −2.7 for low luminosities. For the full range of luminosities and masses considered here, the mass outflow rate in our general-relativistic calculations is approximately a factor of three smaller than in our Newtonian wind models.

Computing the volumetric integral of $\dot{q}$ as in eq. (3.14) yields the net energy deposition rate, Q (see Table 3.1). For the heating function we employ in this paper, Q is roughly proportional to $L_\nu^{2.4}$ for all protoneutron star masses and luminosities. The small variations in this power law index compliment the variation in $\dot{M}$ with L_ν so that the ratio $Q/\dot{M}$ varies by less than 2% over the whole range of L_ν for each mass. In all cases $Q/\dot{M} \simeq GM/R_\nu$ to within 10%. Whereas Qian & Woosley (1996) found that $Q \propto M^{-1}$, we find a more stiff dependence on mass; for high L_ν, Q is proportional to $M^{-1.9}$ for 1.4 $M_\odot \leq M \leq 1.6$ $M_\odot$. In addition, we find that their analytic expression for Q consistently underestimates the net energy deposition in our Newtonian models by as much as $\sim 50\%$.

The wind mechanical power $P_{\rm mech}$ is proportional to $L_\nu^{3.4}$ for low L_ν and $M = 1.4$ $M_\odot$. This index decreases to 3.2 for $M = 2.0$ $M_\odot$. At high luminosity for all masses, $P_{\rm mech} \propto L_\nu^{3.2}$. Although the asymptotic velocity is set by the escape velocity from the protoneutron star and therefore increases with increasing M, it does not increase as a power law in general relativity. In fact, it increases more rapidly. Therefore, even though $\dot{M}$ is approximately proportional to $M^{-2.5}$ at low luminosities, the increase in v_a as M gets large forces $P_{\rm mech}$ to increase.

The efficiency of energy deposition, $Q/L_\nu^{\rm tot}$, ranges from 10^{-3} to 10^{-5} as L_ν decreases. The efficiency of conversion of neutrino energy to hydrodynamical power, $P_{\rm mech}/L_\nu^{\rm tot}$, ranges from only 2×10^{-5} to less than 6×10^{-8} for the models considered here. The efficiency for the conversion of net energy deposition to hydrodynamical power, $P_{\rm mech}/Q$, decreases with luminosity as $L_\nu^{1.4}$ for 1.4 $M_\odot$ with $P_{\rm mech}/Q \simeq 2.4 \times 10^{-3}$ for $L_{\bar{\nu}_e}^{51} = 0.6$. This means that almost all of the net energy deposition goes into overcoming the gravitational potential. The excess energy, manifest at infinity as the mechanical power, is very small in comparison with Q. These quantities may be potentially important if the wind is to emerge and escape to infinity in the expanding supernova envelope.

3.5.2 The Effects of General Relativity

Over the range of masses presented here, we find significant enhancements in the entropy per baryon using the full general-relativistic framework. Over a broad range of luminosities for the 1.4 $M_\odot$ protoneutron star we find that s_a is 25–30 units less in our Newtonian calculations than in our analogous general-relativistic calculations.

Typical reductions in $\dot{M}$ and Q are of order a factor of three and two, respectively. These differences were anticipated by Qian & Woosley (1996) and Cardall & Fuller (1997) and more recently realized in the wind calculations of Otsuki et al. (2000). As the latter showed, the general-relativistic effects on s_a are much more the result of using the general-relativistic hydrodynamic formulation than of incorporating the general-relativistic corrections to $\dot{q}$ expressed in eqs. (3.27) and (3.28). The inclusion of general relativity in the hydrodynamics makes the structure of the protoneutron star more compact than in a Newtonian description. This makes the temperature and density gradients steeper just exterior to R_ν and particularly in the heating region. Although dT/dr decreases rapidly, $d\rho/dr$ drops much faster. This effectively increases the specific energy deposition per unit mass and the entropy is enhanced significantly.

For comparison, we calculated several wind models with eqs. (3.5)$-$(3.7) that included the enhancement to $\dot{q}$ due to the bending of null geodesics, but did not include any redshift factors on L_ν or $\langle\varepsilon_\nu\rangle$. For the 1.4 M$_\odot$ model with $L^{51}_{\bar{\nu}_e} = 8.0$ (see Table 3.1) this change nearly doubled both Q and $\dot{M}$, while decreasing τ_ρ from 3.68 to 1.95 ms. Although more heating occurred at larger radii, the peak in $\dot{q}$ also increased so as to offset any potential gain in s_a. The net enhancement was just 6 units in entropy. Conversely, keeping all the redshift terms and eliminating Φ from $\Xi(r)$ in eq. (3.28) increased τ_ρ by more than 30% and left s_a virtually unchanged.

Because the bending of null geodesics increases the net energy deposition close to the neutron star and the redshift terms act to decrease energy deposition over the whole profile, it is clear from this comparison that only an increase in $\dot{q}(r)$ that does not significantly increase Q can have large effects on s_a (see §3.8.3 and Qian and Woosley 1996).

3.5.3 The Electron Fraction

Figure 3.7 shows the evolution of the neutron (X_n), proton (X_p), alpha (X_α), and electron fraction (Y_e) as a function of radius for the $L^{51}_{\bar{\nu}_e} = 8.0$ fiducial model (Table 3.1 and Figs. 3.1-3.6). The electron fraction profile is computed using eq. (3.15), solved simultaneously with the wind equations. In computing the wind solutions we assume nuclear statistical equilibrium between free nucleons and alpha particles. Y_e comes to within a few percent of its asymptotic value (Y_e^a) in just the first five kilometers. This quick evolution is due primarily to the low matter velocities in the inner region. For $L_{\bar{\nu}_e}/L_{\nu_e} = 8/6.15$ and $\langle\varepsilon_{\bar{\nu}_e}\rangle/\langle\varepsilon_{\nu_e}\rangle = 14/11$, eq. (3.16) predicts that $Y_e^a \simeq 0.478$. Solving the differential equation we find remarkable agreement: $Y_e \simeq 0.477$ at $r = 20$ km. Just beyond this, for $r \gtrsim 30$ km, free nucleons form α particles and Y_e rises slightly as X_α increases until $Y_e = 0.485$ at $r \simeq 150$ km. This is the α effect, whose import in this context was first noted by Fuller & Meyer (1995) and McLaughlin, Fuller, & Wilson (1996). The magnitude here is only of order 1%. For $Y_e^a < 0.5$, we find generally that the magnitude of the α effect increases as the luminosity decreases for a given R_ν. In addition, for models in which $L_{\bar{\nu}_e}/L_{\nu_e}$ and $\langle\varepsilon_{\bar{\nu}_e}\rangle/\langle\varepsilon_{\nu_e}\rangle$ are larger, and, hence, Y_e^a is naively lower (à la eq. 3.16), the magnitude of the α effect is also enhanced. However, for a reasonable range of $L_{\bar{\nu}_e}/L_{\nu_e}$ and $\langle\varepsilon_{\bar{\nu}_e}\rangle/\langle\varepsilon_{\nu_e}\rangle$ as well as total neutrino luminosities, the α effect never increases Y_e^a by more than $\sim$10%. That is, if $Y_e = 0.40$ before α particle formation, we find that the α effect increases Y_e to no more than approximately 0.44.

Since in these fiducial models we decrease the average neutrino energies with luminosity, the threshold effect in the charged-current reactions, manifest in eq. (3.16) by the neutron/proton mass difference (Δ), becomes important. Despite the fact that $L_{\bar{\nu}_e}/L_{\nu_e}$ and $\langle\varepsilon_{\bar{\nu}_e}\rangle/\langle\varepsilon_{\nu_e}\rangle$ are maintained as above, Y_e^a eventually becomes greater than 0.5. As Y_e^a becomes much larger (~ 0.52), it experiences what might also be termed an α effect: because an α particle has $Y_e = Z/A = 0.50$, the onset of X_α formation *decreases* Y_e^a.

3.5.4 The Dynamical Timescale

In discussing our results, in order to make an apposite comparison with previous studies, we quote τ_ρ (eq. 3.36) at $T = 0.5$ MeV. However, using such a scale to characterize the nature of the resulting nucleosynthesis is suspect. Figure 3.8 shows τ_ρ as a function of radius for the wind models presented in Figs. 3.1-3.5. The dots on each line of constant neutrino luminosity mark the range 0.5 MeV $\gtrsim T(r) \gtrsim 0.1$ MeV, the temperature range relevant for neutron-capture nucleosynthesis. Although the r-process may continue at temperatures well below 0.1 MeV, we include these dots to guide the eye. The dynamical timescale of the wind, or the expansion timescale, has been defined in several different ways by many researchers. No clear consensus exists. Cardall & Fuller (1997) defined their dynamical timescale as the e-folding time of the temperature at $T = 0.5$ MeV. Hoffman, Woosley, & Qian (1997) defined their dynamical timescale in the same way, but then used an expansion timescale (1.28 times the dynamical time) to discuss their results. Qian & Woosley (1996) and Freiburghaus et al. (1999) used the ratio r/v at $T = 0.5$ MeV to characterize the expansion. Finally, Meyer & Brown (1997) connect the e-folding time of the density with their expansion timescale, $r/2v$, by using the equation for $\dot{M}$ and dropping the acceleration term. With these assumptions, they obtain

$$\tau_\rho^{\mathrm{MB}}(t) = \tau_0 \left(1 + \frac{t}{2\tau_0}\right), \tag{3.37}$$

where t is the time on a Lagrangean mass element in the flow. Figure 3.8 shows clearly that any simple parameterization of the dynamical time, using any definition, is an oversimplification. For $L_{\bar{\nu}_e}^{51} = 8$, τ_ρ increases by a factor of three over this range of temperatures. Equation (3.37) captures the increase of τ_ρ with radius for high luminosities, but overestimates the slope by about a factor of two. At low luminosities, of course, eq. (3.37) does not capture $\tau_\rho(t)$ at all. At these luminosities, the dynamical timescale actually decreases over this range of temperatures. This arises because a region of positive curvature in the $v(r)$ profile of Fig. 3.1 develops between 40 km and 200 km at low luminosities. This observation simply underscores the danger in considering a single dynamical time that is meant to characterize an actual wind profile.

Figure 3.9 shows tracks of constant mass in the plane of s_a versus τ_ρ for luminosities from $L^{51}_{\bar{\nu}_e} = 8.0$ to $L^{51}_{\bar{\nu}_e} = 0.70$, for $R_\nu = 10$ km. Although the indices vary slightly for different masses, $s_a \propto L_\nu^{-0.25}$ and $\tau_\rho \propto L_\nu^{-1.4}$, so that s_a is approximately proportional to $\tau_\rho^{0.2}$. One can imagine that these curves represent evolutionary cooling tracks in time in the space of s_a and τ_ρ for constant R_ν and M. Simple extrapolation of this power law allows one to estimate at what τ_ρ a given entropy might obtain, for a given mass and neutron star radius. For example, the 1.4 $M_\odot$ trajectory in Fig. 3.9 will not reach $s_a \simeq 200$ until $\tau_\rho \simeq 0.4$ seconds. The corresponding neutrino luminosity at this point is $L^{51}_{\bar{\nu}_e} \simeq 0.22$. Knowing that $\dot{M} \propto L_\nu^{2.4}$ allows one to estimate the mass outflow rate as $\dot{M} \simeq 1.8 \times 10^{-8}$ $M_\odot$ s^{-1}. These simple power laws and a knowledge of how L_ν might behave in time allow us to put powerful constraints on the likely wind epoch of r-process nucleosynthesis, as we demonstrate in §3.6.

Wanajo et al. (2000) found that their dynamical timescale saturated at high neutrino luminosities near $2 - 3 \times 10^{52}$ erg s^{-1}. This conclusion is an artifact of their definition for the dynamical timescale and their numerical approach to the wind problem. Our solution shows that for constant average neutrino energies, even up to $L_\nu^{\rm tot} \simeq 8 \times 10^{52}$ erg s^{-1}, τ_ρ continues to decrease, roughly as $\tau_\rho \propto L_\nu^{-0.75}$. The entropy also decreases as the luminosity increases; $s_a \propto L_\nu^{-0.15}$. Since these power laws are for constant average neutrino energy, we deduce from the fiducial models that $\tau_\rho \propto L_\nu^{-0.75} \langle\varepsilon_\nu\rangle^{-2.6}$ and $s_a \propto L_\nu^{-0.15} \langle\varepsilon_\nu\rangle^{-0.4}$. These are to be compared with the analytic results of Qian & Woosley (1996) who did not include general-relativistic effects: $\tau_{\rm dyn} \propto L_\nu^{-1} \langle\varepsilon_\nu\rangle^{-2}$ and $s_a \propto L_\nu^{-1/6} \langle\varepsilon_\nu\rangle^{-1/3}$. In addition, although we find that τ_ρ decreases as R_ν decreases, for constant protoneutron star mass, neutrino luminosity, and average neutrino energy, using either the Newtonian or general-relativistic wind equations, we find that τ_ρ is generally 10%–15% shorter in the Newtonian case. This result is owed in part to the fact that the increase in $\dot{q}$ due to the bending of neutrino trajectories is insufficient to counter the decrease in $\dot{q}$ caused by gravitational redshift of the neutrino luminosity and energy (Cardall & Fuller 1997). (See Table 3.1 for a comparison between the Newtonian and general-relativistic calculations for the 1.4 $M_\odot$ and $L^{51}_{\bar{\nu}_e} = 8.0$ fiducial model.)

3.5.5 Limitations of The Steady-State Approximation

To conclude this section, we include a few words about the degree to which the protoneutron star wind can be considered quasi-stationary. There are several timescales of importance. The first is τ_d, the timescale for decay of the neutrino luminosity, set by the power-law index δ in the relation $L_\nu \propto t^{-\delta}$: $\tau_d = t/\delta$. The second is the time τ_m for matter to move from R_ν to the critical point R_c, where it loses sonic contact with the rest of the flow. The third relevant timescale is the sound crossing time, τ_s, between R_ν and R_c. τ_s varies from just ~ 10 ms to more than 250 ms over the range of L_νs presented here. For low luminosities, $\tau_s \propto L_\nu^{-1.4}$. τ_m is proportional to $L_\nu^{-2.8}$ for all luminosities and varies from 4 seconds to more than 5000 seconds for the same range of L_νs. However, these numbers for τ_m are quite deceiving. In our models, due to the exponential density gradient just exterior to R_ν, the matter is effectively trapped for $r \lesssim 12$ km. In fact, for the lowest luminosity cases presented here, the matter velocity for $r \lesssim 10.5$ km can be of order 10 cm s^{-1}. In effect, then, the region shown in the inset in Fig. 3.2 is an atmosphere in hydrostatic equilibrium *from* which the wind emerges. From this region the matter would escape on timescales much longer than the total protoneutron star cooling time. If, instead, we redefine τ_m as the time necessary for a Lagrangean mass element to go from the peak of the heating profile (see Fig. 3.4) at $r \sim 12$ km to R_c, we find that τ_m is of order ~ 10 ms for

$L^{51}_{\bar{\nu}_e} = 8.0$ and $\tau_m \sim 1$ second for $L^{51}_{\bar{\nu}_e} = 0.5$. The steady-state approximation is only valid if $\tau_m, \tau_s \ll \tau_d$. For example, taking $L_\nu(t) \propto t^{-0.9}$ and high neutrino luminosities, $\dot{M}$ drops 10% in roughly τ_d. At these luminosities, τ_d is approximately $20 - 30$ ms. Although both τ_m and τ_s are less than τ_d, they are not significantly so. We conclude that the steady-state assumption might be reasonably employed, but that caution is warranted.

3.6 The Evolution of Protoneutron Star Winds

With the eigenvalue problem solved and some of the systematics in hand, in this section we explore possible evolutionary trajectories using the steady-state solutions. Beyond surveying the entire relevant parameter space, we endeavor to model the whole of the Kelvin-Helmholtz cooling phase, including radial contraction and the simultaneous evolution of the luminosity and average neutrino energy.

Perhaps a second after core bounce, as the wind emerges, the protoneutron star atmosphere will be extended ($R \sim 30 - 50$ km) and perhaps highly luminous ($L^{\rm tot}_\nu \sim 5 \times 10^{52}$ erg s^{-1}). As the neutron star cools it will contract quasi-hydrostatically. This may take as many as several seconds, depending upon the nuclear equation of state. The average neutrino energies during contraction may increase, peak near the time at which R_ν settles, and then decrease roughly linearly in time (Pons et al. 1999). The luminosity may decay quasi-exponentially or as a power law in time (Burrows and Lattimer 1986; Burrows 1988; Pons et al. 1999).

Figure 3.10 shows the luminosity, radius, and average energy as a function of time for our evolutionary models. This picture is merely schematic, but illustrates a representative scenario. In the following discussion we take $L^{\rm tot}_\nu \propto t^{-0.9}$. A simple rescaling in time can be performed for other power-law indices or exponential luminosity decay. Two possible tracks for the time evolution of $R_\nu(t)$ are shown. The short dashed line is linear contraction such that $R_\nu(t = 0.4\,{\rm s}) = 20.3$ km and $R_\nu(t = 1\,{\rm s}) = 10$

km. This is the evolutionary model, which we label as '$R_\nu(t) \propto 1 - at$'. For comparison, the dot-dashed line has $R_\nu(t)$ proportional to $t^{-1/3}$. This model also has $R_\nu(t = 0.4\,\mathrm{s}) = 20.3$ km. At $t \simeq 3.2$ seconds, $R_\nu = 10$ km. The power 1/3 was obtained from a rough fit over approximately one second of post-explosion evolution in a supernova model of S. Bruenn. In this calculation the supernova was simulated in one-dimension artificially for a Woosley and Weaver (1995) 15 $\mathrm{M}_\odot$ progenitor starting from the collapse calculations of Bruenn, De Nisco, & Mezzacappa (2001). We focus on the model with $R_\nu(t) \propto 1 - at$ instead of the model with $R_\nu(t) \propto t^{-1/3}$ because it reaches a more compact configuration (i.e., maximum M/R_ν) at earlier times, that is, with higher luminosity. As we explore in the next section, large M/R_ν, coupled with high luminosity and/or average neutrino energy gives short dynamical timescales and relatively high entropies, both potentially important for r-process nucleosynthesis in the protoneutron star context.

In order to determine appropriate numbers for the ratios $\langle\varepsilon_{\nu_\mu}\rangle/\langle\varepsilon_{\bar{\nu}_e}\rangle$, $\langle\varepsilon_{\bar{\nu}_e}\rangle/\langle\varepsilon_{\nu_e}\rangle$, $L_{\bar{\nu}_e}/L_{\nu_\mu}$, and $L_{\bar{\nu}_e}/L_{\nu_e}$ we surveyed supernova simulations (e.g., Mayle, Wilson, and Schramm 1987; Burrows, Hayes, and Fryxell 1995; Mezzacappa et al. 2001; Liebendörfer et al. 2001; Bruenn, De Nisco, and Mezzacappa 2001; Rampp and Janka 2000; S. Bruenn 2001, private communication) and protoneutron star cooling calculations (Burrows and Lattimer 1986; Pons et al. 1999; J. Pons 2000, private communication). The common assumption of equipartition in luminosity between the three neutrino species is generally not realized in these calculations. In fact, $L_{\nu_\mu} + L_{\bar{\nu}_\mu} + L_{\nu_\tau} + L_{\bar{\nu}_\tau}$ is usually of order 50−60% of L_ν^{tot}. In addition, the ratio $\langle\varepsilon_{\bar{\nu}_e}\rangle/\langle\varepsilon_{\nu_e}\rangle$ ranges from 1.1 to 1.4 and $L_{\bar{\nu}_e}/L_{\nu_e}$ from 1.0 to 1.4. The ratio of $\langle\varepsilon_{\bar{\nu}_e}\rangle$ to $\langle\varepsilon_{\nu_\mu}\rangle$ also varies significantly. Like the fiducial models presented in §3.5, we use $L_{\bar{\nu}_e}$ to index our evolutionary models in this section and set $\langle\varepsilon_{\nu_\mu}\rangle/\langle\varepsilon_{\bar{\nu}_e}\rangle = 1.6$, $\langle\varepsilon_{\bar{\nu}_e}\rangle/\langle\varepsilon_{\nu_e}\rangle = 1.3$, $L_{\bar{\nu}_e}/L_{\nu_\mu} = 1.4$, and $L_{\bar{\nu}_e}/L_{\nu_e} = 1.3$. At any time, all luminosities and average energies can then be computed from Fig. 3.10. We chose $\langle\varepsilon_{\bar{\nu}_e}\rangle/\langle\varepsilon_{\nu_e}\rangle$ and $L_{\bar{\nu}_e}/L_{\nu_e}$ so as to accord with the literature while also minimizing Y_e^a (eq. 3.16), this being potentially favorable for r-process nucleosynthesis (but see §3.8.1). Note that with $\langle\varepsilon_{\bar{\nu}_e}\rangle/\langle\varepsilon_{\nu_e}\rangle = 1.3$ and $L_{\bar{\nu}_e}/L_{\nu_e} = 1.3$ and the magnitude of the average energies set by Fig. 3.10, $Y_e^a \sim 0.46$ at early times. We feel these numbers are merely representative. We explore potentially important modifications to our prescription in §3.8.3.

For each point along the evolutionary models represented in Fig. 3.10 we calculate the steady-state wind solution. We do this for a range of protoneutron star masses from 1.4−2.0 M$_\odot$. Neutrino luminosity is always quoted as the local neutrino luminosity at the surface of the protoneutron star, not the luminosity at infinity.

3.6.1 Results: Evolutionary Models

Shown in Fig. 3.11 are evolutionary trajectories for M = 1.4, 1.6, 1.8, and 2.0 M$_\odot$ in the plane of τ_ρ versus asymptotic entropy, s_a. Note that s_a does not include contributions from β-decays during nucleosynthesis. During r-process nucleosynthesis these processes may increase s_a by $\gtrsim 10$ units, depending on the dynamical timescale (Meyer and Brown 1997). However, because we post-process our wind models to obtain the nucleosynthetic yield and include only alpha particles and free nucleons in the equation of state we employ in solving the eigenvalue problem (see §3.2), such an entropy increase is not included in s_a. Figure 3.11 is analogous to Fig. 3.9, but for changing $R_\nu(t)$, $\langle\varepsilon_\nu\rangle(t)$, and $L_\nu^{\rm tot}(t)$ using the evolution depicted in Fig. 3.10. The evolutionary trajectories labelled with '$R_\nu \propto 1-at$' are solid lines with small dots. For comparison, we also show the evolution for $M = 1.4$ M$_\odot$ with $R_\nu(t) \propto t^{-1/3}$ as a thin solid line without dots. The small dots on each evolutionary track are separate L_νs. All tracks start with $L^{51}_{\bar{\nu}_e} = 8.0$. The lowest luminosity shown on this plot is $L^{51}_{\bar{\nu}_e} = 0.4$ for each track. The time evolution for any mass begins with high luminosity, large R_ν, and, hence, low s_a ($\sim 50-70$) and moderate τ_ρ (~ 9 ms). As R_ν gets smaller in the first second of evolution, the trajectories with $R_\nu \propto 1-at$ move to much higher s_a and slightly smaller τ_ρ before they cease contraction at $R_\nu = 10$ km. The s_a reached at this luminosity is set by M/R_ν, with the 2.0 $\mathrm{M}_\odot$ model reaching $s_a \simeq 150$. Our evolutionary models contract from ~ 20 km to $R_\nu = 10$ km in approximately 1 second. At this point in the evolution, R_ν is fixed and each track makes a sharp turn toward much longer τ_ρ and only moderately higher s_a. This turnoff point is marked with a large open circle on each track and has $L^{51}_{\bar{\nu}_e} = 3.4$ and $L^{\rm tot}_\nu = 1.57 \times 10^{52}$ erg s^{-1}. At this point the trajectories join lines of constant R_ν, like those in Fig. 3.9. Due to the relatively slow contraction, the model with $R_\nu(t) \propto t^{-1/3}$ never exhibits such a sharp turn in the $s_a - \tau_\rho$ plane and eventually joins the other 1.4 $\mathrm{M}_\odot$ evolutionary track at $\tau_\rho \sim 0.015$ seconds, corresponding to $t \simeq 3.15$ seconds and $L^{51}_{\bar{\nu}_e} = 1.3$. Note that the turnoff point at $L^{51}_{\bar{\nu}_e} = 3.4$ marks the point of minimum τ_ρ for each model with $R_\nu \propto 1 - at$. Table 3.2 gives the global properties of our neutrino-driven wind models at $L^{51}_{\bar{\nu}_e} = 8.0$, $L^{51}_{\bar{\nu}_e} = 3.4$, and $L^{51}_{\bar{\nu}_e} = 0.4$, including the asymptotic electron fraction, Y_e^a. For comparison, we also include in Table 3.2 the model with $R_\nu(t) \propto t^{-1/3}$ at $L^{51}_{\bar{\nu}_e} = 3.4$.

Having solved for $\dot{M}$ at every point along these evolutionary tracks and assuming that $L_\nu(t) \propto t^{-0.9}$, we calculate the total mass ejected in the wind as a function of time:

$$M_{\rm ej}(t) = \int_0^t \dot{M}(t')\,dt'. \tag{3.38}$$

Figure 3.12 shows this integral for all five of the models presented in Fig. 3.11. The dashed line shows $M_{\rm ej}(t)$ for the model with $R_\nu(t) \propto t^{-1/3}$. As one would expect, because of the slower radial contraction of the protoneutron star, this model ejects more matter than the corresponding trajectory with $R_\nu \propto (1 - at)$. In this case, the difference is about 30%. The small dots on each of the solid lines mark $L_\nu(t)$ for each model and correspond to the luminosity points on each track in Fig. 3.11. The large dots on each line mark $L^{51}_{\bar{\nu}_e} = 3.4$, the luminosity at which each track in Fig. 3.11 reaches $R_\nu = 10$ km and turns sharply. Note that the 2.0 $\mathrm{M}_\odot$ model ejects only $\sim 6 \times 10^{-5}$ $\mathrm{M}_\odot$ of material, about three times less than the 1.4 $\mathrm{M}_\odot$

model. Extrapolating the results of Fig. 3.12 we can compute the total $M_{\rm ej}^{\rm tot}$ for $t \to \infty$. We can then compute, at any time, the mass yet to be ejected by the wind, $\Delta M_{\rm ej}(t) = M_{\rm ej}^{\rm tot} - M_{\rm ej}(t)$. Figure 3.13 shows $\Delta M_{\rm ej}(t)$ versus time for each track in Fig. 3.11. The lines and dots correspond with those in Fig. 3.12. In Fig. 3.11, we plot lines of constant $\log_{10}[\Delta M_{\rm ej}(t)]$ in units of $M_\odot$ as dashed lines connecting big dots on each of the four evolutionary trajectories with $R_\nu \propto (1 - at)$. The thick dashed line on the far right side of the plot, labelled -6.0, is the line beyond which, only 10^{-6} $M_\odot$ will be ejected.

In the calculations presented here, we have arbitrarily defined the point in time when the wind begins. The absolute magnitude of $M_{\rm ej}$ in Fig. 3.12 for each model is therefore also arbitrary. Only the ratios of these ejected masses or $\Delta M_{\rm ej}(t)$ for an individual trajectory are of real import. The -6.0 line in Fig. 3.11 is of particular significance because if all (or most) supernovae produce r-process elements then the total yield per supernova must be $10^{-5} - 10^{-6}$ $M_\odot$ (e.g., Qian 2000). Therefore, if an r-process epoch is to exist along any of the trajectories shown in Fig. 3.11, then it must begin at or before the line labelled -6.0 in order to eject sufficient mass. If r-processing begins to the right of this line, less than 10^{-6} $M_\odot$ will be ejected. For any $L_\nu(t)$ and $R_\nu(t)$, such a bound must exist. We have explored the position of this boundary for a variety of relationships for $L_\nu(t)$. Taking reasonable e-folding timescales (τ) and $L_\nu(t) \propto e^{-t/\tau}$ the -6.0 line moves to even shorter τ_ρ. For slower power law decay, the boundary moves to longer τ_ρ. For $M = 1.4$ $M_\odot$ and $L_\nu(t) \propto t^{-0.8}$ it moves from $\tau_\rho \simeq 0.07$ to $\tau_\rho \simeq 0.085$ seconds. Although the wind may eventually evolve to arbitrarily long dynamical timescales, we conclude that the range of τ_ρ relevant for r-process nucleosynthesis is significantly constrained by the $\log_{10}[\Delta M_{\rm ej}] = -6$ line in Fig. 3.11. In fact, this range is smaller than previous calculations suggest. In addition, note that even if a given wind model produces r-process elements, only a fraction of the total mass ejected during that r-processing epoch will be in r-process elements; much of the mass will remain in alpha particles.

Conservatively, then, if transonic protoneutron star winds are the primary site for the r-process, this constraint on the amount of mass ejected per supernova implies that the epoch of r-process nucleosynthesis must occur for τ_ρ less than ~ 0.085 seconds.

For this range in τ_ρ, there is also only a relatively small range of s_a available to the transonic protoneutron star wind. As evidenced by the calculations of Takahashi, Witti, & Janka (1994) and Qian & Woosley (1996) and borne out in Fig. 3.11, s_a as large as $\simeq 400$ is simply outside what can be obtained for reasonable dynamical timescales, even including the effects of general relativity. If we extrapolate the curves shown here to later times (lower luminosities), even the 2.0 $M_\odot$ trajectory does not reach 400 until $\tau_\rho \simeq 0.5$ seconds. At this point $\dot{M} \simeq 1.5\times10^{-9}$ $M_\odot$ s^{-1}. If r-processing could occur during these late stages, it would need to persist for many thousands of seconds to yield even 10^{-6} $M_\odot$ of ejecta. Moreover, the survey calculations of Hoffman, Woosley, & Qian (1997) and Meyer & Brown (1997) show that with $s_a \sim 400$ and $\tau_\rho \sim 0.5$ seconds, one requires $Y_e^a \lesssim 0.3$ to achieve an appreciable third peak r-process. A Y_e^a this low is extremely unlikely. As the protoneutron star cools, the neutrino luminosity and average neutrino energy will be correlated. Protoneutron star cooling calculations (Burrows and Lattimer 1986; Pons et al. 1999) indicate that the average neutrino energies will fall throughout these late evolutionary stages as the luminosity decreases. As the magnitude of $\langle\varepsilon_{\bar{\nu}_e}\rangle$ and $\langle\varepsilon_{\nu_e}\rangle$ decrease, the asymptotic electron fraction (eq. 3.16) must increase on account of the energy threshold for the reaction $\bar{\nu}_e p \to n e^+$ (the 'threshold effect'). For the 1.4 $M_\odot$ model, these constraints are even more severe. This track reaches $s_a \sim 400$ only when τ_ρ is several *seconds* and $\dot{M}$ is of order 10^{-11} $M_\odot$ s^{-1}.

Note that for a given mass and τ_ρ, s_a is 10-30 units higher in Fig. 3.9 than in Fig. 3.11 owing to the lower average neutrino energies for a given luminosity in our fiducial models (§3.5) than in the evolutionary models we consider in this section. One might argue that by quickly decreasing $\langle\varepsilon_\nu\rangle$ for all neutrino species with respect to the luminosity that the trajectory would move more quickly to higher s_a, and, hence, be more likely to yield r-process ejecta. While such a change would certainly drive s_a higher, it would also make τ_ρ increase faster, decrease $\dot{M}$ significantly, and the threshold effect would drive Y_e^a higher. Thus, such a modification can only make the constraints tighter.

We conclude that the late-time r-process as obtained in Woosley et al. (1994) is extremely unlikely in the context of a transonic wind. In essence, because s_a is initially set by M/R_ν for a given model, once each trajectory reaches $R_\nu(t) = 10$ km, the wind evolves quickly to much larger τ_ρ and only modestly higher asymptotic entropy. That is, for constant R_ν, s_a is roughly proportional to $\tau_\rho^{0.2}$. By the time a transonic wind evolves to high entropy, the dynamical timescale is too long and Y_e^a is too high to allow for a robust r-process. The slope of the trajectories in the $s_a - \tau_\rho$ plane shown in Fig. 3.11 guarantee that if the wind enters a regime of very high entropy it does so with very large τ_ρ and minute $\dot{M}$, so as to preclude any significant r-process yield.

Instead, we propose an r-process epoch just a second or two after explosion, coinciding with the end of the protoneutron star contraction phase. In this scenario, the wind moves into an early-time r-processing regime in the $s_a - \tau_\rho$ plane and then out of this regime at later times so that the constraint on $M_{\rm ej}$ is satisfied. With this in mind, the behavior of the wind trajectories during contraction, and particularly the point in each track where τ_ρ is at a minimum ($L_{\bar{\nu}_e}^{51} = 3.4$), is suggestive and tantalizing. As Hoffman, Woosley, & Qian (1997) noted, a small dynamical timescale, even for only moderate entropies, can yield a successful r-process. More recently, Otsuki et al. (2000) have shown that a successful r-process can be realized in this context. For these reasons we turn our attention to an early-time, high luminosity, short-τ_ρ, and modest entropy r-process. For reference, in Fig. 3.11, we include long dashed lines of constant Y_e, taken from the r-process survey calculations of Meyer & Brown (1997), above and to the left of which, for a given Y_e^a, production of the third r-process peak at $A \sim 195$ is assured. Caution is encouraged in taking these lines too seriously. They were computed along specific T and ρ trajectories for fixed Y_e^a and dynamical timescale, $\tau^{\rm MB}$, given by eq. (3.37), which overestimates $d\tau/dt$ by roughly a factor of two at these high luminosities (see Fig. 3.8 and §3.5.1). These lines are only suggestive.

3.7 Nucleosynthesis in the Evolutionary Protoneutron Star Wind Models

Any successful r-process site must do more than simply produce nuclei with $A \gtrsim 195$. Observations of r-nuclei in ultra metal-poor halo stars (notably, CS22892-052, HD115444, and CS31082-001) show that the abundance pattern for $A \gtrsim 135$ is nearly identical to the scaled solar r-process abundance (Sneden et al. 1996; Burris et al. 2000; Westin et al. 2000; Hill et al. 2001). Simply producing the platinum peak is no guarantee that the solar abundance distribution is reliably reproduced (Meyer and Brown 1997). In the wind scenario, particularly, one must construct the time-integrated yield as the neutrino luminosity decays and the global wind structure evolves.

For each luminosity point on the 1.4 $M_\odot$ evolutionary trajectory with $R_\nu \propto (1-at)$ in Fig. 3.11 we obtained a unique $\dot{M}$ and velocity, temperature, and density profile. For each individual profile my collaborator Bradley S. Meyer of Clemson University used his r-process network code to compute the nucleosynthetic yield (Y) as a function of the atomic mass, A. With $Y(A)$ and $\dot{M}$ at every point, assuming $L_\nu(t) \propto t^{-0.9}$, we compute the weighted sum to get the total amount of ejected material at each A, $M_{\rm ej}(A)$. For the 1.4 $M_\odot$ model we find no significant nucleosynthesis beyond $A \sim 100$. In fact, most of the mass is concentrated at a peak in Sr, Y, and Zr. Inspecting the yield at each luminosity (time) reveals that when the protoneutron star has contracted to $R_\nu = 10$ km, the point of minimum τ_ρ in Fig. 3.11 denoted by a large open circle, the nucleosynthetic flow reaches a maximum in A. That is, all the points with $\tau_\rho \gtrsim 0.006$

seconds on the 1.4 $M_\odot$ evolutionary track, even though they have higher entropy, produce lower average A ejecta. This can be understood simply: as the dynamical timescale of the wind gets longer, more seed nuclei are formed. Hence, for a given Y_e^a and s_a, the neutron-to-seed ratio decreases (Hoffman, Woosley, and Qian 1996; Meyer and Brown 1997; Freiburghaus et al. 1999). Therefore, the point of minimum τ_ρ, when M/R_ν reaches a maximum, affords the best possibility for a robust r-process. For all protoneutron star masses, the evolutionary models with $R_\nu \propto (1 - at)$ turn sharply at $L_{\bar{\nu}_e}^{51} = 3.4$ and for τ_ρ between 6 and 7 ms. Unfortunately, although the $L_{\bar{\nu}_e}^{51} = 3.4$ point produced the highest average A ejecta of any other luminosity along the 1.4 $M_\odot$ track in Fig. 3.11, the nucleosynthesis did not even proceed to the second abundance peak.

We also calculated the nucleosynthetic yield for the 1.6, 1.8, and 2.0 $M_\odot$ trajectories at $L_{\bar{\nu}_e}^{51} = 3.4$, assuming that these points of minimum τ_ρ would also yield the highest average A ejecta of any of the points in a given mass trajectory. None successfully generated nucleosynthesis beyond the second r-process abundance peak. Even the 2.0 $M_\odot$ model, which has $s_a \simeq 151$ and $\tau_\rho \simeq 0.0068$ seconds for $L_{\bar{\nu}_e}^{51} = 3.4$, did not proceed beyond $A \sim 135$. Hence, for the Y_e^as derived and the time evolution we have assumed, we fail to produce viable r-process nucleosynthesis in any of our evolutionary transonic protoneutron star wind models.

3.8 What is To Be Done?

We have already ruled out the possibility of a late-time r-processing epoch at long dynamical timescales and high entropies ($s_a \gtrsim 400$) using constraints on the amount of material ejected, the slope of the evolutionary tracks in the $s_a - \tau_\rho$ plane, and the inexorable rise in Y_e^a as the protoneutron star cools.

We are left wondering what reasonable modifications might generically yield third-peak r-process nucleosynthesis for a canonical protoneutron star with 1.4 $M_\odot$ and

$R_\nu = 10$ km. In this section we further explore the viability of the early-time r-process. We consider the likely range of Y_e^a, s_a, and τ_ρ accessible to transonic neutrino-driven winds, and present the physical conditions we require for production of the both the second and third r-process abundance peaks.

3.8.1 The Asymptotic Electron Fraction: Y_e^a

One might argue that Y_e^a is simply too high in these winds to yield successful nucleosynthesis. There are several important points in this regard. First, our evolutionary models, which failed to produce nucleosynthesis beyond $A \sim 135$, all had $Y_e^a \sim 0.46$ at $L_{\bar{\nu}_e}^{51} = 3.4$. This Y_e^a favors the formation of $A \sim 90$ nuclei and produces many seed nuclei, thus decreasing the neutron-to-seed ratio for a given entropy and dynamical timescale. Second, both Woosley et al. (1994) and Wanajo et al. (2000) obtained unacceptably large over-productions of nuclei near $A \sim 90$ in the early phase of their wind calculations, at high luminosity and low entropy. Third, Hoffman et al. (1996) find that this overproduction problem is solved if $Y_e^a \gtrsim 0.485$. These three points together imply that if the r-process occurs generically in protoneutron star winds then Y_e^a must be either less than 0.40 or greater than 0.48 to avoid the overproduction problem at $A \sim 90$. Naively, it might seem that $Y_e^a \lesssim 0.40$ is favored because this would naturally increase the neutron-to-seed ratio by increasing the number fraction of neutrons. However, there are several reasons why $Y_e^a \gtrsim 0.48$ might actually be viable. First, for $Y_e^a \gtrsim 0.485$ Hoffman et al. (1996) found that some interesting p-process elements were produced, which were previously unaccounted for (e.g., ^{92}Mo). Second, the most detailed transport studies done to date (Mezzacappa et al. 2001; Liebendörfer et al. 2001; Rampp and Janka 2000) indicate that $\langle\varepsilon_{\bar{\nu}_e}\rangle/\langle\varepsilon_{\nu_e}\rangle \simeq 1.1-1.2$ and $L_{\bar{\nu}_e}/L_{\nu_e} \simeq 1.1$. Depending on the magnitude of $\langle\varepsilon_{\bar{\nu}_e}\rangle$ and $\langle\varepsilon_{\nu_e}\rangle$, these numbers put $Y_e^a \gtrsim 0.48$, as per eq. (3.16). Third, Hoffman, Woosley, & Qian (1997) find that as Y_e^a increases from 0.48 to ~ 0.495 the requisite entropy for third-peak production actually *decreases* for fixed dynamical timescale. The last point implies that having a high Y_e^a might slightly relieve the constraints on s_a set by an early-time, high-luminosity r-process. The fact that some p-process elements might also be produced in a high Y_e^a environment is attractive. Together, we feel that the above points make it plausible that $Y_e^a \gtrsim 0.48$ in protoneutron star winds. Such a conclusion, constrains the three-dimensional space $s_a - \tau_\rho - Y_e^a$ significantly.

Of course, having $Y_e^a \sim 0.30 - 0.35$ might also cure the overproduction problem at $A \sim 90$ while increasing the neutron-to-seed ratio dramatically, so as to allow for third-peak production at the entropies and timescales obtained for the 1.4 $M_\odot$ evolutionary model in Fig. 3.11. However, to attain $Y_e^a \lesssim 0.35$ one requires $L_{\bar{\nu}_e}/L_{\nu_e} \gtrsim 1.55$ for $\langle\varepsilon_{\bar{\nu}_e}\rangle/\langle\varepsilon_{\nu_e}\rangle = 20$ MeV/12 MeV. Such conditions would be extreme in light of the detailed transport calculations carried out to date. However, if Y_e^a does reach values this low in profiles like those in Fig. 3.11, there are two constraints worth pointing out. The first is that Y_e^a must evolve with the neutrino luminosities and average energies so that very little mass is left to be ejected by the time Y_e^a increases to 0.40. Otherwise, the same overproduction problems at $A \sim 90$ may occur. The second constraint is that if Y_e^a is sufficiently low to guarantee third-peak production, it must eject not more than $\sim 10^{-5}$ $M_\odot$ of r-process material per supernova.

We conclude that Y_e^a may be $\gtrsim 0.47$ in protoneutron star winds. This follows from the fact that Y_e^a below 0.40 is very unlikely and if Y_e^a is in the range 0.40−0.46, models suffer from overproduction of $A \sim 90$ nuclei. With this in mind, in the next section we consider modifications to our transonic wind models that might increase the entropy or decrease the dynamical timescale.

3.8.2 Entropy and Dynamical Timescale

One might choose to increase s_a by changing the bulk protoneutron star characteristics. Increasing the ratio M/R_ν increases s_a significantly with only modest decreases in τ_ρ. However, this ratio cannot be increased arbitrarily. $M \gtrsim 1.5$ M$_\odot$ may be disfavored in light of neutron star binary observations (Arzoumanian 1995) and $R_\nu < 9$ km seems unlikely due to constraints on the high density nuclear equation of state (e.g., Lattimer and Prakash 2001). In order to explore this, however, we varied M and R_ν at $L^{51}_{\bar{\nu}_e} = 3.4$ in our evolutionary models with $R_\nu \propto 1 - at$. In Table 3.3, we summarize these results for M =1.8 M$_\odot$, 1.6 M$_\odot$, and 1.4 M$_\odot$. These models should be compared with the models with $L^{51}_{\bar{\nu}_e} = 3.4$ in Table 3.2. Unfortunately, for $Y_e^a \simeq 0.46$ for each model, we did not obtain third-peak r-process nucleosynthesis. Increasing Y_e^a artificially in our nucleosynthesis calculations to 0.48, the neutron-to-seed ratio stays low and we fail to generate r-process elements beyond the second peak.

Although reasonable increases in M/R_ν are favorable for the r-process, they are insufficient for strong third-peak nucleosynthesis. Therefore, in an effort to obtain a robust r-process in a canonical 1.4 M$_\odot$, R_ν =10 km protoneutron star, we are only left with the option of modifications to the energy deposition profile.

3.8.3 Possible Modifications to $\dot{q}$

Qian & Woosley (1996) showed that an artificial energy source at radii between 20 km and 30 km, beyond the peak in $\dot{q}$ could substantially increase the entropy and decrease the dynamical timescale. In fact, any extra energy source that broadens the energy deposition profile, thus increasing $\dot{q}$ in a region of low mass density, increases s_a and decreases τ_ρ.

We noted in §3.6 the difference in entropy, for a given τ_ρ, between the fiducial tracks in Fig. 3.9 and the evolutionary tracks in Fig. 3.11. Comparing the $M = 1.6$ M$_\odot$ tracks on both plots, the difference in s_a between the two at $\tau_\rho = 0.02$ seconds is ~12 units. The fiducial model (with higher s_a) has a total neutrino luminosity almost twice that of the evolutionary model, but its average neutrino energies are more than 35% lower. The increase in entropy is caused by an interplay between the charged-current heating rate ($\dot{q}_{cc}$) and the neutrino-electron scattering heating rate ($\dot{q}_{\nu e}$). The former is proportional to $L_{\bar{\nu}_e}\langle\varepsilon^2_{\bar{\nu}_e}\rangle + L_{\nu_e}\langle\varepsilon^2_{\nu_e}\rangle$, while $\dot{q}_{\nu_i e}$ is proportional to $\sum_i L_{\nu_i}\langle\varepsilon_{\nu_i}\rangle$. Clearly, for fixed neutrino luminosities, as the average neutrino energy drops, $\dot{q}_{\nu_i e}$ becomes more important relative to $\dot{q}_{cc}$. Because $\dot{q}_{cc} \to 0$ as the alpha fraction increases (see Figs. 3.6 and 3.7), the fact that $\dot{q}_{\nu_i e}$ increases in importance effectively broadens the energy deposition profile, thus increasing the entropy. Although the heating rate due to $\nu_i\bar{\nu}_i$ annihilation peaks close to the protoneutron star surface, it also contributes to the total energy deposition rate at radii larger than where $\dot{q}_{cc} \to 0$. Because $q_{\nu_i\bar{\nu}_i} \propto \sum_i L^2_{\nu_i}\langle\varepsilon_{\nu_i}\rangle$, for fixed neutrino luminosity and decreasing average neutrino energy, this process also becomes more important relative to q_{cc}, thereby enhancing the effect on s_a. Although the total effect here is relatively small, at short τ_ρ any increases in s_a are of potential significance. Small average energies coupled with higher luminosities are one way to achieve moderately higher s_a and shorter τ_ρ. Note that due to the threshold effect (eq. 3.16) in the charged-current reactions, if one decreases $\langle\varepsilon_{\bar{\nu}_e}\rangle$ and $\langle\varepsilon_{\nu_e}\rangle$, Y_e^a will increase, and any potential gains in s_a might be mitigated. However, as we discussed in §3.8.1, Fig. 10 of Hoffman, Woosley, & Qian (1997) shows that the entropy required for third-peak nucleosynthesis actually decreases for high Y_e^a.

Similarly, one might also increase $\langle\varepsilon_{\nu_\mu}\rangle$ and L_{ν_μ} relative to the same quantities for the electron and anti-electron types. Since the ν_μ- and ν_τ-type neutrinos do not participate in the charged-current reactions, any increase in their luminosity or average energy effectively increases the importance of $\dot{q}_{\nu_i e}$ and $\dot{q}_{\nu_i\bar{\nu}_i}$ with respect to $\dot{q}_{cc}$. As we noted in §3.6, the evolution of luminosity and energy shown in Fig. 3.10 is only suggestive. For this reason we explored modifications to the ratios $\langle\varepsilon_{\nu_\mu}\rangle/\langle\varepsilon_{\bar{\nu}_e}\rangle = 1.6$, $\langle\varepsilon_{\bar{\nu}_e}\rangle/\langle\varepsilon_{\nu_e}\rangle = 1.3$, $L_{\bar{\nu}_e}/L_{\nu_\mu} = 1.4$, and $L_{\bar{\nu}_e}/L_{\nu_e} = 1.3$. For our extreme 2.0 $M_\odot$ evolutionary model with $L^{51}_{\bar{\nu}_e} = 3.4$ (see Table 3.2 for comparison), we set $L_{\nu_e} = L_{\bar{\nu}_e} = L_{\nu_\mu}$ and $\langle\varepsilon_{\nu_e}\rangle = 15$ MeV, $\langle\varepsilon_{\bar{\nu}_e}\rangle = 22$ MeV, and $\langle\varepsilon_{\nu_\mu}\rangle = 34$ MeV. This increased Y_e^a from 0.469 to 0.484, increased Q by more than a factor of three, decreased s_a

by 17 units to $\sim$134, and decreased τ_ρ by 40% to 4.1 ms. These modifications were insufficient to produce third-peak nucleosynthesis.

Following Qian & Woosley (1996), we artificially increased $\dot{q}(r)$ in the region 20 km $\leq r \leq$ 50 km for our 1.4 M$_\odot$ evolutionary model at $L^{51}_{\bar{\nu}_e} = 3.4$ so that Q (eq. 3.14) went from 1.21×10^{49} erg s^{-1} to 1.33×10^{49} erg s^{-1}, an increase of 10%. Because Q is the volume integral of $\rho\dot{q}$ and ρ is small at these radii ($10^6 - 10^7$ g cm^{-3}), $\dot{q}$ must be enhanced substantially in order to affect a 10% change in Q. With this extra energy deposition we found that maximum increases in s_a and decreases in τ_ρ, depending on the degree of augmentation of $\dot{q}$ as a function of r, were 17 units and 50%, respectively. $\dot{M}$ increased by just 8%. We made the same sort of modification to the 2.0 M$_\odot$ model with $L_{\nu_e} = L_{\bar{\nu}_e} = L_{\nu_\mu}$ and $\langle\varepsilon_{\nu_e}\rangle = 15$ MeV, $\langle\varepsilon_{\bar{\nu}_e}\rangle = 22$ MeV, and $\langle\varepsilon_{\nu_\mu}\rangle = 34$ MeV. In this case, we increased Q by 6% and found that s_a was increased from 134 to 150 and that τ_ρ decreased from 4.1 ms to 2.6 ms. That τ_ρ can decrease so significantly as a result of $\lesssim$ 10% changes in Q demonstrates the importance of conducting a full transport study in this context. We save such an investigation for a future work, but emphasize that the shape of the energy deposition profile may be the final arbiter in determining the true potential of this site as the seat of r-process nucleosynthesis.

3.8.4 The Early-Time r-Process

Although we have described the general physics of protoneutron star winds, the resulting nucleosynthesis, and modifications to our models that might enhance the wind's entropy and decrease its dynamical timescale, none of the models we have presented so far produces a robust, third-peak r-process. However, setting $M = 2.0$ M$_\odot$, $R_\nu = 9$ km, $L_{\bar{\nu}_e} = L_{\nu_e} = L_{\nu_\mu} = 8.0 \times 10^{51}$ erg s^{-1}, and $\langle\varepsilon_{\nu_e}\rangle = 14.5$ MeV, $\langle\varepsilon_{\bar{\nu}_e}\rangle = 22$ MeV, $\langle\varepsilon_{\nu_\mu}\rangle = 34$ MeV, and adding an artificial heating source between 20 km and 50 km that increases Q by 4%, we derive a wind with $s_a \simeq 150$, $\tau_\rho \simeq 1.3$ ms, and $Y_e^a \sim 0.477$.

This extremely compact and luminous protoneutron star yields a wind profile that produces third-peak r-process nucleosynthesis. We have found that for $s_a \sim 150$ and $0.47 \lesssim Y_e^a \lesssim 0.495$, we require $\tau_\rho \lesssim 1.3$ ms in order to generate a significant $A \sim 195$ yield. These are the necessary conditions we derive from our general-relativistic wind models for an early-time protoneutron star r-process epoch. If a wind trajectory, like those in Fig. 3.11 were to pass into the region $s_a \sim 150$ and $\tau_\rho \lesssim 1.3$ ms with Y_e^a less than 0.50, some third-peak material would be produced. Note that Otsuki et al. (2000) attained third-peak nucleosynthesis for similar wind conditions. Artificially setting Y_e^a equal to 0.40, their model with $s_a \sim 140$ and $\tau_\rho \sim 1.2$ ms successfully produced abundance peaks at $A \sim 130$ and $A \sim 195$.

Although a full nucleosynthesis survey, using real wind profiles, is required to map the space $100 \lesssim s_a \lesssim 200$, $\tau_\rho \lesssim 1.5$ ms, and $0.46 \lesssim Y_e \lesssim 0.50$, we note some features of potential importance for the short τ_ρ, early-time r-process. First, as we decrease Y_e^a from 0.495 to 0.47, for a given τ_ρ and s_a, the neutron-to-seed ratio stays roughly constant. Hence, the ratio of the abundance yield at $A \sim 130$ to that at $A \sim 195$ is relatively insensitive to Y_e^a. Second, r-process nucleosynthesis at very short timescales and high electron fractions is possible because the number of seed nuclei formed is very small. As a consequence, we expect the nucleosynthetic yield in this regime to be sensitive to changes in the input nuclear physics and, in particular, the three-body reactions important in seed nuclei formation (e.g., ^{4}He$(\alpha n,\gamma)^9$Be; Kajino et al. 2001).

Our requisite conditions for third-peak nucleosynthesis, $\tau_\rho \lesssim 1.3$ ms, $s_a \simeq 150$, and high Y_e^a, disfavor r-process nucleosynthesis generically in neutrino-driven winds from neutron stars with M =1.4 M$_\odot$. Our results in Table 3 indicate that even for $R_\nu = 8$ km, s_a is 35 units too small and τ_ρ is a factor of about three too long for the r-process to proceed to the third abundance peak. We find these gaps in entropy and timescale very difficult to bridge. For $M = 1.4$ M$_\odot$ we require $R_\nu \lesssim 6.5$ km to reach this s_a and τ_ρ. It is unlikely that any high-density nuclear equation of state could accommodate such a small radius. Even taking $M = 1.6$ M$_\odot$ and $R_\nu = 9$ km, without invoking an artificial heating source, we fail to reach $\tau_\rho \lesssim 1.3$ ms and $s_a \simeq 150$. Although the importance of the distribution of energy deposition and extra heating sources should be borne in mind, our unmodified wind models require a very massive and highly luminous protoneutron star with small radius. Indeed, considering the fact that our successful wind models originate from neutron stars with $M \gtrsim 2.0$ M$_\odot$ and $R_\nu \lesssim 9$ km, we are forced to consider the possibility that the primary site for the r-process is not a protoneutron star at all. A neutrino-driven outflow generated near the event horizon of a black hole might bear many of the characteristics of our successful protoneutron star models. Perhaps very short timescale outflows or jets originating from the compact inner accretion disk created in the collapsar models of MacFadyen & Woosley (1999) attain the necessary conditions for r-process nucleosynthesis. Such outflow models would benefit by being generated in a region with high M/R_ν, without being subject to the constraints imposed on neutron stars by the nuclear equation of state.

3.9 Discussion

We have constructed a robust and efficient algorithm for solving the neutrino-driven protoneutron star wind problem using both general relativity and Newtonian gravity. We employed physical boundary conditions for the transonic wind, a well-motivated neutrino energy deposition function, and an equation of state suited to this problem. For the first time, we included the differential equation for the evolution of Y_e in radius and the proper sonic point boundary condition. Using this computational tool, we studied the structure and systematics of neutrino-driven winds with an eye toward assessing the suitability of this site for r-process nucleosynthesis. We have examined a wide range of protoneutron star radii, masses, and neutrino spectral characteristics. By positing an expression for $L_\nu^{\rm tot}(t)$, we have modeled potential contraction and cooling scenarios that might exist in Nature and calculated the total mass ejected for the corresponding evolutionary trajectories. Employing general relativistic hydrodynamics, we find significant enhancements in the asymptotic entropy of the wind, in good agreement with the post-Newtonian models of Qian & Woosley (1996), the analytic approximations of Cardall & Fuller (1997), and the work of Otsuki et al. (2000). In addition, we find that modest modifications to the net energy deposition rate can markedly improve the conditions for r-process nucleosynthesis. Indeed, we feel that changes in the profile of energy deposition represent the most viable alterations to our models, which might lead to robust r-process nucleosynthesis in the protoneutron star context.

Our results indicate that only an early-time epoch of r-process nucleosynthesis at high L_ν, small τ_ρ, and modest entropy is possible. A late-time r-process, at very high entropy ($\gtrsim 300$), long τ_ρ, and low L_ν is not viable. There are several components to this argument. As the luminosity of the protoneutron star decays, both the asymptotic entropy and dynamical timescale of the wind increase. The former is conducive to r-process nucleosynthesis. The latter is not. Hence, the inexorable rise in both compete. Fundamentally, for the transonic wind, we find that the asymptotic entropy does not increase fast enough to compensate for the deleterious rise in τ_ρ. In addition, as the luminosity decays and τ_ρ increases, $\dot{M}$ decreases. For example, our 1.4 $M_\odot$ evolutionary model only reaches $s_a \sim 300$ when $\dot{M} \sim 5\times10^{-10}$ $M_\odot$ s^{-1} and $\tau_\rho \sim 5$ seconds. Clearly, even if the r-process could exist under these conditions, such an epoch would have to continue for many thousands of seconds to produce even 10^{-6} $M_\odot$ of r-process ejecta. Finally, the continued rise in Y_e^a at late times as $\langle\varepsilon_{\nu_e}\rangle$ and $\langle\varepsilon_{\bar{\nu}_e}\rangle$ decrease (due to the energy threshold for the reaction $\bar{\nu}_e p \rightarrow ne^+$, the *threshold effect*) also argues against a high-s_a, long-τ_ρ r-process.

For these reasons, we conclude that if r-process nucleosynthesis occurs in protoneutron star winds, it must occur at early times, at or just after the moment when R_ν reaches a minimum. Our 1.4 $M_\odot$ evolutionary trajectory with $R_\nu \propto 1 - at$ in Fig. 3.11 does not attain sufficiently high entropies and short timescales for successful third peak r-process nucleosynthesis. We have calculated the nucleosynthetic yield at every luminosity (time) in this trajectory and at no point does the resulting nucleosynthesis go beyond $A \sim 100$. Interestingly, however, we find that the luminosity point that yields the highest average A ejecta corresponds to the point in time where R_ν reaches a minimum. This point is also a minimum in τ_ρ for the trajectory. We calculated the nucleosynthesis at this same luminosity point for each mass in Fig. 3.11. Even for the 2.0 M$_\odot$ model with $s_a \sim 150$, we did not obtain nucleosynthesis beyond the second abundance peak. As evidenced by the survey calculations of Hoffman, Woosley, & Qian (1997) and Meyer & Brown (1997) and the wind calculations of Otsuki et al. (2000), these models are outside a regime of successful third-peak nucleosynthesis. However, in §3.8.3 we have shown that reasonable modifications to the spectral character of the neutrinos and the energy deposition function might conceivably shorten τ_ρ sufficiently for the r-process to proceed in some of these models. In §3.8.4, we found that winds with $s_a \simeq 150$, $\tau_\rho \lesssim 1.3$ ms, and $0.47 \lesssim Y_e^a \lesssim 0.495$ can generate third-peak r-process elements.

If transonic protoneutron star winds are the primary site for r-process nucleosynthesis, then a successful r-process wind model must enter this $s_a - \tau_\rho - Y_e^a$ regime. The wind, starting just after re-ignition of the supernova shock, begins with large R_ν and $L_\nu^{\rm tot}$ and, hence, low entropy ($s_a \sim 50$) and short dynamical timescales (τ_ρ is several ms). In order to avoid overproduction of $A \sim 90$ nuclei, Y_e^a is high ($\gtrsim 0.48$) during this low entropy contraction phase (see §3.8.1; Hoffman et al. 1996). As the protoneutron star contracts, it moves to much higher entropy and shorter τ_ρ. Just as R_ν reaches a minimum and the protoneutron star is at its most compact, s_a is sufficiently high (~ 150), and τ_ρ is sufficiently short ($\lesssim 1.3$ ms) to guarantee successful third peak r-process nucleosynthesis. This epoch does not persist. Because R_ν is now constant in time the wind evolves quickly along trajectories like those in Figs. 3.9 and 3.11 with $s_a \propto \tau_\rho^{0.2}$ to much longer timescales and only moderately larger s_a. This, coupled with the rise in Y_e^a due to the threshold effect, effectively shuts off the r-process so that no more than $\sim 10^{-5}$ $M_\odot$ is ejected. We emphasize that this scenario requires the wind to move into and then out of an r-processing regime in the space of $s_a - \tau_\rho - Y_e^a$.

Such a picture is provocative, but not yet convincing. Simply obtaining a wind solution that has proper s_a, τ_ρ, and Y_e^a to guarantee production of the third peak is hardly sufficient to explain the remarkable agreement between the r-element abundances with atomic masses at and beyond barium in ultra-metal-poor halo stars and the observed solar r-process inventory. It is difficult to understand how such a scenario might consistently reproduce the barium abundance, all the lanthanides, the platinum peak, and the actinides (Cayrel et al. 2001; Hill et al. 2001). In addition, while the data for these halo stars show remarkable consistency with the solar abundances above $A \sim 135$, below this mass they are markedly inconsistent and there is significant star-to-star scatter. Perhaps some subset of all supernovae account for the region below $A \sim 135$ and never undergo a vigorous r-process. Perhaps others do obtain the required s_a, τ_ρ, and Y_e^a and account for the full range of nuclides, including the first abundance peak and proceeding to uranium (Wasserburg and Qian 2000; Qian and Wasserburg 2000; Sneden et al. 1996; Burris et al. 2000). As we demonstrate in §3.6 with our $R_\nu \propto t^{-1/3}$ model, slow radial contraction of the protoneutron star may preclude any significant r-process yield, as the wind would then never enter a regime of short dynamical timescale with $s_a \sim 150$.

The supernova progenitor structure might be important in this regard. The two-dimensional calculations of Burrows, Hayes, & Fryxell (1995) and the one-dimensional results from Janka & Müller (1995) indicate that a transonic protoneutron star wind can form just tenths of seconds after the successful re-ignition of the supernova shock. The pressure of the wind is sufficient for it to emerge into the expanding supernova ejecta. However, Janka & Müller (1995) found that as the supernova shock passes through the Si-O interface in their one-dimensional 15 $M_\odot$ progenitor it causes a strong reverse shock that slows the wind expansion from a $v \sim 2 \times 10^9$ cm s^{-1} to a few times 10^8 cm s^{-1}. It is possible that a termination or reverse shock might generally disrupt the transonic wind as it propagates toward the protoneutron star. Exactly how far in radius the reverse shock propagates will be a function of the hydrodynamical power of both the wind and the reverse shock as the neutrino luminosity decays, each being functions of the progenitor structure. With sufficient power, the reverse shock may continue to the sonic point. This would put the whole region between the protoneutron star surface and the supernova shock in sonic contact, thereby converting a transonic wind into a subsonic breeze. We have conducted preliminary hydrodynamical calculations, which suggest this could occur in certain circumstances. Steady-state solutions to the wind problem can also be formulated in this context, but with an outer boundary pressure set by conditions at the supernova shock. Qian & Woosley (1996) explored the effects of an external boundary pressure on their wind models. This increased the wind entropy by just 11 units, but increased the dynamical timescale by more than 60%. Such a change would be detrimental to an early-time, short-τ_ρ r-process. However, it may be that the reverse shock does not have sufficient power to disrupt the wind interior to the sonic point. In the steady-state, across the shock boundary, the velocity will decrease, the density will increase so as to maintain $\dot{M}$, and both the temperature and entropy will increase.

In order to test the effects of a termination or reverse shock on the nucleosynthesis, we inserted a shock by hand at a radius ($r_{\rm sh}$) of 4000 km in our wind model with $M = 2.0$ M$_\odot$ and $R_\nu = 9$ km (see §3.8.4), far outside the sonic point ($r \simeq 180$ km). At $r_{\rm sh}$ the matter velocity was 5.1×10^9 cm s^{-1}, ρ was 17 g cm^{-3}, and T was approximately 0.023 MeV. Using the Rankine-Hugoniot shock jump conditions, we estimate that $v \simeq 7v'$, $\rho \simeq \rho'/7$, and $T \sim T'/2$, where unprimed quantities are for the wind just before the shock ($r < r_{\rm sh}$), and primed quantities are for the flow just after the shock ($r > r_{\rm sh}$). These conditions increase s_a by about 10 units in the post-shock region and increase τ_ρ significantly, due to the sudden decrease in v. This had subtle, but potentially significant effects on the resulting r-process yield. To appreciate this, one must understand that without the slowing of the fluid trajectory by passage through the reverse shock, the r-process freeze-out in our wind models occurs for temperatures below 0.01 MeV, because only then are beta decays along the r-process path fast enough to compete with the rapid material expansion. By contrast, if the material slows (and reheats) by passage through the shock, the r-process freeze-out happens at higher temperatures, typically near 0.05 MeV. Although the average number of neutrons captured per seed nucleus is the same for the shocked and unshocked (but otherwise identical) trajectories, the distribution of those neutron captures is different. In particular, for the case considered here, the shocked trajectory had a factor of three larger yield at A$\sim$195. The reason is that, when the trajectory slowed and reheated by shock passage, the nuclear flow changed and allowed more nuclei to leak out of the N=82 closed shell and proceed up to N=126 (A$\sim$195) at the expense of flow from the N=50 closed shell (A$\sim$80) to N=130. An additional interesting effect was that, unlike the unshocked trajectory, the shocked trajectory showed evidence of formation of a rare-earth element peak at A$\sim$165. Surman et al. (1997) argued that this peak forms during freeze-out as the r-process path rapidly moves through the Z$\sim$60, N$\sim$104 region of somewhat enhanced nuclear stability in the nuclide chart. In the winds we study here, the shocked trajectories favor such a freeze-out while the unshocked trajectories do not. We conclude that the finer details of the r-process abundance curve may depend in interesting ways on the location and strength of a termination or reverse shock.

These hydrodynamical issues are part of the larger question of fallback in Type-II supernovae. It is possible that the most massive supernova progenitors, with their extended hydrogen envelopes and dense core structures, experience significant fallback over timescales much longer than the cooling time (Chevalier 1989; Woosley and Weaver 1995). Even if the wind were able to emerge from the neutron star for 10-20 seconds after explosion, it might not have sufficient power to overcome extended fallback over minutes and hours. Even without a large overlying hydrogen envelope

(Type Ib, Ic), the neutrino-driven wind may be hindered by any progenitor with a large inner core and outer core binding energy. Therefore, we speculate that an early-time r-process, unencumbered by fallback or reverse shocks, is most likely in less massive Type-II, -Ib, or -Ic supernova progenitors. Accretion-induced collapse may offer even more potential in this context for a fully developed, early-time transonic wind as, in this case, there is no overlying mantle to impede the wind's emergence (Fryer et al. 1999).

3.10 Conclusions

Our major conclusions are the following:

- For a given mass outflow rate, we find a significantly shorter dynamical timescale (τ_ρ) than indicated by many previous investigations.

- Because the temperature, density, and velocity gradients often used in defining a dynamical timescale evolve on a mass element as it moves away from the protoneutron star, employing a unique dynamical timescale to characterize the wind is not recommended.

- For a given protoneutron star radius, the asymptotic entropy (s_a) is proportional to $\tau_\rho^{0.2}$.

- A late-time, high entropy ($s_a \gtrsim 300$), long timescale neutrino-driven wind, is not a viable astrophysical site for r-process nucleosynthesis. Although the wind may eventually realize very high entropy, the mass outflow rate will be too small and the dynamical timescale too long at such an epoch to account for the galactic r-process abundance.

- The third-peak r-process elements can be produced in significant abundance in protoneutron star winds only at early times, at modest entropy ($s_a \sim 150$), and very short dynamical timescale ($\tau_\rho \sim 1$ ms).

- Winds originating from protoneutron stars with mass 1.4 $M_\odot$ and radius $R_\nu =$ 10 km do not produce elements beyond $A \sim 100$ at any time during wind evolution.

- We derive that third-peak r-process arises naturally in the context of spherical, transonic protoneutron star winds only in the unlikely case of protoneutron stars with $M \gtrsim 2.0$ $M_\odot$ and $R_\nu \lesssim 9$ km.

- Shocks in the protoneutron star wind, exterior to the sonic point, caused by the wind's interaction with the inner supernova can significantly influence the third-peak and rare-earth r-process element abundances.

All of these conclusions hold for the generally high Y_e's (0.46-0.49) derived in this work. Only in the unlikely case that Y_e in the wind is $\lesssim 0.35$ are our conclusions dramatically altered. In this case, third-peak r-process nucleosynthesis might be obtained in our transonic models for protoneutron star masses less than 2.0 $M_\odot$ and radii greater than 9 km, at early times in the wind evolution. The uncertainty in the spectral characteristics of the electron and anti-electron neutrinos in determining the asymptotic electron fraction during wind formation and evolution is primary on our list of unresolved issues. Others include:

- the character of the energy deposition profile as obtained from detailed neutrino transport in a self-consistent calculation,

- the high-density nuclear equation of state, which would elucidate the range of protoneutron star masses and radii relevant,

- the hydrodynamical interaction of the wind and shocks in the expanding post-supernova environment,

- the effects of rotation and magnetic fields,

- exactly how, even given successful third-peak nucleosynthesis for a given model, the universality of the observed r-process distribution for $A \gtrsim 135$ can be accounted for generically by the progenitor-dependent parameter space of neutrino-driven winds.

These last points leave the prospect of the r-process in this context an open question. We conclude from this study that if the r-process occurs in protoneutron star winds, it most likely occurs at early times after the preceding supernova, in winds with very short dynamical timescales ($\lesssim 1.3$ ms), moderate entropies (~ 150), and, possibly, high electron fractions ($0.47 \lesssim Y_e^a \lesssim 0.495$). In contrast to the early-time scenario, because protoneutron star winds only enter a high entropy ($s_a \gtrsim 300$) regime with very low $\dot{M}$ ($\lesssim 10^{-9}$ M$_\odot$ s^{-1}) and extremely long timescales ($\tau_\rho \gtrsim$ seconds), a late-time r-process is simply not viable. Conditions suitable for an early-time r-process are realized in our models only by very compact protoneutron stars with $M = 2.0$ M$_\odot$ and $R_\nu \lesssim 9$ km. The conditions necessary for third-peak r-process nucleosynthesis are not realized in neutrino-driven transonic winds from canonical neutron stars with $M = 1.4$ M$_\odot$ and $R_\nu = 10$ km. In fact, for this neutron star mass, we require $R_\nu \lesssim 6.5$ km. Although such neutron star masses and radii are not entirely excluded by current high density equations of state, such radii seem unlikely to obtain in the early post-supernova phase. The short-timescale jet outflows from the dense inner accretion disk around a black hole formed in the collapsar models of MacFadyen & Woosley (1999) might attain the necessary entropies and timescales for the r-process, since in that context M/R_ν can be significantly larger than in the protoneutron star context. Importantly, it should be noted that we consistently produce r-process nucleosynthesis *below* $A \sim 135$. Perhaps protoneutron stars of canonical mass and radius (1.4 M$_\odot$, 10 km) produce elements in this mass range generically, thus accounting (due to progenitor structure and temporal characteristics of the neutrino spectrum) for the variations in abundance observed in these elements in ultra-metal-poor halo stars.

TABLE 3.1. Fiducial Wind Models: 1.4 $M_\odot$

$L^{51}_{\bar{\nu}_e}$	$L_\nu^{\rm tot}$ (10^{51} erg s^{-1})	$\dot{\rm M}$ ($M_\odot$ s^{-1})	Q (10^{48} erg s^{-1})	$P_{\rm mech}$ (10^{48} erg s^{-1})	τ_ρ (ms)	$s_{\rm a}$
8.0	37.0	9.05×10^{-5}	35.1	0.848	3.68	83.9
7.0	32.4	6.56×10^{-5}	25.1	0.561	4.24	86.4
6.0	27.6	4.47×10^{-5}	17.1	0.346	5.01	89.5
5.0	23.1	2.84×10^{-5}	10.9	0.194	6.14	93.4
4.0	18.5	1.63×10^{-5}	6.28	0.0929	7.93	98.4
3.0	13.9	8.03×10^{-6}	3.09	0.0346	11.29	105.4
2.0	9.25	3.74×10^{-6}	1.14	8.59×10^{-3}	19.19	116.2
1.0	4.63	5.44×10^{-7}	0.211	8.24×10^{-4}	49.54	137.6
0.6	2.78	1.58×10^{-7}	0.062	1.50×10^{-4}	100.9	156.3

TABLE 3.2. Evolutionary Wind Models: $L_{\bar{\nu}_e}^{51} = 8.0$, 3.4, and 0.4

Mass ($M_\odot$)	$L_{\bar{\nu}_e}^{51}$	$L_\nu^{\rm tot}$ (10^{51} erg/s)	R_ν (km)	$\dot{M}$ ($M_\odot$ s^{-1})	Q (10^{48} erg/s)	$P_{\rm mech}$ (10^{48} erg/s)	τ_ρ (ms)	$s_{\rm a}$	Y_e^a
2.0	8.0	37.0	20.3	2.19×10^{-4}	53.3	1.27	10.45	67.08	0.467
1.8	8.0	37.0	20.3	3.03×10^{-4}	67.2	1.67	9.87	59.05	0.465
1.6	8.0	37.0	20.3	4.38×10^{-4}	83.8	2.27	9.27	51.39	0.463
1.4	8.0	37.0	20.3	6.69×10^{-4}	108.2	3.25	8.63	44.02	0.460
2.0	3.4	15.7	10.0	9.80×10^{-6}	5.94	0.0826	6.83	151.61	0.469
1.8	3.4	15.7	10.0	1.39×10^{-5}	7.34	0.108	6.78	129.43	0.467
1.6	3.4	15.7	10.0	2.04×10^{-5}	9.29	0.148	6.56	109.70	0.465
1.4	3.4	15.7	10.0	3.14×10^{-5}	12.1	0.213	6.21	91.78	0.462
1.4[a]	3.4	15.7	14.7	9.03×10^{-4}	21.8	0.424	9.98	64.01	0.457
2.0	0.4	1.85	10.0	1.24×10^{-7}	0.0757	1.97×10^{-4}	75.49	234.20	0.492
1.8	0.4	1.85	10.0	1.72×10^{-7}	0.0923	2.48×10^{-4}	75.21	198.88	0.491
1.6	0.4	1.85	10.0	2.46×10^{-7}	0.114	3.23×10^{-4}	72.92	167.40	0.490
1.4	0.4	1.85	10.0	3.67×10^{-7}	0.144	4.44×10^{-4}	69.14	138.92	0.489

[a] The 1.4 $M_\odot$ trajectory in Fig. 3.11 with $R_\nu \propto t^{-1/3}$, for $L_{\bar{\nu}_e}^{51} = 3.4$.

TABLE 3.3. Fiducial Wind Models: 1.4 $M_\odot$

Mass ($M_\odot$)	$L_\nu^{\rm tot}$ (km)	R_ν (10^{51} erg s^{-1})	$\dot{\rm M}$ ($M_\odot$ s^{-1}) ($M_\odot$ s^{-1})	Q (10^{48} erg s^{-1})	$P_{\rm mech}$ (10^{48} erg s^{-1})	τ_ρ (ms)	$s_{\rm a}$
1.8	15.7	9.0	1.01×10^{-5}	6.18	0.092	5.63	146.44
1.6	15.7	9.0	1.48×10^{-5}	7.79	0.122	5.61	122.98
1.4	15.7	9.0	2.29×10^{-5}	10.2	0.174	5.39	102.15
1.4	15.7	8.5	1.94×10^{-5}	9.25	0.157	4.97	108.48
1.4	15.7	8.0	1.62×10^{-5}	8.35	0.141	4.54	115.86

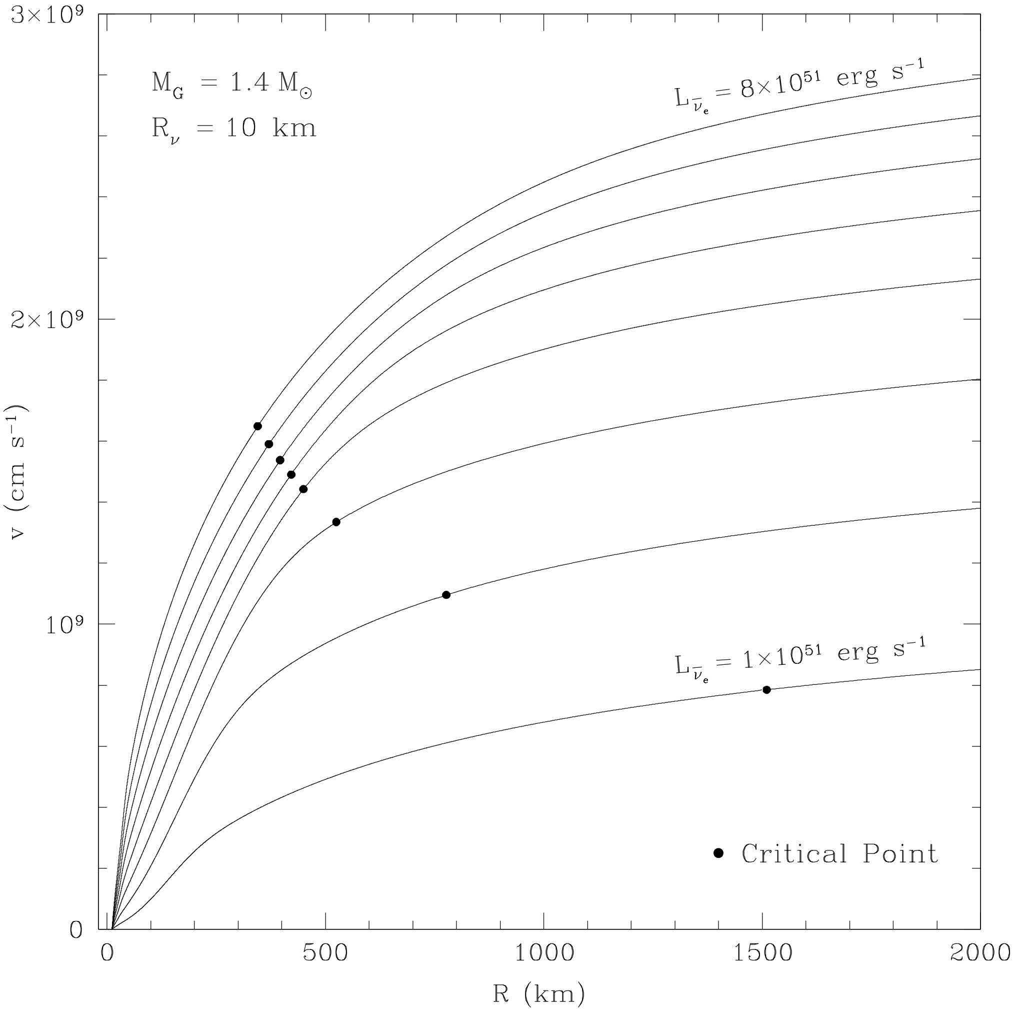

FIGURE 3.1. Matter velocity (v) in cm s^{-1} as measured in the Schwarzschild frame as a function of radius (R) in km for a 1.4 $M_\odot$ (gravitational) protoneutron star with $L_{\bar{\nu}_e}$ = 8, 7, 6, 5, 4, 3, 2, and $1{\times}10^{51}$ erg s^{-1}. For $L_{\bar{\nu}_e} = 8\times10^{51}$ erg s^{-1}, we set $\langle\varepsilon_{\nu_e}\rangle$ = 11 MeV, $\langle\varepsilon_{\bar{\nu}_e}\rangle$ = 14 MeV, and $\langle\varepsilon_{\nu_\mu}\rangle$ = 23 MeV. For each subsequent luminosity, the average neutrino energy for each species was decreased according to $\langle\varepsilon_\nu\rangle \propto L_\nu^{1/4}$. The luminosities were set in the ratios $L_{\bar{\nu}_e}/L_{\nu_e} = 1.3$ and $L_{\bar{\nu}_e}/L_{\nu_\mu} = 1.4$. The dots mark the critical point for each wind profile, where the matter velocity is equal to the local speed of sound. The neutrinosphere radius is held fixed at 10 km. For all profiles, for $r \lesssim 60$ km, the flow is nearly homologous with $v \propto L_\nu r$.

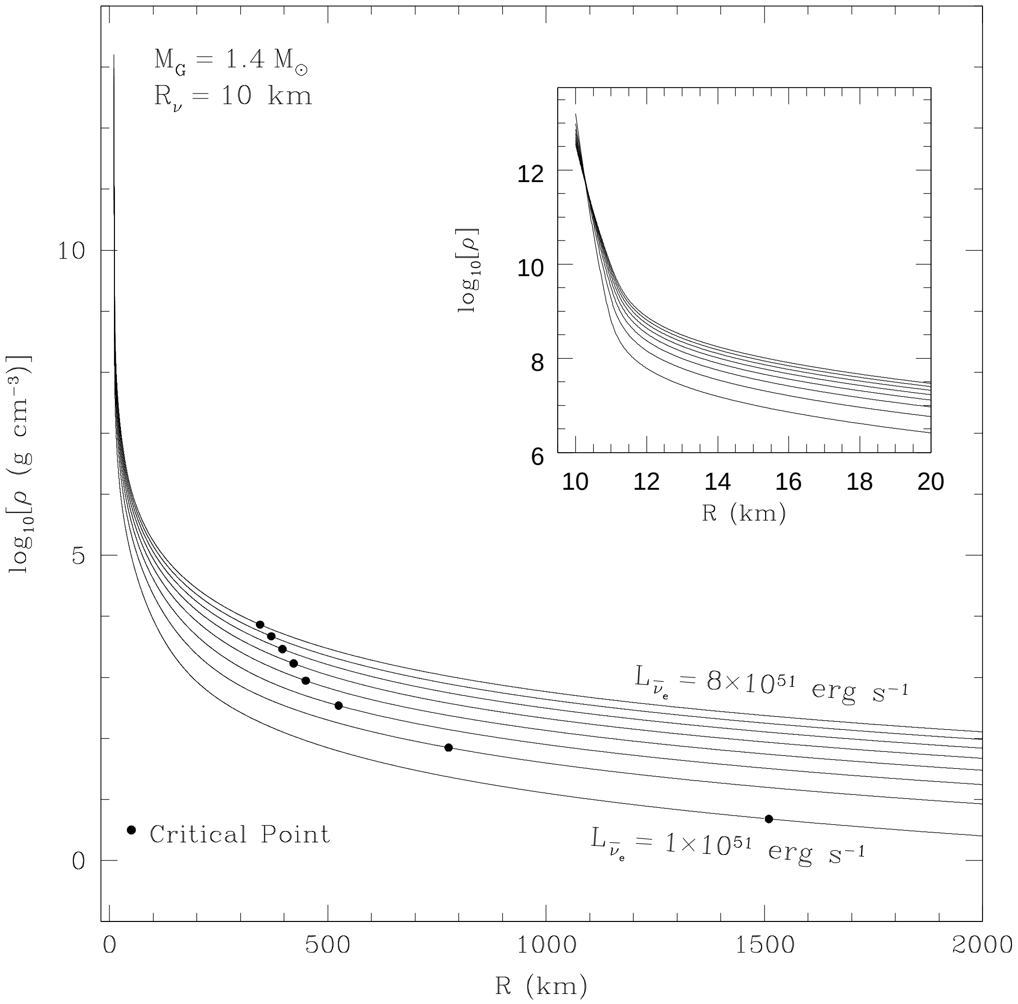

FIGURE 3.2. Log$_{10}$ of the mass density (ρ) in g cm^{-3} versus radius (R) in km for the same range of neutrino luminosities as in Fig. 3.1 and for the same protoneutron star characteristics. Dots mark the critical point. The inset shows $\log_{10}\rho$ versus R for the region close to the protoneutron star. Note the steep density gradient, which drops precipitously over as much as five orders of magnitude in just over a kilometer. As the neutrino luminosity decreases, $\rho(R_\nu)$ increases in order to maintain our inner integral boundary condition on the ν_e neutrino optical depth (eq. 3.22).

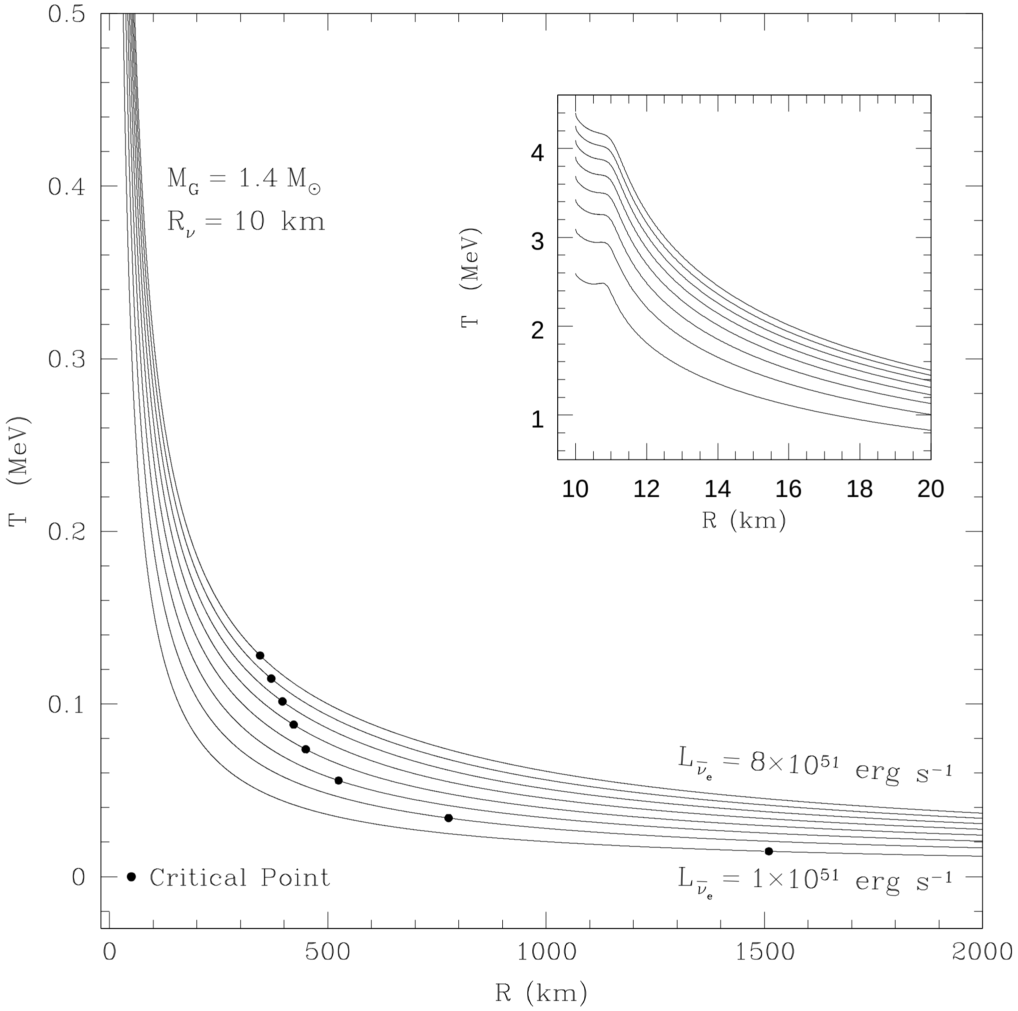

FIGURE 3.3. Matter temperature (T) in MeV versus radius in km for the same profiles as in Fig. 3.1. Dots mark the critical point. Note that the important regime of possible r-processing lies between 0.5 MeV and approximately 0.08 MeV, a region extending out to 700 km for the highest luminosities and to less than 200 km for the lowest luminosities shown. Comparing the temperature in this range of radii to those in Fig. 3.1, it's clear that the assumption of constant outflow velocity (Meyer and Brown 1997) is a poor approximation during nucleosynthesis in neutrino-driven winds. The inset shows the structure of the temperature as a function of radius very close to the neutrinosphere. The bump in T is caused by the onset of heating (compare with Fig. 3.4).

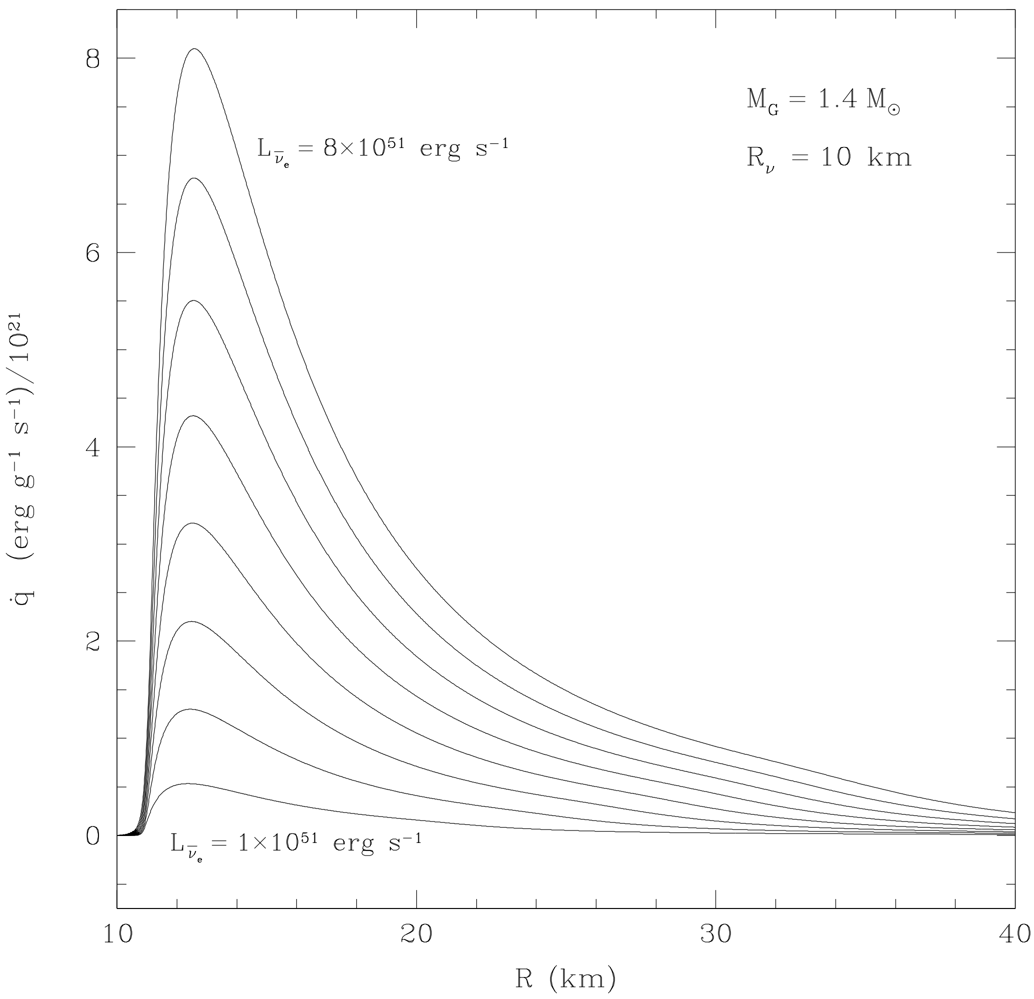

FIGURE 3.4. Energy deposition rate ($\dot{q}$) in units of 10^{21} erg g^{-1} s^{-1} as a function of radius (in km) for the wind models in Figs. 3.1–3.3. $\dot{q}$ profiles for $\bar{\nu}_e$ neutrino luminosities from 8×10^{51} erg s^{-1} to 1×10^{51} erg s^{-1} are depicted. The total heating rates (Q; eq. 3.14) for each of these models are given in Table 3.1.

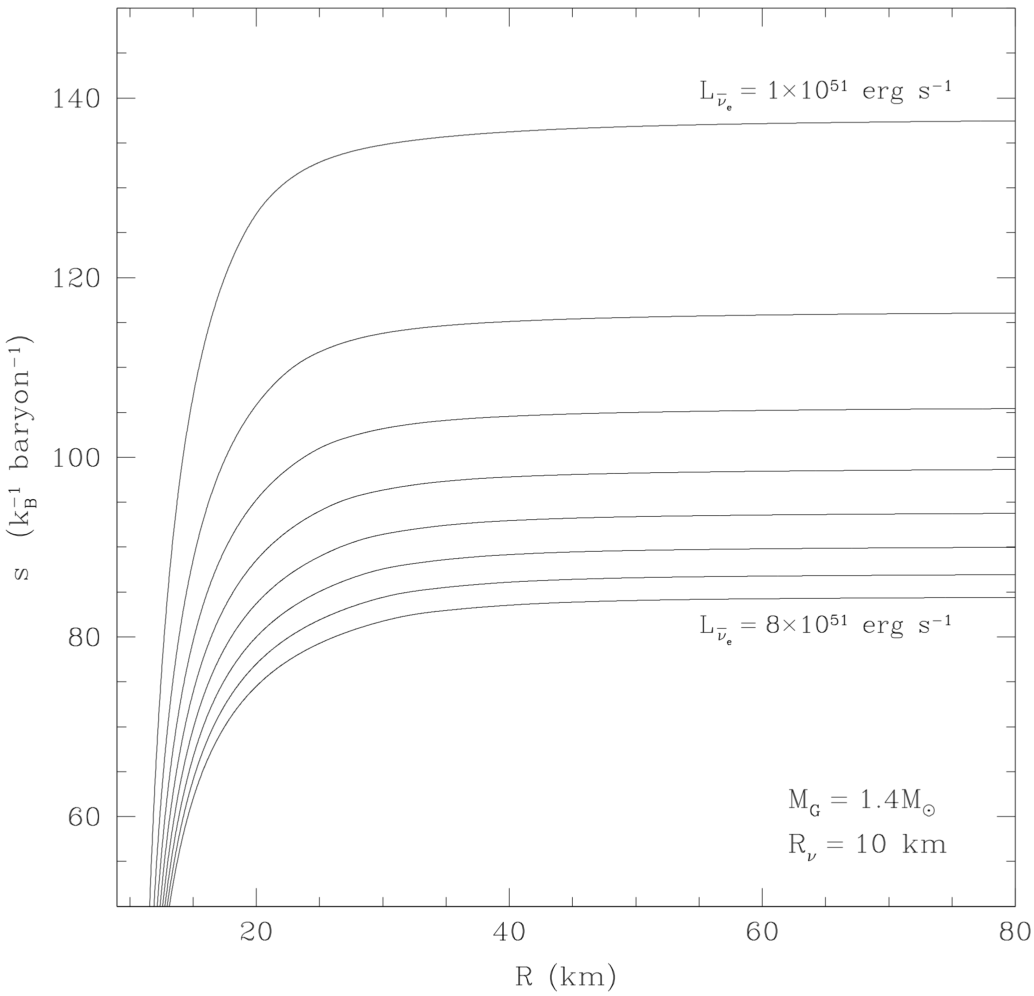

FIGURE 3.5. Entropy (s, per baryon per k_B) versus radius in km for the same protoneutron star wind models as in Figs. 3.1-3.4. Note that the entropy asymptotes quickly; comparing this figure to Fig. 3.3, we can see that in most cases s increases less than 10 units for $T < 0.5$ MeV.

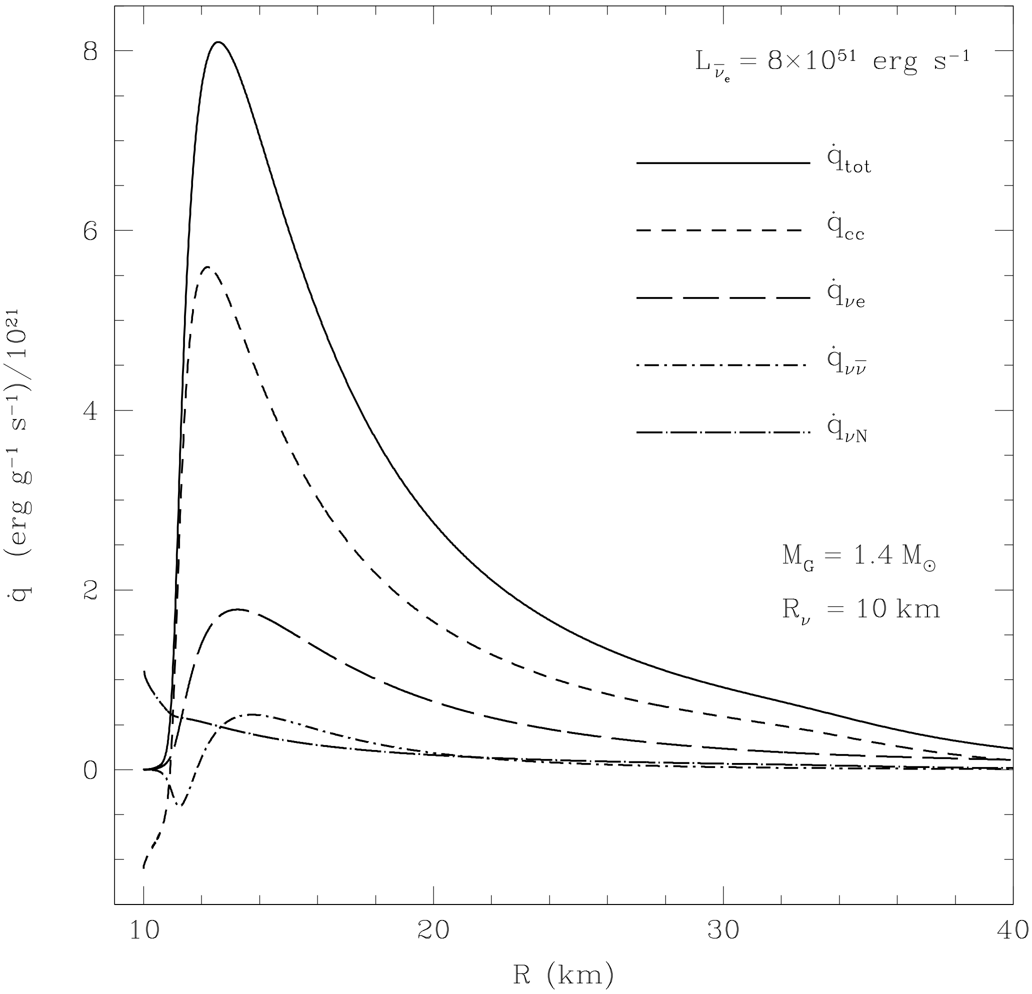

FIGURE 3.6. Contributions of specific neutrino processes to the energy deposition rate for $L_{\bar{\nu}_e} = 8\times10^{51}$ erg s^{-1}, $R_\nu = 10$ km, and $M = 1.4$ M$_\odot$. The solid line shows the total heating rate due to all processes, the short-dashed line is the net contribution from the charged-current reactions ($\dot{q}_{cc}$) (eqs. 3.24 and 3.25), the long dashed line is neutrino-electron/positron scattering ($\dot{q}_{\nu e}$; eq. 3.31), the short dot-dashed line is the net energy deposition rate due to $\nu_i\bar{\nu}_i \leftrightarrow e^+e^-$ ($\dot{q}_{\nu\bar{\nu}}$; eqs. 3.33 and 3.35), and the long dot-dashed line is for neutrino-nucleon scattering ($\dot{q}_{\nu N}$; eq. 3.32). Note the fairly rapid decrease in $\dot{q}_{cc}$ at $r \sim 35$ km is due to the recombination of free neutrons and protons into α particles. As the neutrino luminosity decreases in these models, this transition moves inward in radius so that, for the lowest luminosities, the charged current processes end abruptly at ~ 25 km. For models with larger M/R_ν $\dot{q}_{\nu e}$ and $\dot{q}_{\nu\bar{\nu}}$ become more important relative to $\dot{q}_{cc}$. However, even for $M = 2.0$ M$_\odot$ and $R_\nu = 10$ km, $\dot{q}_{cc}$ dominates at the peak in $\dot{q}_{\rm tot}$.

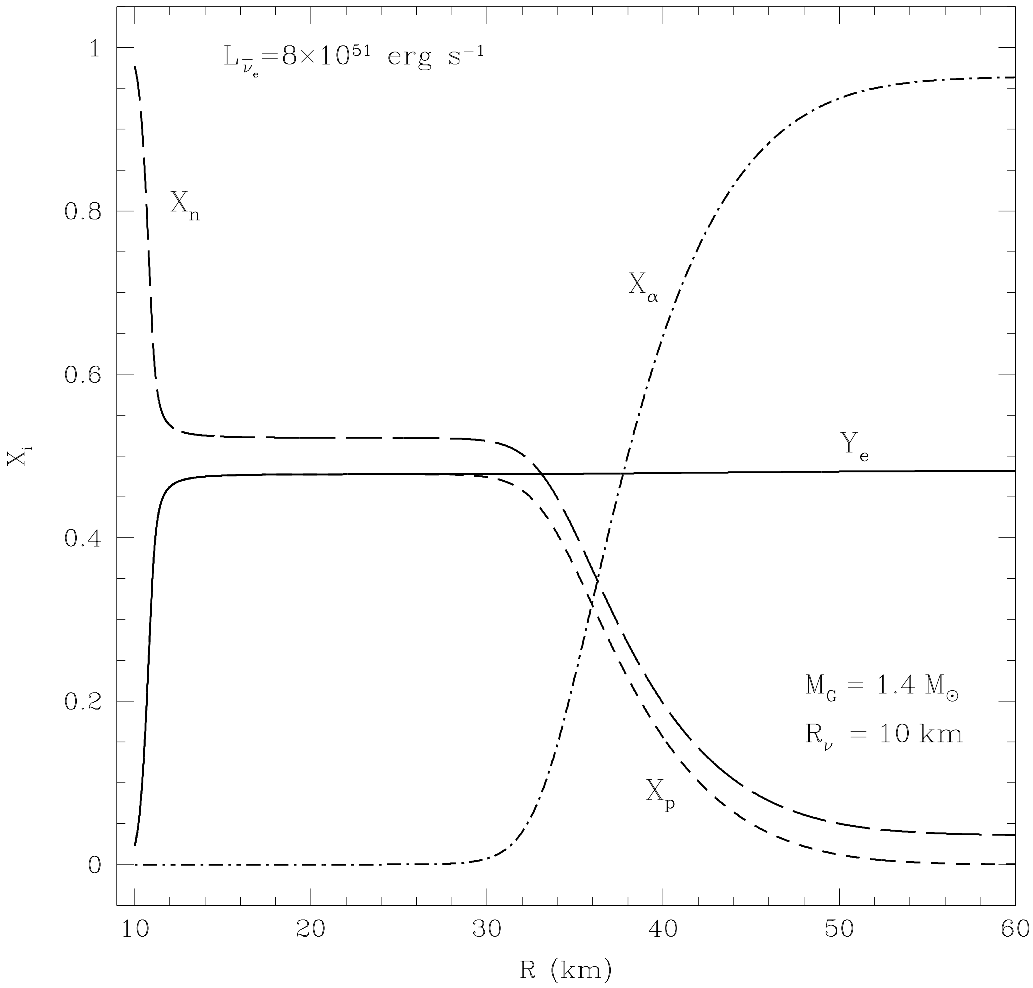

FIGURE 3.7. The electron fraction (Y_e, solid line), proton fraction (X_p, short dashed line), neutron fraction (X_n, long dashed line), and alpha fraction (X_α, dot-dashed line) for the highest luminosity wind model ($L_{\bar{\nu}_e} = 8 \times 10^{51}$ erg s^{-1}) in Figs. 3.1-3.5, corresponding to the heating profile in Fig. 3.6. Note the transition at $r \sim 35$ km where α particles form and effectively shut off the charged-current heating rate. The asymptotic Y_e is set very close to the neutron star ($r \sim 15$ km) and only undergoes small subsequent change as a result of the α-effect (Fuller and Meyer 1995; McLaughlin, Fuller, and Wilson 1996)). In this case, Y_e changes by $\sim$1% beyond $r = 20$ km. The asymptotic electron fraction, Y_e^a, is well-approximated by eq. (3.16) in the text.

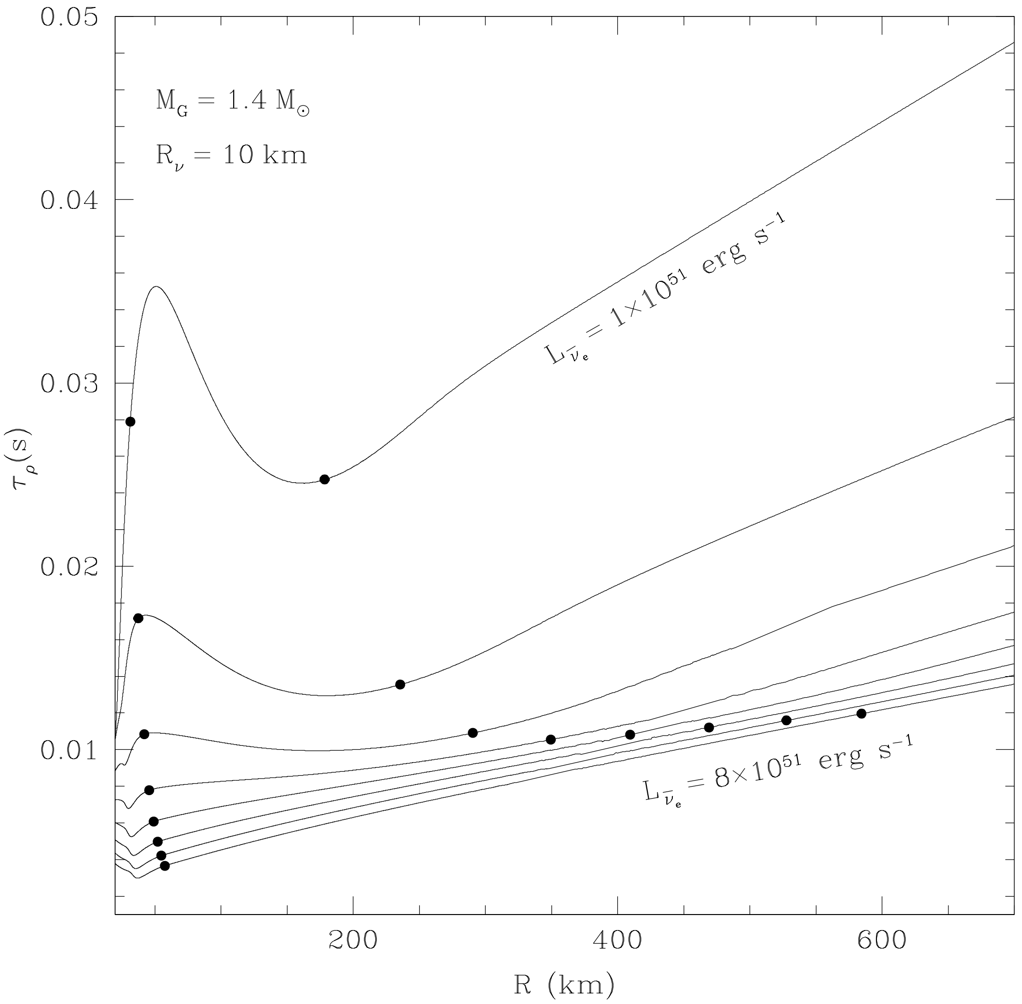

FIGURE 3.8. Dynamical timescale (τ_ρ) defined in eq. (3.36) versus radius for the eight models shown in Figs. 3.1-3.5. On each line, the first point marks the radius at which $T(r) = 0.5$ MeV. The second point marks where $T(r) = 0.1$ MeV. Note that for high luminosities, τ_ρ increases by more than a factor of three over the range of radii and temperatures relevant for r-process nucleosynthesis. For the lowest luminosities $d\tau_\rho/dr$ changes sign and τ_ρ actually decreases by $\sim$30% between the two points on the $L_{\bar{\nu}_e} = 1 \times 10^{51}$ erg s^{-1} curve.

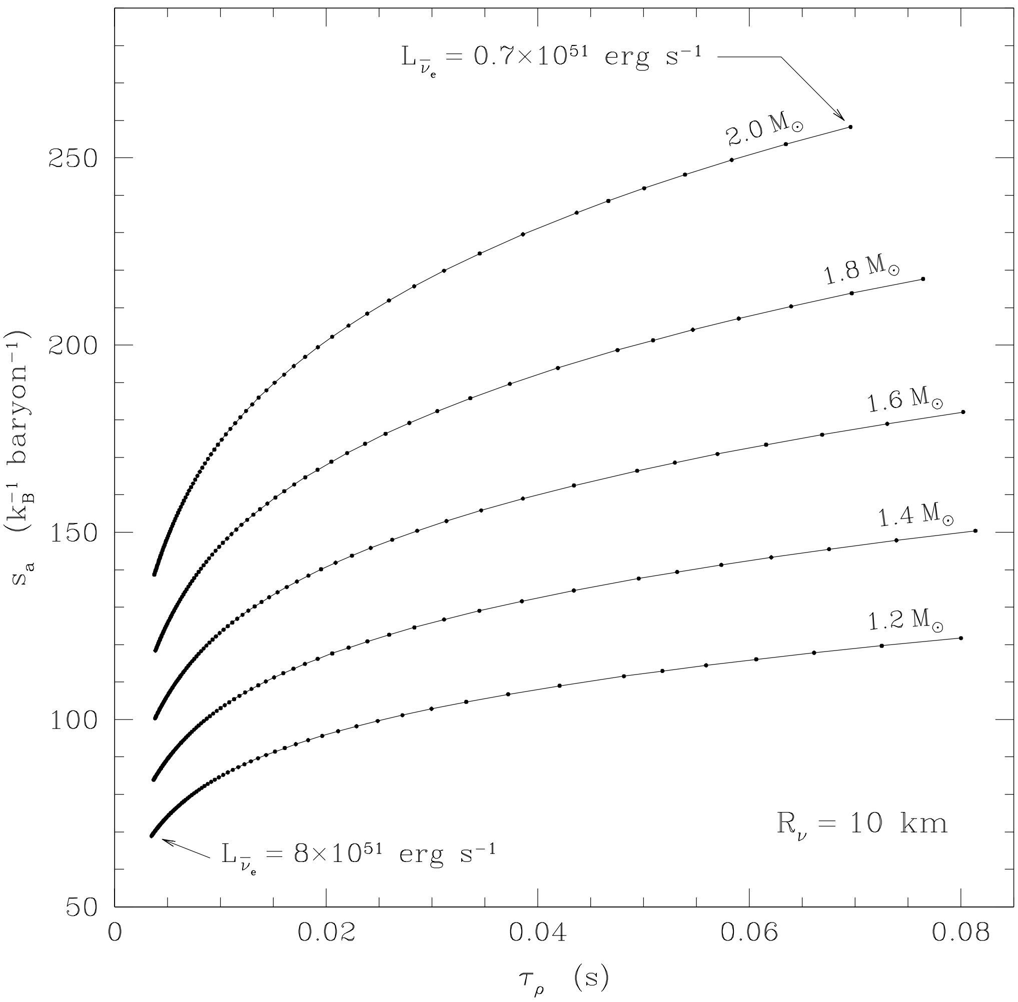

FIGURE 3.9. Tracks for constant protoneutron star mass in the plane of asymptotic entropy (s_a, per k_B per baryon) and dynamical timescale (τ_ρ, eq. 3.36) in seconds. R_ν is held constant at 10 kilometers. Each track covers a range in luminosity from $L_{\bar{\nu}_e} = 8.0\times10^{51}$ erg s^{-1} to $L_{\bar{\nu}_e} = 0.7\times10^{51}$ erg s^{-1}. Small dots are the points for which a model with a given luminosity was calculated. All masses are gravitational masses. In these models, we take $\langle\varepsilon_{\nu_e}\rangle = 11$ MeV, $\langle\varepsilon_{\bar{\nu}_e}\rangle = 14$ MeV, and $\langle\varepsilon_{\nu_\mu}\rangle = 23$ MeV for $L_{\bar{\nu}_e} = 8.0\times10^{51}$ erg s^{-1}. For each subsequent luminosity, the average energies were decreased according to $\langle\varepsilon_\nu\rangle \propto L_\nu^{1/4}$. In Table 3.1, we summarize the global properties at several luminosities along the 1.4 M$_\odot$ trajectory in this figure.

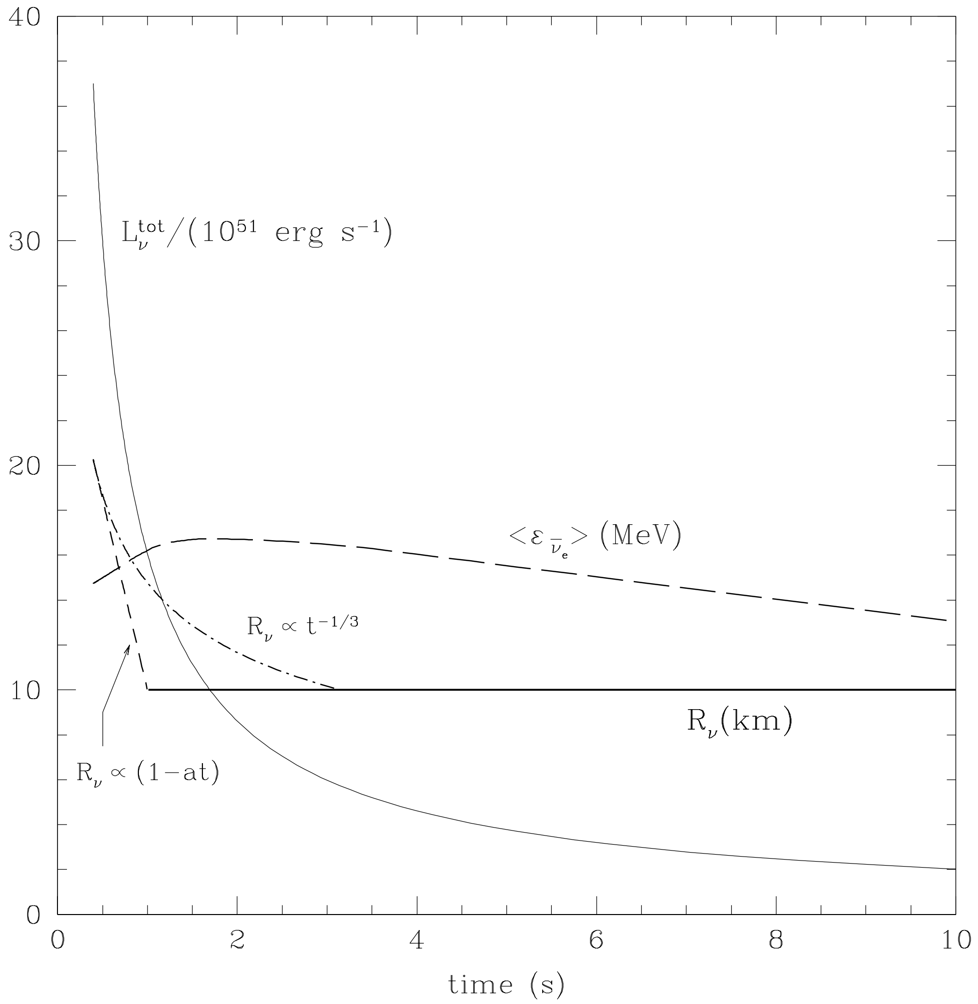

FIGURE 3.10. A schematic showing total neutrino luminosity in 10^{51} erg s^{-1} (thin solid line), average $\bar{\nu}_e$ neutrino energy in MeV (long dashed line), and neutrinosphere radius (R_ν) in km. Two possible evolutions for $R_\nu(t)$ are shown. Linear contraction such that $R_\nu(t = 0.4\,\mathrm{s}) = 20.3$ km and $R_\nu(t = 1\,\mathrm{s}) = 10.0$ km, which we label as '$R_\nu(t) \propto 1 - at$', is shown as a short dashed line. Contraction with $R_\nu(t) \propto t^{-1/3}$ is shown as a dot-dashed line. The thick solid line denotes 10 km, the final R_ν for the protoneutron star. L_ν^{tot} is proportional to $t^{-0.9}$. We set $\langle\varepsilon_{\nu_\mu}\rangle/\langle\varepsilon_{\bar{\nu}_e}\rangle = 1.6$, $\langle\varepsilon_{\bar{\nu}_e}\rangle/\langle\varepsilon_{\nu_e}\rangle = 1.3$, $L_{\bar{\nu}_e}/L_{\nu_\mu} = 1.4$, and $L_{\bar{\nu}_e}/L_{\nu_e} = 1.3$.

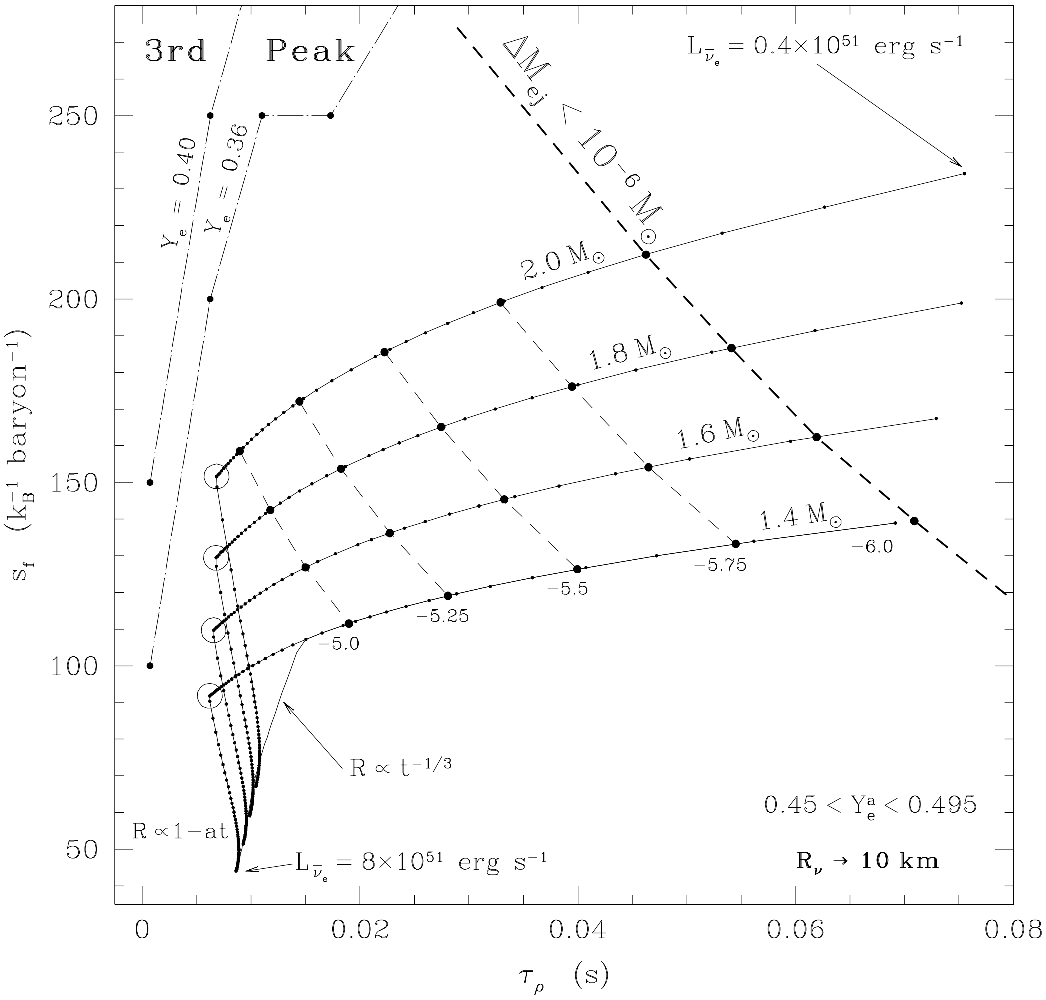

FIGURE 3.11. Evolutionary wind models in the plane of asymptotic entropy (s_a per k_B per baryon) and dynamical timescale (τ_ρ, eq. 3.36) in seconds. Tracks with $R_\nu(t) \propto (1-at)$ (see Fig. 3.10) for $M = 1.4$, 1.6, 1.8, and 2.0 M$_\odot$ are shown as solid lines with small dots. The solid line without dots is the track with $R_\nu(t) \propto t^{-1/3}$ for 1.4 M$_\odot$. All tracks start with $R_\nu \simeq 20.3$ km and $L^{51}_{\bar{\nu}_e} = 8.0$ and end at $L^{51}_{\bar{\nu}_e} = 0.4$. The large open circles mark $L^{51}_{\bar{\nu}_e} = 3.4$ for each mass trajectory. Dashed lines are lines of constant $\log_{10}[\Delta M_{\rm ej}]$ (see eq. 3.38, Fig. 3.13, and text for details). The dashed line, marked with −6.0, delineates the time when only 10^{-6} M$_\odot$ of material is yet to be ejected. For given Y_e^a, the dash-dotted lines indicate production of the third-peak r-process nuclei in the calculations of Meyer & Brown 1997. See §3.6 for discussion.

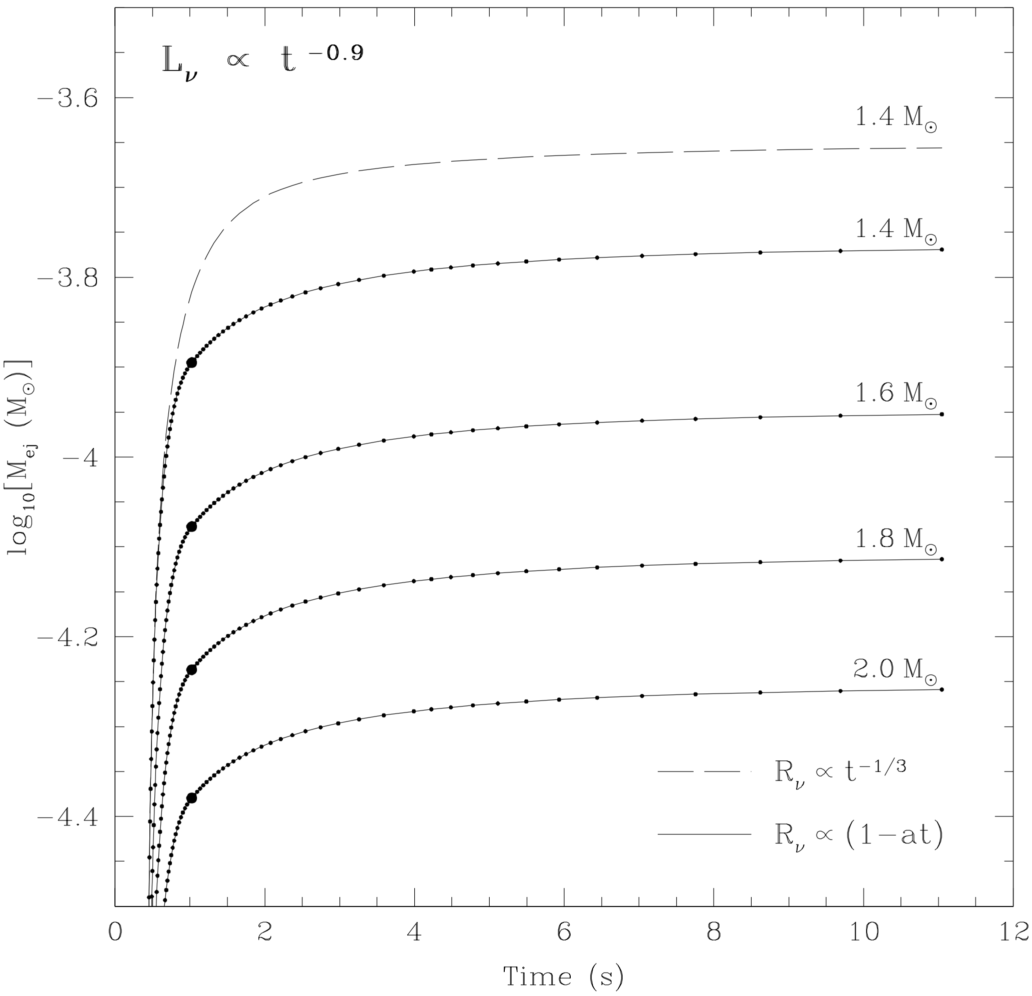

FIGURE 3.12. The log of the integrated total mass ejected $M_{\rm ej}$ (eq. 3.38) in units of $M_\odot$ as a function of time in seconds, assuming $L_\nu(t)^{\rm tot} \propto t^{-0.9}$ for the tracks of constant mass shown in Fig. 3.11. Evolutionary models with $R_\nu(t) \propto (1 - at)$ (see Fig. 3.10) are shown as solid lines with small dots, which correspond to the dots in Fig. 3.11, indicating luminosity (time). $M_{\rm ej}$ for the track in Fig. 3.11 with $R_\nu(t) \propto t^{-1/3}$ and $M = 1.4\ M_\odot$ is shown here as a long dashed line without dots. The large dot on each of the solid curves at $t \sim 1$ second shows the point at which the model has contracted to $R_\nu = 10$ km. This corresponds to the point on Fig. 3.11 where a given track of constant mass with $R_\nu(t) \propto (1 - at)$ takes a sharp turn at $\tau_\rho \sim 0.006$ seconds.

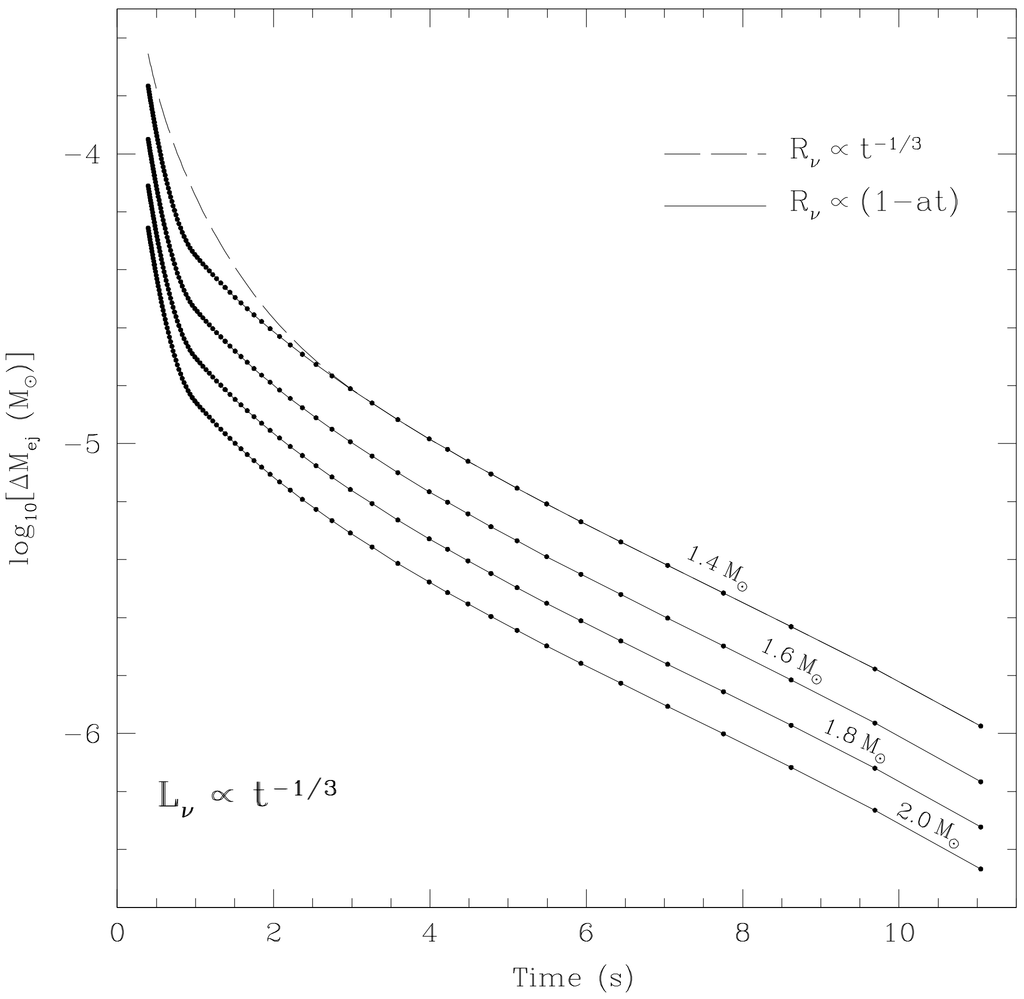

FIGURE 3.13. $\mathrm{Log}_{10}[\Delta M_{\rm ej}(= M_{\rm ej}^{\rm tot} - M_{\rm ej}(t))]$, in units of $\mathrm{M}_\odot$, versus time in seconds for the models in Fig. 3.12. The long dashed line is for the model with $R_\nu(t) \propto t^{-1/3}$. The four solid lines with dots correspond to those in Figs. 3.11 and 3.12 for the 1.4, 1.6, 1.8, and 2.0 $\mathrm{M}_\odot$ evolutionary models, which we label with '$R_\nu(t) \propto 1 - at$'. Lines of constant $\log_{10}[\Delta M_{\rm ej}]$ are shown in Fig. 3.11 as dashed lines connecting big dots on the evolutionary models with $R_\nu(t) \propto (1 - at)$.

Chapter 4
Dynamical Models of Core-Collapse Supernovae

4.1 Introduction

In the last few years a new milestone in the modeling of core-collapse supernovae has been reached. Rampp (2000), Rampp & Janka (2000), Rampp & Janka (2002), Liebendörfer et al. (2001), Liebendörfer, Mezzacappa, & Thielemann (2001), Mezzacappa et al. (2001), and this work represent the next generation in precise, dynamical models of core-collapse supernovae in one spatial dimension. Although supernova simulations including a realistic equation of state and state-of-the-art hydrodynamics have been around for several decades (e.g. Bowers & Wilson 1982; Bruenn 1985; Mayle, Wilson, & Schramm 1987), only the work of the last few years includes a more precise treatment of neutrino transport, which does not appeal to approximate techniques like flux-limiting or diffusion.

In §4.2, we review the necessary components of any supernova model and present the methods we have employed. We review our implementation of the high-density nuclear equation of state, our neutrino transport algorithm, and our hydrodynamical scheme. In §4.4 we present results from a set of core-collapse supernova simulations; we present a prototypical simulation of an $11\,M_\odot$ progenitor from Woosley & Weaver (1995) and we then compare the hydrodynamical structures and neutrino spectra obtained with the $11\,M_\odot$ progenitor to those for $15\,M_\odot$ and $20\,M_\odot$ progenitors (§4.4.2). In §4.4.3 we recalculate our fiducial $11\,M_\odot$ progenitor with changes to the high-density nuclear equation of state and in §4.4.4 we vary the input physics to show the importance of particular neutrino processes and corrections to the standard neutrino opacities. In §4.4.5 and §4.4.6 we emphasize the role of nucleon-nucleon bremsstrahlung and inelastic neutrino-electron scattering, respectively, in shaping the emergent neutrino spectra. Throughout, we focus particularly on the neutrino breakout phenomenon and the early post-bounce epoch. As a final step, we convolve our time-dependent spectra with terrestrial neutrino detectors in order to make predictions about the neutrino signature of breakout and the first 250 milliseconds of post-bounce evolution from the next galactic supernova.

4.2 Ingredients

Ingredients in simulations of core-collapse supernovae include a thermodynamically consistent high-density nuclear equation of state, a hydrodynamics solver coupled to a radiation transport solver for all neutrino species, and all the relevant microphysics, which enters in the collision terms of the transport equation. We discuss our implementation and the particulars of each below.

4.2.1 Equation of State

Essential in the modeling of core-collapse supernovae is a physically reasonable and thermodynamically consistent equation of state. We employ the equation of state due to Lattimer & Swesty (1991) (the LSEOS), based on the finite-temperature liquid drop model of nuclei developed in Lattimer et al. (1985). It treats the matter in nuclear statistical equilibrium (NSE) and is valid only for temperatures above $T \sim 0.25$ MeV and densities between 5×10^6 g cm^{-3} and 1×10^{15} g cm^{-3}. In this EOS, NSE is maintained between free neutrons, protons, alpha particles, and a representative heavy nucleus specified by an atomic mass, A, and proton number, Z - both of which may take non-integer values. Photons are also included, as are electrons and positrons of arbitrary degeneracy and relativity.

We have designed an efficient three-dimensional tabular version of this EOS, taking the matter temperature (T), mass density (ρ), and electron fraction (Y_e) as variables. The table consists of 180 equally spaced zones in $\log_{10}[\rho\ (\mathrm{g\ cm^{-3}})]$ with $6.4 \leq \log_{10}[\rho\ (\mathrm{g\ cm^{-3}})] \leq 15.1$, 50 equally spaced zones in Y_e with $0.05 \leq Y_e \leq 0.51$ and 180 equally spaced zones in $\log_{10}[T\ (\mathrm{MeV})]$. The table is not cubic. For $\log_{10}[\rho\ (\mathrm{g\ cm^{-3}})] = 6.4$, $-0.8 \leq \log_{10}[T\ (\mathrm{MeV})] \leq 1$. At $\log_{10}[\rho\ (\mathrm{g\ cm^{-3}})] = 15.1$, $0 \leq \log_{10}[T\ (\mathrm{MeV})] \leq 1.6$. We find this range of temperatures and densities sufficient for all calculations we perform. At each point in the table we save the specific internal energy (E), the pressure (P), the entropy per baryon (s), the specific heat at constant volume (C_V), the neutron, proton, alpha particle, and heavy nucleus fractions (X_n, X_p, X_α, X_H, respectively), A and Z/A for the heavy nucleus, the electron chemical potential (μ_e), $\Gamma_s = \partial \ln P/\partial \ln \rho|_s$, $\partial P/\partial T|_\rho$, $\hat{\mu} = \mu_n - \mu_p$, and the derivatives $\partial\hat{\mu}/\partial T$ and $\partial\hat{\mu}/\partial Y_e$. In total, our tabular LSEOS takes up ~200 Megabytes of memory. Given T, ρ, and Y_e, the EOS performs three six-point bivariant interpolations (Abromowitz & Stegun 1972) in the $T-\rho$ planes nearest to and bracketing the given Y_e point. A quadratic interpolation is then executed between Y_e points to obtain the desired thermodynamic quantity. This procedure is employed for all quantities in the table except the mass fractions of neutrons, protons, alpha particles, and the heavy nucleus. Two four-point bivariant interpolations in the $T-\rho$ plane are combined with a linear interpolation between Y_e planes for these quantities. The table uses integer arithmetic to find nearest neighbor points, thus alleviating the need for time-intensive search algorithms. Because most hydrodynamics routines update specific internal energy, we include a Newton-Raphson/bisection scheme which iterates on temperature, given a fixed internal energy, until the root is found to within a part in 10^8. Similar iteration routines are employed if one wishes to iterate on entropy or pressure.

We have performed an extensive set of tests of our tabular implementation of the LSEOS to ensure that thermodynamical consistency is maintained during dynamical simulations. It is through these tests that we have determined the number of T, ρ, and Y_e points to employ. As a first test, we compressed a single fluid element (zero-dimensional hydrodynamics) adiabatically over eight orders of magnitude in density using the first law of thermodynamics;

$$E_{n+1} = E_n - P\left(V_{n+1} - V_n\right), \tag{4.1}$$

where $V^{-1} = \rho$, n denotes the timestep number, and we tested $P = P_n$, $P = (P_{n+1} + P_n)/2$, and $P = P_{n+1}$. Given an initial ρ ($\sim 10^7$ g cm^{-3}) and a variety of initial temperatures and Y_es, we studied the degree to which adiabaticity was maintained in increasing the density of the fluid element up to $\sim 10^{15}$ g cm^{-3}. Since, $ds = 0$ in eq. (4.1), the total fractional change in entropy in compressing the fluid element ($[s_f(\rho = 10^{15}) - s_i(\rho = 10^7)]/s_i(\rho = 10^7) = \Delta s/s_{\rm i}$) is a measure of the thermodynamic consistency of the EOS. For constant fractional changes in the density (or V) of 1% at each step, our table gives $\Delta s/s_{\rm i} \sim 0.5\%$. This is to be compared with the actual analytic LSEOS, from which the table was composed, which yields $\Delta s/s_{\rm i} \sim 0.25\%$. The number of temperature and density points used in the table does effect $\Delta s/s_{\rm i}$. For example, using just 100 T, 100 ρ, and 50 Y_e points over the same ranges as the larger table raises $\Delta s/s_{\rm i}$ to about $\sim 1.25\%$. In all our calculations we opted for the larger table. However, it is important to mention that each of these results for $\Delta s/s_{\rm i}$ (for the large and small tables and the analytic LSEOS) are dependent on the hydrodynamics scheme employed. In this case, a Crank-Nicholson pressure update ($P = (P_{n+1} + P_n)/2$) requiring iteration to get P_{n+1} was used and found to give the smallest $\Delta s/s_{\rm i}$ for a given fractional density change per timestep. For comparison, a fully explicit scheme using $P = P_n$ gave larger $\Delta s/s_{\rm i}$ by a factor of $2 - 3$ for an otherwise identical compression calculation.

As a second set of tests, we coupled the LSEOS to several different one-dimensional Lagrangian hydrodynamics schemes. Without heating and cooling due to neutrinos and before any hydrodynamical shocks form, each mass zone should remain isentropic during the collapse of a massive progenitor star. Using a variety of zoning schemes with both artificial-viscosity and Riemann solvers for shock capturing and resolution, we found that higher-order EOS interpolation schemes as described in Swesty (1996) are not needed to maintain adiabaticity to within 1% during collapse and bounce. An important conclusion from these calculations is that in assessing the degree of thermodynamic consistency of a given EOS by performing adiabatic compression and collapse tests, one must pay particular attention both to the hydrodynamics algorithm itself and to the coupling between hydrodynamics and EOS through the first law. In this sense, a thermodynamically consistent EOS is only as good as the hydrodynamics routine it is coupled to.

Figures (4.1-4.4) show several views of the tabular Lattimer-Swesty EOS we have constructed. Figure (4.1) shows the atomic mass (A) of the representative heavy nucleus as returned by the LSEOS in the plane of $\log_{10} T$ and $\log_{10}\rho$, for $Y_e = 0.204$. Note the phase transition between heavy nuclei and free nucleons at high temperatures and densities. Figure (4.2) shows the specific heat at constant volume (C_V) for $Y_e = 0.31$. Figure (4.3) shows $\Gamma_s = d\ln P/d\ln\rho|_s$ for $Y_e = 0.50$. The very steep increase in Γ_s above $\rho \sim 10^{14}$ g cm^{-3} reflects the stiffening of nuclear matter above nuclear densities, which causes the shock that eventually becomes the supernova. Also note that in the LSEOS Γ_s drops into an unphysical regime ($\Gamma_s < 1$) right at the high-density phase transition. Although in a realistic core-collapse simulation the matter which reaches such high densities does so at considerably lower Y_e, we have found it necessary to put a firm, physical, lower bound on Γ_s during our dynamical calculations. A number of quantities saved in our LSEOS table are important only for neutrino transport. One such quantity, shown in Fig. (4.4) for $Y_e = 0.35$, is $\hat{\mu}(= \mu_n - \mu_p)$, an important quantity in defining the equilibrium phase-space distribution functions for ν_e and $\bar{\nu}_e$ neutrinos.

The LSEOS extends down to only $\sim 5 \times 10^6$ g cm^{-3} and its validity in this density regime is guaranteed only for fairly high temperatures - the assumption of NSE being thereby satisfied. For calculations in which an explosion occurs, the shock will quickly evolve down the progenitor density gradient to regions where the LSEOS breaks down. For this reason we have coupled the Helmholtz EOS (Timmes & Arnett

1999; Timmes & Swesty 2000), which contains electrons and positrons at arbitrary degeneracy and relativity, photons, nuclei and nucleons as non-relativistic ideal gases, and Coulomb corrections to our tabular version of the LSEOS. At $\rho = 6 \times 10^7$ g cm^{-3} we assume the LSEOS is valid. At $\rho = 4 \times 10^7$ g cm^{-3} we employ only the Helmholtz EOS. For densities between the two, we quadratically interpolate all relevant thermodynamic quantities. Because the LSEOS assumes NSE and the Helmholtz EOS takes non-NSE abundances, there is no thermodynamic consistency between the two EOSs. Fortunately, in thermodynamical regimes relevant for core collapse at these densities, the electron-positron/photon component of the matter dominates the pressure. Therefore, one expects few hydrodynamical artifacts in piecing together these two equations of state. In fact, given a realistic composition for the Helmholtz EOS, at a density of $\rho = 5 \times 10^7$ g cm^{-3}, pressure differences between the LSEOS and Helmholtz EOS are $\sim 1\%$ in the stellar profiles we employ in this study. Differences in entropy, however, are of order 5-10%.

4.2.2 Neutrino Transport

The mass densities, temperatures, and compositions that obtain during core-collapse conspire to produce regions in the very core of a supernova where the mean-free-path for neutrinos is just meters and the transport may be handled using simple diffusion theory. The escape time from these regions can be many seconds for high-energy neutrinos. Simultaneously, there are regions at larger radius where each neutrino species decouples from the matter and free-streams to infinity. In between, at modest optical depth, where the neutrino mean-free path may be a modest fraction of the size of the object as a whole, the full transport problem must be solved in order to obtain accurate values of the local neutrino flux and energy density - both being crucial to the energy deposition profile and the subsequent evolution.

Our general Boltzmann transport solver is due primarily to Eastman & Pinto

(1993), who developed an algorithm for solving the comoving Lagrangean transport equation using the Feautrier variables, the tangent-ray method for spatial and angular discretization, and Accelerated Lambda Iteration (ALI) to speed convergence (see e.g., Mihalas & Mihalas 1984). The method, as applied to neutrino transport and the supernova problem, is described in Burrows et al. (2000). For details on the transport algorithm itself, see Eastman & Pinto (1993). Below we summarize the basic equations and approximations employed.

From Mihalas & Mihalas (1984) and Mihalas (1980) the time-dependent, spherically symmetric (one spatial dimension), comoving transport equation, correct to order (v/c), can be written

$$\frac{1}{c}\frac{DI_\nu}{Dt} + \frac{\mu}{r^2}\frac{\partial}{\partial r}(r^2 I_\nu) + \frac{\partial}{\partial \mu}\left[(1-\mu^2)\left[\frac{1}{r} + \frac{\mu}{c}\left(\frac{v}{r} - \frac{\partial v}{\partial r}\right)\right] I_\nu\right]$$
$$-\frac{\partial}{\partial \varepsilon_\nu}\left[\varepsilon_\nu\left[(1-\mu^2)\frac{v}{cr} + \frac{\mu^2}{c}\frac{\partial v}{\partial r}\right] I_\nu\right] + \left[(3-\mu^2)\frac{v}{cr} + \frac{1+\mu^2}{c}\frac{\partial v}{\partial r}\right] I_\nu + \mathcal{A}_\nu =$$
$$\eta_\nu - \chi_\nu I_\nu + \frac{\kappa_s}{4\pi}\int \Phi(\mathbf{\Omega}, \mathbf{\Omega}')\, I_\nu(\mathbf{\Omega}')\, d\mathbf{\Omega}' \ , \tag{4.2}$$

where

$$\mathcal{A}_\nu = \frac{a}{c^2}\left[3\mu - (1-\mu^2)\frac{\partial}{\partial \mu} - \varepsilon_\nu \frac{\partial}{\partial \varepsilon_\nu}\right] I_\nu, \tag{4.3}$$

a is the matter acceleration, I_ν is the specific intensity, $\mu = \cos\theta$ is the cosine of the zenith angle, r is the radial coordinate, ε_ν is the neutrino energy, $D/Dt = \partial/\partial t + \nabla \cdot v$ is the advective derivative, and η_ν is the emissivity of the medium. $\Phi(\mathbf{\Omega}, \mathbf{\Omega}')$ is a phase function for neutrino scattering into the beam. Although we include it here for completeness, in practice we do not include the acceleration term $\mathcal{A}_\nu$. The total extinction coefficient, χ_ν, is the sum of the absorption and scattering terms: $\chi_\nu = \kappa_a + \kappa_s$. Each is the sum of a number of individual processes;

$$\kappa_s = \sum_i n_i\, \sigma_i^s \qquad \text{and} \qquad \kappa_a = \sum_i n_i\, \sigma_i^a \ , \tag{4.4}$$

where σ_i is the cross section for process i in cm^2 and n_i is the number density of absorbers or scatterers, respectively. Following Eastman & Pinto (1993) and Mihalas

& Mihalas (1984), and dropping the acceleration term, we may rewrite eq. (4.2) as

$$\frac{1}{c}\frac{DI_\nu}{Dt} + \mu\frac{\partial I_\nu}{\partial r} + \frac{1-\mu^2}{r}(1-\beta Q\mu)\frac{\partial I_\nu}{\partial \mu} + \frac{\beta}{r}\left(1+Q\mu^2\right)\left(3 - \frac{\partial}{\partial \ln \varepsilon_\nu}\right) I_\nu$$

$$= \eta_\nu - \chi_\nu I_\nu + \frac{\kappa_s}{4\pi}\int \Phi(\mathbf{\Omega},\mathbf{\Omega}')\, I_\nu(\mathbf{\Omega}')\, d\mathbf{\Omega}' \;, \tag{4.5}$$

where $Q \equiv \partial \ln v/\partial \ln r - 1$ and B_ν is the blackbody radiation distribution. Because the specific intensity is related directly to the neutrino phase-space distribution function (f_ν) by

$$\frac{I_\nu(\mu,\varepsilon_\nu)}{\varepsilon_\nu^3} = \frac{cg}{(2\pi\hbar c)^3}\, f_\nu(\mu,\varepsilon_\nu) \;, \tag{4.6}$$

where $g = 1$ for massless neutrinos, we may rewrite the transport equation as a Boltzmann equation for the time and space evolution of f_ν. From eqs. (4.2) and (4.6) we have that

$$\frac{1}{c}\frac{Df_\nu}{Dt} + \mu\frac{\partial f_\nu}{\partial r} + \frac{1-\mu^2}{r}(1-\beta Q\mu)\frac{\partial f_\nu}{\partial \mu} - \frac{\beta}{r}\left(1+Q\mu^2\right)\frac{\partial f_\nu}{\partial \ln \varepsilon_\nu}$$

$$= \tilde{\eta}_\nu - \chi_\nu f_\nu + \frac{\kappa_s}{4\pi}\int \Phi(\mathbf{\Omega},\mathbf{\Omega}')\, f_\nu(\mathbf{\Omega}')\, d\Omega', \tag{4.7}$$

where $\tilde{\eta}_\nu = (2\pi\hbar c)^3\, \eta_\nu/\varepsilon_\nu^3 c$. Our transport algorithm assumes isotropic scattering. The full anisotropic angular redistribution implied by the integral term in eqs. (4.2), (4.5), and (4.7) is approximated by assuming the form

$$\Phi_i(\mathbf{\Omega},\mathbf{\Omega}') = \Phi_i(\mathbf{\Omega}\cdot\mathbf{\Omega}') = (1+\delta_i\,\mathbf{\Omega}\cdot\mathbf{\Omega}') = (1+\delta_i\mu) \tag{4.8}$$

for the scattering angular phase function. This is equivalent to a first-order Legendre expansion in the scattering angle for elastic scattering. The sign of δ_i determines if the process is peaked in the forward or backward direction. That is, if $\delta_i > 0$ the neutrino has a higher probability of scattering into the forward hemisphere. With eq. (4.8), the differential cross section for a scattering process i is written in terms of the total scattering cross section:

$$\frac{d\sigma_i^s}{d\Omega} = \frac{\sigma_i^s}{4\pi}(1+\delta_i\mu) \;. \tag{4.9}$$

This implies that the angular redistribution term in eqs. (4.2), (4.5), and (4.7) becomes

$$\frac{\kappa_s}{4\pi}\int \Phi(\mathbf{\Omega},\mathbf{\Omega}')\, I_\nu(\mathbf{\Omega}')\, d\mathbf{\Omega}' = \kappa_s J_\nu + \frac{\kappa_s \delta_T}{4\pi}\mathbf{\Omega}\cdot\mathbf{F}_\nu\ , \tag{4.10}$$

where

$$\delta_T = \frac{\sum_i n_i\,\sigma_i\,\delta_i}{\sum_i n_i\,\sigma_i}, \tag{4.11}$$

F_ν is the neutrino flux defined by

$$\frac{1}{4\pi}F_\nu = H_\nu = \frac{1}{2}\int_{-1}^{1} I_\nu\,\mu\,d\mu. \tag{4.12}$$

H_ν is the first moment of the radiation field and J_ν is the zeroth moment;

$$J_\nu = \frac{1}{2}\int_{-1}^{1} I_\nu\,d\mu = \frac{c}{4\pi}E_\nu, \tag{4.13}$$

where E_ν is the neutrino energy density. In practice, we drop the term proportional to $\mathbf{\Omega}\cdot\mathbf{F}_\nu$ in eq. (4.10), but employ eq. (4.9) to derive the scattering opacity κ_s.

Integrating eq. (4.5) and $\mathbf{\Omega}\times$ eq. (4.5) over $d\mathbf{\Omega}$ yields the zeroth and first moment equations, respectively:

$$\begin{aligned}&\frac{1}{c}\frac{DJ_\nu}{Dt} + \frac{1}{r^2}\frac{\partial}{\partial r}(r^2 H_\nu) - \frac{\beta Q}{r}(3P_\nu - J_\nu)\\ &+\frac{\beta}{r}\left(3 - \frac{\partial}{\partial \ln\varepsilon_\nu}\right)(J_\nu + QP_\nu) = \kappa_a^*(B_\nu - J_\nu)\end{aligned} \tag{4.14}$$

and

$$\begin{aligned}&\frac{1}{c}\frac{DH_\nu}{Dt} + \frac{\partial P_\nu}{\partial r} + \frac{3P_\nu - J_\nu}{r} - \frac{\beta Q}{r}(4N_\nu - 2H_\nu) + \frac{\beta}{r}\left(3 - \frac{\partial}{\partial \ln\varepsilon_\nu}\right)(H_\nu + QN_\nu)\\ &= -\left(\kappa_a^* + \kappa_s - \frac{1}{3}\kappa_s\delta_T\right)H_\nu = -\left(\kappa_a^* + \kappa_{tr}\right)H_\nu\ ,\end{aligned} \tag{4.15}$$

where P_ν and N_ν are the second, and third angular moments of the specific intensity, given by

$$P_\nu = \frac{1}{2}\int_{-1}^{1} I_\nu\,\mu^2\,d\mu \tag{4.16}$$

and

$$N_\nu = \frac{1}{2}\int_{-1}^{1} I_\nu\, \mu^3\, d\mu. \tag{4.17}$$

In eqs. (4.14) and (4.15), κ_a^* is the absorptive opacity corrected for stimulated emission (see §B.1). In eq. (4.15) κ_{tr} is the total transport cross section, defined in terms of the individual transport cross sections as $\kappa_{tr} = \sum_i n_i\, \sigma_i^{tr}$. For a particular scattering process i,

$$\sigma_i^{tr} = \int \frac{d\sigma_i}{d\Omega}(1-\mu)\, d\Omega = \sigma_i \left(1 - \frac{1}{3}\delta_i\right) \ . \tag{4.18}$$

Integrating eq. (4.14) over neutrino energy we obtain the neutrino energy equation:

$$\frac{DE}{Dt} + \frac{1}{r^2}\frac{\partial}{\partial r}(r^2 F) - \frac{v}{r}(3p-1)QE + 4\frac{v}{r}(1+Qp)E = 4\pi \int_0^\infty \kappa_a^*(B_\nu - J_\nu)\, d\varepsilon_\nu \ , \tag{4.19}$$

where E and F are the integrated neutrino energy density and flux, respectively. p is the energy-integrated spectral Eddington factor ($p_\nu = P_\nu/J_\nu$). This equation gives us the energy update used in our solution to the first law of thermodynamics in coupling to the equations of hydrodynamics. In addition, the integral over ε_ν of eq. (4.15) for all neutrino species gives the momentum deposition due to neutrinos and is included as a force term in the hydrodynamical momentum equation. To complete the coupling of the radiation field to matter, we must account for compositional changes due to the charged-current neutrino interactions. This is accomplished by solving for ΔY_e at each timestep using the set of equations

$$\rho N_a \frac{DY_e}{Dt}_{\pm} = \pm 4\pi \int_0^\infty \kappa_a^*(B_\nu - J_\nu)_{\pm} \frac{d\varepsilon_\nu}{\varepsilon_\nu}, \tag{4.20}$$

where N_A is Avogadro's number, and the $\pm$ is for the $\bar{\nu}_e$ and ν_e equations, respectively.

The moment equations (eqs. 4.14 & 4.15) are solved simultaneously with the transport equation, which is rewritten in terms of the Feautrier variables:

$$U_\nu(\mu) = \frac{1}{2}(I_\nu(\mu) + I_\nu(-\mu)) \qquad \text{and} \qquad V_\nu(\mu) = \frac{1}{2}(I_\nu(\mu) - I_\nu(-\mu)). \tag{4.21}$$

The equations for U_ν and V_ν are then obtained from eq. (4.5) which, in the isotropic scattering limit ($\delta_T = 0$), are simply

$$\frac{1}{c}\frac{DU_\nu}{Dt} + \mu\frac{\partial V_\nu}{\partial r} - \frac{1-\mu^2}{r}\beta Q\mu\frac{\partial U_\nu}{\partial \mu} + \frac{\beta}{r}\left(3 - \frac{\partial}{\partial \ln\varepsilon}\right)(1+Q\mu^2)U_\nu$$
$$= \eta_\nu - \chi_\nu U_\nu + \kappa_s J_\nu \tag{4.22}$$

and

$$\frac{1}{c}\frac{DV_\nu}{Dt} + \mu\frac{\partial U_\nu}{\partial r} - \frac{1-\mu^2}{r}\beta Q\mu\frac{\partial V_\nu}{\partial \mu} + \frac{\beta}{r}\left(3 - \frac{\partial}{\partial \ln\varepsilon}\right)(1+Q\mu^2)V_\nu = -\chi_\nu V_\nu\ . \tag{4.23}$$

More details on the technique for solution and the implicit coupling to matter with the Accelerated Lambda Operator can be found in Burrows et al. (2000).

Inelastic Neutrino Scattering: The scattering phase function, $\Phi(\mathbf{\Omega}, \mathbf{\Omega}')$, in eqs. (4.2), (4.5), and (4.7) represents the probability that a neutrino described by the angular coordinate $\mathbf{\Omega}$ will scatter into $\mathbf{\Omega}'$. The source, in eq. (4.7), for a given angle μ, is represented by a sum over contributions from all other angles. In that sense, a neutrino with any $\mathbf{\Omega}'$ may contribute to the phase space occupation at $\mathbf{\Omega}$ simply by scattering into the beam of $\mathbf{\Omega}$. Analogously, one may also include inelastic neutrino scattering. In this case we might specify a phase function that represents the probability for scattering from ε_ν' into the beam described by the neutrino energy ε_ν. In fact, one may conceive of a general phase function, $I(\varepsilon_\nu, \varepsilon_\nu', \cos\theta)$, where $\cos\theta$ is the cosine of the scattering angle, which connects points in energy and momentum space through a collision term on the right hand side of the Boltzmann equation. This term, analogous to the case of pure elastic scattering, takes the form (e.g. Bruenn 1985)

$$= (1-f_\nu)\int \frac{d^3p_\nu'}{c(2\pi\hbar c)^3} f_\nu'\, I^{\rm in}(\varepsilon_\nu, \varepsilon_\nu', \cos\theta) - f_\nu \int \frac{d^3p_\nu'}{c(2\pi\hbar c)^3}(1-f_\nu')\, I^{\rm out}(\varepsilon_\nu, \varepsilon_\nu', \cos\theta). \tag{4.24}$$

The first term is the source. That is, the contribution to f_ν at μ and ε_ν depends on the distribution f_ν' at μ' and ε_ν'. Note that Pauli blocking in the final state is taken into account explicitly. The source term is comparable, then, to the integral term in eq. (4.7). The second term, the sink, is equally transparent when compared with the $-\chi_\nu f_\nu$ term in eq. (4.7). Taking $I^{\rm out}(\varepsilon_\nu, \varepsilon'_\nu, \cos\theta) \propto n_i \sigma_i \delta(\varepsilon_\nu - \varepsilon'_\nu)$, ignoring neutrino blocking, and integrating over $d^3p'_\nu$ trivially, we arrive at $-\chi_\nu f_\nu$. (See Appendix B.3 for a detailed discussion of our numerical implementation of the inelastic scattering source and sink terms.)

4.2.3 Hydrodynamics

The coupling of the neutrino radiation to matter is done implicitly in operator-split fashion, using the Accelerated Lambda operator to obtain '$\partial J/\partial S$' after each hydrodynamic update (Burrows et al. 2000). A version of the hydro code of Fryxell et al. 1989, itself a realization of the piecewise parabolic method (PPM) of Colella & Woodward (1984), was originally used to handle the hydrodynamics. It is automatically conservative, second-order accurate in space and time, and employs a Riemann solver. Although this technique resolves shocks well, there is no natural way to include the radiation pressure term in the solution to the Riemann problem. During most epochs in supernova evolution, this term is negligible. During breakout, however, when electron neutrino luminosities approach 10^{54} erg s^{-1} locally, this term can be important and can even dominate the other purely hydrodynamical terms in the Riemann problem. For this reason, we decided to couple our transport algorithm to schemes that employ artificial viscosity for shock resolution.

For the results presented in this thesis, which focus on only the early phase of post-bounce evolution, we employ an explicit Lagrangean hydrodynamics scheme devised for this project by Adam Burrows. The drawback to explicit schemes is that they are Courant-limited. In effect, the maximum timestep at each step must be less than the minimum single-zone sound-crossing time on the computational grid. In the core at bounce the zone size in our calculations is $\sim$ 200 meters. The sound speed at nuclear densities approaches $\sim c/3$. Hence, our explicit timestep is $\sim 10^{-6}$ seconds. In order to adequately address the delayed mechanism of supernovae we must evolve the calculation for ~ 1 second post-bounce. This would require $\sim 10^6$ timesteps. The solution to the transport equation for all species is computationally expensive and on current single processor machines 10^6 timesteps is prohibitively large. In order to circumvent this problem we sub-cycle the hydrodynamics after shock breakout and shock stall. After these most dynamical phases are over we take $2-4$ hydro steps per transport step, thus cutting the total computational load significantly.

4.3 The Fiducial Model Configuration

We take as a reference model a 11 $M_\odot$ progenitor from Woosley & Weaver (1995). The model employs 300 mass zones out to M= $1.45M_\odot$, where M is the interior mass so that at $r = 0$, M=0 and in this progenitor at M= $1.45M_\odot$, $r \simeq 2500\,\mathrm{km}$. For the models presented here, which focus on collapse and the early ($\sim 100 - 200$ ms) evolution, we find this zoning sufficient. The angular zoning for the neutrino radiation field is handled automatically by the tangent-ray algorithm. For a given radial zoning, angular bins at each radius are constructed by casting tangent rays onto the concentric circles of each interior radial zone. Therefore, at the nth zone we have $n-1$ angular bins so that throughout the regions important to transport we maintain exquisite angular resolution, the outermost zone having 299 angles in each quadrant of the unit circle. Because of our Lagrangean formulation, at every timestep the grid changes in radius and the angular grouping changes accordingly. We solve the transport equation for ν_e neutrinos, $\bar{\nu}_e$ neutrinos, and ν_μ neutrinos, where 'ν_μ' stands for ν_μ, $\bar{\nu}_\mu$, ν_τ, and $\bar{\nu}_\tau$. Although in principle the neutrino microphysics is different between ν_μ, $\bar{\nu}_\mu$, ν_τ, and $\bar{\nu}_\tau$ we make the assumption standard in the field that they can be treated identically. The energy grouping is different for each species. For ν_e neutrinos, $1 \leq \varepsilon_{\nu_e}$ (MeV) ≤ 320. For $\bar{\nu}_e$ neutrinos, $1 \leq \varepsilon_{\bar{\nu}_e}$ (MeV) ≤ 100. Both are grouped logarithmically. For ν_μ neutrinos, $1 \leq \varepsilon_{\nu_\mu}$ (MeV) ≤ 100 with constant grouping in energy. Our fiducial models employ 40 energy groups for each species. In §4.4.1 compare our results with calculations employing just 10 and 20 energy groups. Although in §4.4.3 we explore the effects of changes in the nuclear compressibility modulus, our fiducial models use $\kappa = 220$ MeV in the LSEOS. For all of the results presented below, we employ the equation of state described in detail in §4.2.1.

Our *standard* set of microphysics includes all of the emission/absorption and scattering processes described in Appendix B, including the inelastic treatment of neutrino-electron scattering. However, in our fiducial models we do not include inelastic neutrino-nucleon scattering, but include it only as a purely elastic scattering opacity source.

4.4 Results

Figure (4.5) shows velocity v (in cm s^{-1}, upper left panel), $\log_{10}[\rho]$ (in g cm^{-3}, upper right panel), entropy s (in k$_B$ baryon^{-1}, lower left panel), and temperature T (in MeV, lower right panel), as a function of mass coordinate in $\mathrm{M}_\odot$ at five snapshots in time in our $11\,\mathrm{M}_\odot$ fiducial model. Fig. (4.5) is to be compared with Fig. (4.6), which shows the electron fraction (Y_e) as a function of mass in the same model. The thin solid line in Figs. (4.5) and (4.6) is the initial configuration. The thick solid line is at hydrodynamical bounce (approximately 200 ms after we start the calculation). Bounce coincides with the core density reaching $\sim 2\times10^{14}$ g cm^{-3}, where the EOS stiffens dramatically, as indicated by the large increase in Γ_s near nuclear densities in Fig. (4.3). Note that Y_e in the very core reaches its minimum value *before* bounce. At core densities of $\sim 2\times10^{12}$ g cm^{-3} the electron-neutrino outward diffusion speed becomes smaller than the the inward collapse speed and the neutrinos are effectively trapped. Soon afterwards, the process primarily responsible for the preceding decrease in Y_e, $e^-p\rightarrow n\nu_e$, is balanced by its inverse. This balance is called beta equilibrium. Although we have included inelastic neutrino-electron scattering in our fiducial model, the long dashed line in Fig. (4.6) shows the bounce Y_e profile if one turns off this equilibration process. Because small changes in the Y_e profile at bounce can affect the shock energetics significantly (Burrows & Lattimer 1983) and because inelastic neutrino-electron scattering affects the approach to beta equilibrium by modifying the neutrino phase space occupancy, inelastic neutrino-electron scattering should be included in a full treatment (Bruenn 1985; Mezzacappa & Bruenn 1993abc). We discuss this process and its effects more fully in §4.4.6.

At bounce, a strong sound wave is formed deep in the core, which propagates down the density gradient set up by the infalling outer stellar material. The sound wave steepens into a shock near M$\simeq$0.6M$_\odot$, just $\sim$ 0.5 ms after bounce. The dotted line in Fig. (4.5) shows the shock fully formed and at maximum positive velocity (1.9×10^9 cm s^{-1}). Note the attending generation of entropy and increase in temperature. As the shock moves outward in mass and radius it dissociates nuclei into free nucleons. Although the matter is hot in this region, the electrons are still quite degenerate and the process $e^- p \rightarrow n\nu_e$ builds a sea of electron neutrinos that are trapped and advected with the matter. Figures (4.7) and (4.8) show the luminosity as a function of mass for several post-bounce times. The former shows the whole evolution of $L_{\nu_e}(M,t)$ from bounce all the way through breakout. Although the shock does not form until M$\simeq$0.6M$_\odot$, a phase-transition front moves with the wave generated at bounce. This causes the initial luminosity peak seen in Fig. (4.7) at M$\simeq$0.5M$_\odot$, or, in this model, at a radius of just 11 km. The sudden drop in L_{ν_e} at M$\simeq$ 0.6 $-$ 0.7 M$_\odot$ comes from a sharp decrease in X_p, coincidentally nearly simultaneous with shock formation. Just as the shock is forming, but before the temperature rises dramatically as shown in the lower right panel of Fig. 4.5 (dotted line), a region of heavy nuclei persists and causes the decrease in L_{ν_e} at M$\simeq$ 0.6 $-$ 0.7 M$_\odot$. Figure (4.8) shows specific snapshots between the 1 ms (dotted) line and the 17 ms (short dashed) line in Figs. (4.5) and (4.6). At 2.4 ms after bounce the spike reaches a local maximum at M$\simeq$ 0.85M$_\odot$, with L_{ν_e} exceeding 1.4×10^{54} erg s^{-1}. This spike roughly denotes the position of the shock. It is at this moment that the shock crosses the ν_e neutrinosphere (R_{ν_e}). The neutrinosphere for any neutrino species (R_ν) is set by the following integral criterion:

$$\tau_\nu(R_\nu, \varepsilon_\nu) = \int_{R_\nu}^{\infty} \kappa_\nu(\varepsilon_\nu, r)\rho(r)\, dr = \frac{2}{3}, \qquad (4.25)$$

where κ_ν is the total opacity. At just 3.2 ms after bounce, one can see clearly that the breakout pulse of electron neutrinos is beginning to move ahead of the shock. Having moved into a region where the optical depth is below $\sim 2/3$, the neutrinos begin to free-stream. Both Figs. (4.7) and (4.8) show a marked decrease in the breakout ν_e

luminosity pulse just as it begins to propagate ahead of the shock, between the lines labeled 't=2.4 ms' and 't=4.7 ms' in Fig. (4.8). The local maximum of L_{ν_e} at 2.4 ms occurs at a radius of approximately $r_{\rm peak} \simeq 41$ km. We expect the peak luminosity ($L_{\nu_e}^{\rm peak}$) to be attenuated by an amount $\sim \exp(-\tau_a)$ in propagating to infinity ($L_{\nu_e}^{\infty}$), where τ_a is the total absorptive optical depth exterior to $r_{\rm peak}$. From the results presented here, we find $\tau_a(r_{\rm peak}) \sim 1.9$ at $\varepsilon_{\nu_e} \simeq 12$ MeV. This simple estimate shows that we should expect $L_{\nu_e}^{\rm peak}$ to decay by $\sim 85\%$. With $L_{\nu_e}^{\rm peak} \simeq 1.45 \times 10^{54}$ erg s^{-1} we expect $L_{\nu_e}^{\infty} \sim 0.22 \times 10^{54}$ erg s^{-1} and find from the simulation that $L_{\nu_e}^{\infty} \simeq 0.25 \times 10^{54}$ erg s^{-1}, in good agreement with our estimate. This asymptotic luminosity is shown clearly as the bump in the last line in Fig. (4.8), labeled 'Breakout Pulse', which has moved out to 1.35 $M_\odot$. Behind the pulse, at M$\simeq$ 1.08 $M_\odot$, is a sharper peak in the luminosity that denotes the shock position. During this breakout phase of shock evolution, much of the shock energy is sapped by the neutrino losses that attend electron capture on free protons. This process also creates a characteristic deleptonization trough manifest by the marked decrease in Y_e in Fig. (4.6) near M$\simeq$0.8 $M_\odot$. The shock stalls quickly and in just a few milliseconds after bounce all velocities are ≤ 0. Note the negative entropy gradient between M$\simeq$ 0.75 $M_\odot$ and M$\simeq$ 0.95 $M_\odot$. Depending upon the compositional gradients in this region, in a multi-dimensional simulation this region might be convectively unstable.

Although the shock continues to move outward in mass as matter flows through it from the free-falling outer core, all matter velocities are $\leq$0 as the shock reaches at $r \sim 80-90$ km. The short dashed lines in Figs. (4.5) and (4.6) show the configuration of the model 17 ms after bounce and $\sim$ 10 ms after the shock has stalled. The dot-dashed line shows these basic hydrodynamical quantities 200 ms post-bounce. The shock has consumed another 0.2 $M_\odot$ of infalling material and the entropy behind the shock has increased dramatically. The temperature over the whole post-shock profile has increased as a result of the compressional work done on these zones by the infalling stellar material. In particular, at the peak in the temperature profile at M$\sim$0.7 $M_\odot$,

T increased by $\sim$4 MeV between $t = 17\,\mathrm{ms}$ and $t = 200\,\mathrm{ms}$. In these hundreds of milliseconds after bounce, the shock moves outward in radius to $\sim 175\,\mathrm{km}$. Although it is in this epoch that neutrino heating behind the shock is thought to revive it, no explosion is seen in our simulations at this time. Figure (4.9) shows the evolution of selected mass zones in our $11\,\mathrm{M}_\odot$ model as a function of time. Small oscillations are visible just after bounce and the shock position is made clear by the change in the infalling matter velocity between 100 km and 200 km during the 280 ms of evolution shown here. Although the neutrino-driven mechanism is not the focus of this work, from this figure and from many similar calculations we see no evidence of impending explosion.

In Fig. (4.8) we showed L_{ν_e} as a function of mass at various snapshots in time. The last snapshot shows the ν_e breakout pulse at $1.35\mathrm{M}_\odot$ and propagating at the speed of light to the edge of the grid. Complementary to Fig. (4.8), the time evolution of L_{ν_e} at infinity is shown in Fig. (4.10) (thick solid line). The luminosity of anti-electron neutrinos ($L_{\bar{\nu}_e}$, thin solid line) and the combined luminosity of ν_μ, $\bar{\nu}_\mu$, ν_τ, and $\bar{\nu}_\tau$ (collectively, L_{ν_μ}, dotted line) are also shown for the first 250 ms of evolution. Note that just before the major breakout pulse of electron neutrinos, there is another small peak that reaches $\sim 0.72 \times 10^{53}$ erg s^{-1}. This peak results from the deleptonization of the core as the Y_e drops in Fig. (4.6) from the initial model to $Y_e \simeq 0.27$. There is a small dip in L_{ν_e} just after this initial rise. This dip in the asymptotic luminosity signals the end of the infall/collapse phase of the supernova. After the initial increase in L_{ν_e} due to deleptonization, L_{ν_e} decreases because of the increased opacity in the dense collapsing core. The high opacity decreases the local luminosity at small radii and isolates a peak in luminosity at larger radii caused by deleptonization. If it were not for shock formation, L_{ν_e} at infinity would continue to decline. The main breakout pulse just after the small downturn in L_{ν_e} results from the dissociation of nuclei and subsequent electron capture on free protons, as described above and shown in Fig. (4.7).

In Fig. (4.11) we show the corresponding average neutrino energy for each species over the same time interval as Fig. (4.10). There are many ways one might present the average neutrino energy. The literature does not consistently employ a unique prescription and considerable confusion exists. The average energy we present in our figures is the *rms* average energy, defined by:

$$\langle\varepsilon_\nu\rangle = \left[\frac{\int d\varepsilon_\nu \varepsilon_\nu^2 J_\nu(\varepsilon_\nu)}{\int d\varepsilon_\nu J_\nu(\varepsilon_\nu)}\right]^{1/2} . \tag{4.26}$$

We use this definition in order to make comparisons with other recent work (Liebendörfer et al. 2001; Rampp et al. 2002). After approximately 50 ms, the average energies show a nearly linear increase with time. Mezzacappa et al. (2001) and Liebendörfer et al. (2001) find similar behavior. In addition, although we employ a different progenitor, the values for the average neutrino energies they obtain compare well with those presented in Fig. (4.11). For example, 250 ms after bounce in their 13 $M_\odot$ progenitor, Mezzacappa et al. (2001) obtain $\langle\varepsilon_{\nu_\mu}\rangle \simeq 21$ MeV, $\langle\varepsilon_{\bar{\nu}_e}\rangle \simeq 16$ MeV, and $\langle\varepsilon_{\nu_e}\rangle \sim 14$ MeV. We find that $\langle\varepsilon_{\nu_\mu}\rangle \simeq 20$ MeV, $\langle\varepsilon_{\bar{\nu}_e}\rangle \simeq 15.5$ MeV, and $\langle\varepsilon_{\nu_e}\rangle \sim 13$ MeV.

Figure (4.12) shows the luminosity spectrum of electron neutrinos at infinity in units of 10^{52} erg s^{-1} MeV^{-1}. The thick solid line denotes the maximum peak breakout pulse luminosity and corresponds to the 2.55×10^{53} erg s^{-1} peak in L_{ν_e} in Fig. (4.10). The thin solid lines in this plot show the rise up to the peak and the simultaneous shift in $\langle\varepsilon_{\nu_e}\rangle$ depicted in Fig. (4.11). The dashed lines show the evolution of the luminosity spectrum after the breakout pulse. The pre-breakout lines show the spectrum at 11.6, 5.1, and 1.3 ms before the peak in the breakout pulse. The dashed, post-breakout, lines show the spectrum at 4.2, 9.6, and 40.5 ms after the ν_e breakout pulse. Although the peak energy is dropping in this figure as the luminosity decays, the high energy tail becomes broader and with our definition of the average energy (eq. 4.26) $\langle\varepsilon_{\nu_e}\rangle$ increases. Figure (4.13) shows the emergent spectrum much later (at 210 ms after bounce) and for all three neutrino species. The thick solid line shows the ν_e spectrum, the thin solid line shows the $\bar{\nu}_e$ spectrum, and the dotted line shows the combined ν_μ

spectrum. The post-bounce energy hierarchy one expects from simple considerations of the opacity sources for the various species, $\langle\varepsilon_{\nu_e}\rangle < \langle\varepsilon_{\bar{\nu}_e}\rangle < \langle\varepsilon_{\nu_\mu}\rangle$, is evident in both Figs. (4.11) and (4.13).

Although this exact progenitor model has not been used in any of the recent supernova modeling done by groups employing sophisticated neutrino transport (Rampp 2000; Rampp & Janka 2000, 2002; Liebendörfer et al. 2001; Liebendörfer, Mezzacappa, & Thielemann 2001; Mezzacappa et al. 2001), we find that the basic structures and systematics are similar between groups. In particular, our core entropy ($s_{\rm core}$) drops slightly at the beginning of the calculation and then climbs during bounce to $s_{\rm core} \simeq 1.32\ k_B$ baryon^{-1}. We observe similar behavior for our $15\,{\rm M}_\odot$ progenitor with $s_{\rm core} \simeq 1.33\ k_B$ baryon^{-1}. Without inelastic neutrino-electron scattering we obtain $s_{\rm core} \simeq 1.16\ k_B$ baryon^{-1}. The absolute magnitude of these results and the effect of neutrino-electron scattering on $s_{\rm core}$ are duplicated in the work of Rampp (2000) whose Figs. (5.3a) and (5.6b) shows that with and without neutrino-electron scattering in their $15\,{\rm M}_\odot$ model they obtain $s_{\rm core} \simeq 1.3$ and $1.14\ k_B$ baryon^{-1}, respectively. A recent collapse calculation by Liebendörfer et al. (2002b) of a $13\,{\rm M}_\odot$ progenitor also shows $s_{\rm core} \sim 1.3\ k_B$ baryon^{-1}. Core Y_e ($Y_e^{\rm core}$) in our $11\,{\rm M}_\odot$ model drops to 0.266 and 0.293 at bounce in our models with and without neutrino-electron scattering, respectively. Both numbers from Rampp (2000) are slightly higher; his Fig. (5.3b) gives the corresponding numbers as approximately 0.28 and $0.30 - 0.31$, respectively. Liebendörfer et al. (2002b) have $Y_e^{\rm core} \simeq 0.30$, including neutrino-electron scattering. Peak positive velocities in all calculations reach $\sim 2 \times 10^9$ cm s^{-1} at M$\simeq 0.7{\rm M}_\odot$ - in very good agreement with previous work. However, one important difference bears mention. Our peak breakout electron-neutrino luminosity is slightly lower than that obtained in other work. Both Liebendörfer et al. (2001) and Rampp & Janka (2000) obtain $L_{\nu_e}^{\rm peak}$ of $\sim 3.5\times10^{53}$ erg s^{-1} with comparable progenitors. Indeed, Liebendörfer et al. (2002a) present the breakout pulse for several different progenitors and finds virtually identical $L_{\nu_e}^{\rm peak}$ for all models. We obtain $L_{\nu_e}^{\rm peak} \simeq 2.55 \times 10^{53}$ erg s^{-1} in our 11M$_\odot$ and virtually the same number with the 15M$_\odot$ and 20M$_\odot$ models we present in §4.4.2. Our results consistently give lower $L_{\nu_e}^{\rm peak}$ by about 30%. Because this luminosity pulse results from the most dynamical phase in supernova modeling, it is important to note that no full supernova simulations have been constructed that match our results in angular and spectral resolution. For comparison, the work of Mezzacappa et al. (2001) and Liebendörfer et al. (2001), typically employ just eight angular bins at each radial point and twelve energy groups. In particular, we suspect that poorer angular resolution may change the formation and propagation of the breakout pulse. The recent work of Liebendörfer et al. (2002b) has shown that they experience significant numerical diffusion of their breakout pulse as it propagatoes from the point of decoupling to the edge of their computational grid. The peak asymptotic luminosity they quote, $L_{\nu_e}^{\rm peak}$ $\sim$3.5$\times$10^{53} erg s^{-1}, is sampled at 500 km in their calculations. This peak drops to $\sim$2.6$\times$10^{53} erg s^{-1} in propagating to $\sim$2000 km (see their Fig. 14 and Fig. 20). Our $L_{\nu_e}^{\rm peak}$ does not experience the same numerical degradation. For example, we find that the electron-neutrino breakout pulse decreases from $\sim$2.7$\times$10^{53} erg s^{-1} at 500 km to approximately 2.55$\times$10^{53} erg s^{-1} at 2500 km in our fiducial 11 M$_\odot$ model.

Two hundred milliseconds after bounce, the shock has moved out to about 200 km in radius. A region of net heating called the gain region, has formed between the gain radius R_g $\simeq$100 km (where heating balances cooling) and the shock. Between the ν_e neutrinosphere ($R_{\nu_e} \simeq 60$ km for $\varepsilon_{\nu_e} = 10.7$ MeV) and R_g is a region of net cooling. Figure (4.14) shows the angular distribution of the radiation field (the specific intensity, I_ν) in this epoch. The outer near-circle (thick solid line) in this figure shows the normalized radiation field for $\varepsilon_{\nu_e} = 320$ MeV. Because the neutrino opacity is proportional to ε_ν^2, the radiation field $I_\nu(\theta)$ is isotropic at this high energy and the flux is virtually zero. Also shown is $I_\nu(\theta)$ for other neutrino energies down to 1 MeV (also a thick solid line). Only every other neutrino energy calculated is shown. Going from high to low energies, one sees that the radiation field becomes less isotropic, the lowest energies being the most forward-peaked. The $\varepsilon_{\nu_e} = 10.7\,\mathrm{MeV}$ point is highlighted (middle thick solid line) to show the angular distribution of the radiation field at the neutrinosphere for that energy. A glance at Fig. (4.14) shows how forward-peaked the radiation field is at the point of decoupling (the neutrinosphere), for a given energy (in this case, 10.7 MeV). Note that in this calculation, R_{ν_e} occurs at our 270th radial zone, so that in each quadrant of the polar plot there are 269 angular bins.

Also of interest is the dependence of the angular distribution on radius for a given energy. Figure (4.15) shows how $I_{\nu_e}(\theta, \varepsilon_{\nu_e} = 10.7\text{ MeV})$ evolves from the neutrinosphere radius ($\sim$60 km, outer thick solid line) to the shock radius ($R_s \simeq 200\,\mathrm{km}$, inner thick solid line). Also shown is $I_{\nu_e}(\theta)$ at R_g, where heating balances cooling, and $I_{\nu_e}(\theta)$ at larger radii, where heating dominates.

4.4.1 Spectral Resolution

Our fiducial model employs 40 energy groups for each neutrino species, with the actual grouping described in §4.3. In an effort to understand the effects of degrading the spectral resolution, we have run the same $11\mathrm{M}_{\odot}$ model, with the same spatial zoning and the same physics as the fiducial model, but with 20 and 10 energy groups. All three calculations were carried out to 250 milliseconds after bounce.

We observe only small quantitative differences and virtually no qualitative differences in the overall evolution of all quantities in comparing the run with 40 energy groups to that with only 20. Over the whole post-bounce evolution, $\langle\varepsilon_{\nu_e}\rangle$ is $\sim$0.05 MeV higher in the 20-group calculation, a difference of just 0.5% at 250 ms. However, L_{ν_e} is higher by 2% in the model with just 20 energy groups. Differences in the average energy and luminosity of $\bar{\nu}_e$ and ν_μ neutrinos amount to less than $\sim 1\%$ overall, with each of these quantites lower in the 20 group calculation than in the model run with 40 energy groups. The basic hydrodynamical quantities were similarly unaffected.

The core entropy was reproduced in the the 20-group model to within 0.5%, with the higher resolution model having slightly lower entropy. The core Y_e at bounce was just 0.5% lower in the model with 20 groups. The only qualitative difference observed between the two models was a slight oscillation in the velocity versus mass profile inside $0.5\mathrm{M}_{\odot}$just before bounce.

We find significant qualitative and quantitative differences between our 10-group model and our models with higher spectral resolution. The small oscillations observed in the matter velocity in the 20-group model are much more pronounced with just 10 groups on infall. There are similar and seemingly correlated oscillations in Y_e. Oscillations very similar to these have been observed in Rampp (2000) and Mezzacappa & Bruenn (1993c). The oscillations result from insufficient spectral resolution of the Fermi surface of electron neutrinos. In addition to the oscillations, many components of the hydrodynamic and neutrino spectral evolution are affected by the use of only 10 energy groups in our calculation. At bounce, the core entropy, which had come within 5% of that obtained in the 20- and 40-group calculations ($s_{\mathrm{core}} \sim 1.35\ k_B$ baryon^{-1}), dropped to 0.8 k_B baryon^{-1}. This, of course, also manifests itself in the temperature profile. The core temperature after bounce reaches only 7.5 MeV, as compared with the 11 MeV obtained in the calculations with 20 and 40 energy groups. Despite the fact that the core Y_e was slightly higher in the 10 group calculation, the peak positive shock velocity just after bounce was 15% lower. The ν_e breakout pulse was 10% lower in the 10-group model than in the 40- or 20-group models. L_{ν_e} was $\sim 0.03 \times 10^{53}$ erg s^{-1} higher in the low-resolution model throughout the post-bounce evolution, this difference amounting to $\sim 8\%$ at 250 ms. In addition, we find that $L_{\bar{\nu}_e}(t)$ is qualitatively different in the 10 group model. It peaks faster and higher than the 40-group model, but drops off more quickly in time. Although $L_{\bar{\nu}_e}$ at 250 ms is just 9% lower in the 10-group model than the 40-group model, the slope of the luminosity is steeper and that difference will grow in time. The average energy for all species is higher in the 10-group calculation than in the 40-group calculation, but not by more than a few percent over the whole post-bounce evolution.

In sum, we conclude that 10 neutrino energy groups are insufficient for resolving the neutrino radiation field. We see the largest differences in the emergent spectrum for the electron neutrinos. This is likely due to the fact that the ε_{ν_e} grouping must extend to $\sim$ 300 MeV in order to resolve the Fermi energy of the electron neutrinos within the core. Because ν_e transport, through the charged-current interaction (see §B.1.1), affects the dynamics so significantly, failure to resolve the ν_e radiation field affects most observables. Our model employing 20 energy groups comes quite close to reproducing our results with 40 energy groups. Differences are no larger than 2% and, for most quantities, the fractional differences are closer to 0.5−1%. Considering the large decrease in computation time (a factor of 2), 20 groups is probably sufficient for all but the most detailed models. In comparison, with 21 energy groups Rampp (2000) finds that the ν_e Fermi surface is under-resolved, as the large oscillations he sees in the trapped lepton fraction demonstrate. Typical recent calculations by Rampp & Janka (2002) employ 20 − 30 energy groups spaced geometrically. Mezzacappa et al. (2001) and Liebendörfer et al. (2001) employ 12 energy groups.

4.4.2 Other Progenitors: 15 $\mathrm{M}_\odot$ and 20 $\mathrm{M}_\odot$ Models

A complete theory of core-collapse supernovae must hope to understand the detailed dynamics and neutrino signatures of all possible supernova progenitors. If successful neutrino-driven supernova models were obtained, one might hope to find systematic trends between, for example, the progenitor mass and the peak neutrino luminosity, final supernova energy, or mass of the nascent protoneutron star. We begin such an investigation by first considering the dynamics and emergent neutrino characteristics of two more massive progenitors.

Figures (4.16) and (4.17) show the neutrino luminosity in erg s^{-1} at the outer edge of the grid, as a function of time for three different progenitor masses: 11 $\mathrm{M}_\odot$

(thick solid line), 15 $M_\odot$ (thin solid line), and 20 $M_\odot$ (dotted line). Figure (4.16) shows L_{ν_e} and Fig. (4.17) shows both $L_{\bar{\nu}_e}$ and L_{ν_μ}. Note in Fig. (4.16) that the breakout pulse is remarkably similar in magnitude and structure for each progenitor, a result recently obtained in the work of Liebendörfer et al. (2002a). Interestingly, as discussed in §4.4, our ν_e breakout pulse reaches $\sim 2.55 \times 10^{53}$ erg s^{-1}, whereas Liebendörfer et al. (2002a) obtain a characteristic peak L_{ν_e} of $\sim 3.5 \times 10^{53}$ erg s^{-1}. Note that our 20$M_\odot$ model, which also employs 300 spatial zones, 40 neutrino energy groups, and the tangent-ray algorithm for angular binning, reaches a somewhat lower peak luminosity at $\sim 2.225 \times 10^{53}$ erg s^{-1}.

In Fig. (4.17) $L_{\bar{\nu}_e}$ and L_{ν_μ} are virtually identical in both the 11$M_\odot$ and 15$M_\odot$ models over the first 100 ms of post-bounce evolution and only later develop small differences. In marked contrast, the 20 $M_\odot$ model exhibits higher neutrino luminosities for all species after electron-neutrino breakout. For L_{ν_e} and $L_{\bar{\nu}_e}$ the difference between the 11$M_\odot$ model and the 20$M_\odot$ model is a factor of two at 200 milliseconds after bounce. For L_{ν_μ}, the difference is a factor of 1.5. In addition, L_{ν_μ} and $L_{\bar{\nu}_e}$ peak approximately 100 ms later in the 20$M_\odot$ model than in the 11$M_\odot$ progenitor.

In Figs. (4.18) and (4.19) we show the evolution of the average neutrino energy for each species (defined by eq. 4.26), and progenitor. One hundred milliseconds after bounce the differences become significant. Not only are the spectra for the 20$M_\odot$ model harder, but the average energies are increasing faster than those for the 11$M_\odot$ and 15$M_\odot$ models. Some of these systematics can be understood by inspecting Fig. (4.20), which shows the mass flux ($\dot{M}$) as a function of radius in units of $M_\odot$ s^{-1} for the 11$M_\odot$ (thick solid line), 15$M_\odot$ (thin solid line), and 20$M_\odot$ (dotted line) models. Also shown are the positions of the neutrinosphere for the average emerging neutrino energy. Open triangles correspond to R_{ν_e}, whereas filled squares and open circles denote $R_{\bar{\nu}_e}$ and R_{ν_μ}, respectively. In the steady-state, the total luminosity of a given neutrino species should be given approximately by the accretion luminosity, written in terms of $\dot{M}$ and R_ν: $L_\nu^{\rm acc} \sim GM_\nu \dot{M}/R_\nu$, where M_ν is the mass enclosed by

R_ν. This reflects the role of the neutrino luminosity in carrying away the energy of infall. To zeroth order, the higher mass flux in the $20\,M_\odot$ model in Fig. (4.20) explains the higher luminosity at that epoch in Figs. (4.16) and (4.17). This conclusion is modified slightly by the actual radial positions of the various neutrinospheres for each progenitor in this epoch and the mass enclosed within R_ν. Given the simple expression for $L_\nu^{\rm acc}$, the ratio of the total neutrino luminosity of the $20\,M_\odot$ model to that of the $11\,M_\odot$ model should be approximately

$$\frac{L_\nu^{20\,\mathrm{M}_\odot}}{L_\nu^{11\,\mathrm{M}_\odot}} = \left(\frac{M_\nu^{20\,\mathrm{M}_\odot}}{M_\nu^{11\,\mathrm{M}_\odot}}\right)\left(\frac{\dot{M}^{\,20\,\mathrm{M}_\odot}}{\dot{M}^{\,11\,\mathrm{M}_\odot}}\right)\left(\frac{R_\nu^{11\,\mathrm{M}_\odot}}{R_\nu^{20\,\mathrm{M}_\odot}}\right) \sim 2.5.$$

We find that the actual ratio, as obtained by solving the full problem, is ~ 1.9.

Although we obtain higher average neutrino luminosities and energies for the $20\,\mathrm{M}_\odot$ progenitor, there is no sign of explosion or developing explosion in this model. In fact, approximately 200 ms after bounce the shock in this progenitor has reached $r \sim 190$ km and begins to recede; at approximately 250 ms, it has dropped to $r \sim 150$ km. In contrast, both the $11\,\mathrm{M}_\odot$ and $15\,\mathrm{M}_\odot$ progenitors maintain shock radii of 180-190 km throughout this epoch. Although none of these simulations yields an explosion, the lower mass models seem more promising.

4.4.3 Changes in the Nuclear Equation of State

One might expect that large modifications to the nuclear equation of state could have a significant impact on the collapse and bounce dynamics, as well as on the emergent neutrino spectra. We have not yet studied nuclear equations of state based on finite-temperature mean-field theory, nor have we incorporated with exotic particle species and phase transitions. Such equations of state are of considerable interest, but are not always easily incorporated into existing dynamical codes. In addition, the neutrino microphysics would have to be made consistent with the presence of exotic constituents (e.g., neutrino-meson and neutrino-quark interactions).

Performing an albeit limited exploration of the parameter space available to high-density equations of state, we have constructed three tabular versions of the LSEOS (see §4.2.1) with different nuclear compressibilities: κ = 180, 220, and 375 MeV. For all of our fiducial models we have taken κ = 220 MeV. In order to illustrate the role of the nuclear compressibility, we have run collapse and bounce simulations with all three κs, evolving each to 200 ms after bounce. Figure (4.22) shows the temperature profile in an 11M$_\odot$ progenitor for calculations with κ = 180 (dashed lines) and κ = 375 (solid lines) ~2 ms and ~100 ms after bounce. The model with κ = 180 reaches a higher core temperature, but has a steeper negative temperature gradient, reaching a minimum at M$\simeq$ 0.4 M$_\odot$. The peak temperature at M$\simeq$ 0.65 M$_\odot$ is also higher for the lower compressibility model. Overall, however, the two models are remarkably similar. Peak velocities in both calculations reach 2×10^9 cm s^{-1} at M~ 0.7 M$_\odot$. In addition, the entropy and Y_e profiles are qualitatively identical for all three κs. Although the ν_e breakout luminosity pulse for the model with κ = 375 is 1 ms delayed compared with the corresponding pulse for both κ = 180 and κ = 220, the shape and magnitude of the pulses are identical. The evolution of the luminosity and average neutrino energy for all neutrino species (apart from the 1 ms offset for κ = 375) is similarly identical for the first ~ 30 ms after bounce (see Fig. 4.23).

After 50 ms, the differences between the models with κ = 180 and κ = 375 in the neutrino luminosities and spectra become discernible. Figure (4.23) shows the luminosity of each species at the edge of the grid as a function of time for both models. The post-bounce neutrino luminosity for all species is lower in the κ = 375 model. At 200 ms after bounce the fractional difference is approximately 4%, 5%, and 9% for L_{ν_e}, $L_{\bar{\nu}_e}$, and L_{ν_μ}, respectively. The model with κ = 375 also produces characteristically softer spectra with the average energy for each species being ~3% lower. Although $\langle\varepsilon_{\nu_e}\rangle$ and $\langle\varepsilon_{\bar{\nu}_e}\rangle$ are lower by a few percent in the model with κ = 375, $\langle\varepsilon_{\nu_\mu}\rangle$ is not evolving to higher energies as quickly as in the model with κ = 180. For all models, $\langle\varepsilon_{\nu_\mu}$ evolves linearly in time, but the model with the softer EOS evolves with a larger slope than the model with $\kappa = 375$.

These differences in spectra and some of the basic hydrodynamical quantities are not large enough to affect the post-bounce dynamics significantly on 100 ms timescales. In fact, 200 ms after bounce, there is very little difference between the shock position, gain radius, or neutrinosphere positions in these two models. Perhaps larger differences between models with different compressibilities develop on one- and ten-second timescales in the post-explosion protoneutron star cooling epoch. This might be important both for detectability of the neutrino signature at late times and the evolution of the neutrino-driven protoneutron star wind, as detailed in Chapter 3.

4.4.4 Modifications to the Standard Cross Sections

The work of Burrows & Sawyer (1998,1999), Raffelt & Seckel (1998), Janka et al. (1996), and Reddy, Prakash, & Lattimer (1998) all point to a reduction of the dominant neutral- and charged-current opacity sources for neutrinos at high density due to nucleon-nucleon correlations caused by the strong interaction and Fermi statistics. Such modifications to the standard neutrino opacities are discussed in Appendix B depend on the model for strong interactions employed. Ideally, they should be included consistently in constructing the nuclear equation of state (Reddy, Prakash, & Lattimer 1998). Although they did not take into account these changes to the nuclear EOS, Rampp et al. (2002) have recently investigated the role of nuclear correlations in their dynamical models. They found modest enhancements in L_{ν_e} and L_{ν_μ} and considerable enhancements in $L_{\bar{\nu}_e}$ ($\sim 20\%$). Although inclusion of these processes did not lead to explosions, they did affect the dynamics and it seems they should not be absent from a full treatment of the problem.

In a future work we will incorporate the dynamical structure function formalism of Burrows & Sawyer (1998,1999) and Reddy, Prakash, & Lattimer (1998). For now, we provide a set of simple tests, varying some of our cross sections and reaction rates in order to test the sensitivity of the observables and the dynamics.

Artificial Opacity Reduction: In Liebendörfer (2000), erroneous explosions were obtained in one-dimensional models of supernovae because of an artificially decreased neutral-current neutrino-nucleon opacity. As a simple test, we have decreased the neutrino-neutron (σ_n) and neutrino-proton (σ_p) cross section (see §B.2.1) by a factor of 10 everywhere, for all neutrino energies. Despite the violence done to our cross sections, because the dynamics during collapse and bounce are dominated by neutral-current scattering on nuclei and the charged-current process $\nu_e n \leftrightarrow e^- p$, the breakout phenomenon is only modestly affected; the peak ν_e breakout pulse is just 10% higher than in our fiducial model and reaches 2.85×10^{53} erg s^{-1}. Two hundred and fifty milliseconds after breakout, $L_{\nu_e} \simeq 0.25 \times 10^{53}$ erg s^{-1} in our fiducial model. In our model with $\sigma_{n,p}/10$, we obtain $L_{\nu_e} \simeq 0.35 \times 10^{53}$ erg s^{-1}. Figure (4.21) shows L_{ν_e} and $L_{\bar{\nu}_e}$ at infinity as a function of time for the fiducial model and the model presented here. Both L_{ν_e} and $L_{\bar{\nu}_e}$ are increased by $\sim$40$-$50% in the calculation with lower opacity. These changes, however, are modest compared with those for L_{ν_μ} and $\langle \varepsilon_{\nu_\mu} \rangle$. Two hundred and fifty milliseconds after bounce, $L_{\nu_\mu} \simeq 2.4 \times 10^{53}$ erg s^{-1}, a factor of four larger than in the fiducial model. For ν_μ neutrinos, there is no charged-current absorption process on free nucleons to contribute to the total opacity, as there is for the ν_e and $\bar{\nu}_e$ neutrinos. For the ν_μs, the neutral-current scattering dominates the opacity and so changing that opacity source so dramatically has significant consequences for L_{ν_μ} and $\langle \varepsilon_{\nu_\mu} \rangle$.

Importantly, because of the increase in the L_{ν_e} and $L_{\bar{\nu}_e}$ we obtain a larger gain region in this calculation, higher entropy behind the shock, and a larger shock radius 250 ms after bounce. In the fiducial model, at 250 ms post-bounce the shock is sitting at 180 km, whereas in the model with reduced opacities, $R_s \simeq 210$ km. Still, although the dynamics are affected by this drastic decrease in neutrino opacity, we do not obtain an explosion in this first 250 ms of post-bounce evolution.

The Weak Magnetism/Recoil Correction: Our fiducial $11\,\mathrm{M}_\odot$ model includes the weak magnetism/recoil correction (see §B.1.1, §B.1.2, and §B.2.1) to the charged-current opacities for ν_e and $\bar{\nu}_e$ and to the neutral-current scattering opacities off of nucleons for all neutrino species (Vogel 1984; Horowitz 2002). The weak magnetism/recoil correction lowers the cross section for all processes; the terms are largest for anti-neutrinos ($\bar{\nu}_e$ and $\bar{\nu}_\mu$). We ran our fiducial model (see §4.4) without these corrections and found only small differences in the first 250 milliseconds of post-bounce evolution. L_{ν_e}, L_{ν_μ}, $\langle\varepsilon_{\nu_e}\rangle$,and $\langle\varepsilon_{\nu_\mu}\rangle$ are all lower at the 0.5% level without the weak-magnetism correction. $\langle\varepsilon_{\bar{\nu}_e}\rangle$ and $L_{\bar{\nu}_e}$ are less by 4% in this representative $11\mathrm{M}_\odot$ calculation. This slight softening and dimming of the emergent spectra can be understood simply as the result of increasing the total opacity for all species by removing the small weak magnetism correction.

4.4.5 The Role of Nucleon-Nucleon Bremsstrahlung

The effects of bremsstrahlung on the ν_e and $\bar{\nu}_e$ spectra are negligible at virtually all times because for them the charged-current processes $\nu_e n \leftrightarrow pe^-$ and $\bar{\nu}_e p \leftrightarrow ne^+$ dominate. In Chapter 2, we showed that nucleon-nucleon bremsstrahlung might have important consequences for the emergent ν_μ spectra and that it dominates $e^+e^- \rightarrow \nu_\mu\bar{\nu}_\mu$ as a production process. Figure (4.24) shows the effect of bremsstrahlung on the average energy of ν_μs. The plot itself shows the average energy (in MeV) as a function of radius approximately 230 ms after bounce. The inset shows $R_{\nu_\mu}(\varepsilon_{\nu_\mu})$, the neutrinosphere radius defined by eq. (4.25) as a function of energy. The solid line is the fiducial model, with neutrino-electron scattering redistribution and nucleon-nucleon bremsstrahlung. The short dashed line is the same model run through the full evolution, but without nucleon-nucleon bremsstrahlung. The long dashed line shows the same model without neutrino-electron scattering energy redistribution, but with nucleon-nucleon bremsstrahlung. One can see immediately from the inset that at low energies, bremsstrahlung increases the opacity significantly. It is also clear from the main figure that inelastic neutrino-electron scattering profoundly effects the emergent ν_μ spectrum.

Figure (4.25) shows L_{ν_μ} and $\langle\varepsilon_{\nu_\mu}\rangle$ at infinity as a function of time for the fiducial model (thick solid line), which includes nucleon-nucleon bremsstrahlung, and the same model computed without bremsstrahlung (thin solid line). With bremsstrahlung, the average energies of the mu neutrinos are lower and the luminosity is significantly higher. Chapter 2 showed that we could expect these results based on comparisons between the bremsstrahlung and e^+e^--annihilation neutrino production rates. Near the ν_μ neutrinosphere, the bremsstrahlung emission spectrum is peaked at low neutrino energies ($<$ 10 MeV) compared with e^+e^- annihilation. For this reason, we concluded in Chapter 2 that the emergent ν_μ spectra have both higher luminosity and lower average energy. As evidenced by Fig. (4.25), this prediction is borne out in our dynamical models.

4.4.6 The Effects of Inelastic Neutrino-Electron Scattering

Figure (4.26) shows the luminosity at infinity as a function of time for all species in the 11 $M_\odot$ models with (thin solid line) and without (thick solid line) inelastic neutrino-electron scattering, using the prescription described in detail in Appendix B.3.1. Figure (4.27) shows the *rms* neutrino energy for each species for the model without inelastic $\nu_i e^-$ scattering and should be compared with Fig. (4.11). The main ν_e breakout pulse is enhanced slightly and reaches 2.73×10^{53} erg s^{-1}, compared with 2.55×10^{53} erg s^{-1} in the fiducial model. Also noticeable in L_{ν_e} is the decrease in the pre-breakout pulse associated with the deleptonization of the core on infall as described in §4.4. Shown here at $t \sim 0.007$ s, the pre-breakout peak reaches 0.75×10^{53} erg s^{-1} with neutrino-electron scattering and only 0.52×10^{53} erg s^{-1} without. By down-scattering neutrinos during collapse and bounce via $\nu_e e^-$ scattering, more neutrinos are able to escape before the core becomes opaque. Thus, there is a tradeoff. Including inelastic scattering off electrons makes the *collapse* luminosity peak larger, but the main *breakout* luminosity peak smaller. Although the breakout phenomenon is slightly affected, the spectra of ν_e and $\bar{\nu}_e$ neutrinos at 200 ms is dominated by the charged-current interactions and so the effects of νe^- scattering on L_{ν_e}, $L_{\bar{\nu}_e}$, $\langle\varepsilon_{\nu_e}\rangle$, and $\langle\varepsilon_{\bar{\nu}_e}\rangle$ are modest. ν_μ neutrinos are more significantly affected. Throughout the evolution, L_{ν_μ} is decreased by $\sim$30% by including $\nu_\mu e^-$ redistribution. $\langle\varepsilon_{\nu_\mu}\rangle$ is also profoundly altered. Comparing Fig. (4.27) with Fig. (4.11), we see that $\langle\varepsilon_{\nu_\mu}\rangle$ is ~ 6 MeV higher without $\nu_\mu e^-$ redistribution.

Figure (4.6) shows that there is significantly more deleptonization of the core at bounce with inelastic neutrino-electron scattering (thick solid line) than there is without it (long dashed line). The magnitude of the difference in core Y_e at bounce is in keeping with other recent models (e.g., Rampp 2000; see §4.4). The fact that $Y_e^{\rm core}$ is higher at bounce in the latter case has important consequences for the shock energy and the early post-bounce neutrino characteristics. In the model without neutrino-electron scattering, the peak positive velocity after bounce is higher ($\sim$2.5$\times$10^9 cm s^{-1}, compared with $\sim$2.0$\times$10^9 cm s^{-1}) and peaks at larger mass (0.85 M$_\odot$, compared with 0.7 M$_\odot$). In both models, as the shock stalls and the briefly positive velocities achieved become negative, the matter behind the shock, the protoneutron star, oscillates in radius on $5-10$ millisecond timescales. As the protoneutron star pulsates, pressure waves move through the neutrinosphere of each species. These waves act to modulate the luminosity and average neutrino energy. The amplitude of these near-periodic variations in neutrino luminosity and energy are damped on $\sim$10 ms timescales. They are smaller for the model with neutrino-electron scattering because the shock in this model has less energy and the corresponding post-bounce oscillatory mass motions ('ringing') are thereby smaller at the neutrinosphere for each species. The smaller the local changes in temperature and density near the neutrinosphere, the smaller the changes in the local emission and absorption. Hence, we should expect smaller amplitude temporal modulations in the emergent neutrino spectral characteristics.

Also potentially important is the fact that $L_{\bar{\nu}_e}$ rises later in the model with neutrino-electron energy redistribution than in the model without such redistribution. Twenty milliseconds after bounce, Fig. (4.26) shows that $L_{\bar{\nu}_e}$ with $\nu_i e^-$ scattering is approximately half that for the model without this thermalization process. This has important implications for the detection of the ν_e breakout pulse in terrestrial light-water Čerenkov neutrino detectors like SuperKamiokande. In §4.5.1, we show that in such detectors, if one is to identify the ν_e breakout signature uniquely, one must do so within $5-20$ milliseconds of bounce, but before the $\bar{\nu}_e$ signal becomes appreciable. Hence, because neutrino-electron scattering suppresses the $\bar{\nu}_e$ signal during this epoch, it has consequences for the observation of the next galactic supernova.

4.5 Neutrino Detector Signatures

In the winter of 1987, a blue supergiant in the Large Magellanic Cloud, a satellite galaxy to the Milky Way approximately 50 kpc (1 kpc$\simeq 3.1\times10^{21}$cm) away, exploded as a supernova. It became known as SN1987A and is famous both as the most studied supernova and as the first (and only) supernova whose neutrino signature has been observed. A total of just 19 neutrino events were observed in the IMB (Irvine-Michigan-Brookhaven) and Kamioka II detectors. The signal lasted ~10 seconds and confirmed the basics of our theoretical understanding of core collapse; the amount of energy radiated in neutrinos was comparable to that expected in protoneutron star cooling models at the time (Burrows & Lattimer 1986) and the inferred $\bar{\nu}_e$ neutrino spectra had average energies of $\sim10-15$ MeV (Fig. 4.11).

However, the current generation of neutrino detectors might collectively see thousands of neutrino events from the next galactic supernova (Burrows, Klein, & Gandhi 1992). Such a supernova would provide exquisite neutrino luminosity and spectral information that would put severe constraints on the physics of the core during collapse and explosion. Besides elucidating supernova physics, much information on the mass hierarchy of neutrinos and the high-density nuclear equation of state would be collected. Indeed, the neutrino signature might clearly reveal whether a black hole or a neutron star had been created (Burrows 1988). If the former is born, direct eV-scale measurements of mu- and tau-neutrino masses could be made by the current generation of detectors (Beacom, Boyd, & Vogel 2000).

Using the models presented in the preceding sections, we have made predictions about the dynamics and neutrino signals expected from a class of supernova progenitors, with reasonable variations in microphysics and the details of the models. In this section, we go a step further and fold our emergent neutrino spectra with the thresholds and sensitivities of a subset of modern neutrino detectors.

In underground light-water detectors such as a fully-repaired Super Kamiokande (SK), we can expect $\sim$5000 neutrino events from the next galactic supernova at a distance of 10 kpc. In such detectors the primary mechanism for neutrino detection is the $\bar{\nu}_e p \to n e^+$ process. The positron secondary emits Čerenkov radiation. For an electron or positron secondary, the differential number detected can be written (Burrows, Klein, & Gandhi 1992)

$$dN = \frac{N_T}{4\pi D^2} L_\nu^{\rm num}(t', \varepsilon_\nu) \frac{d\sigma(\varepsilon_\nu, \varepsilon_e)}{d\varepsilon_e}\, E(\varepsilon_e)\delta(t - t' - \Delta t)\, dt'\, d\varepsilon_e\, d\varepsilon_\nu\, dt, \qquad (4.27)$$

where ε_e is the electron or positron energy, $E(\varepsilon_e)$ is the detection efficiency, N_T is the number of targets, $L_\nu^{\rm num}$ is the number luminosity of neutrinos, t' is the source time, t is the detector time with D/c subtracted, $\Delta t (\simeq D/2c\,(m_\nu c^2/\varepsilon_\nu)^2)$ is the time delay of a neutrino with mass m_ν, and $d\sigma/d\varepsilon_e$ is the differential cross section for neutrino capture and electron or positron production. For most purposes $d\sigma/d\varepsilon_e \simeq \sigma(\varepsilon_\nu)\delta(\varepsilon_\nu - \varepsilon_e - \Delta)$, where Δ is the reaction threshold (in the case of the reaction $\bar{\nu}_e p \to n e^+$, $\Delta = m_n - m_p + m_e \simeq 1.804$ MeV). Taking this approximation for $d\sigma/d\varepsilon_e$,

$E(\varepsilon_e) = 1$, and $m_\nu = 0$, we obtain

$$\frac{dN}{dt\, d\varepsilon_\nu} = \frac{N_T}{4\pi D^2} L_\nu^{\rm num}(t, \varepsilon_\nu)\sigma(\varepsilon_\nu). \tag{4.28}$$

Using eqs. (4.27) and (4.28), it is a relatively simple matter to fold our time-dependent spectra with terrestrial detectors, including efficiency and threshold corrections, in order to obtain the observed neutrino signal. We consider three different detectors and the early neutrino signal that could be observed from the next galactic supernova. Although eq. (4.27) includes the effects of time-delay due to a finite neutrino mass, in what follows we assume massless neutrinos and employ eq. (4.28).

4.5.1 SuperKamiokande

The SuperKamiokande (SK) neutrino observatory in a light-water Čerenkov detector whose fiducial volume for supernova neutrino detection is ~32 ktonne (Totani et al. 1998). We take as a threshold ~5 MeV (Beacom & Vogel 1998). The background is typically of order several $\times 0.1$ s^{-1} if the full detector volume is considered (Beacom & Vogel 1998) and will not figure into our discussion here.

Light-water Čerenkov detectors offer several different channels for detection of the various neutrino species. The dominant reaction is charged-current absorption of $\bar{\nu}_e$ neutrinos on free protons ($\bar{\nu}_e p \rightarrow n e^+$). The positron secondary emits Čerenkov radiation, which is detected directly. Neutrino scattering on electrons, $\nu_i e^- \rightarrow \nu_i e^-$ also contributes for all neutrino species. For this process, we use the neutrino-electron scattering cross section (Sehgal 1974):

$$\frac{d\sigma_i}{d\varepsilon_e} = \frac{1}{2}\frac{\sigma_o}{m_e c^2}\left[A_i + \left(1 - \frac{\varepsilon_e}{\varepsilon_\nu}\right)^2 B_i\right] \implies \sigma_i = \frac{1}{2}\sigma_o \Lambda_i \left(\frac{\varepsilon_\nu}{m_e c^2} + \frac{1}{2}\right), \tag{4.29}$$

where

$$\Lambda_i = \frac{1}{4}\left(A_i + \frac{1}{3}B_i\right), \quad A_i = (C_V + C_A)^2, \quad B_i = (C_V - C_A)^2,$$

and $C_V = \pm 1/2 + 2\sin^2\theta_W$ for electron types and muon types, respectively. $C_A = +1/2$ for ν_e and $\bar{\nu}_\mu$, and $C_A = -1/2$ for $\bar{\nu}_e$ and ν_μ. Note that the neutrino-electron scattering cross section is $6-7$ times less for the mu- and tau-type neutrinos, owing to the fact that for them the reaction can proceed via only the neutral current. Other important reactions include

$$\nu_e +^{16}\mathrm{O} \rightarrow^{16}\mathrm{F} + e^- \quad (\epsilon_{th} = 15.4\,\mathrm{MeV}), \tag{4.30}$$

$$\nu_e +^{18}\mathrm{O} \rightarrow^{18}\mathrm{F} + e^- \quad (\epsilon_{th} = 1.66\,\mathrm{MeV}), \tag{4.31}$$

$$\bar{\nu}_e +^{16}\mathrm{O} \rightarrow^{16}\mathrm{N} + e^+ \quad (\epsilon_{th} = 11.4\,\mathrm{MeV}), \tag{4.32}$$

and

$$\nu_i +^{16}\mathrm{O} \rightarrow \nu_i' +^{16}\mathrm{O}^* \rightarrow \nu_i' + \gamma + X, \tag{4.33}$$

where $\epsilon_{\rm th}$ is the energy threshold for the reaction. For the neutral-current excitation of ^{16}O (reaction 4.33), the γ secondary has an energy in the range $5-10$ MeV and, hence, is visible by SK. Note that energy resolution for the secondary electron or positron in reactions (4.30), (4.31), and (4.32) is good to no better than $\sim$10–20% (Burrows, Klein, & Gandhi 1992; Totani et al. 1998). For the study carried out here, we calculate event rates in SK due to only $\bar{\nu}_e p \rightarrow n e^+$ and neutrino-electron scattering for all neutrino species. In the results presented here we assume 100% efficiency above the detector threshold.

Figure (4.28) shows the event rate (dN/dt in Hz, thin solid line) via charged-current absorption on free protons and the total integrated number of $\bar{\nu}_e$ events in SK for an 11 M$_\odot$ progenitor supernova at a distance of 10 kpc. Also included for comparison is the computed $\bar{\nu}_e$ luminosity (dotted line). The figure shows the first 900 ms after bounce. In order to evolve to such late times, we modified our fiducial 11 M$_\odot$ model to include only ν_e and $\bar{\nu}_e$ and just 20 energies per species. Nearly 550 events accumulate in the first second after collapse. Because $\bar{\nu}_e p \rightarrow n e^+$ dominates the signal so completely, we neglect $\bar{\nu}_e^{16}\mathrm{O} \rightarrow^{16}\mathrm{N} e^+$ in this figure.

Figure (4.29) shows the integrated number of ν_e and $\bar{\nu}_e$ neutrino events detected in SK, but using our fiducial 11 M$_\odot$ progenitor and only over the first $\sim$ 250 ms after bounce. The inset shows the first 80 ms of the signal. One can distinguish clearly the ν_e signal due to the scattering process $\nu_e e^- \rightarrow \nu_e e^-$ (thin solid line). For comparison, we include the $\bar{\nu}_e p \rightarrow n e^+$ number count (thick solid line) , which eventually overwhelms the signal due to $\nu_e e^- \rightarrow \nu_e e^-$. The combined neutral-current $\nu_{\mu,\tau}$ and $\bar{\nu}_{\mu,\tau}$ signal due to scattering off of electrons is smaller than that due to the process $\nu_e e^- \rightarrow \nu_e e^-$, and does not contribute significantly until after ~ 30 ms after bounce. Figure (4.29) implies that the ν_e breakout signal itself may be observable in SK for a supernova at 10 kpc.

4.5.2 Sudbury Neutrino Observatory

The Sudbury Neutrino Observatory (SNO) in Sudbury, Ontario, is a light- and heavy-water neutrino detector. It is a spherical acrylic vessel 12 meters in diameter, containing 1 ktonne of D_2O, that is surrounded by a cavity filled with light water. The fiducial light-water mass is approximately 1.6 ktonne. SNO is most sensitive to ν_μ and $\bar{\nu}_\mu$ neutrinos via breakup reactions on deuterons:

$$\nu_i + d \rightarrow n + p + \nu_i \quad (\epsilon_{\rm th} = 2.22\,\mathrm{MeV}) \tag{4.34}$$

$$\bar{\nu}_i + d \rightarrow n + p + \bar{\nu}_i \quad (\epsilon_{\rm th} = 2.22\,\mathrm{MeV}). \tag{4.35}$$

The liberated neutron secondary is thermalized in the heavy water and is then detected via capture on other nuclei within the detector volume. Currently, the neutrons from neutral-current events are detected via deuteron capture with an efficiency of $\sim$30% (SNO Collaboration 2002). Several schemes are currently proposed and in development for improved neutron-capture efficiency. The first is to lace the D_2O with two tonnes of NaCl. The thermal neutron absorption cross section on ^{35}Cl is large ($\sim$83% efficiency) and would result in a γ cascade peaked at 8 MeV. The γs would be detected by the $\sim$9600 inward-looking photomultiplier tubes outside of the acrylic vessel. The second proposed neutron detection method involves hanging ^{3}He proportional counters in the acrylic vessel, which would detect the neutrons directly (SNO collaboration webpage[1]). Because the neutrons would have a $\sim$5 ms mean capture time if the ^{35}Cl capture mechanism is employed (which would spread the ν_μ turn-on), the neutral-current signal might be partially compromised with the ^{35}Cl approach. The neutral-current deuteron breakup reactions (reactions 4.34 and 4.35) also contribute to the ν_e and $\bar{\nu}_e$ signal in SNO, but for them the charged-current deuteron capture processes,

$$\nu_e + d \to p + p + e^- \quad (\epsilon_{\rm th} = 1.44\,{\rm MeV}) \tag{4.36}$$

$$\bar{\nu}_e + d \to n + n + e^+ \quad (\epsilon_{\rm th} = 4.03\,{\rm MeV}), \tag{4.37}$$

are more important above $\varepsilon_\nu \simeq 10\,{\rm MeV}$ (Burrows, Klein, & Gandhi 1992). Process (4.37) can be used to observe $\bar{\nu}_e$ neutrinos uniquely via the simultaneous detection of the secondary neutron and the Čerenkov emission from the final-state positron. Although we include the threshold energy in our calculations of the total signal, as with SK we assume a 100% efficiency for SNO above the detector theshold.

In Fig. (4.30) we show the integrated number of ν_e neutrinos detected in SNO via the processes $\nu_e d \to ppe^-$ (dotted line), $\nu_e d \to np\nu_e$ (solid line), and $\nu_e e^- \to \nu_e e^-$ (dashed line) in the first 250 ms after bounce. The total ν_e signal is the thick solid line. For comparison, we provide the contribution to the total number of detected events from all other neutrino species (long dashed line). This signal includes the $\bar{\nu}_e d \to np\bar{\nu}_e$, $\bar{\nu}_e d \to nne^+$, and $\bar{\nu}_e p \to ne^+$ processes in the light-water portion of the detector, as well as the processes $\bar{\nu}_{\mu,\tau} d \to np\bar{\nu}_{\mu,\tau}$, $\nu_{\mu,\tau} d \to np\nu_{\mu,\tau}$, and neutrino-electron scattering throughout the entire detector volume. Note that it might be possible to exclude the charged-current absorption process $\bar{\nu}_e d \to nne^+$ by cutting events that have simultaneous neutron and positron detection. This would lower somewhat the line labeled *Total(other)* and make the early ν_e breakout signal easier to see. However, such a procedure requires accurate signal timing, which would be mitigated by employing the ^{35}Cl neutron capture mechanism mentioned in §4.5.2. As

[1] http://www.sno.phy.queensu.ca/sno/sno2.html#nc

it stands, one might expect to get $\sim$5 events in SNO from the ν_e breakout burst in the first $\sim$10 ms after bounce.

4.5.3 ICARUS

Although it has not yet reached its goal mass, ICARUS is designed to be a 3.6-ktonne drift chamber of pure liquid ^{40}Ar that will be sensitive primarily to electron neutrinos through electron-neutrino capture on Ar:

$$\nu_e + ^{40}\mathrm{Ar} \rightarrow ^{40}\mathrm{K}^* + e^- .$$

Recent shell-model calculations have shown that this process can proceed through super-allowed Fermi transitions to the 4.38 MeV excited isobaric analog state, as well as through several Gamow-Teller (GT) transitions to other lower-lying states in ^{40}K (Ormand et al. 1995). This has recently been investigated experimentally by studying the β^+−decay from ^{40}Ti (Bhattacharya et al. 1998). Employing isospin symmetry, Bhattacharya et al. (1998) inferred the transition strengths of $^{40}\mathrm{Ar} \rightarrow ^{40}\mathrm{K}$ from $^{40}\mathrm{Ti} \rightarrow ^{40}\mathrm{Sc}$. These theoretical and experimental results indicate that the GT transitions enhance the total ν_e capture cross section by a factor of three over the pure Fermi transition cross section. We take the super-allowed Fermi transition cross section from Raghavan (1986);

$$\sigma_{\mathrm{F}} \simeq 1.02 \times 10^{-43} (\varepsilon_{\nu_e} - 5.365)^2 \ \mathrm{cm}^2 \ \ (\epsilon_{\mathrm{th}} = 5.885\,\mathrm{MeV}) \tag{4.38}$$

and we assume that the total ν_e absorption cross section is given by $\sigma^{\mathrm{tot}}_{\nu_e\mathrm{Ar}} = 3\sigma_{\mathrm{F}}$.

The ICARUS detector is currently at 600 tonnes and has recently been approved to expand to 3 ktonnes (ICARUS ETH/CERN webpage[2]). Because of its sensitivity to ν_e neutrinos, ICARUS is of particular importance in detecting the early breakout pulse so prominent in Fig. (4.10). In the results presented below, we assume that the detector efficiency is 100% above threshold and that the detector mass is 3 ktonnes.

[2]see http://www.aquila.infn.it/icarus/

The ν_e breakout signal in ICARUS is very likely detectable. Figure (4.31) shows $N(< t)$ for the ICARUS detector (with 3 ktonnes of Ar). We plot the two dominant detection channels for ν_e neutrinos: ν_eAr absorption (thick solid line) and $\nu_i e^- \rightarrow \nu_i e^-$ (thin solid line). We also include the event rate, dN/dt (in units of $50\,\mathrm{s}^{-1}$), so that the width of the ν_e breakout spike can be compared with the detector signal in the very early phase. Note that the other neutrino species will contribute to the total signal through only the $\nu_i e^- \rightarrow \nu_i e^-$ process and that the combined signal amounts to only two events in the first 250 ms shown in Fig. (4.31). Combining the ν_e-electron scattering and ν_e-Ar absorption rates, ICARUS should expect to detect approximately 10 ν_e events from the breakout pulse alone.

4.6 Summary and Discussion

We have constructed fully dynamical models of supernovae in one spatial dimension. We employ a newly developed algorithm for radiation-hydrodynamics, which gives a full solution to the neutrino transport problem using the Feautrier technique, the tangent-ray method, and Accelerated Lambda Iteration. The code very good angular and spectral resolution of the radiation field. In addition, we have incorporated realistic neutrino microphysics and explored the effects of nucleon-nucleon bremsstrahlung and inelastic neutrino-electron scattering. Our algorithm for incorporating the latter explicitly as a source and a sink in the collision term of the Boltzmann equation is both efficient and robust (see §4.4 & §B.3.1). We have coupled this scheme for radiation transport to an explicit Lagrangean algorithm for Newtonian hydrodynamics, which uses artificial viscosity for shock resolution. Finally, we have constructed and tested an efficient tabular version of the Lattimer-Swesty high-density nuclear equation of state. We have verified the thermodynamic consistency of our implementation and have explored the effects of modifications to this EOS on the emergent neutrino signature and collapse dynamics.

With this tool we have computed the collapse, bounce, and post-bounce evolution of a variety of progenitors. We have varied the microphysics employed and conducted a series of resolution studies for code verification. Also, we have compared key quantities such as core entropy and electron fraction at bounce, peak neutrino breakout luminosity, and the evolution of the neutrino spectra over hundreds of milliseconds with other recent supernova simulations that employ comparably sophisticated algorithms. We evolve most models to several hundred milliseconds after bounce and although all of our models form regions of net neutrino heating behind the shock, none yield explosions in the first 250 milliseconds.

Finally, we have folded our neutrino spectra with the sensitivities and thresholds of several terrestrial underground neutrino detectors. We have focused on those detectors most likely to observe and uniquely identify the electron-neutrino breakout burst. We find that SuperKamiokande, the Sudbury Neutrino Observatory, and the ICARUS detector might all see this signature of core collapse.

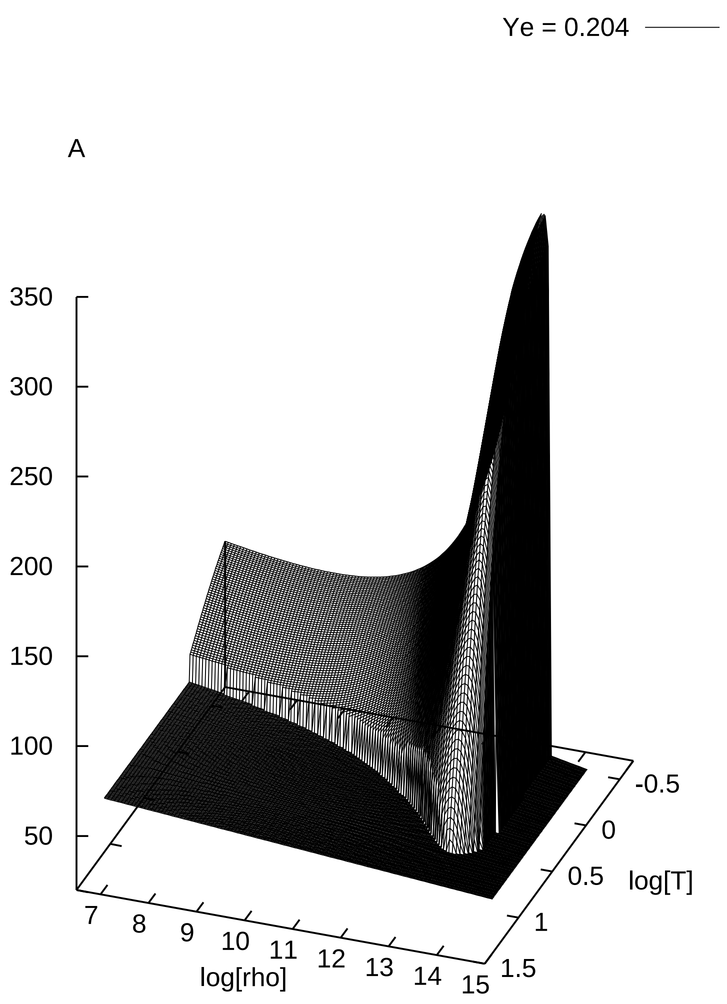

FIGURE 4.1. The atomic mass (A) of the representative heavy nucleus as a function of $\log_{10}\rho$ and $\log_{10}T$ in our tabular version of the Lattimer-Swesty nuclear equation of state for $Y_e = 0.49$. Note the phase transition between heavy nuclei and free nucleons.

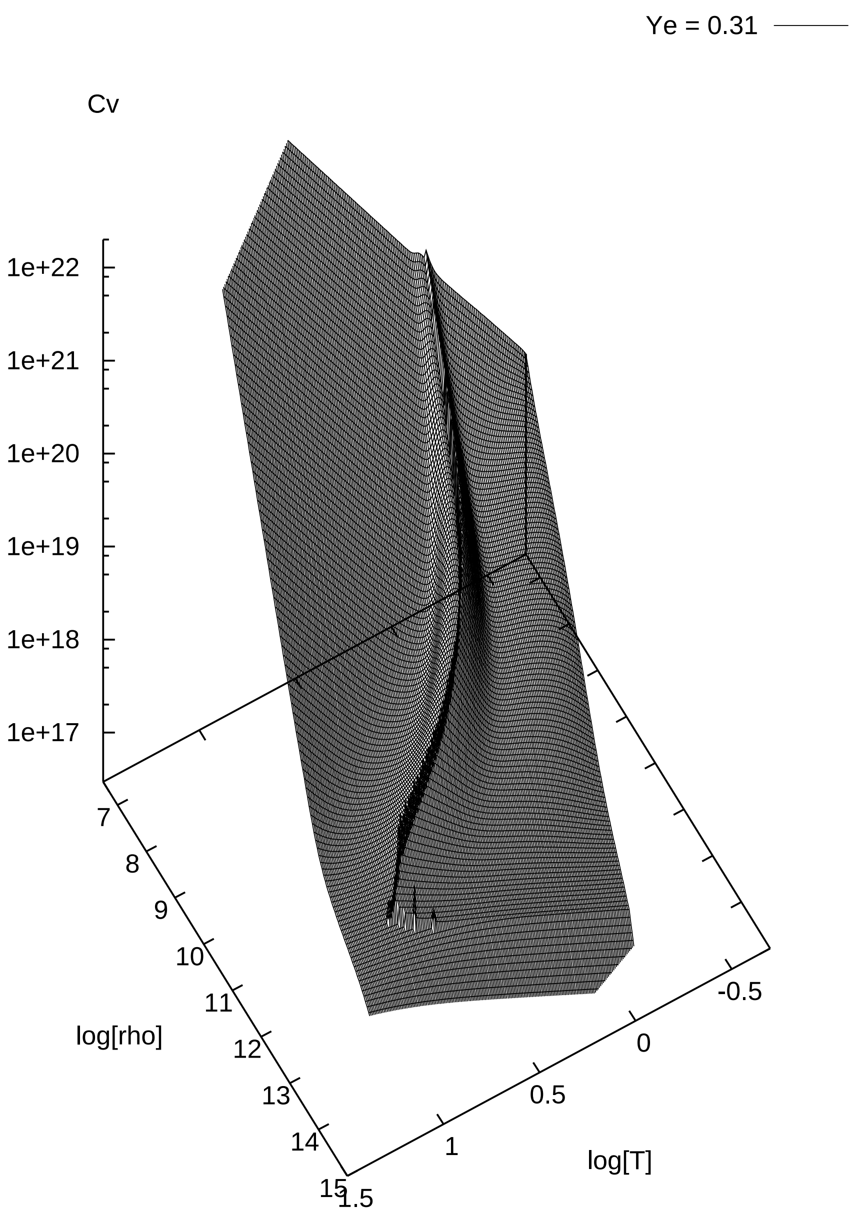

FIGURE 4.2. The specific heat (C_V) as a function of $\log_{10}\rho$ and $\log_{10}T$ in our tabular version of the Lattimer-Swesty nuclear equation of state for $Y_e = 0.10$. Note the phase transition between heavy nuclei and free nucleons. Also note the critical point at high temperatures and densities at the point of inflection in the ridge of C_V along the phase transition.

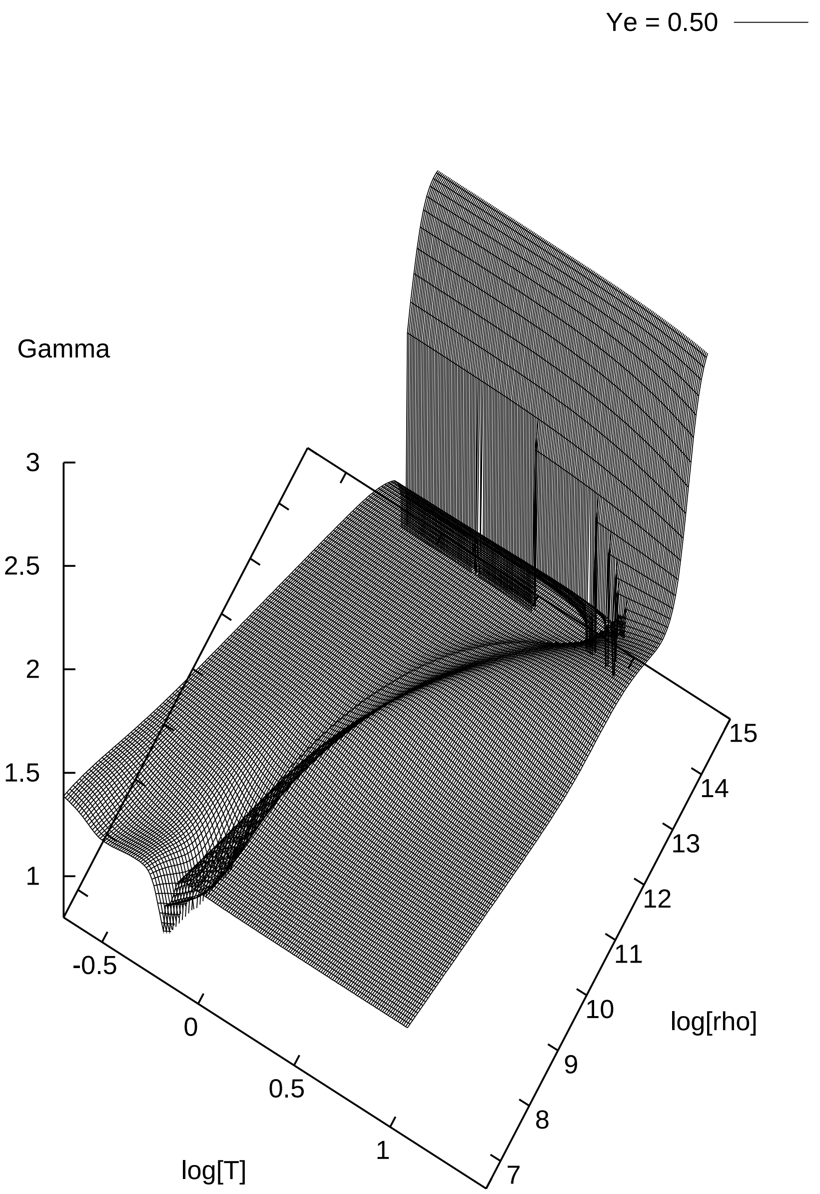

FIGURE 4.3. Gamma ($\Gamma_s = d\ln P/d\ln\rho|_s$) as a function of $\log_{10}\rho$ and $\log_{10}T$ in our tabular version of the Lattimer-Swesty nuclear equation of state for $Y_e = 0.50$. Note that Γ_s as returned by the Lattimer-Swesty EOS drops below 1, an unphysical value, at several points along the phase transition, particularly at high densities, right before the EOS stiffens significantly.

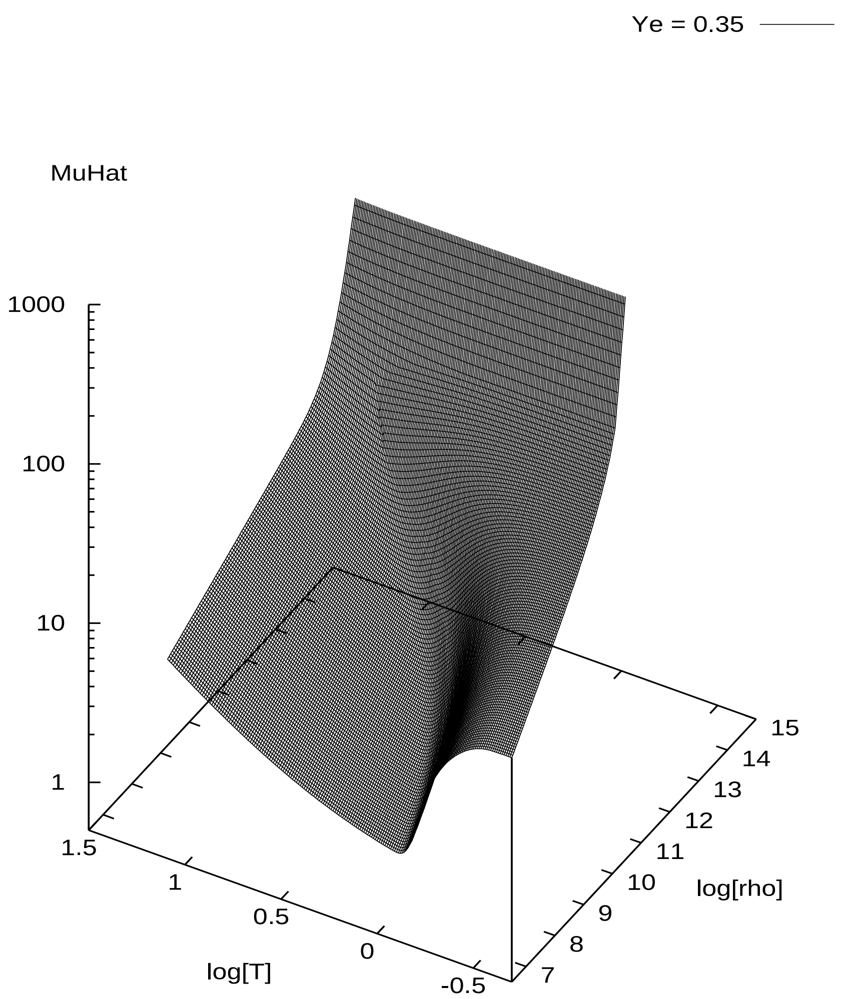

FIGURE 4.4. Muhat ($\hat{\mu} = \mu_n - \mu_p$) as a function of $\log_{10} \rho$ and $\log_{10} T$ in our tabular version of the Lattimer-Swesty nuclear equation of state for $Y_e = 0.42$.

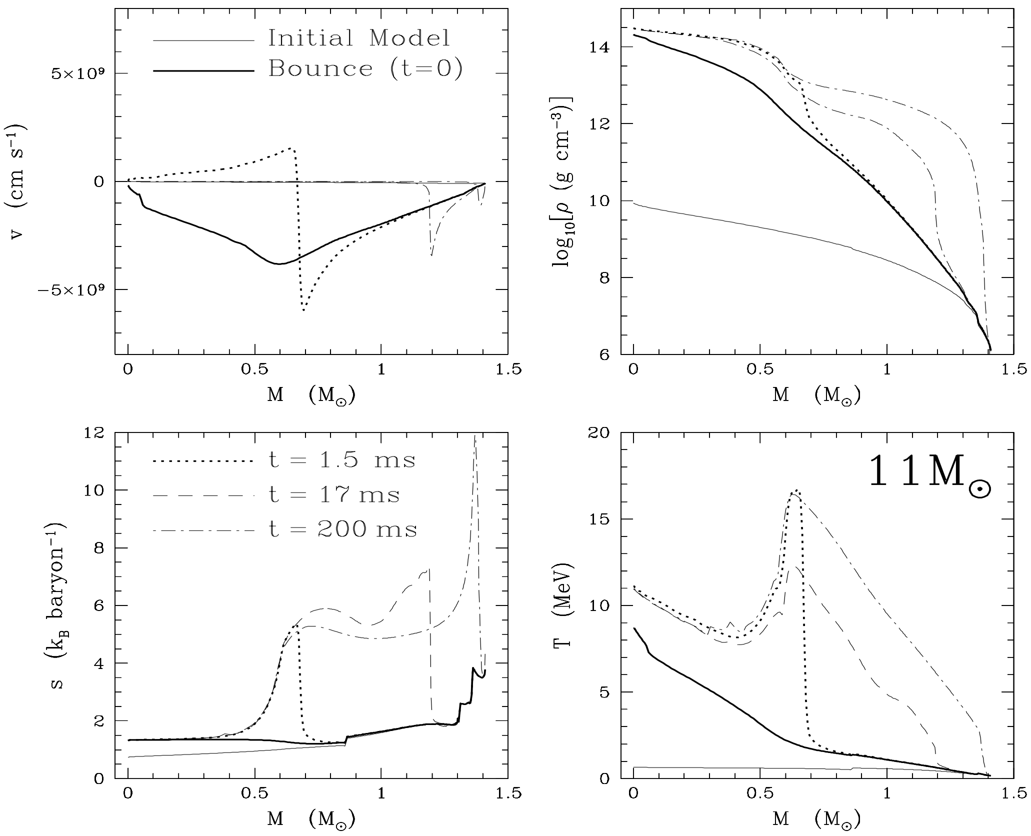

FIGURE 4.5. Velocity v (in cm s^{-1}, upper left panel), $\log_{10}[\rho]$ (in g cm^{-3}, upper right panel), entropy s (in k$_B$ baryon^{-1}, lower left panel), and temperature T (in MeV, lower right panel) in the 11M$_\odot$ progenitor, as a function of mass coordinate in M$_\odot$ for five snapshots in time. The thin solid line shows the initial configuration and the thick solid line shows the model at bounce. The dotted, dashed, and dot-dashed lines are snapshots at 1.5 ms, 17 ms, and 200 ms after bounce, respectively.

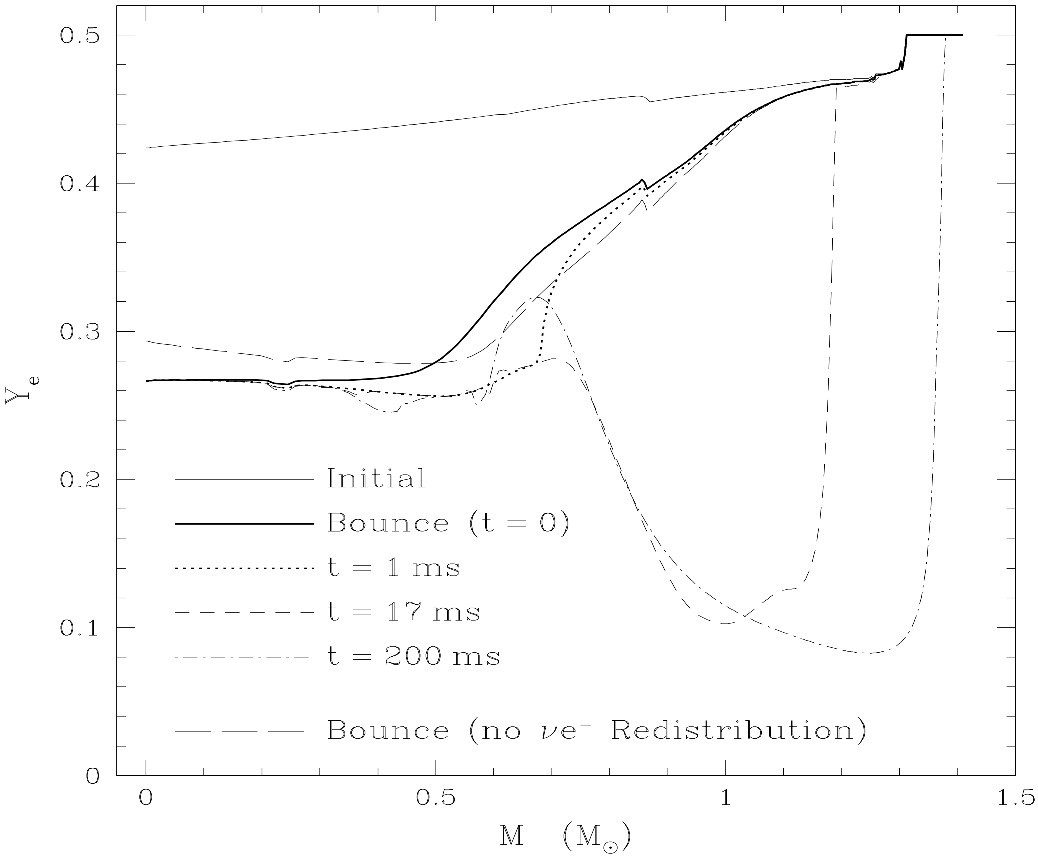

FIGURE 4.6. The electron fraction Y_e in the $11M_\odot$ progenitor, as a function of mass coordinate in $M_\odot$ for five snapshots in time. The thin solid line shows the initial configuration and the thick solid line shows the model at bounce. The dotted, short-dashed, and dot-dashed lines are snapshots at 1 ms, 17 ms, and 200 ms after bounce, respectively. For comparison, we include the bounce Y_e profile with inelastic neutrino-electron redistribution turned off (long dashed line). Compare this figure with Fig. (4.5), which shows the basic hydrodynamical evolution for this same model.

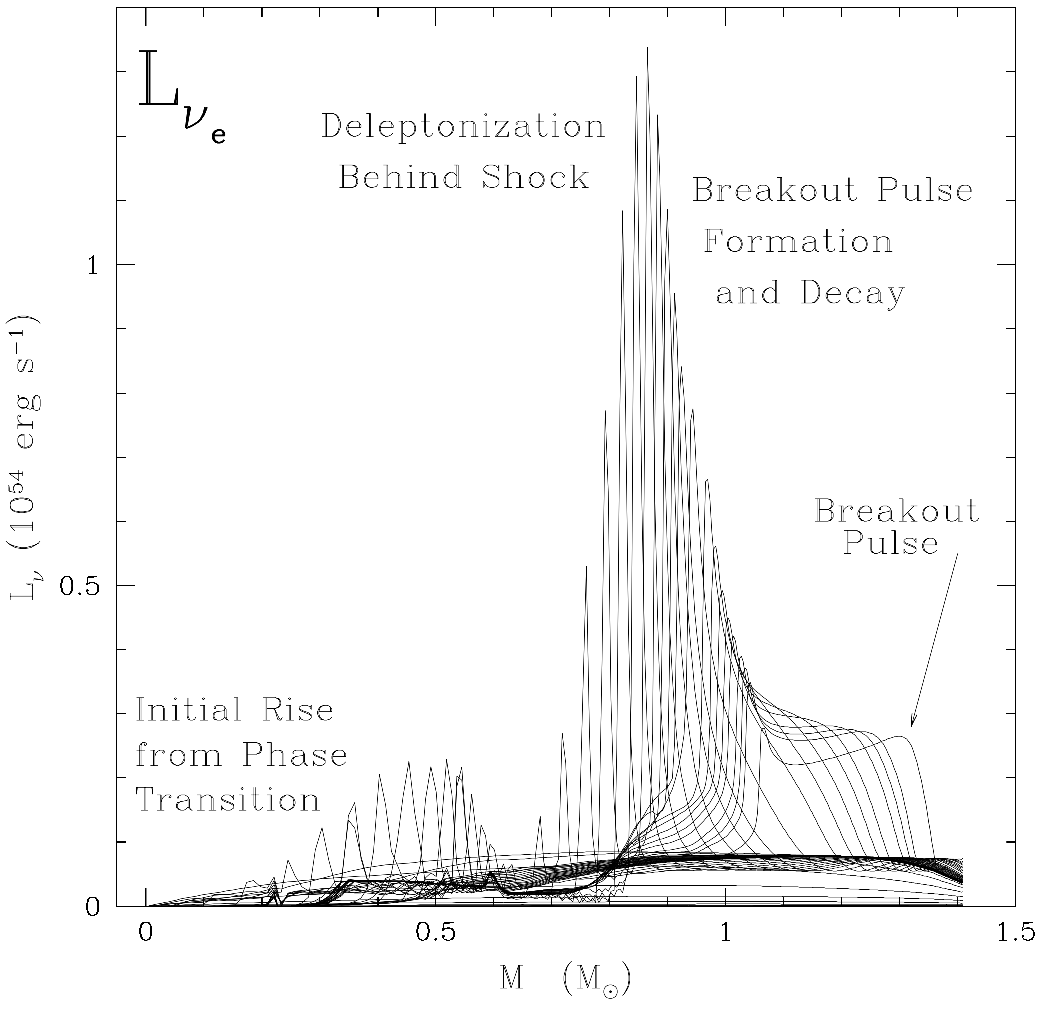

FIGURE 4.7. Snapshots of L_{ν_e} in 10^{54} erg s^{-1} as a function of mass for the fiducial M= 11 $M_\odot$ progenitor, showing the whole envelope of luminosities realized in this progenitor from bounce through electron-neutrino breakout. For comparison, the line labelled 'Breakout Pulse' is identical with that in Fig. 4.8. The initial rise in L_{ν_e} at $\sim 0.3\,M_\odot$ comes from electron capture on newly liberated free protons before the shock forms, but just after hydrodynamical bounce. The second, larger peak forms after shock formation. The temperature and density increase across the shock dissociates nuclei into free nucleons. Subsequent electron capture on free protons generates the breakout pulse, which reaches $L_{\nu_e} \sim 1.5 \times 10^{54}$ erg s^{-1} locally.

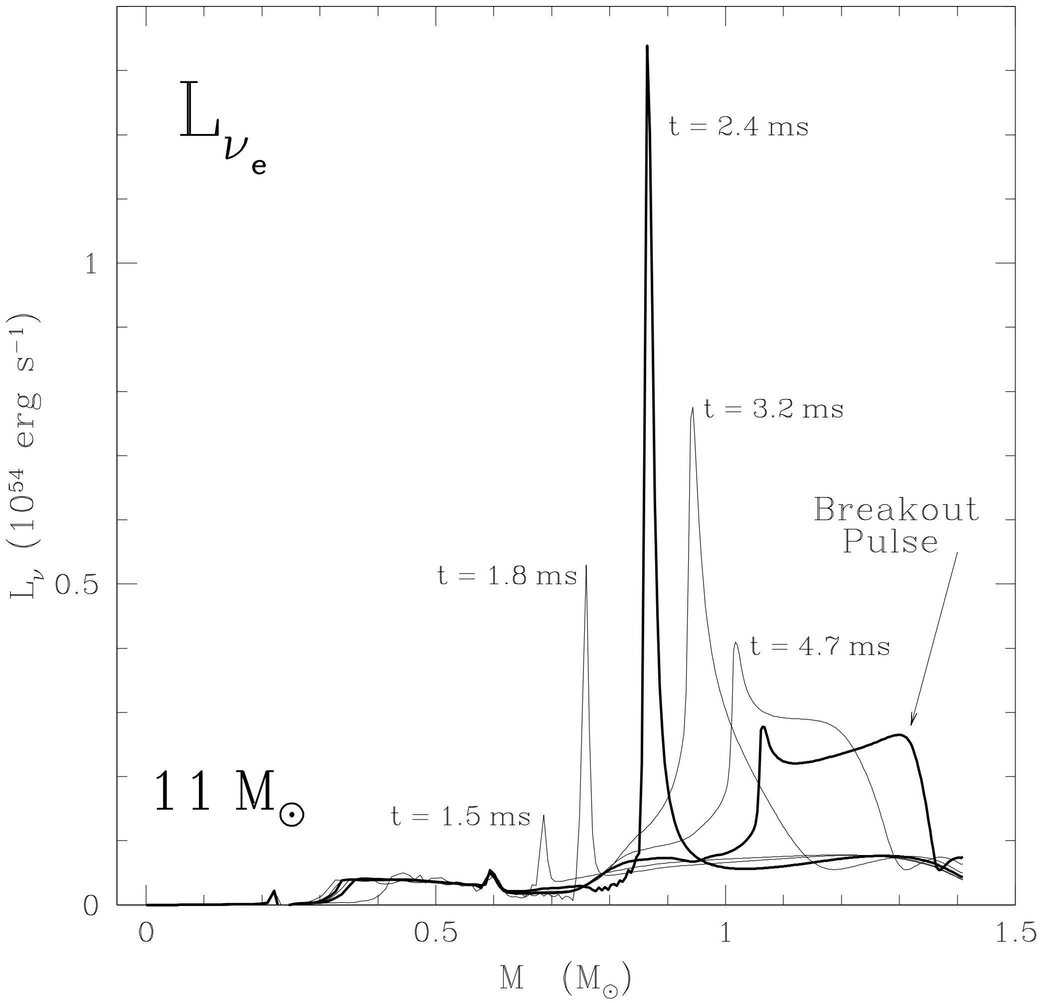

FIGURE 4.8. Snapshots of L_{ν_e} in erg s^{-1} as a function of mass for the fiducial M= 11 $M_\odot$ progenitor. Time is measured relative to bounce. Compare with Fig. 4.7, which shows more snapshots for the same model.

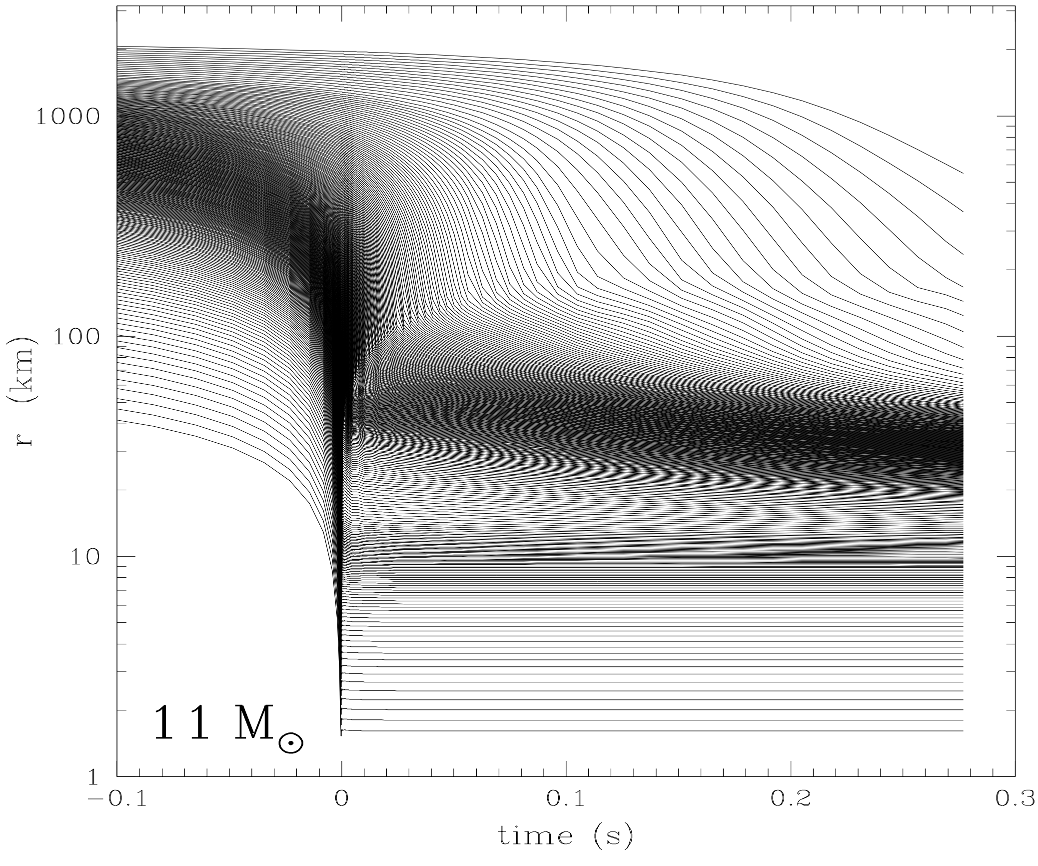

FIGURE 4.9. The radial position (in km) of selected mass shells as a function of time in our fiducial $11 M_\odot$ model.

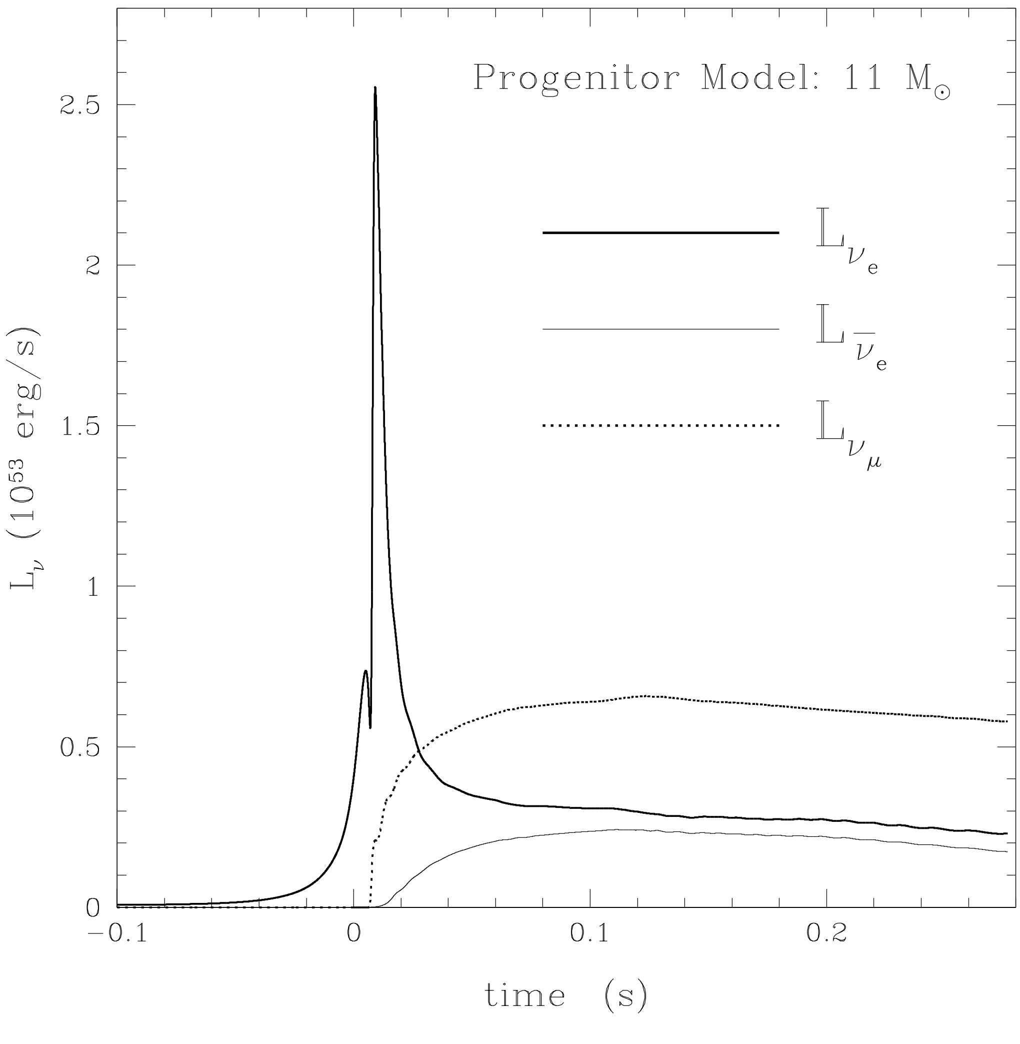

FIGURE 4.10. L_{ν_e} (thick solid line), $L_{\bar{\nu}_e}$ (thin solid line), and L_{ν_μ} (dotted line) measured at the outer edge of the grid in erg s^{-1} as a function of time for the fiducial M= 11 $M_\odot$ progenitor. Time is measured relative to bounce. Note that we define $t = 0$ as the time of hydrodynamical bounce. The finite light travel-time to the edge of the grid creates a $\sim$ 7 ms offset between hydrodynamical bounce and the initial dip before the large ν_e breakout pulse.

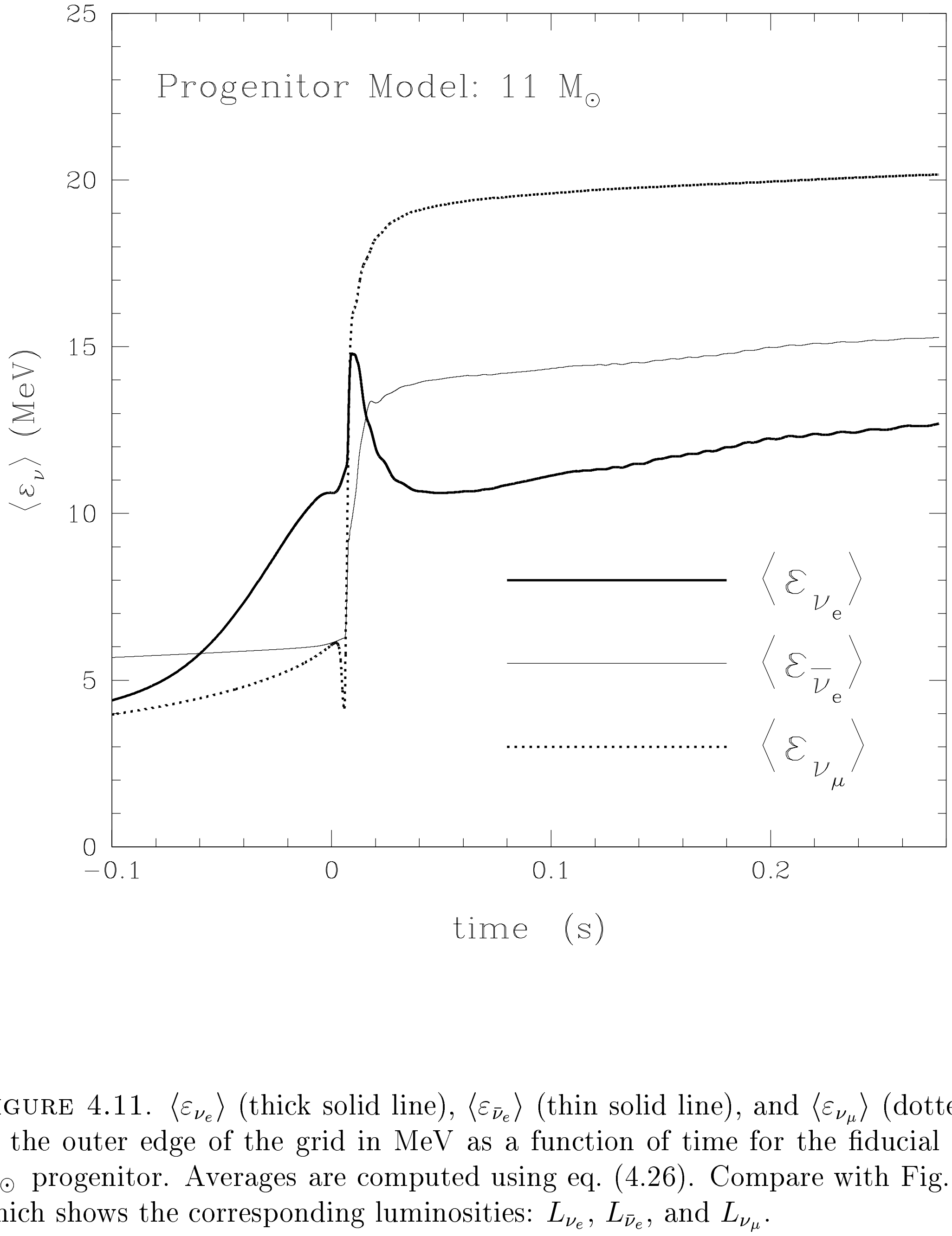

FIGURE 4.11. $\langle\varepsilon_{\nu_e}\rangle$ (thick solid line), $\langle\varepsilon_{\bar{\nu}_e}\rangle$ (thin solid line), and $\langle\varepsilon_{\nu_\mu}\rangle$ (dotted line) at the outer edge of the grid in MeV as a function of time for the fiducial M= 11 $M_\odot$ progenitor. Averages are computed using eq. (4.26). Compare with Fig. (4.10), which shows the corresponding luminosities: L_{ν_e}, $L_{\bar{\nu}_e}$, and L_{ν_μ}.

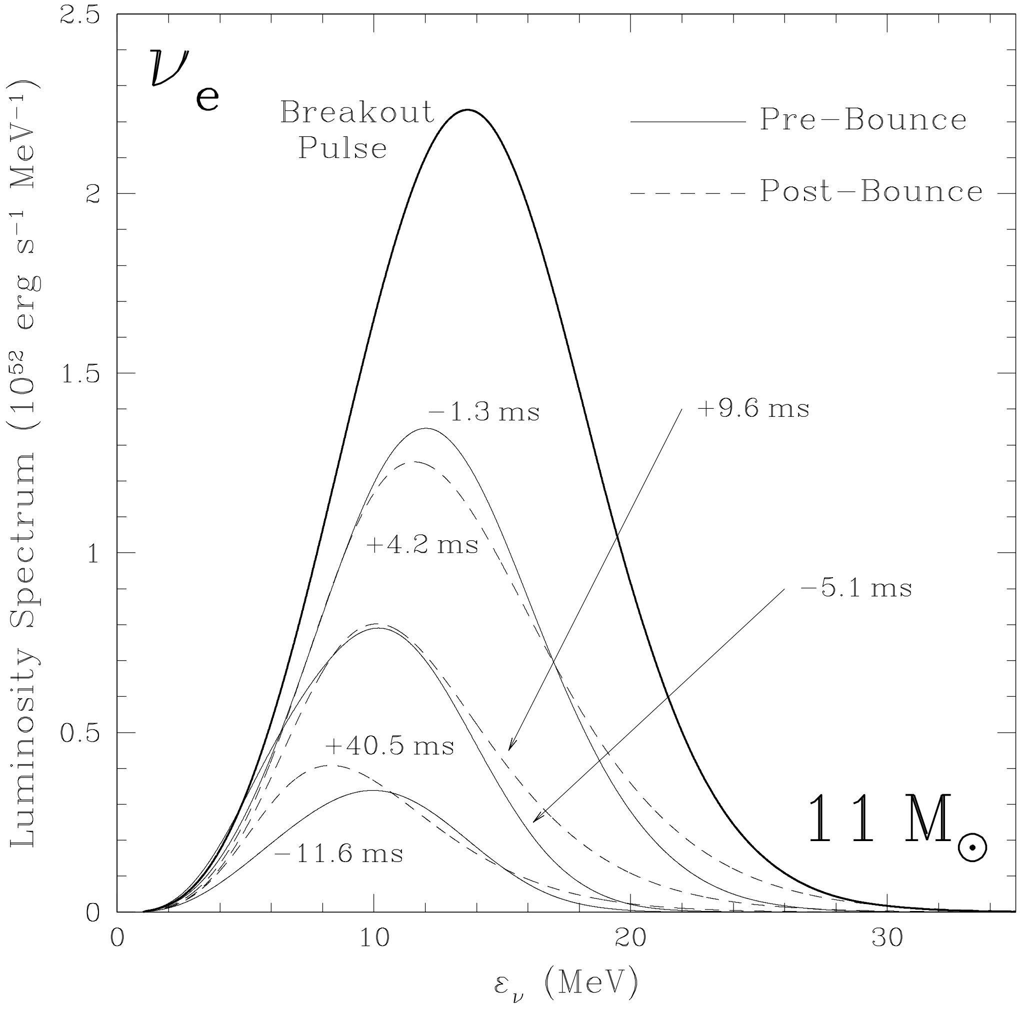

FIGURE 4.12. Luminosity spectrum of ν_e neutrinos at infinity at various pre- (thin solid lines) and post-breakout (dashed lines) times. In this figure, time is measured relative to the peak breakout spectrum (thick solid line). The thin solid lines correspond to 11.6, 5.1, and 1.3 ms before the peak and the dashed lines denote the ν_e spectrum 4.2, 9.6, and 40.5 ms after the peak.

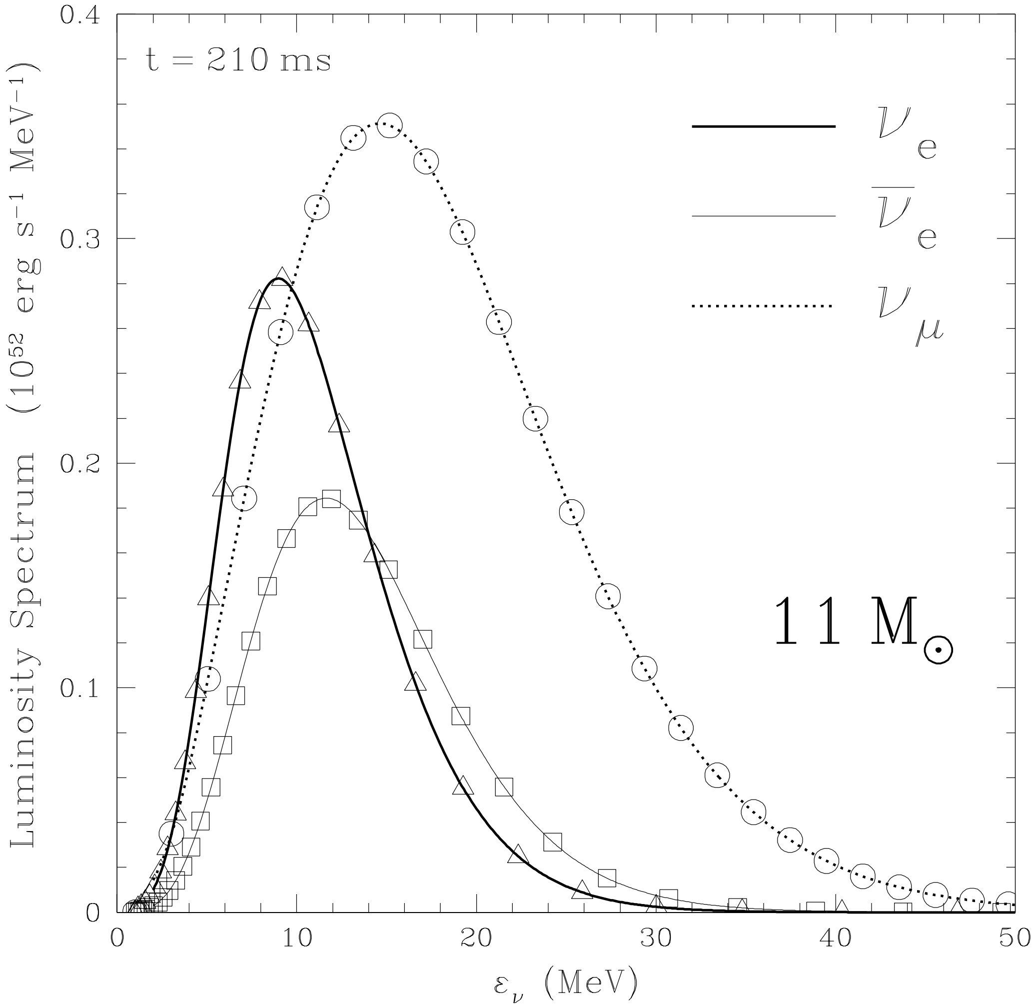

FIGURE 4.13. Luminosity spectrum of ν_e (thick solid line), $\bar{\nu}_e$ (thin solid line), and ν_μ neutrinos (dotted line) at infinity at $t = 210\,\mathrm{ms}$ after bounce. The actual energy groups are denoted by triangles, squares, and circles for ν_e, $\bar{\nu}_e$, and ν_μ neutrinos, respectively.

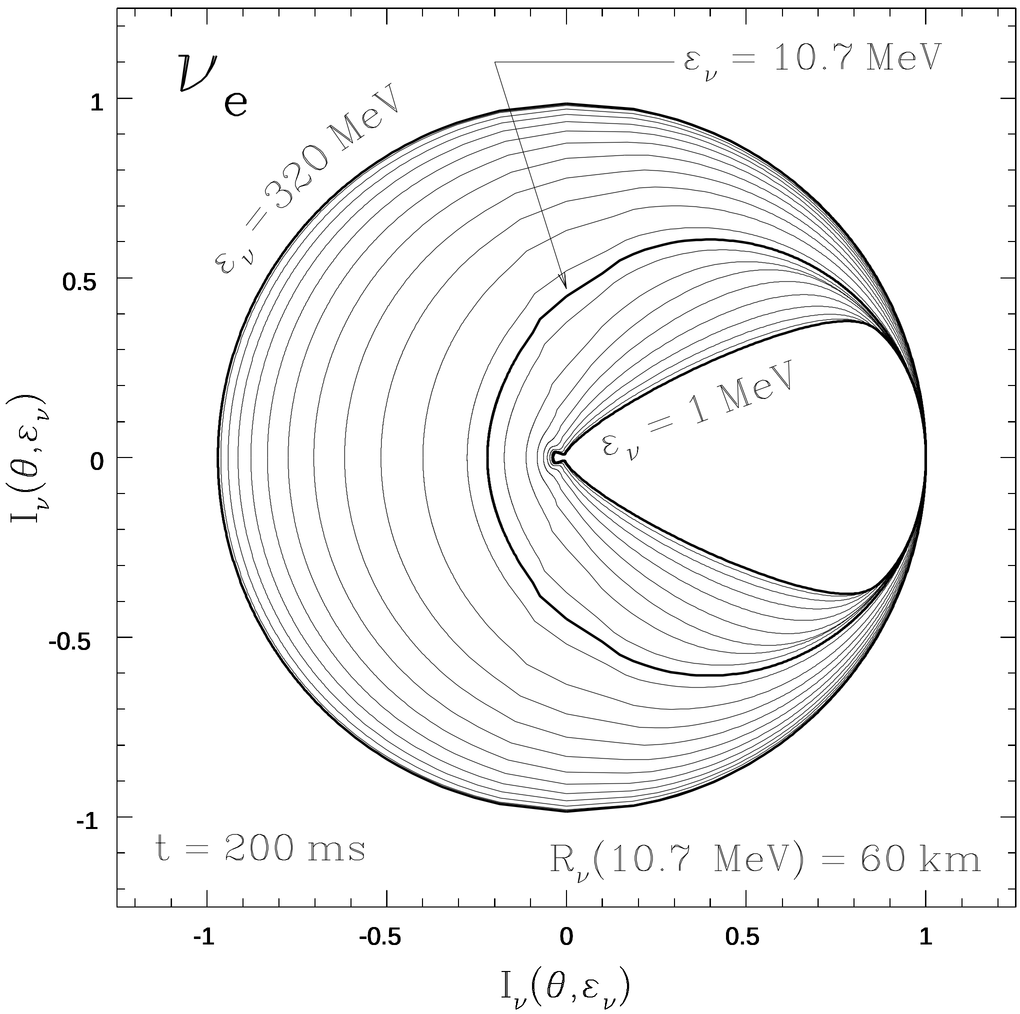

FIGURE 4.14. Polar plot of the normalized specific intensity, constructed from the Feautrier variables at the neutrinosphere for $\varepsilon_\nu \simeq 10.7$ MeV for ν_e neutrinos. This plot shows only every other energy grid point (solid lines). There are 269 angular bins in each quadrant. At the largest energies, the radiation field is nearly isotropic and the flux is quite small. At the lowest energies, the radiation field is beginning to decouple from the matter and I_ν is forward-peaked.

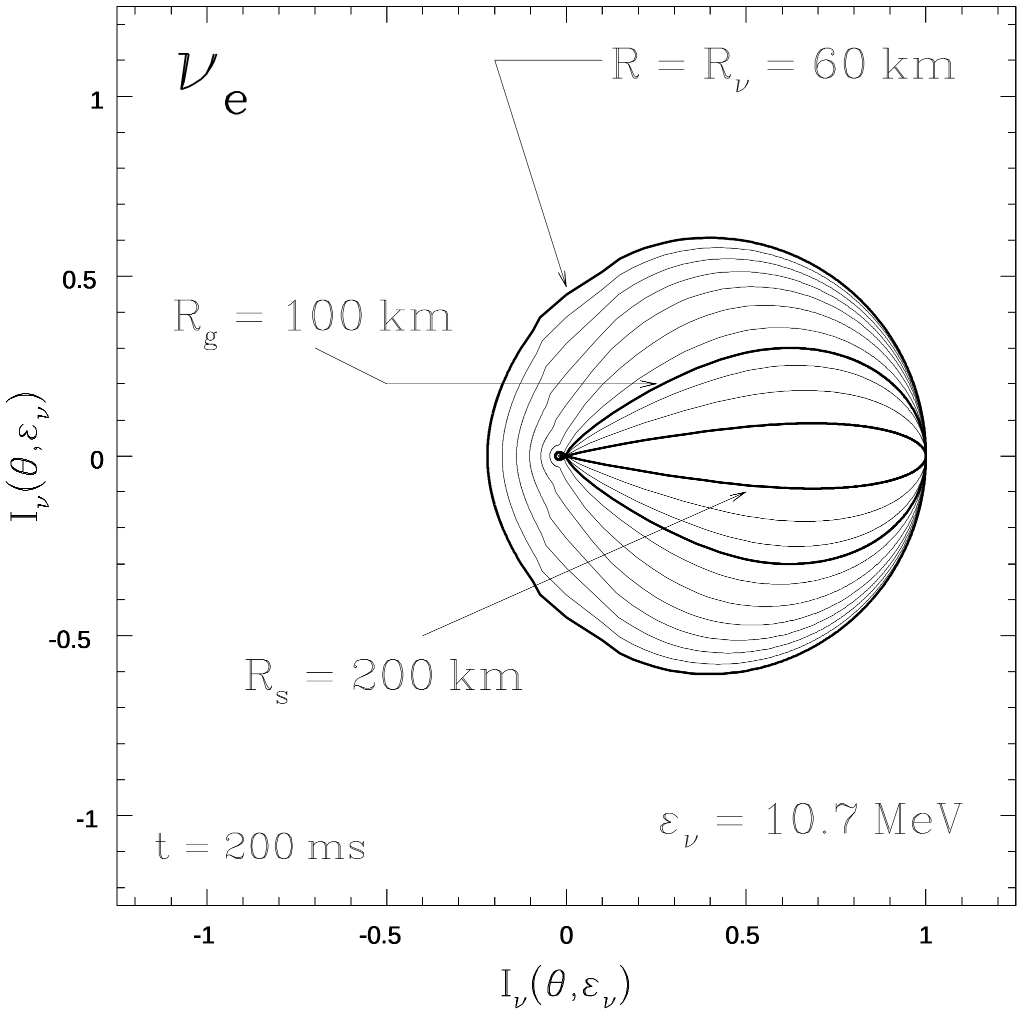

FIGURE 4.15. Polar plot of the specific intensity (I_{ν_e}) as a function of θ for ν_e neutrinos with $\varepsilon_\nu = 10.7$ MeV at selected radii. We maintain the same scale as in Fig. 4.14 for the line labelled '60 km' and normalize the absolute value I_ν for all other radii to that reference I_ν. Thick solid lines denote $I_{\nu_e}(\theta, \varepsilon_\nu = 10.7\,\mathrm{MeV})$ at the neutrinosphere ($R_\nu \simeq 60\,\mathrm{km}$), at the gain radius ($R_g \simeq 100\,\mathrm{km}$), and at the shock radius ($R_s \simeq 200\,\mathrm{km}$) 200 ms after bounce. Thin solid lines show the specific intensity at various intermediate radii.

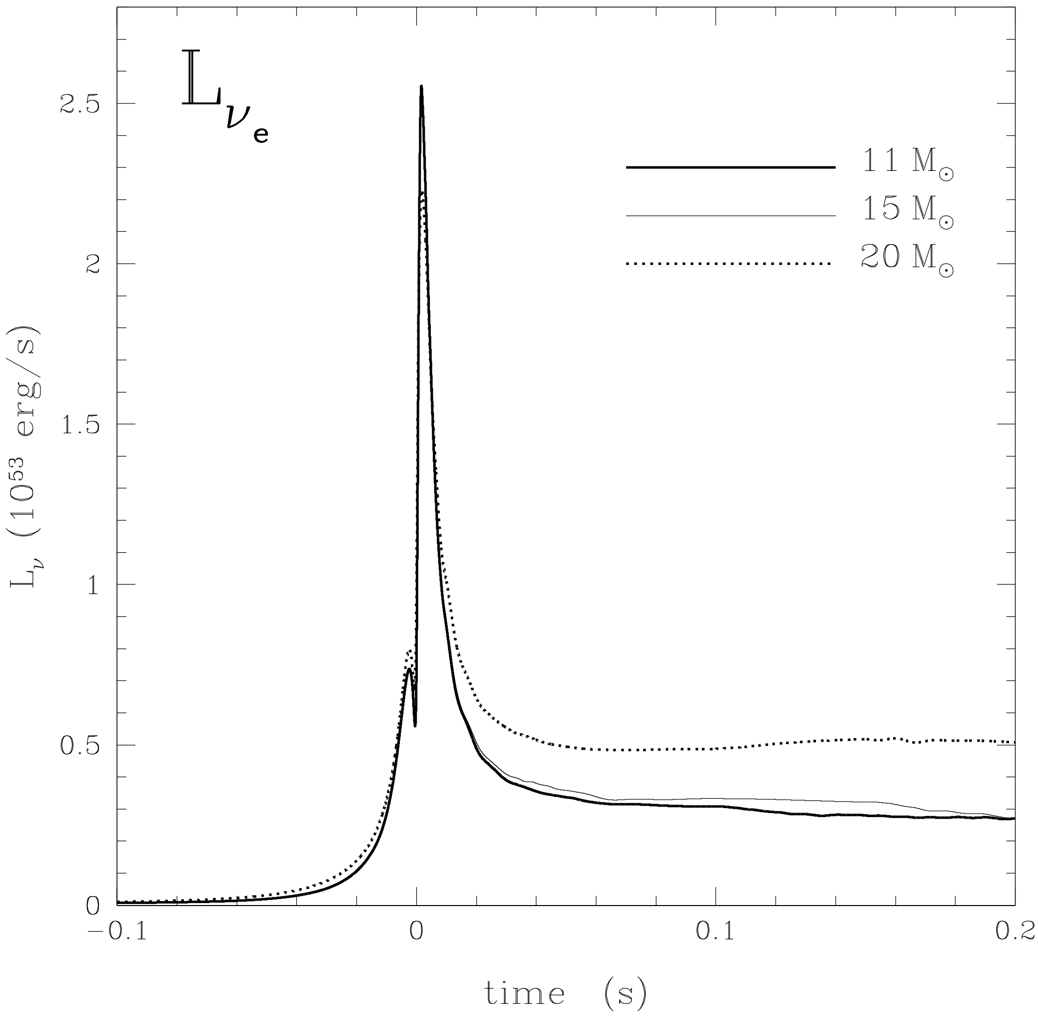

FIGURE 4.16. Electron neutrino luminosity (L_{ν_e}) measured at ~ 1500 km in erg s^{-1} as a function of time, for three different progenitors with masses M= 11 M$_\odot$ (thick solid line), M= 15 M$_\odot$ (thin solid line), and M= 20 M$_\odot$ (dotted line). Compare with Fig. 4.17, which shows $L_{\bar{\nu}_e}$ and L_{ν_μ} for the same models. Time is measured relative to the beginning of the 11M$_\odot$ model ν_e breakout pulse.

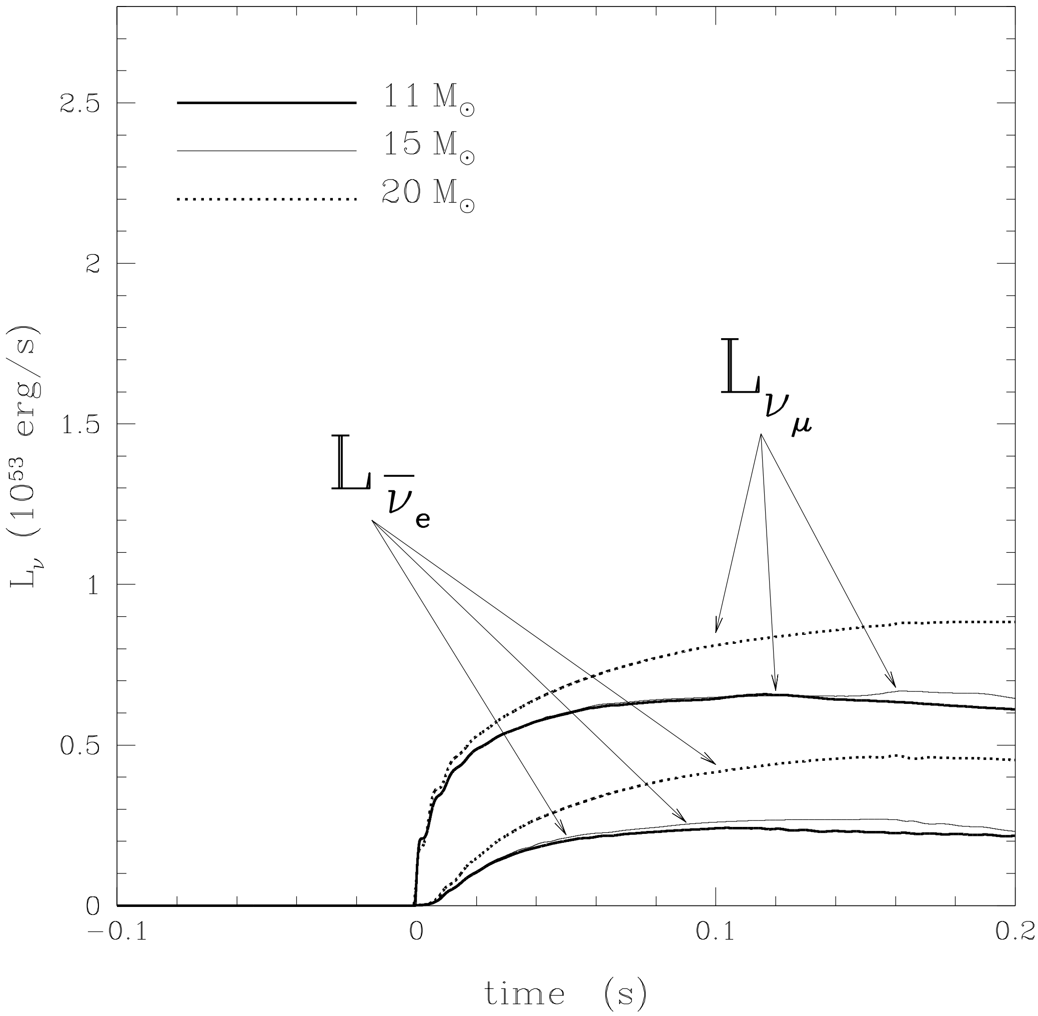

FIGURE 4.17. $L_{\bar{\nu}_e}$ and L_{ν_μ} in erg s^{-1} measured at ~ 1500 km as a function of time, for three different progenitors with masses M= 11 M$_\odot$ (thick solid line), M= 15 M$_\odot$ (thin solid line), and M= 20 M$_\odot$ (dotted line). Compare with Fig. 4.16, which shows L_{ν_e} for the same models.

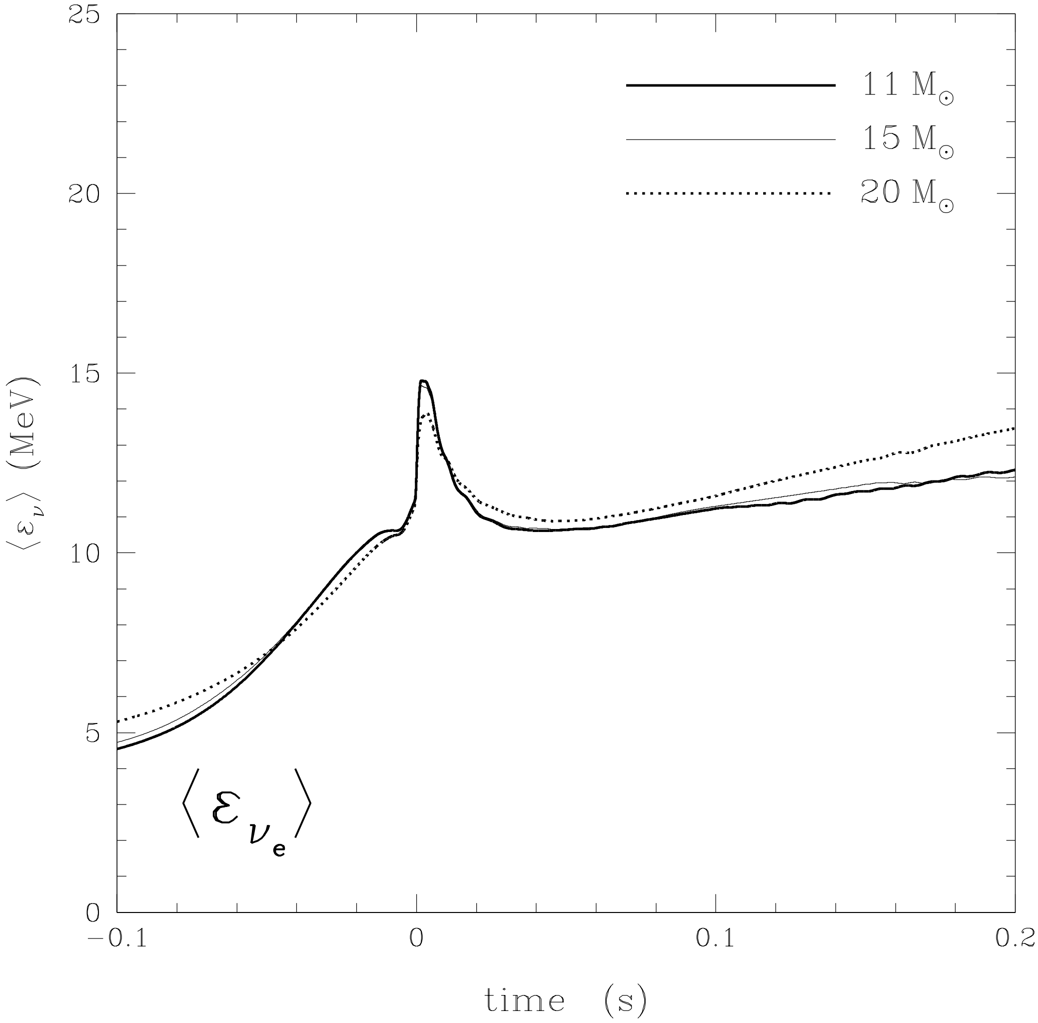

FIGURE 4.18. Electron neutrino average energy ($\langle \varepsilon_{\nu_e} \rangle$) of the emergent spectrum in MeV as a function of time, for three different progenitors with masses M= 11 $M_\odot$ (thick solid line), M= 15 $M_\odot$ (thin solid line), and M= 20 $M_\odot$ (dotted line). Compare with Fig. 4.16, which shows L_{ν_e} for the same models and Fig. 4.19, which shows $\langle \varepsilon_{\bar{\nu}_e} \rangle$ and $\langle \varepsilon_{\nu_\mu} \rangle$. Time is measured relative to the beginning of the 11$M_\odot$ model ν_e breakout pulse.

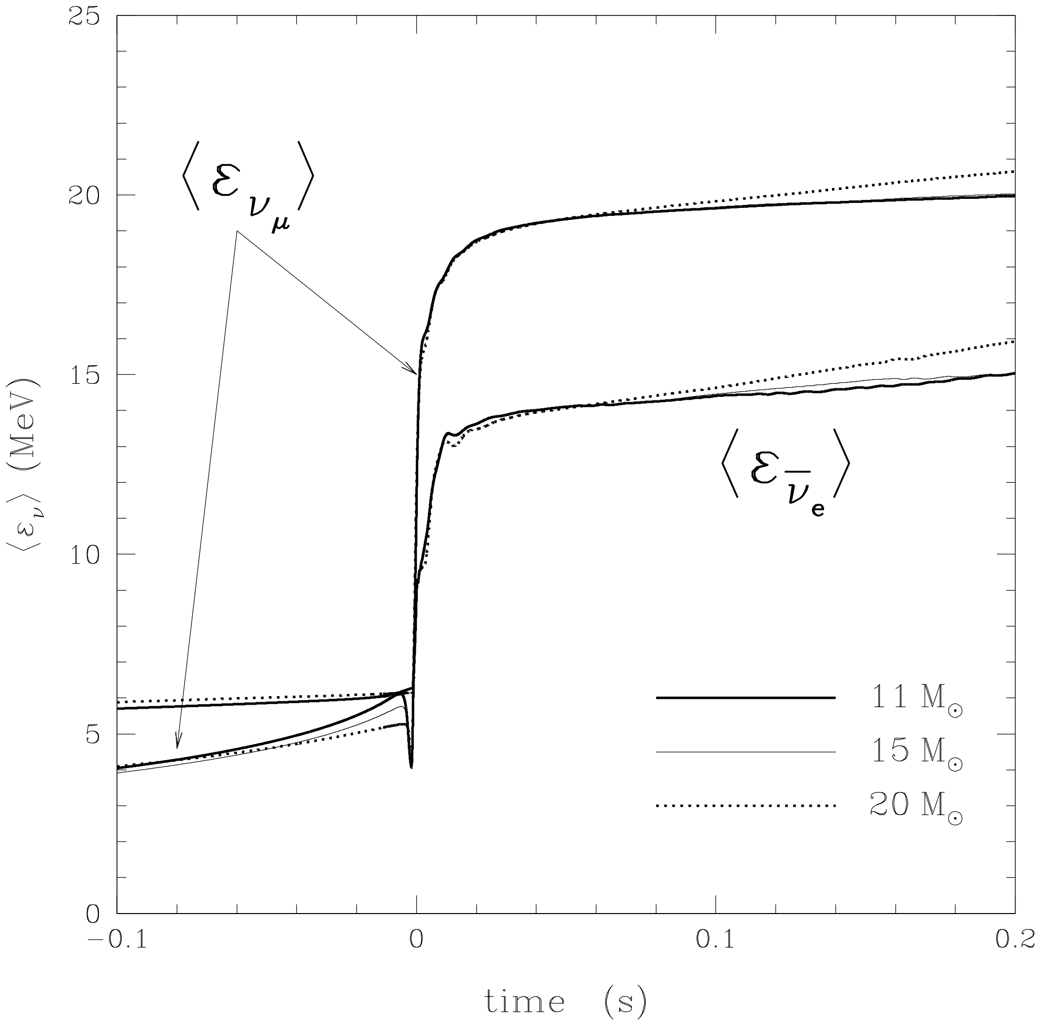

FIGURE 4.19. $\langle \varepsilon_{\nu_e} \rangle$ & $\langle \varepsilon_{\nu_\mu} \rangle$ of the emergent spectrum in MeV as a function of time, for three different progenitors with masses M= 11 $M_\odot$ (thick solid line), M= 15 $M_\odot$ (thin solid line), and M= 20 $M_\odot$ (dotted line). Compare with Figs. 4.17 and Fig. 4.18.

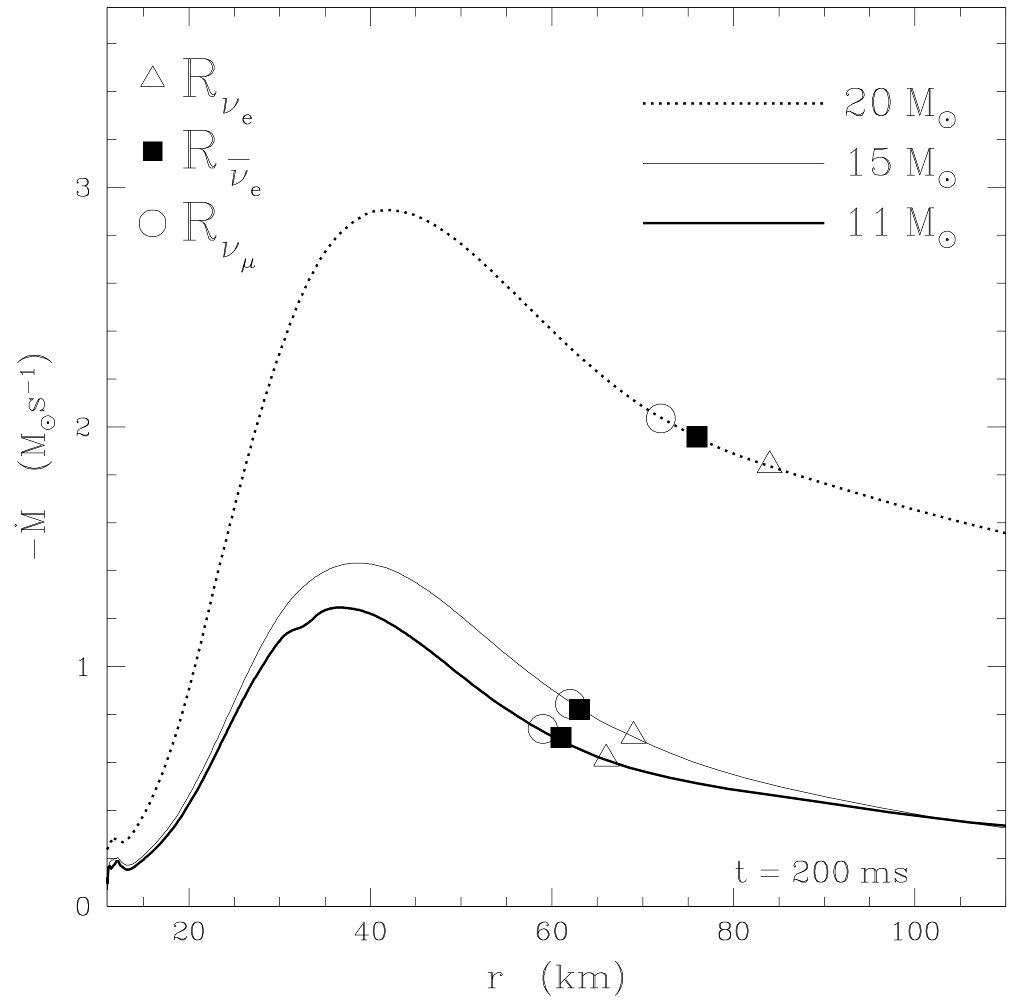

FIGURE 4.20. Mass flux $\dot{M}$ in $M_\odot$ s^{-1} as a function of radius for our $11M_\odot$ (thick solid line), $15M_\odot$ (thin solid line), and $20M_\odot$ (dotted line) models, all at 200 ms after bounce. Open triangles mark the ν_e neutrinosphere (R_{ν_e}) at $\langle\varepsilon_{\nu_e}\rangle \simeq 12$, 12, and 13.5 MeV for the $11M_\odot$, $15M_\odot$, and $20M_\odot$ model, respectively. Filled squares and open circles mark $R_{\bar{\nu}_e}(\langle\varepsilon_{\bar{\nu}_e}\rangle \simeq 15, 15, 16\,\mathrm{MeV})$ and $R_{\nu_\mu}(\langle\varepsilon_{\nu_\mu}\rangle \simeq 20, 20, 21\,\mathrm{MeV})$ for the $11M_\odot$, $15M_\odot$, and $20M_\odot$ models, respectively.

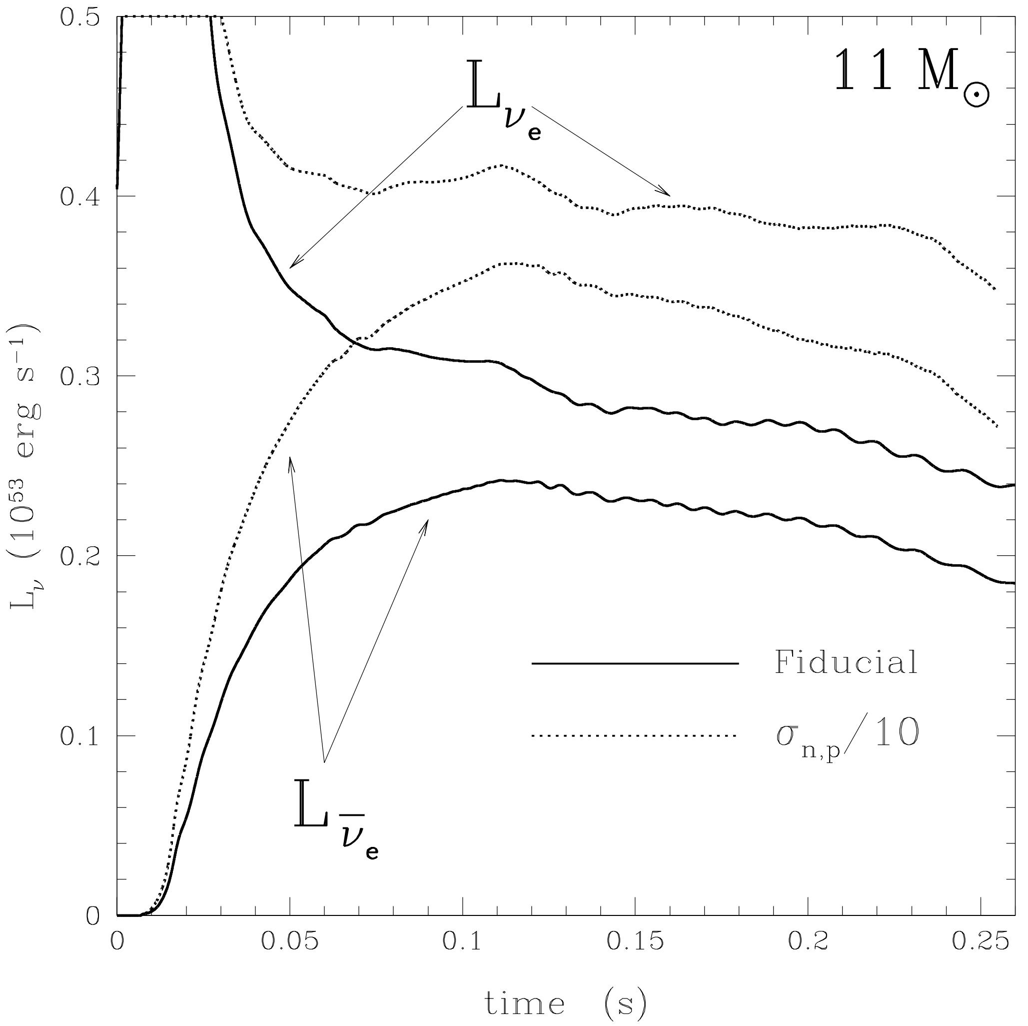

FIGURE 4.21. L_{ν_e} and $L_{\bar{\nu}_e}$ in erg s^{-1} at infinity as a function of time, for the fiducial model and for the model with artificially decreased neutral-current neutrino-neutron and neutrino-proton cross sections.

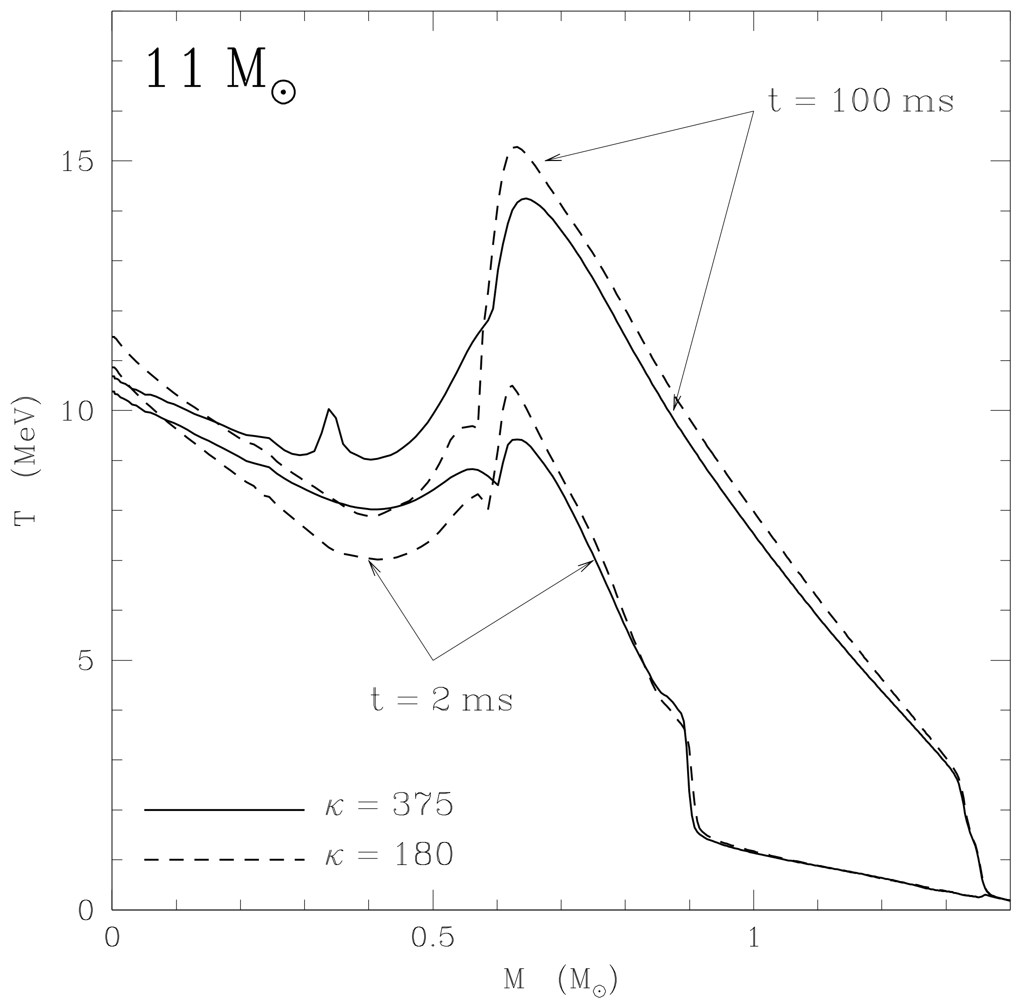

FIGURE 4.22. Temperature (T) in MeV as a function of mass coordinate in units of $M_\odot$ at two snapshots in time ($\sim$ 2 ms and $\sim$ 100 ms post-bounce) for the 11 $M_\odot$ progenitor, using two different nuclear compressibilities, $\kappa = 180$ (dashed lines) and $\kappa = 375$ (solid lines).

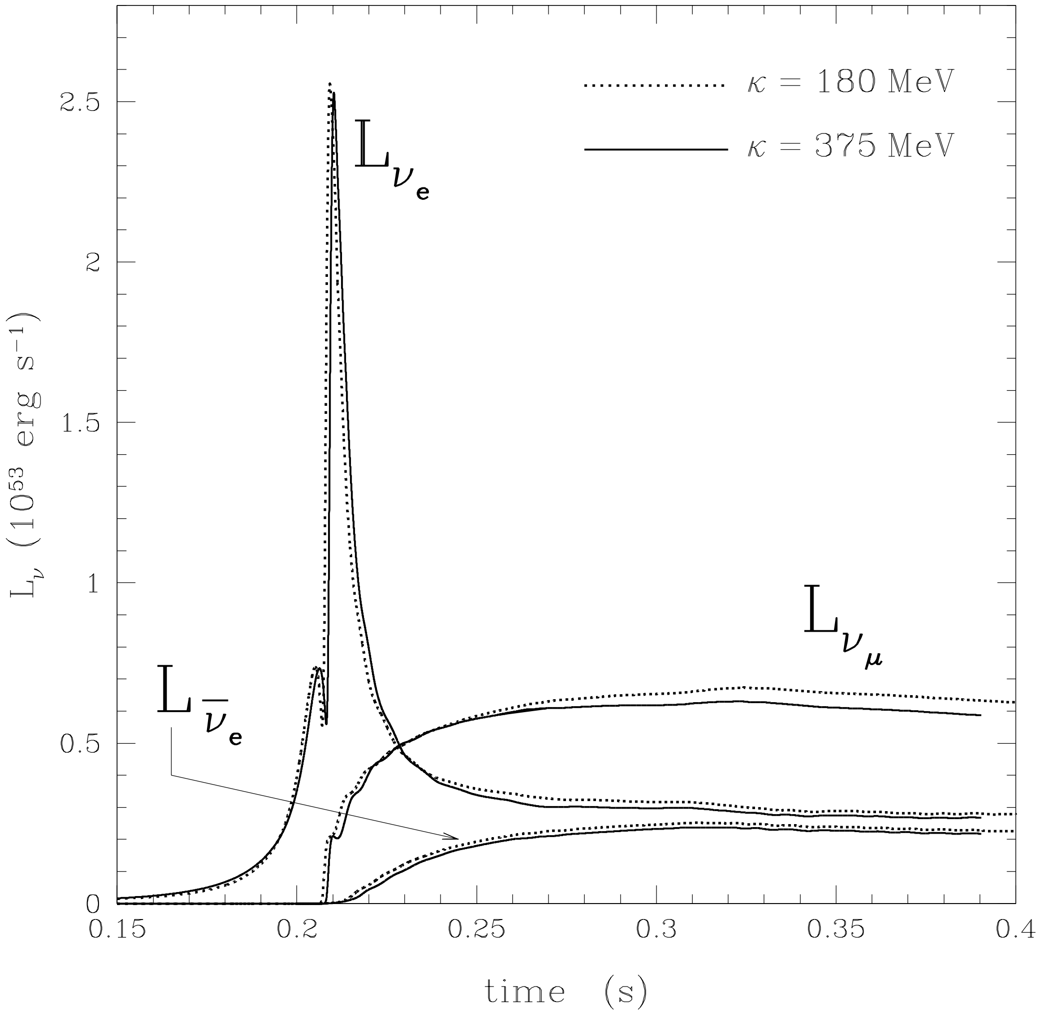

FIGURE 4.23. L_{ν_e}, $L_{\bar{\nu}_e}$, and L_{ν_μ} in units of 10^{53} erg s^{-1} at infinity for $\kappa = 180$ (dotted lines) and $\kappa = 375$ (solid lines).

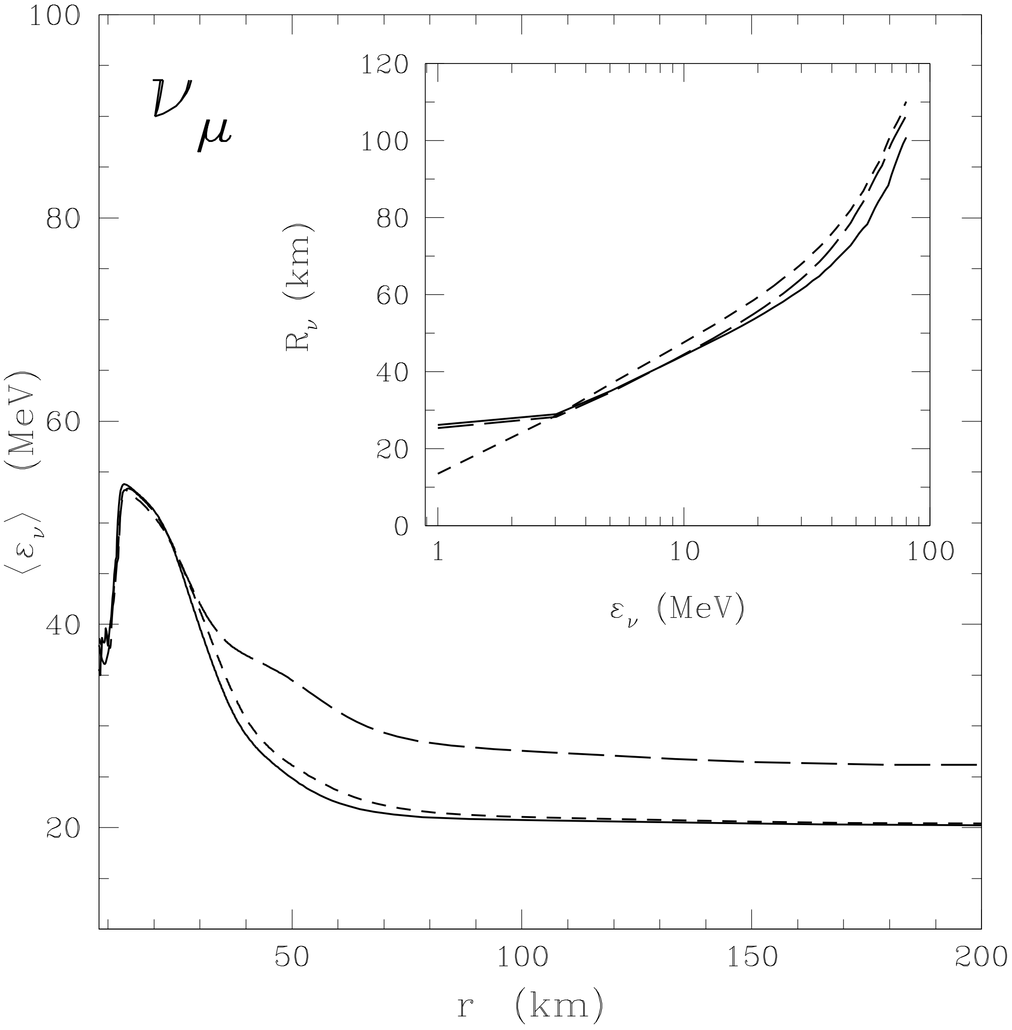

FIGURE 4.24. $\langle \varepsilon_{\nu_\mu} \rangle$ as a function of radius for $11\,M_\odot$ models with bremsstrahlung and inelastic neutrino-electron scattering (solid line), without bremsstrahlung and with inelastic neutrino-electron scattering (short dashed line), and with bremsstrahlung and without inelastic neutrino-electron scattering (long dashed line), approximately 220 ms after bounce. The inset shows the neutrinosphere R_{ν_μ}, defined by eq. (4.25) as a function of energy in the same models.

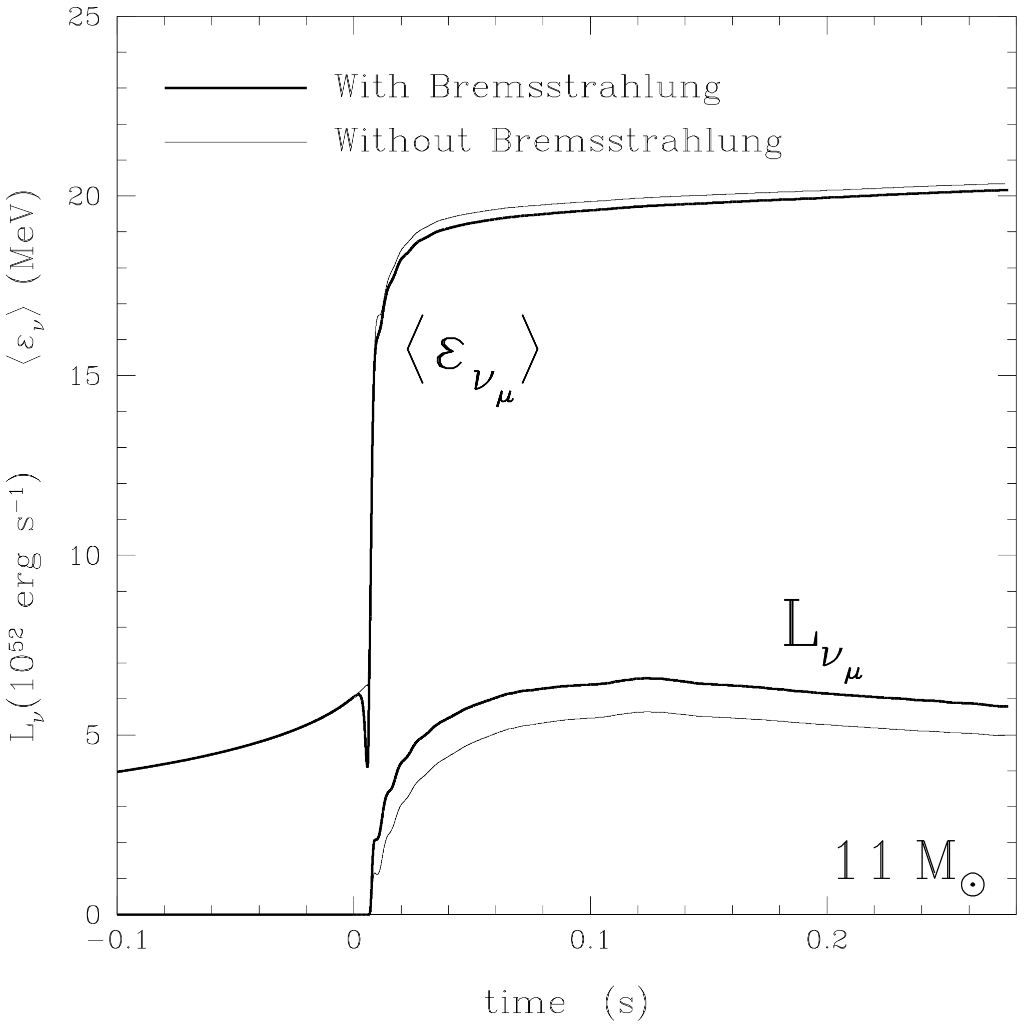

FIGURE 4.25. $\langle \varepsilon_{\nu_\mu} \rangle$ and L_{ν_μ} of the emergent spectrum at infinity as a function of time, for 11 $M_\odot$ models with (thick solid line) and without (thin solid line) nucleon-nucleon bremsstrahlung.

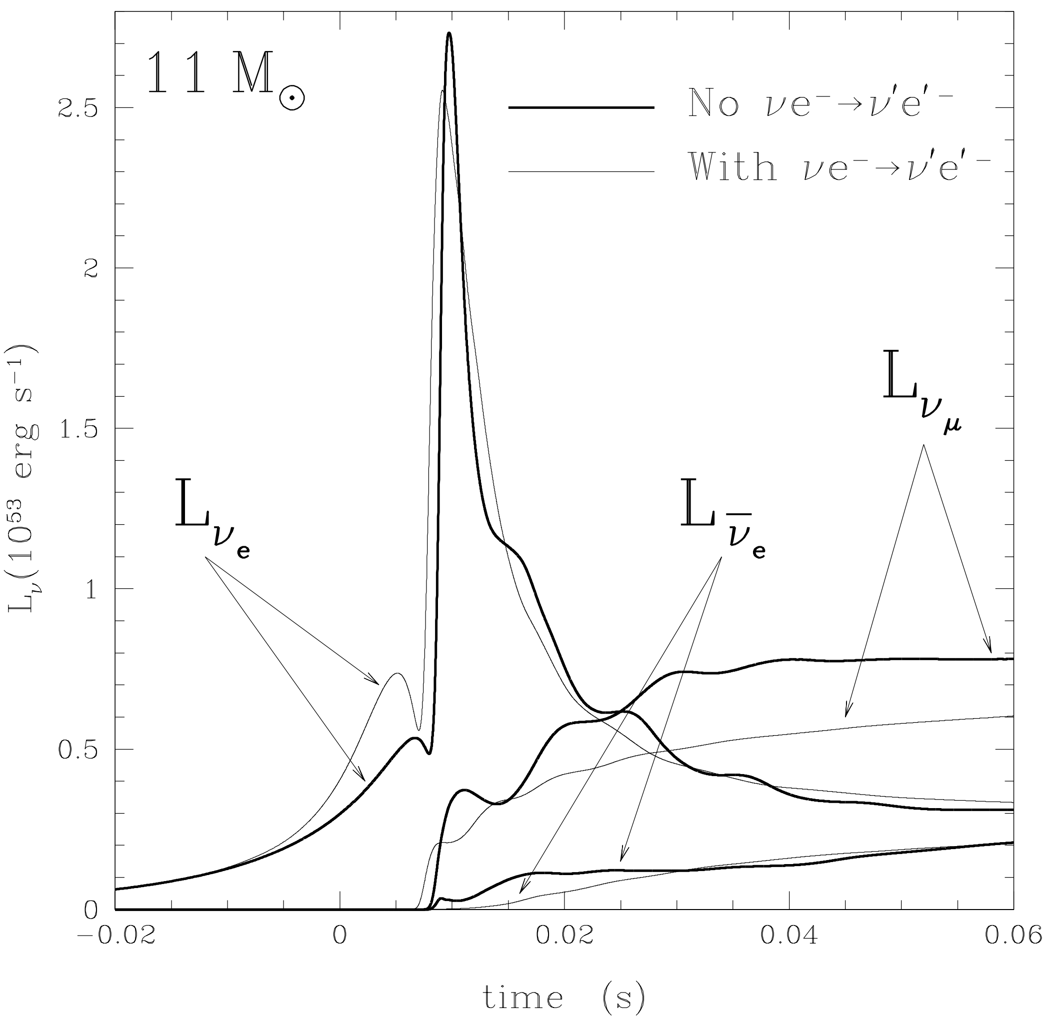

FIGURE 4.26. L_{ν_e}, $L_{\bar{\nu}_e}$, and L_{ν_μ} at infinity for the $11\,\mathrm{M}_\odot$ progenitor with (thick solid lines) and without (thin solid lines) inelastic neutrino-electron scattering as described in Appendix §B.3.1.

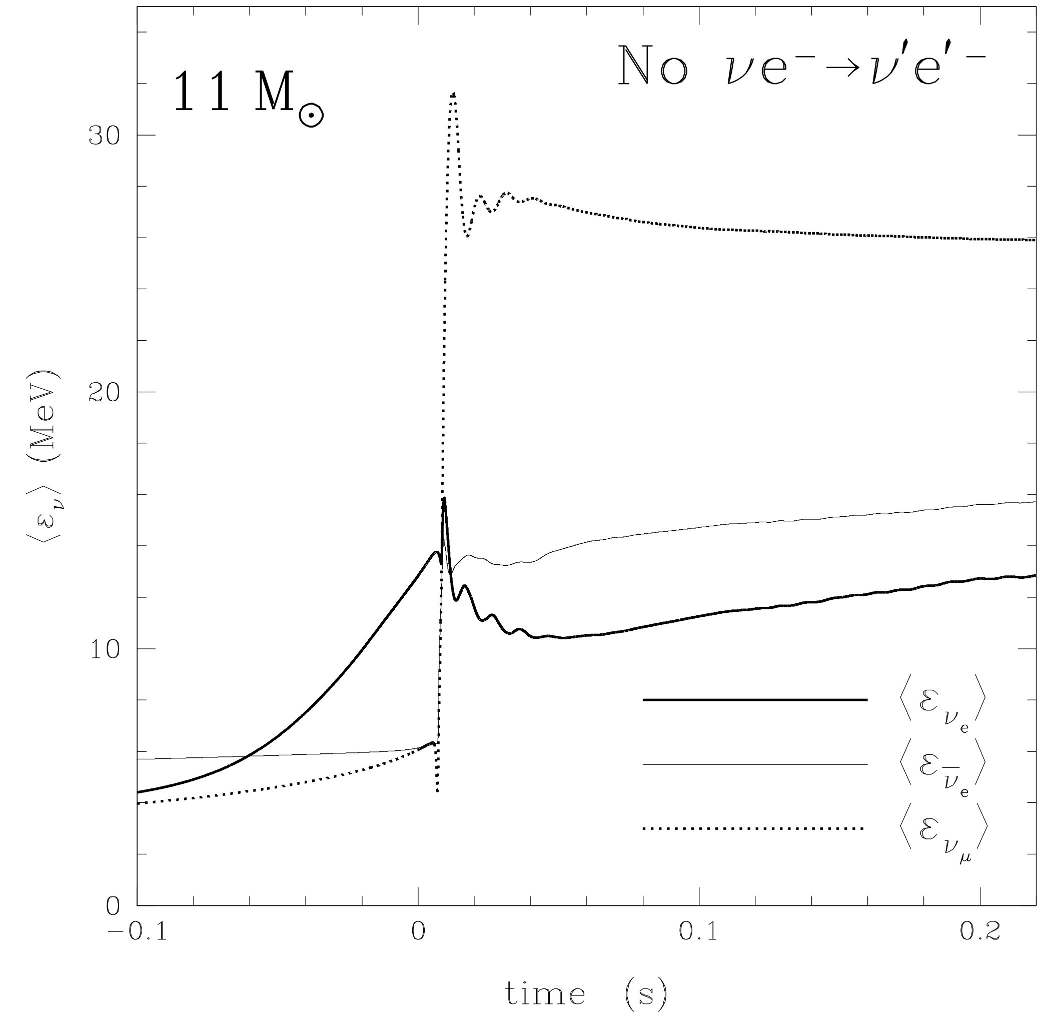

FIGURE 4.27. $\langle \varepsilon_{\nu_e} \rangle$ (thick solid line), $\langle \varepsilon_{\bar{\nu}_e} \rangle$ (thin solid line), and $\langle \varepsilon_{\nu_\mu} \rangle$ (dotted line) at infinity for the 11 M$_\odot$ progenitor without inelastic neutrino-electron scattering. Compare with Fig. (4.26), which shows the corresponding luminosities and Fig. (4.11), which shows the average energy evolution in our fiducial model (including inelastic neutrino-electron scattering).

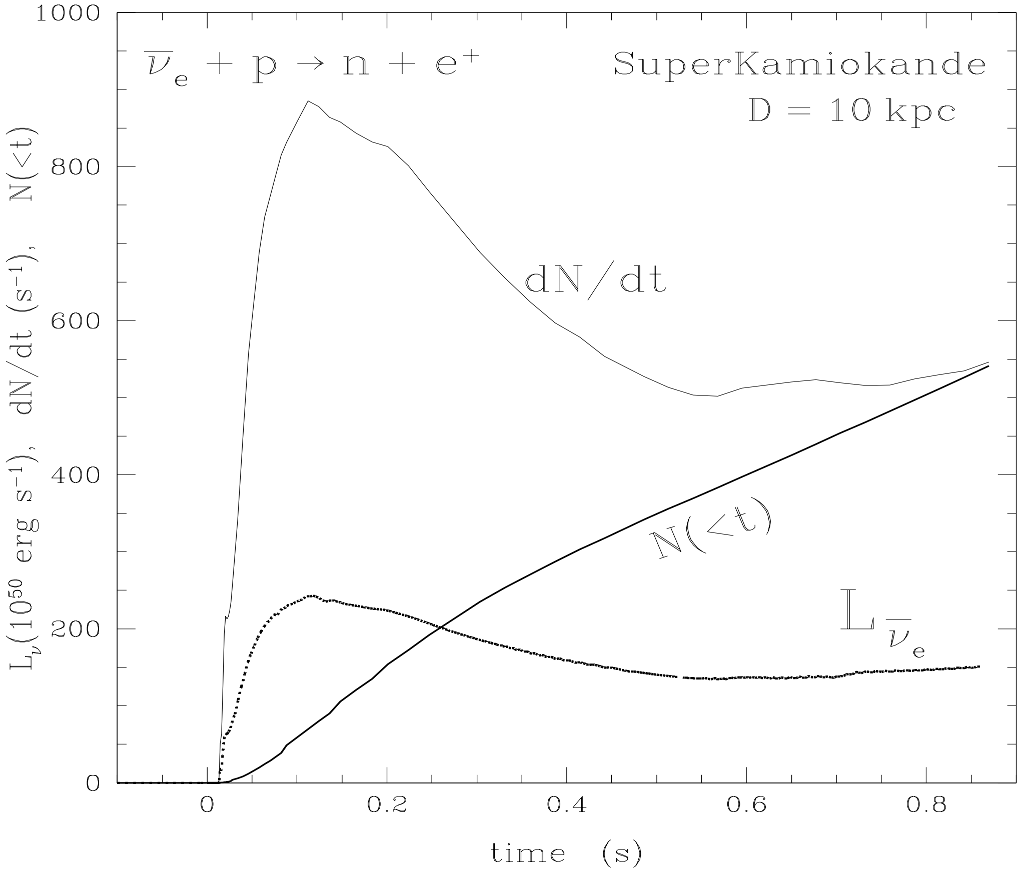

FIGURE 4.28. The event rate (dN/dt, thin solid line) in Hz, and total number detected $N(< t)$ (thick solid line) in SK via charged-current absorption of $\bar{\nu}_e$ neutrinos on free protons for a supernova at a distance of 10 kpc. Also shown for comparison is the luminosity of anti-electron neutrinos (dotted line) as obtained from our 11 $M_\odot$ progenitor model.

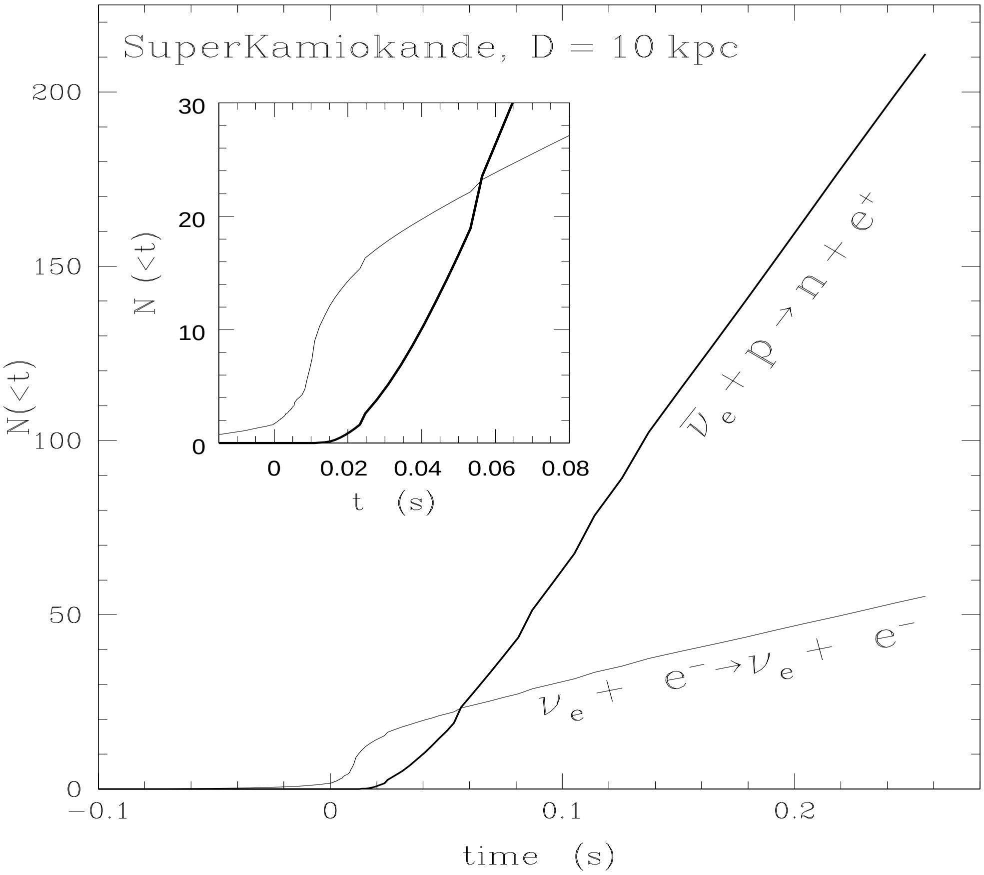

FIGURE 4.29. Integrated number of ν_e events in SK for our fiducial $11\,\mathrm{M}_\odot$ model via the $\nu_e e^- \to \nu_e e^-$ process (thin solid line), as compared with the number of $\bar{\nu}_e$ events from the process $\bar{\nu}_e p \to n e^+$ (thick solid line). The inset shows the same thing, but focuses on the ν_e breakout signal. Note that SK should see a distinct and observable ν_e signature in the first $\sim 30\,\mathrm{ms}$. Nearly 20 ν_e events accumulate before being swamped by the dominant $\bar{\nu}_e$ signal.

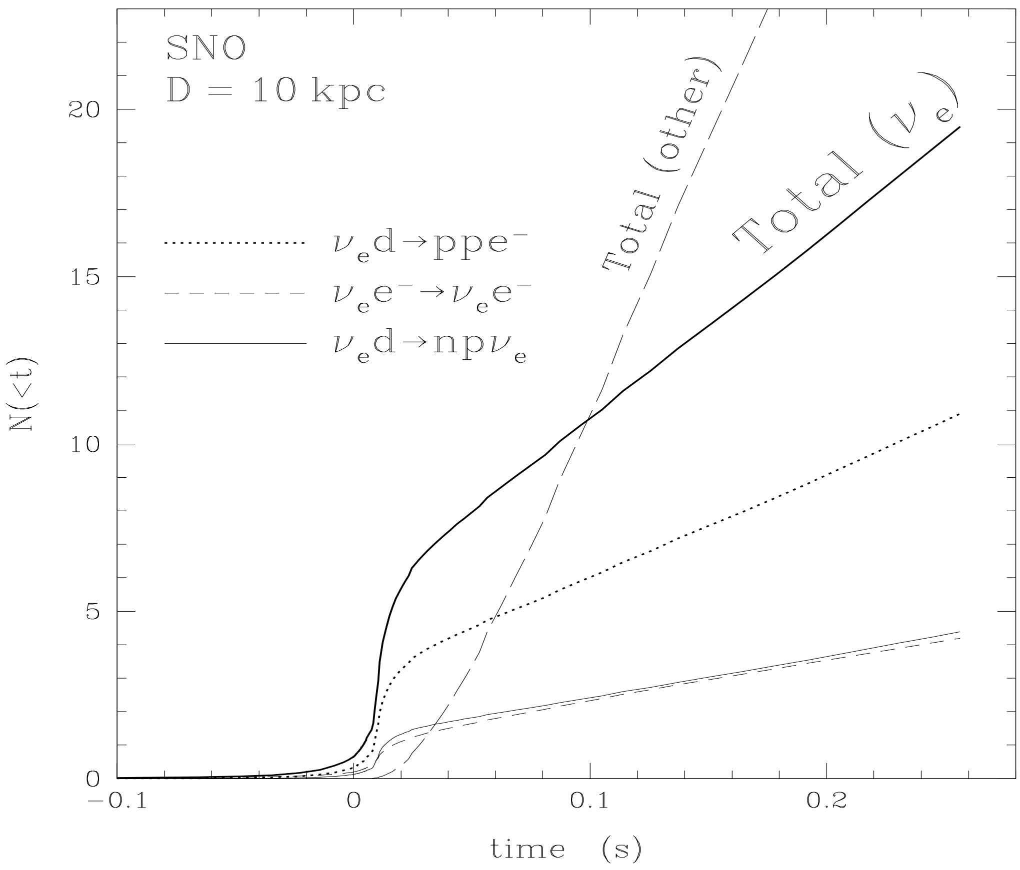

FIGURE 4.30. Integrated number of ν_e neutrinos detected in SNO for a supernova at 10 kpc as a function of time. The individual contributions to the detected signal via the $\nu_e d \rightarrow ppe^-$ (dotted line), $\nu_e d \rightarrow np\nu_e$ (solid line), and $\nu_e e^- \rightarrow \nu_e e^-$ (dashed line) processes are shown. The sum is the thick solid line. The sum of all other processes, including $\bar{\nu}_e d \rightarrow np\bar{\nu}_e$, $\bar{\nu}_e d \rightarrow nne^+$, $\bar{\nu}_e p \rightarrow ne^+$ in the light-water portion of the detector, as well as $\bar{\nu}_{\mu,\tau} d \rightarrow np\bar{\nu}_{\mu,\tau}$, $\nu_{\mu,\tau} d \rightarrow np\nu_{\mu,\tau}$, and $\bar{\nu}_e$-, $\nu_{\mu,\tau}$-, and $\bar{\nu}_{\mu,\tau}$-electron scattering throughout the entire detector volume, is shown as the long dashed line. This signal corresponds to our fiducial $11\,\mathrm{M}_\odot$ core-collapse model.

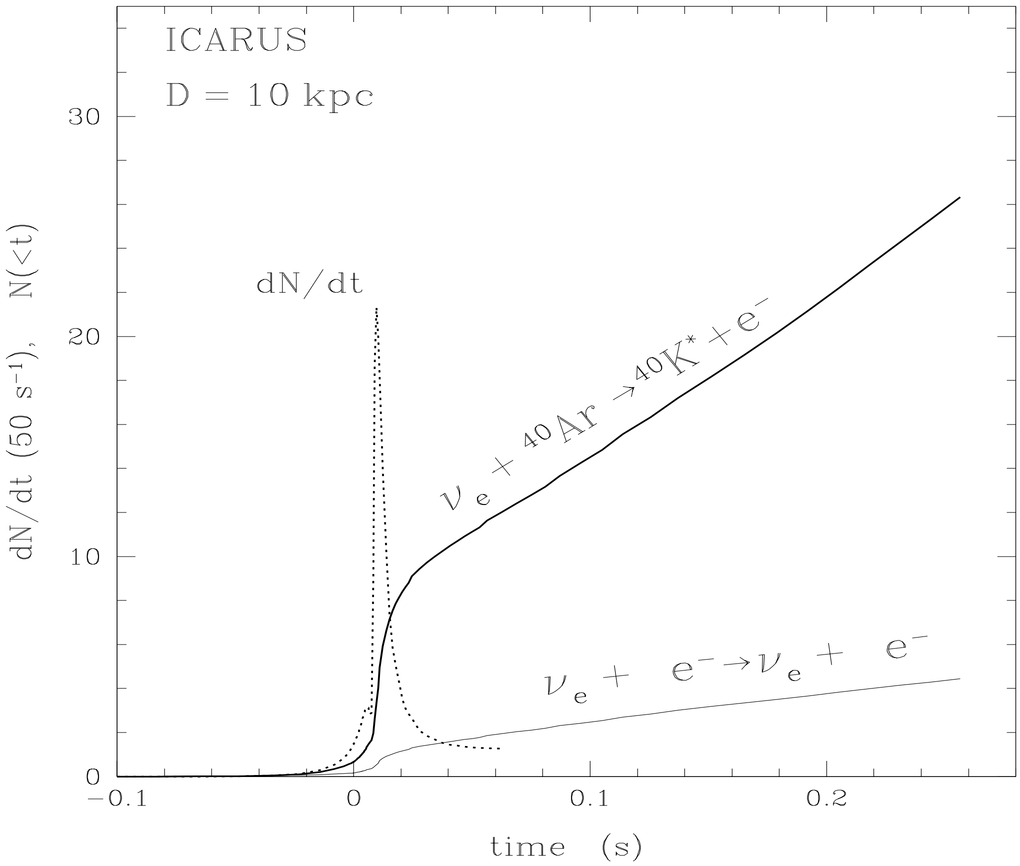

FIGURE 4.31. Integrated number of ν_e events as a function of time via absorption on Argon ($\nu_e\mathrm{Ar} \rightarrow \mathrm{K}^* + e^-$, thick solid line), including the Fermi and Gamow-Teller transitions to ${}^{40}\mathrm{K}^*$ (see §4.5.3), and via ν_e-electron scattering, labeled '$\nu_e e^- \rightarrow \nu_e e^-$' (thin solid line).

Chapter 5
The Future

5.1 The r-Process Problem

In Chapter 3, we developed the first self-consistent models of general relativistic steady-state transonic neutrino-driven protoneutron star winds. With this tool we explored the parameter space of these outflows and focused on their potential as a site for rapid (r) neutron-capture nucleosynthesis. For the first time, we have folded mass outflow constraints with the canonical set of nucleosynthetic constraints: entropy, electron fraction, and dynamical timescale. In short, we have more fully connected speculation on the conditions appropriate for the r-process with the actual physics of protoneutron star winds. Like the supernova problem, the r-process problem is itself unsolved. The models we constructed in Chapter 3 failed to yield a robust r-process for realistic protoneutron star properties. Despite circumstantial evidence that the production of heavy elements is connected with supernovae, it is difficult to understand how the seemingly universal r-process abundance pattern observed in ultra-metal-poor halo stars can originate from the multi-dimensional parameter space of just-post-supernova environments.

Several improvements to the models presented in Chapter 3 should be made at the next level of refinement in order to more fully understand this important component of the protoneutron star cooling epoch.

Neutrino Transport: The success or failure of the r-process to produce the heaviest nuclei in wind models depends sensitively on the neutron fraction as seed nuclei begin to form. This depends on the local anti-electron and electron-neutrino energy density and flux. In Chapter 3 these quantities were calculated using a simple spherical dilution prescription. Instead of positing such quantities, they should be derived from more complete simulations. For this reason, models that consistently produce neutrino-driven winds from full supernova simulations employing sophisticated neutrino transport should be constructed.

Rotation and Magnetic Fields: The effect of rotation and magnetic fields on outflows and the angular momentum evolution of stars is a classic problem in theoretical astrophysics. The angular momentum evolution of the sun, for example, is affected significantly by the joint action of these two effects. Rotation and magnetic fields might play an important role in the just-post-supernova environment. Both have been largely unexplored. If the wind dynamics are affected by such phenomena very near the protoneutron star, then the matter entropy and dynamical timescale - both so crucial in determining the r-process yield - will likely be affected as well. The one-dimensional models presented in Chapter 3 should first be extended to include rotation and magnetic fields to model the equatorial region (Weber & Davis 1967). Beyond that, however, multi-dimensional magnetohydrodynamical simulations will likely be required to asses the influence of these effects on the wind dynamics.

Hydrodynamics: In Chapter 3 we explored the effect of a reverse shock in the wind on the resulting nucleosynthesis. We can expect reverse shock generically, engendered by the interaction of the supernova shock with the overlying shell-structure of the progenitor as it explodes. Do these shocks bury the wind? If a successful r-process is generated very near the protoneutron star just after explosion, does that matter escape to infinity? A series of hydrodynamical studies with simple parameterizations of the wind development might begin to answer such questions.

5.2 Dynamical Models

Although we focused in Chapter 4 on the early post-bounce evolution and the neutrino breakout phenomenon, our models do not seem to yield explosions in the first 250 milliseconds. This result is in agreement with all other one-dimensional models of supernovae that do not employ ad hoc neutrino luminosity enhancements mechanisms. Nevertheless, one-dimensional models are an important tool for testing the effects of changes in the microphysics and for understanding the problem in detail. There are several improvements to the models presented in Chapter 4 that should be made in our next effort.

Neutrino Microphysics: Source terms such as $\nu_e\bar{\nu}_e \leftrightarrow \nu_\mu\bar{\nu}_\mu$ (Buras et al. 2002) should be included, as well as the full structure function formalism of Burrows & Sawyer (1998,1999) and Reddy, Prakash, & Lattimer (1998).

Implicit Hydrodynamics: The explicit hydrodynamics scheme we currently employ is Courant-limited, as described in §4.2.3. We will soon couple our transport scheme to implicit hydrodynamics, which will allow us to take much larger timesteps after bounce and shock-stall. This will facilitate extending the calculations of Chapter 4 to ~ 1 second after bounce and beyond, allowing us to more completely address the delayed explosion mechanism.

5.3 Acknowledgments

It is a pleasure to thank several scientific collaborators who contributed in part to the research presented in the preceding chapters. In particular, Jorge E. Horvath generalized the simple non-degenerate nucleon-nucleon bremsstrahlung formalism presented in §2.3.4 for nucleons at arbitrary degeneracy. Sanjay Reddy contributed to Chapters 2 and 4 by providing tables for calculation of the polylogarithmic integrals necessary in evaluating the relativistic structure functions for neutrino-electron scattering. The r-process network calculations necessary to assess the composition of the protoneutron star wind ejecta in Chapter 3 were carried out by Bradley S. Meyer of Clemson University. Evonne Marietta also contributed to the protoneutron star wind study by making her electron-positron equation of state available. Ron Eastman and Phil Pinto provided the basic transport algorithm used in our dynamical simulations of Chapter 4. Adam Burrows has provided an algorithm for explicit hydrodynamics and the scheme for implicit coupling of the radiation field to matter through the Lambda operator. Eli Livne has provided explicit and implicit schemes for hydrodynamics. Itamar Lichtenstadt has provided an invaluable service in comparing weak interaction rates and the Lattimer-Swesty equation of state with our own implementation.

Appendix A
The Steady-State Wind Equations

A.1 Some Simple Thermodynamic Identities

Expanding the pressure (P) differentially in ρ and T, we have that

$$dP = \left.\frac{\partial P}{\partial \rho}\right|_T \delta\rho + \left.\frac{\partial P}{\partial T}\right|_\rho \delta T. \tag{A.1}$$

This implies that

$$\left.\frac{\partial P}{\partial \rho}\right|_s = \left.\frac{\partial P}{\partial \rho}\right|_T + \left.\frac{\partial P}{\partial T}\right|_\rho \left.\frac{\partial T}{\partial \rho}\right|_s. \tag{A.2}$$

Defining (D) as

$$D = \frac{T}{\rho}\left.\frac{\partial P}{\partial T}\right|_\rho, \tag{A.3}$$

we obtain

$$\left.\frac{\partial P}{\partial \rho}\right|_s = \left.\frac{\partial P}{\partial \rho}\right|_T + \frac{D^2}{C_V T}, \tag{A.4}$$

where

$$C_V = \left.\frac{\partial E}{\partial T}\right|_\rho, \tag{A.5}$$

the specific heat at constant volume. These manipulations yield a convenient expression for the adiabatic sound speed ($c_s = \partial P/\partial\rho|_s$) in terms of the isothermal sound speed ($c_T = \partial P/\partial\rho|_T$):

$$c_s^2 = c_T^2 + \frac{D^2}{C_V T}. \tag{A.6}$$

Note that from eq. (A.1) we may also write that

$$\frac{dP}{dr} = \left.\frac{\partial P}{\partial \rho}\right|_T \frac{d\rho}{dr} + \left.\frac{\partial P}{\partial T}\right|_\rho \frac{dT}{dr}. \tag{A.7}$$

A.2 Steady-State Hydrodynamics

Assuming time-independent wind solutions, the equation for mass conservation simplifies to

$$\nabla \cdot (\rho \mathbf{v}) = 0, \tag{A.8}$$

implying that the mass-outflow rate ($\dot{\mathrm{M}}$) of a wind is a constant in radius. In spherical symmetry, $\dot{\mathrm{M}} = 4\pi r^2 \rho v =$ constant. This expression yields a differential equation for the evolution of the matter velocity in radius,

$$\frac{1}{v}\frac{dv}{dr} = -\frac{1}{\rho}\frac{d\rho}{dr} - \frac{2}{r}. \tag{A.9}$$

The equation for momentum conservation, neglecting the mass of the wind itself, is simply

$$v\frac{dv}{dr} = -\frac{1}{\rho}\frac{dP}{dr} - \frac{GM}{r^2} + F_\nu, \tag{A.10}$$

where M is the total mass of the protoneutron star. Although we include it here for completeness, the radiation force due to the neutrinos (F_ν) is neglected in the present wind study. This approximation is justified because the neutrino Eddington luminosity ($L_\nu^{\mathrm{Edd}} = 4\pi GMc/\kappa_\nu$) is much larger than the neutrino luminosities we assume following the supernova and accompanying protoneutron star cooling. κ_ν is the total neutrino opacity and is dominated by $\nu_e n \to pe^-$ and $\bar{\nu}_e p \to ne^+$ for the electron and anti-electron neutrino, respectively. The mu and tau neutrino opacity is dominated by neutral-current scattering off free nucleons, the wind heating region being unpopulated by nuclei. Including these processes, one finds that $L_\nu^{\mathrm{Edd}} \sim 10^{55}$ erg s^{-1}. We are thus safe in taking $F_\nu = 0$ because we consider winds with only $L_\nu^{\mathrm{tot}} < 5 \times 10^{52}$ erg s^{-1}.

Because neutrinos contribute both heating and cooling to the flow, we must couple to these equations into the first law of thermodynamics. We define the net heating rate; $\dot{q} =$ Heating − Cooling. That is, we have

$$\frac{d\epsilon}{dt} = \dot{q} = T\frac{ds}{dt} + \frac{P}{\rho^2}\frac{d\rho}{dt}, \tag{A.11}$$

where $\rho = V^{-1}$ and $d/dt = [\partial/\partial t + v \cdot \nabla]$. In the steady state, $\partial/\partial t = 0$ and we obtain

$$\dot{q} = Tv\frac{ds}{dr} = C_V v\frac{dT}{dr} - \frac{vT}{\rho^2}\left.\frac{dP}{dT}\right|_\rho \frac{d\rho}{dr}. \tag{A.12}$$

Taking eq. (A.7) and dropping F_ν, we can rewrite eq. (A.10) as

$$v\frac{dv}{dr} = -\frac{1}{\rho}\left[\left.\frac{\partial P}{\partial \rho}\right|_T \frac{d\rho}{dr} + \left.\frac{\partial P}{\partial T}\right|_\rho \frac{dT}{dr}\right] - \frac{GM}{r^2} \tag{A.13}$$

We can now eliminate dT/dr using eq. (A.12)

$$v\frac{dv}{dr} = -\frac{1}{\rho}\left\{\left.\frac{\partial P}{\partial \rho}\right|_T \frac{d\rho}{dr} + \left.\frac{\partial P}{\partial T}\right|_\rho \left[\frac{T}{C_V\rho^2}\left.\frac{dP}{dT}\right|_\rho \frac{d\rho}{dr} + \frac{\dot{q}}{C_V v}\right]\right\} - \frac{GM}{r^2} \tag{A.14}$$

The terms $d\rho/dr$ can be eliminated using the equation for mass conservation, eq. (A.9). Using eq. (A.6) and combining terms proportional to dv/dr, we obtain an expression for dv/dr in terms of thermodynamic quantities returned by the equation of state (D, P, C_V, c_s, etc.), the basic dependent hydrodynamical variables (ρ, v, and T), and the neutrino energy deposition function ($\dot{q}$). Equation (A.14) is then easily cast in the form of eq. (3.9). With eq. (3.9) in hand, eq. (3.10) easily follows from eq. (A.9) and eq. (3.11) then follows from eq. (A.12).

A.3 The General-Relativistic Wind Equations

Thorne, Flammang, & Zytkow (1981) and Flammang (1982) present a derivation of the hydrodynamical equations for steady-state accretion in a Schwarzschild spacetime. We begin with the form presented by Nobili, Turolla, & Zampieri (1991). The general form is presented in eqs. (3.1), (3.2), and (3.3). Simple thermodynamic and algebraical manipulations analogous to those presented for the Newtonian case yield eqs. (3.5), (3.6), and (3.7). The reader is referred to these papers for a more detailed explication.

Appendix B
Neutrino Microphysics

Below we describe the input physics necessary to evaluate the source and sink terms in the interaction term of the Boltzmann or transport equation. The fundamental cross sections, derived from the Standard Model of electroweak interactions, are presented, as are the necessary embellishments and additions to such formulae required for application in the supernova context. In addition, we highlight our technique for incorporating inelastic neutrino scattering in time-dependent solutions to the transport equation.

Many of the cross sections we discuss below can be written in terms of a characteristic neutrino interaction cross section (σ_o);

$$\sigma_o = \frac{4G^2(m_e c^2)^2}{\pi(\hbar c)^4} \simeq 1.7 \times 10^{-44} \ \ \mathrm{cm}^2 \ . \tag{B.1}$$

In what follows, we take the axial vector coupling constant (g_A) $=-1.26$ and $\sin^2\theta_W \simeq 0.231$ (Particle Data Group 1998).

B.1 Absorption and Emission

The interaction term for absorption and emission, which appears on the right-hand side of the Boltzmann equation, may be written as

$$\mathcal{L}^{\mathrm{int}}[f_\nu] = \eta_\nu(1-f_\nu) - \chi_\nu f_\nu, \tag{B.2}$$

where η_ν is the emissivity and χ_ν is the inverse mean-free path, uncorrected for stimulated absorption. In local thermodynamical equilibrium, the emission and absorption must balance and

$$\mathcal{L}^{\mathrm{int}}[f_\nu^{\mathrm{eq}}] = 0. \tag{B.3}$$

This implies that

$$\eta_\nu = \chi_\nu \frac{f_\nu^{\rm eq}}{(1-f_\nu^{\rm eq})}, \tag{B.4}$$

Substituting into eq. (B.2) we have that

$$\begin{aligned}
\mathcal{L}^{\rm int}[f_\nu] &= \chi_\nu \frac{f_\nu^{\rm eq}}{(1-f_\nu^{\rm eq})}(1-f_\nu) - \chi_\nu f_\nu \\
&= \frac{\chi_\nu}{(1-f_\nu^{\rm eq})}\left[f_\nu^{\rm eq} - f_\nu\right] \\
&= \kappa_a^* \left[f_\nu^{\rm eq} - f_\nu\right],
\end{aligned} \tag{B.5}$$

where the last two relationships define the absorptive opacity, κ_a^*, corrected for stimulated absorption, in terms of χ_ν, the pure absorption inverse mean-free path. Equation (B.5) manifestly drives f_ν to its equilibrium value,

$$f_\nu^{\rm eq} = \left[\exp\left(\varepsilon_\nu - \mu_\nu\right)/T + 1\right]^{-1}. \tag{B.6}$$

Writing eq. (B.5) in the form

$$\mathcal{L}^{\rm int}[f_\nu] = \tilde{\eta}_\nu - \kappa_a^* f_\nu \tag{B.7}$$

and employing eq. (B.3), we derive Kirchhoff's Law, $\tilde{\eta}_\nu = \kappa_a^* f_\nu^{\rm eq}$. Kirchhoff's Law saves us from the need to evaluate both $\tilde{\eta}_\nu$ and κ_a^* separately. In practice, we compute χ_ν, which is generally of the form $N\sigma_a$, where N is the number density of absorbers and σ_a is the cross section for absorption. We then compute $\kappa_a^* = (1-f_\nu^{\rm eq})^{-1}\chi_\nu$ and use Kirchhoff's Law to get $\tilde{\eta}_\nu$. For electron neutrinos, the production process $\nu_e n \leftrightarrow e^- p$ implies $\mu_{\nu_e} + \mu_n = \mu_e + \mu_p$. For a given local matter temperature, density and composition, the equation of state returns $\hat{\mu} = \mu_n - \mu_p$ and μ_e. For a given neutrino energy, taking $\mu_{\nu_e} = \mu_e - \hat{\mu}$, eq. (B.6) gives $f_\nu^{\rm eq}$. Similarly, $\mu_{\bar{\nu}_e} = -\mu_e + \hat{\mu}$. For production of ν_μ neutrinos, we neglect the analogous charged-current process $\nu_\mu n \to \mu^- p$ because of the very large energy threshold and because the number density of μ^- is very small at the temperatures and densities encountered in most regimes of the supernovae. Since other processes like $e^+e^- \leftrightarrow \nu_\mu\bar{\nu}_\mu$ and $nn \leftrightarrow nn\nu_\mu\bar{\nu}_\mu$ do contribute to the luminosity of ν_μ neutrinos, $\mu_{\nu_\mu} = 0$ and $f_{\nu_\mu}^{\rm eq}$ is a function of ε_{ν_μ} and T alone.

B.1.1 $\nu_e n \leftrightarrow e^- p$

The absorption of electron neutrinos by neutrons and the inverse process, by which electrons capture on protons, dominate much of the collapse dynamics. As the progenitor becomes unstable, $e^- p \to n\nu_e$ robs the core of electron degeneracy pressure. In the early phase, at core densities below 10^{12} g cm^{-3}, the matter is transparent to the final state electron neutrino and they escape. As a consequence, the electron fraction in the core decreases from about ~ 0.42 to ~ 0.30 as the mass density increases from about 10^{10} g cm^{-3} to above 5×10^{12} g cm^{-3}. At these higher densities, the core becomes opaque to electron neutrinos and the process $\nu_e n \to e^- p$ begins to compete with its inverse, resulting in a (beta) chemical equilibrium that halts the decrease in the electron fraction. The core electron fraction and, indeed, the total trapped lepton fraction, are essential in determining the total energy of the shock. This, in turn, effects the core structure after the shock has stalled. Hence, this balance between $e^- p \to n\nu_e$ and $\nu_e n \to e^- p$ has consequences for the subsequent evolution.

After the core collapses to nuclear densities and the equation of state stiffens, driving a hydrodynamical shock into the free-falling outer core, this absorption and emission process plays an equally important role. As the shock sweeps up nuclei it dissociates them into free neutrons and protons. The high electron number density throughout the entire regime leads to copious ν_e production via $e^- p \to n\nu_e$. The neutrinos, however, are still in an optically thick regime and so their local luminosity swells as they are advected with the matter behind the shock. Eventually, the shock traverses the $\tau_{\nu_e} \sim 2/3$ surface for the electron neutrinos and the neutrino pulse, formerly trapped behind the shock, can escape to infinity. The process $e^- p \to n\nu_e$ is thereby central to the breakout phenomenon.

Ignoring proton blocking in the final state, and assuming stationary nucleons, the total $\nu_e - n$ absorption cross section is given by (e.g. Bruenn 1985)

$$\sigma^a_{\nu_e n} = \sigma_o \left(\frac{1+3g_A^2}{4}\right) \left(\frac{\varepsilon_{\nu_e}+\Delta_{np}}{m_e c^2}\right)^2 \left[1-\left(\frac{m_e c^2}{\varepsilon_{\nu_e}+\Delta_{np}}\right)^2\right]^{1/2} (1-f_{e^-})W_M \ , \quad \text{(B.8)}$$

where $\Delta_{np} = m_n - m_p \simeq 1.2933$ MeV, $\varepsilon_{e^-} = \varepsilon_{\nu_e} + \Delta_{np}$, and f_{e^-} is the electron phase-space occupation, a Fermi-Dirac distribution function. W_M is the weak magnetism correction; $W_M \simeq (1 - 1.01\varepsilon_\nu/m_n)$ (Vogel 1984).

In transport calculations we require the inverse mean free path. Thus, accounting for stimulated absorption and assuming non-degenerate nucleons, the absorptive opacity for use in our transport solution is given by

$$\kappa^*_a = \sigma^a_{\nu_e n} X_n \rho N_A (1 - f^{\rm eq}_{\nu_e})^{-1}, \quad \text{(B.9)}$$

where N_A is Avogadro's number, X_n is the neutron fraction, and $f^{\rm eq}_{\nu_e}$ is given by eq. (B.6) with $\mu_\nu = \mu_e - \hat{\mu}$. Note that if the equation of state employed is thermodynamically consistent, the quantity $(1 - f_{e^-})(1 - f^{\rm eq}_{\nu_e})^{-1}$ can be replaced by $f_{e^-}(\varepsilon_\nu + \Delta_{np})/f^{\rm eq}_{\nu_e}$. At high densities, nucleons are no longer non-degenerate and $X_n \rho N_A$ should be replaced by

$$\eta_{np} = 2\int \frac{d^3 p_n}{(2\pi\hbar c)^3} f_n (1 - f_p), \quad \text{(B.10)}$$

which takes into account the effects of final state nucleon blocking.

B.1.2 $\bar{\nu}_e p \leftrightarrow e^+ n$

After collapse, bounce, and shock breakout, the process $\bar{\nu}_e p \leftrightarrow e^+ n$ together with $\nu_e n \leftrightarrow e^- p$ constitute the dominant heating and cooling mechanisms. Ignoring nucleon blocking in the final state (Bruenn 1985),

$$\sigma^a_{\bar{\nu}_e p} = \sigma_o \left(\frac{1+3g_A^2}{4}\right) \left(\frac{\varepsilon_{\bar{\nu}_e}-\Delta_{np}}{m_e c^2}\right)^2 \left[1-\left(\frac{m_e c^2}{\varepsilon_{\bar{\nu}_e}-\Delta_{np}}\right)^2\right]^{1/2} (1-f_{e^+})W_{\bar{M}}, \quad \text{(B.11)}$$

where $\varepsilon_{e^+} = \varepsilon_{\bar{\nu}_e} - \Delta_{np}$, $\varepsilon_{\bar{\nu}_e} \geq \Delta_{np} + m_e$, and $W_{\bar{M}} \sim (1 - 7.1\varepsilon_\nu/m_p)$ (Vogel 1984). Although we include it here for completeness, the final-state positron blocking term is rarely important given the degeneracy of the electrons in nearly every regime important in the supernova dynamics. The opacity is easily constructed from $\sigma^a_{\bar{\nu}_e p}$;

$$\kappa^*_a = \sigma^a_{\bar{\nu}_e p} X_p \rho N_A (1 - f^{\rm eq}_{\bar{\nu}_e})^{-1}, \tag{B.12}$$

where $f^{\rm eq}_{\bar{\nu}_e}$ is given by eq. (B.6) with $\mu_\nu = -\mu_e + \hat{\mu}$. As in §B.1.1, the quantity $X_p \rho N_A$ should be replaced at very high densities with an expression analogous to eq. (B.10) to capture the effects of final-state nucleon blocking.

B.1.3 $\nu_e A \leftrightarrow A' e^-$

From Bruenn (1985) the total $\nu_e - A$ absorption cross section, is approximated by

$$\sigma^a_A = \frac{\sigma_o}{14}\, g^2_A\, N_p(Z)\, N_n(N) \left(\frac{\varepsilon_\nu + Q'}{m_e c^2}\right)^2 \left[1 - \left(\frac{m_e c^2}{\varepsilon_\nu + Q'}\right)^2\right]^{1/2} (1 - f_{e^-})\; e^{(\mu_n - \mu_p - Q')\beta}\ . \tag{B.13}$$

$Q' = M_{A'} - M_A + \Delta \sim \mu_n - \mu_p + \Delta$, Δ is the energy of the neutron $1f_{5/2}$ state above the ground state and is taken to be 3 MeV (Fuller et al. 1982), and the quantities $N_p(Z)$ and $N_n(N)$ are approximated by: $N_p(Z) = 0$, $Z - 20$, and 8 for $Z < 20$, $20 < Z < 28$, and $Z > 28$, respectively. $N_n(N) = 6$, $40 - N$, and 0 for $N < 34$, $43 < N < 40$, and $N > 40$, respectively. The opacity, corrected for stimulated absorption, is then

$$\kappa^*_a = X_H\, \rho N_A \sigma^a_A (1 - f^{\rm eq}_{\nu_e})^{-1}. \tag{B.14}$$

Figure (4.1) shows the atomic mass of the representative heavy nucleus in the Lattimer-Swesty equation of state as described in §4.2.1. One can see clearly that since $N_n(N) = 0$ for $N > 40$, this absorption and emission process plays a role only during the very early phase of collapse. Typically at densities near $\rho \sim 10^{12}$ g cm^{-3} $\kappa^*_a \to 0$.

B.1.4 $\nu_i\bar{\nu}_i \leftrightarrow e^+e^-$

Both neutral and charged current Feynman diagrams contribute to the matrix element for the process $e^+e^- \rightarrow \nu\bar{\nu}$. From Dicus (1972), the total matrix element, after a Fierz transformation, can be written as

$$\mathcal{M} = i\frac{G}{\sqrt{2}}\bar{u}_\nu(q)\gamma^\alpha(1-\gamma^5)v_\nu(q')\bar{v}_e(p')\gamma_\alpha(C_V - C_A\gamma_5)u_e(p), \tag{B.15}$$

where p and p' are the four-momenta of the electron and positron, respectively, and q and q' are the four-momenta of the neutrino and anti-neutrino, respectively. Squaring and averaging over final spin states and taking the extreme relativistic limit in which $m_e = 0$,

$$\frac{1}{4}\sum_s |\mathcal{M}|^2 = 16G^2[(C_V + C_A)^2 p\cdot q'\, p'\cdot q + (C_V - C_A)^2 p\cdot q\, p'\cdot q']. \tag{B.16}$$

The production kernel is defined by

$$R^p(\varepsilon_\nu, \varepsilon_{\bar{\nu}}, \cos\theta) = \frac{1}{2\varepsilon_\nu\varepsilon_{\bar{\nu}}}\int \frac{d^3\vec{p}}{(2\pi)^3 2\varepsilon}\frac{d^3\vec{p}'}{(2\pi)^3 2\varepsilon'} f_{e^-}f_{e^+}\left(\frac{1}{4}\sum_s |\mathcal{M}|^2\right)(2\pi)^4\delta^4(\mathrm{P}), \tag{B.17}$$

where ε and ε' are the electron and positron energy, respectively, and $\delta^4(\mathrm{P})$ is the total four-momentum-conserving delta function. f_{e^-} and f_{e^+} are Fermi-Dirac distribution functions for the electron and positron, respectively. The differential production spectrum for final state neutrinos can then be written as (Bruenn 1985)

$$\frac{dQ}{d\varepsilon_\nu d\Omega} = (1 - f_\nu)\frac{\varepsilon_\nu^3}{(2\pi)^3}\int \frac{d^3 p_{\bar{\nu}}}{(2\pi)^3} R^p(\varepsilon_\nu, \varepsilon_{\bar{\nu}}, \cos\theta)\,(1 - f_{\bar{\nu}})\ , \tag{B.18}$$

where $d\Omega$ is the differential solid angle for the neutrino. Expanding the production kernel in a Legendre series in the scattering angle, $\cos\theta = \mu\mu' + [(1-\mu^2)(1-\mu'^2)]^{1/2}\cos\phi$,

$$\begin{aligned} R^p(\varepsilon_\nu, \varepsilon_{\bar{\nu}}, \cos\theta) &= \frac{1}{2}\sum_l (2l+1)\Phi_l^p(\varepsilon_\nu, \varepsilon_{\bar{\nu}})P_l(\cos\theta) \\ &\sim \frac{1}{2}\Phi_0^p(\varepsilon_\nu, \varepsilon_{\bar{\nu}}) + \frac{3}{2}\Phi_1^p(\varepsilon_\nu, \varepsilon_{\bar{\nu}})\cos\theta. \end{aligned} \tag{B.19}$$

Φ_0^p, in eqs. (2.29) and (B.19), is given by (Bruenn 1985; Yueh & Buchler 1976)

$$\Phi_0^p(\varepsilon_\nu, \varepsilon_{\bar{\nu}}) = \frac{G^2}{\pi} \int_0^{\varepsilon_\nu+\varepsilon_{\bar{\nu}}} d\varepsilon\; f_{e^-} f_{e^+}\, H_0(\varepsilon_\nu, \varepsilon_{\bar{\nu}}, \varepsilon), \tag{B.20}$$

where f_{e^+} is a function of $\varepsilon'(=\varepsilon_\nu + \varepsilon_{\bar{\nu}} - \varepsilon)$ and

$$H_0(\varepsilon_\nu, \varepsilon_{\bar{\nu}}, \varepsilon) = (V+A)^2\, J_0^I(\varepsilon_\nu, \varepsilon_{\bar{\nu}}, \varepsilon) + (V-A)^2\, J_0^{II}(\varepsilon_\nu, \varepsilon_{\bar{\nu}}, \varepsilon)\ . \tag{B.21}$$

Each J_0 in eq. (B.21) is a polynomial in ε_ν, $\varepsilon_{\bar{\nu}}$, and ε of dimension [energy]. They are related to each other by (Bruenn 1985)

$$J_0^I(\varepsilon_\nu, \varepsilon_{\bar{\nu}}, \varepsilon) = J_0^{II}(\varepsilon_{\bar{\nu}}, \varepsilon_\nu, \varepsilon)\ . \tag{B.22}$$

Both J_0^I and J_0^{II} can be found in Bruenn (1985) (correcting for the typo in their eq. C67). From eqs. (2.29) and (B.21) we see that the differences between the spectra for ν_μs and $\bar{\nu}_\mu$s for a given temperature and electron degeneracy (η_e) arise solely from the relative weighting constants $(V+A)^2$ and $(V-A)^2$ in eq. (B.21) for J_0^I and J_0^{II}, respectively. Indeed, in this approximation the same can be said for the difference in the spectrum between ν_e and ν_μ neutrinos.

Ignoring phase space blocking of neutrinos in the final state and taking the relativistic limit ($m_e \to 0$), the total electron-positron annihilation rate for electron or mu- and tau-type neutrino production can be written in terms of the electron and positron distribution functions (Dicus 1972):

$$Q_{\nu_e\bar{\nu}_e} = K_i \left(\frac{1}{m_e c^2}\right)^2 \left(\frac{1}{\hbar c}\right)^6 \int\!\!\int f_{e^-} f_{e^+} (\varepsilon_{e^-}^4 \varepsilon_{e^+}^3 + \varepsilon_{e^-}^3 \varepsilon_{e^+}^4)\, d\varepsilon_{e^-}\, d\varepsilon_{e^+}\ , \tag{B.23}$$

where $K_i = (1/18\pi^4) c\sigma_o (C_V^2 + C_A^2)$. $C_V = 1/2 + 2\sin^2\theta_W$ for electron types, $C_V = -1/2 + 2\sin^2\theta_W$ for mu and tau types, and $C_A^2 = (1/2)^2$. Rewriting eq. (B.23) in terms of the Fermi integral $F_n(\eta)$:

$$Q_{\nu_e\bar{\nu}_e} = K_i\,(kT) \left(\frac{kT}{m_e c^2}\right)^2 \left(\frac{kT}{\hbar c}\right)^6 [F_4(\eta_e)F_3(-\eta_e) + F_4(-\eta_e)F_3(\eta_e)]\ , \tag{B.24}$$

where $\eta_e \equiv \mu_e/kT$ and

$$F_n(\eta) \equiv \int_0^\infty \frac{x^n}{e^{x-\eta}+1}\,dx\ . \tag{B.25}$$

For $\nu_e\bar{\nu}_e$ production, eq. (B.23) can also be written as

$$Q_{\nu_e\bar{\nu}_e} \simeq 9.7615\times 10^{24}\left[\frac{kT}{\mathrm{MeV}}\right]^9 f(\eta_e)\ \left(\frac{\mathrm{ergs}}{\mathrm{cm^3\,s}}\right)\ , \tag{B.26}$$

where

$$f(\eta_e) = \frac{F_4(\eta_e)F_3(-\eta_e)+F_4(-\eta_e)F_3(\eta_e)}{2F_4(0)F_3(0)}\ . \tag{B.27}$$

For $\nu_\mu\bar{\nu}_\mu$ and $\nu_\tau\bar{\nu}_\tau$ production combined,

$$Q_{\nu_{\mu,\tau}\bar{\nu}_{\mu,\tau}} \simeq 4.1724\times 10^{24}\left[\frac{kT}{\mathrm{MeV}}\right]^9 f(\eta_e)\ \left(\frac{\mathrm{ergs}}{\mathrm{cm^3\,s}}\right)\ . \tag{B.28}$$

In the limit of high temperatures and ignoring electron phase space blocking, the $\nu_i\bar{\nu}_i$ annihilation rate can be written (Janka 1991):

$$Q_{\nu_i\bar{\nu}_i} = 4K_i\pi^4\left(\frac{1}{m_ec^2}\right)\left(\frac{4\pi}{c}\right)^2\int J_{\nu_i}J_{\bar{\nu}_i}(\varepsilon_{\nu_i}+\varepsilon_{\bar{\nu}_i})\,\Phi\left(q_{\nu_i},q_{\bar{\nu}_i},p_{\nu_i},p_{\bar{\nu}_i}\right)\,d\varepsilon_{\nu_i}\,d\varepsilon_{\bar{\nu}_i}\ , \tag{B.29}$$

where J_ν is the zeroth moment as defined in eq. (4.13), ε_ν is the neutrino energy and K_i is defined as before, i.e. $K_i = (1/18\pi^4)c\sigma_o(C_V^2+C_A^2)$. In eq. (B.29)

$$\Phi\left(q_{\nu_i},q_{\bar{\nu}_i},p_{\nu_i},p_{\bar{\nu}_i}\right) = \frac{3}{4}\left[1-2q_{\nu_i}q_{\bar{\nu}_i}+p_{\nu_i}p_{\bar{\nu}_i}+\frac{1}{2}(1-p_{\nu_i})(1-p_{\bar{\nu}_i})\right]\ , \tag{B.30}$$

where $q_\nu = \langle\mu_{\nu_i}\rangle = H_\nu/J_\nu$ and $p_\nu = \langle\mu_{\nu_i}^2\rangle = P_\nu/J_\nu$. Eq. (B.29) can be rewritten in terms of the invariant distribution function f_ν:

$$Q_{\nu_i\bar{\nu}_i} = K_i\left(\frac{1}{m_ec^2}\right)^2\left(\frac{1}{\hbar c}\right)^6\int f_{\nu_i}f_{\bar{\nu}_i}(\varepsilon_{\nu_i}^4\varepsilon_{\bar{\nu}_i}^3+\varepsilon_{\nu_i}^3\varepsilon_{\bar{\nu}_i}^4)\,\Phi\left(q_{\nu_i},q_{\bar{\nu}_i},p_{\nu_i},p_{\bar{\nu}_i}\right)\,d\varepsilon_{\nu_i}\,d\varepsilon_{\bar{\nu}_i}. \tag{B.31}$$

Note that when the radiation field is isotropic ($\Phi = 1$) and $\eta_e = 0$ the total rate for e^+e^- annihilation given in eq. (B.23) equals that for $\nu_i\bar{\nu}_i$ annihilation given in eq. (B.31), as expected.

B.1.5 Nucleon-Nucleon Bremsstrahlung

Refer to §2.3.4 in Chapter 2 for a complete discussion of our bremsstrahlung formalism. Although we derive general expressions, accurate for arbitrary nucleon degeneracy, we employ the simpler and computationally less expensive non-degenerate approximation given in eqs. (2.56) and (2.57).

B.2 Scattering Opacities

Elastic scattering enters the interaction term of the transport equation as a purely isotropic scattering opacity, κ_s. Particularly for neutrino scattering on free alpha particles and nuclei, all that is needed is a cross section for scattering and a number density of scatterers. The product is the inverse mean-free-path for scattering and enters χ_ν as κ_s in eq. (4.5).

B.2.1 $\nu_i(n,p) \leftrightarrow \nu_i(n,p)$

Neutrino-nucleon scattering contributes significantly to the total opacity for all neutrino species during much of the post-bounce evolution. Although neutrino-nucleon scattering may be modified significantly at high densities, due both to blocking effects in the final state and correlations induced by strong interactions (Burrows & Sawyer 1998), we neglect such effects here and present the simple scattering opacity due to neutral-current neutrino-neutron and neutrino-proton scattering. The total $\nu_i n$ scattering cross section is

$$\sigma_n = \frac{\sigma_o}{4}\left(\frac{\varepsilon_\nu}{m_e c^2}\right)^2\left(\frac{1+3g_A^2}{4}\right) \ . \tag{B.32}$$

From eq. (4.9) we obtain the differential cross section

$$\frac{d\sigma_n}{d\Omega} = \frac{\sigma_n}{4\pi}(1+\delta_n\mu) \ , \tag{B.33}$$

where, from Schinder (1990),

$$\delta_n = \frac{1 - g_A^2}{1 + 3g_A^2} \ . \tag{B.34}$$

The transport cross section as defined by eq. (4.18) is simply

$$\sigma_n^{tr} = \frac{\sigma_o}{4}\left(\frac{\varepsilon_\nu}{m_e c^2}\right)^2 \left(\frac{1 + 5g_A^2}{6}\right) \ . \tag{B.35}$$

Similarly for $\nu_i p$ scattering we have that

$$\sigma_p = \frac{\sigma_o}{4}\left(\frac{\varepsilon_\nu}{m_e c^2}\right)^2 \left(4\sin^4\theta_W - 2\sin^2\theta_W + \frac{(1 + 3g_A^2)}{4}\right), \tag{B.36}$$

which, in terms of $C'_V = 1/2 + 2\sin^2\theta_W$ and $C'_A = 1/2$, is simply

$$\sigma_p = \frac{\sigma_o}{4}\left(\frac{\varepsilon_\nu}{m_e c^2}\right)^2 \left[(C'_V - 1)^2 + 3g_A^2(C'_A - 1)^2\right]. \tag{B.37}$$

The differential cross section is then

$$\frac{d\sigma_p}{d\Omega} = \frac{\sigma_p}{4\pi}(1 + \delta_p \mu) \ , \tag{B.38}$$

where, from Schinder (1990),

$$\delta_p = \frac{(C'_V - 1)^2 - g_A^2(C'_A - 1)^2}{(C'_V - 1)^2 + 3g_A^2(C'_A - 1)^2}, \tag{B.39}$$

and the transport cross section is

$$\sigma_p^{tr} = \frac{\sigma_o}{6}\left(\frac{\varepsilon_\nu}{m_e c^2}\right)^2 \left[(C'_V - 1)^2 + 5g_A^2(C'_A - 1)^2\right] \ . \tag{B.40}$$

Horowitz (2002) has recently derived expressions that include a weak magnetism correction analogous to those previously discussed for the charged-current absorption rates $\nu_e n \leftrightarrow p e^-$ and $\bar{\nu}_e n \leftrightarrow n e^+$. We take the following form for the weak magnetism correction, a fit to the actual correction factor for the transport cross sections:

$$\sigma_{n,p}^{tr} \rightarrow \sigma_{n,p}^{tr}(1 + C_{W_M}\varepsilon_\nu / m_{n,p}), \tag{B.41}$$

where, for neutrino-neutron scattering $C_{W_M} \simeq -0.766$, for neutrino-proton scattering $C_{W_M} \simeq -1.524$, for anti-neutrino-neutron scattering $C_{W_M} \simeq -7.3656$, and for anti-neutrino-proton scattering $C_{W_M} \simeq -6.874$.

B.2.2 $\nu_i e^- \leftrightarrow \nu_i e^-$

The opacity due to neutrino-electron scattering can be large compared with that of other processes at low neutrino energies ($\varepsilon_\nu \lesssim 5$ MeV) and at high matter temperatures. When we do not calculate the scattering opacity explicitly using the formalism of §B.3, we employ the following expression from Bowers & Wilson (1982), which interpolates between analytic limits derived in Tubbs & Schramm (1975):

$$\sigma_e = \frac{3}{8}\sigma_o \left(m_e c^2\right)^{-2} \varepsilon_\nu \left(T + \frac{\mu_e}{4}\right) \left[(C_V + C_A)^2 + \frac{1}{3}(C_V - C_A)^2\right] , \tag{B.42}$$

where $C_V = 1/2 + 2\sin^2\theta_W$ for electron types, $C_V = -1/2 + 2\sin^2\theta_W$ for mu and tau neutrino types, $C_A = +1/2$ for ν_e and $\bar{\nu}_\mu$, and $C_A = -1/2$ for $\bar{\nu}_e$ and ν_μ.

B.2.3 $\nu_i \alpha \leftrightarrow \nu_i \alpha$

Because of the high temperatures achieved throughout during collapse, bounce, and shock propagation, alpha particles exist in significant abundance only near the shock. Even so, they exist over a very small region in radius. That said, the scattering cross section and corresponding opacity in this regime are relatively large. The total and transport scattering cross sections for $\nu_i - \alpha$ scattering are simply

$$\sigma_\alpha = \frac{3}{2}\sigma_\alpha^{tr} = 4\,\sigma_o \left(\frac{\varepsilon_\nu}{m_e c^2}\right)^2 \sin^4\theta_W . \tag{B.43}$$

B.2.4 $\nu_i A \leftrightarrow \nu_i A$

During infall, the dominant opacity for all neutrino species is coherent scattering off nuclei. The cross section, which is proportional to the atomic mass (A) of the representative heavy nucleus squared, increases rapidly in the core as the star collapses, since A may reach several hundred. The differential transport cross section for $\nu_i - A$ scattering may be written as

$$\frac{d\sigma_A}{d\Omega} = \frac{\sigma_o}{64\pi}\left(\frac{\varepsilon_\nu}{m_e c^2}\right)^2 A^2 \left\{Q\mathcal{C}_{FF} + \mathcal{C}_{LOS}\right\}^2 \langle \mathcal{S}_{ion}\rangle (1+\mu)(1-\mu) , \tag{B.44}$$

where Z is the atomic number and $Q = [1 - (2Z/A)(1 - 2\sin^2\theta_W)]$. Leinson et al. (1988) investigated the polarization correction $\mathcal{C}_{LOS}$ and found that

$$\mathcal{C}_{LOS} = \frac{Z}{A}\left(\frac{1 + 4\sin^2\theta_W}{1 + (kr_D)^2}\right), \tag{B.45}$$

where

$$r_D = \sqrt{\frac{\pi\hbar^2 c}{4\alpha p_F E_F}}, \tag{B.46}$$

$k^2 = |\mathbf{p} - \mathbf{p}'|^2 = 2(\varepsilon_\nu/c)^2(1 - \mu)$, $\alpha \simeq 137^{-1}$, and r_D is the Debye radius of the medium. Note that $r_D \sim 10\hbar/p_F$ for the ultra relativistic limit ($p_F >> m_e c$). Following Tubbs & Schramm (1975) and Burrows, Mazurek, & Lattimer (1981), the form factor term $\mathcal{C}_{FF}$ in eq. (B.44) is written as

$$\mathcal{C}_{FF} = e^{-y(1-\mu)/2}\ , \tag{B.47}$$

where $y = 4b\varepsilon_\nu^2$, $b = \frac{1}{6}\langle r^2\rangle/(\hbar c)^2$, and r is the radius of the nucleus.

$$y \simeq \left(\frac{\varepsilon_\nu}{56\,\mathrm{MeV}}\right)^2\left(\frac{A}{100}\right)^{2/3}\ . \tag{B.48}$$

The ion-ion correlation correction, $\langle\mathcal{S}_{ion}\rangle$, in eq. (B.44) was investigated by Horowitz (1997) who approximated it with the expansion

$$\langle\mathcal{S}_{ion}(\epsilon)\rangle = \left[1 + exp\left(-\sum_{i=0}^{6}\beta_i(\Gamma)\epsilon^i\right)\right]^{-1}\ , \tag{B.49}$$

where

$$\Gamma = \frac{(Ze)^2}{a}\frac{1}{kT}\quad,\quad \epsilon_i = \frac{\varepsilon_{\nu_i}}{\hbar c a}\quad,\quad a = \left(\frac{3}{4\pi n_{ion}}\right)^{1/3}, \tag{B.50}$$

a is the interparticle spacing, n_{ion} is the number density of ions, Γ is the ratio of Coulomb potential between ions to the thermal energy in the medium, and β_i are specified functions of Γ for each neutrino species.

Setting $\mathcal{C}_{LOS} = 0$, $\mathcal{C}_{FF} = 1$, and $\langle\mathcal{S}_{ion}\rangle = 1$ in eq. (B.44) and denoting the total $\nu_i - A$ scattering cross section under these assumptions we have that

$$\sigma_{o,A} = \frac{\sigma_o}{16}\left(\frac{\varepsilon_\nu}{m_e c^2}\right)^2 A^2\left[1 - \frac{2Z}{A}(1 - 2\sin^2\theta_W)\right]^2\ . \tag{B.51}$$

Following Burrows, Mazurek, & Lattimer (1981), assuming that $\langle \mathcal{S}_{ion} \rangle = 1$ and $\mathcal{C}_{LOS} = 0$ in eq. (B.44) we derive a transport cross section:

$$\sigma^{tr}_{o,A} = \frac{\sigma_{o,A}}{2} \int_{-1}^{+1} (1+\mu)(1-\mu) e^{-y(1-\mu)}\, d\mu \;=\; \sigma_{o,A}\, f(y) \tag{B.52}$$

where

$$f(y) = \left[\frac{y(e^{-2y}+1) - (1-e^{-2y})}{y^3} \right] \;. \tag{B.53}$$

Note that in the limit of small y, $f(y)$ may be expanded and yields the desired result to zeroth order:

$$f(y) \sim (2/3) - (2/3)y + (6/15)y^2 + \dots \;. \tag{B.54}$$

In practice, we evaluate the total scattering cross section by integrating eq. (B.44) with four-point Gauss-Legendre quadratures.

B.3 Inelastic Neutrino Scattering

Many authors have addressed the issue of inelastic neutrino-electron scattering as an important energy redistribution process, which helps thermalize the neutrinos and increases their energetic coupling to the matter in supernova explosions (Bruenn 1985; Mezzacappa & Bruenn 1993). Comparatively little attention has been paid to inelastic neutrino-nucleon scattering. Chapter 2 showed that, at least for mu and tau neutrinos, this process cannot be ignored. Here, we review the Legendre expansion formalism for approximating the angular dependence of the scattering kernel, detail our own implementation of scattering terms in the Boltzmann equation, and include a discussion of neutrino-nucleon energy redistribution.

The general collision integral for inelastic scattering may be written (Bruenn 1985) as

$$\begin{aligned} \mathcal{L}^{\rm scatt}_\nu[f_\nu] = (1-f_\nu) \int \frac{d^3 p'_\nu}{c(2\pi\hbar c)^3} f'_\nu\, R^{\rm in}(\varepsilon_\nu, \varepsilon'_\nu, \cos\theta) \\ -f_\nu \int \frac{d^3 p'_\nu}{c(2\pi\hbar c)^3} (1-f'_\nu)\, R^{\rm out}(\varepsilon_\nu, \varepsilon'_\nu, \cos\theta) \end{aligned} \tag{B.55}$$

$$= \tilde{\eta}_\nu^{\rm scatt} - \tilde{\chi}_\nu^{\rm scatt} f_\nu \tag{B.56}$$

where $\cos\theta$ is the cosine of the scattering angle, ε_ν is the incident neutrino energy, and ε'_ν is the scattered neutrino energy. Although we suppress it here, the incident and scattered neutrino phase space distribution functions (f_ν and f'_ν, respectively) have the following dependencies: $f_\nu = f_\nu(r,t,\mu,\varepsilon_\nu)$ and $f'_\nu = f'_\nu(r,t,\mu',\varepsilon'_\nu)$. μ and μ' are the cosines of the angular coordinate of the zenith angle in spherical symmetry and are related to $\cos\theta$ through

$$\cos\theta = \mu\mu' + [(1-\mu^2)(1-\mu'^2)]^{1/2}\cos(\phi-\phi'). \tag{B.57}$$

$R^{\rm in}$ is the scattering kernel for scattering **in**to the bin (ε_ν, μ) from any bin (ε'_ν, μ') and $R^{\rm out}$ is the scattering kernel for scattering **out** of the bin (ε_ν, μ) to any bin (ε'_ν, μ'). The kernels are Green functions, correlation functions that connect points in energy and momentum space. In fact, one may also write $R(\varepsilon_\nu, \varepsilon'_\nu, \cos\theta)$ as $R(q,\omega)$, where $\omega(=\varepsilon_\nu - \varepsilon'_\nu)$ is the energy transfer and $q(=[\varepsilon_\nu^2 + \varepsilon_\nu'^2 - 2\varepsilon_\nu\varepsilon'_\nu\cos\theta]^{1/2})$ is the momentum transfer, so that the kernel explicitly reflects these dependencies.

It is clear from eq. (B.55) that the source, or the net scattering into the beam (ε_ν, μ) is a function of the occupancy (f'_ν) in all other beams. The sink term also depends on f'_ν through the blocking term $(1-f'_\nu)$, reflecting the Fermi-Dirac statistics of the neutrino. A solution to the Boltzmann or transport equation yields f_ν (and, hence, f'_ν) at all times, radii, energies, and angles. f_ν is not known a priori and cannot be assumed to be Fermi-Dirac. Only in equilibrium should f_ν approach a Fermi-Dirac distribution, characterized by the local temperature and with a chemical potential that reflects the local neutrino number density. The transport problem is difficult enough without the added complication of non-linear integral source terms. The full implicit solution, including energy and angular redistribution, is numerically intense and beyond the scope of this project. Instead, we make several simplifications that make the problem tractable and efficiently solved.

First, as stated in §4.2.2, we assume isotropic scattering. The second important simplification comes from detailed balance, a consequence of the fact that these scattering rates must drive the distribution to equilibrium; $R^{\rm in} = e^{-\beta\omega}R^{\rm out}$, where $\beta = 1/T$. We may therefore deal only with $R^{\rm out}$. The scattering kernels dealt with specifically in this section, those for inelastic neutrino-nucleon and neutrino-electron scattering, have complicated dependencies on scattering angle and the angular integration over scattered neutrino phase space, implicit in eq. (B.55), cannot be computed analytically. For this reason, we approximate the angular dependence of the scattering kernel with a truncated Legendre series (Bruenn 1985). That is, we take

$$R^{\rm out}(\varepsilon_\nu, \varepsilon'_\nu, \cos\theta) = \sum_{l=0}^{\infty} \frac{2l+1}{2}\Phi(\varepsilon_\nu, \varepsilon'_\nu, \cos\theta)P_l(\cos\theta), \tag{B.58}$$

where

$$\Phi_l(\varepsilon_\nu, \varepsilon'_\nu) = \int_{-1}^{+1} d(\cos\theta)\, R^{\rm out}(\varepsilon_\nu, \varepsilon'_\nu, \cos\theta)P_l(\cos\theta). \tag{B.59}$$

In practice, we expand only to first order so that

$$R^{\rm out}(\varepsilon_\nu, \varepsilon'_\nu, \cos\theta) \sim \frac{1}{2}\Phi_0(\varepsilon_\nu, \varepsilon'_\nu) + \frac{3}{2}\Phi_1(\varepsilon_\nu, \varepsilon'_\nu)\cos\theta. \tag{B.60}$$

Substituting into the first term on the right-hand-side of eq. (B.55) (the source) gives

$$\tilde{\eta}_\nu^{\rm scatt} = (1-f_\nu)\int_0^\infty \frac{d\varepsilon'_\nu \varepsilon'^2_\nu}{c(2\pi\hbar c)^3}\, e^{-\beta\omega}\int_{-1}^{+1} d\mu' f'_\nu \int_0^{2\pi} d\phi' \left[\frac{1}{2}\Phi_0 + \frac{3}{2}\Phi_1\cos\theta\right] \tag{B.61}$$

Substituting for $\cos\theta$ using eq. (B.57) and using the definitions

$$\tilde{J}_\nu = \frac{1}{2}\int_{-1}^{+1} d\mu f_\nu \tag{B.62}$$

and

$$\tilde{H}_\nu = \frac{1}{2}\int_{-1}^{+1} d\mu\mu f_\nu \tag{B.63}$$

we have that

$$\tilde{\eta}_\nu^{\rm scatt} = (1-f_\nu)\frac{4\pi}{c(2\pi\hbar c)^3}\int_0^\infty d\varepsilon'_\nu \varepsilon'^2_\nu e^{-\beta\omega}\left[\frac{1}{2}\Phi_0\tilde{J}'_\nu + \frac{3}{2}\Phi_1\mu\tilde{H}'_\nu\right]. \tag{B.64}$$

Integrating over μ to get the source for the zeroth moment equation,

$$\frac{1}{2}\int_{-1}^{+1} d\mu\,\tilde{\eta}_\nu^{\text{scatt}} = \frac{4\pi}{c(2\pi\hbar c)^3}\int_0^\infty d\varepsilon'_\nu \varepsilon'^2_\nu e^{-\beta\omega}\left[\frac{1}{2}\Phi_0\tilde{J}'_\nu(1-\tilde{J}_\nu) - \frac{3}{2}\Phi_1\tilde{H}_\nu\tilde{H}'_\nu\right]. \tag{B.65}$$

Similarly, we may write the sink term of the Boltzmann equation collision term, employing the Legendre expansion

$$\tilde{\chi}_\nu^{\text{scatt}} = \frac{4\pi}{c(2\pi\hbar c)^3}\int_0^\infty d\varepsilon'_\nu \varepsilon'^2_\nu\left[\frac{1}{2}\Phi_0(1-\tilde{J}'_\nu) - \frac{3}{2}\Phi_1\mu\tilde{H}'_\nu\right]. \tag{B.66}$$

The contribution to the zeroth moment equation is then

$$\frac{1}{2}\int_{-1}^{+1} d\mu(-\tilde{\chi}_\nu^{\text{scatt}} f_\nu) = -\frac{4\pi}{c(2\pi\hbar c)^3}\int_0^\infty d\varepsilon'_\nu \varepsilon'^2_\nu\left[\frac{1}{2}\Phi_0(1-\tilde{J}'_\nu)\tilde{J}_\nu - \frac{3}{2}\Phi_1\tilde{H}_\nu\tilde{H}'_\nu\right]. \tag{B.67}$$

Combining these equations, we find that

$$\begin{aligned}\frac{1}{2}\int_{-1}^{+1} d\mu\,\mathcal{L}_\nu^{\text{scatt}}[f_\nu] &= \frac{4\pi}{c(2\pi\hbar c)^3}\int_0^\infty d\varepsilon'_\nu \varepsilon'^2_\nu \\ &\times \left\{\frac{1}{2}\Phi_0\left[\tilde{J}'_\nu(1-\tilde{J}_\nu)e^{-\beta\omega} - (1-\tilde{J}'_\nu)\tilde{J}_\nu\right] - \frac{3}{2}\Phi_1\tilde{H}_\nu\tilde{H}'_\nu(e^{-\beta\omega}-1)\right\}. \end{aligned} \tag{B.68}$$

One can see immediately that including another term in the Legendre expansion (taking $R^{\text{out}} \sim (1/2)\Phi_0 + (3/2)\Phi_1\cos\theta + (5/2)\Phi_2(1/2)(3\cos^2\theta - 1)$) necessitates including $\tilde{P}_\nu$ and $\tilde{P}'_\nu$, the second angular moment of the neutrino phase-space distribution function, in the source and sink terms. Our transport scheme solves both the moment equations for the spectral Eddington factors $p_\nu = \tilde{P}_\nu/\tilde{J}_\nu$ and $g_\nu = \tilde{N}_\nu/\tilde{J}_\nu$, where

$$\tilde{P}_\nu = \frac{1}{2}\int_{-1}^{+1} d\mu\mu^2 f_\nu \quad \text{and} \quad \tilde{N}_\nu = \frac{1}{2}\int_{-1}^{+1} d\mu\mu^3 f_\nu. \tag{B.69}$$

It is therefore possible for us to include only terms up to $R^{\text{out}} \propto \cos^3\theta$ in our Legendre expansion of the scattering kernel. In practice, however, we retain only the linear term. We discuss this approximation in the next two sections.

B.3.1 Neutrino-Electron Scattering

The scattering kernel $R(\varepsilon_\nu, \varepsilon'_\nu, \cos\theta)$ in §B.3 is related to the fully relativistic structure function for neutrino-electron scattering;

$$R^{\rm out}(\varepsilon_\nu, \varepsilon'_\nu, \cos\theta) = 2G^2 \frac{q_\mu^2}{\varepsilon'_\nu \varepsilon_\nu}[A\mathcal{S}_1(q,\omega) + \mathcal{S}_2(q,\omega) + B\mathcal{S}_3(q,\omega)](1-e^{-\beta\omega})^{-1}. \quad \text{(B.70)}$$

The relativistic structure functions ($\mathcal{S}_i$) are given in terms of the imaginary part of the polarization functions as in eqs. (2.24), (2.25), and (2.26). Each of the retarded polarization functions in eqs. (2.24-2.26) can be written in terms of one-dimensional integrals over electron energy (ε_e), which we label I_n (Reddy, Prakash, & Lattimer 1998);

$$\mathrm{Im}\Pi^R_L(q,\omega) = \frac{q_\mu^2}{2\pi|q|^3}\left[I_2 + \omega I_1 + \frac{q_\mu^2}{4} I_0\right], \quad \text{(B.71)}$$

$$\mathrm{Im}\Pi^R_T(q,\omega) = \frac{q_\mu^2}{4\pi|q|^3}\left[I_2 + \omega I_1 + \left(\frac{q_\mu^2}{4} + \frac{q^2}{2} + m^2\frac{q^2}{q_\mu^2}\right) I_0\right], \quad \text{(B.72)}$$

$$\mathrm{Im}\Pi^R_A(q,\omega) = \frac{m^2}{2\pi|q|} I_0, \quad \text{(B.73)}$$

and

$$\mathrm{Im}\Pi^R_{VA}(q,\omega) = \frac{q_\mu^2}{8\pi|q|^3}\left[\omega I_0 + 2I_1\right]. \quad \text{(B.74)}$$

Reddy, Prakash, & Lattimer (1998) were able to express the I_n's in terms of polylogarithmic integrals such that

$$I_0 = Tz\left(1 - \frac{\xi_1}{z}\right), \quad \text{(B.75)}$$

$$I_1 = T^2 z\left(\eta_e - \frac{z}{2} - \frac{\xi_2}{z} - \frac{e_-\xi_1}{zT}\right), \quad \text{(B.76)}$$

and

$$I_2 = T^3 z\left(\eta_e^2 - z\eta_e + \frac{\pi^2}{3} + \frac{z^2}{3} + 2\frac{\xi_3}{z} - 2\frac{e_-\xi_2}{Tz} + \frac{e_-^2\xi_1}{T^2 z}\right), \quad \text{(B.77)}$$

where $\eta_e = \mu_e/T$ is the electron degeneracy, $z = \beta\omega$, ω is the energy transfer, and

$$e_- = -\frac{\omega}{2} + \frac{q}{2}\sqrt{1 - 4\frac{m^2}{q_\mu^2}}. \quad \text{(B.78)}$$

In eqs. (B.75-B.77), the ξ_n's are differences between polylogarithmic integrals; $\xi_n = \mathrm{Li}_n(-\alpha_1) - \mathrm{Li}_n(-\alpha_2)$, where

$$\mathrm{Li}_n(y) = \int_0^y \frac{\mathrm{Li}_{n-1}(x)}{x}\,dx, \tag{B.79}$$

and $\mathrm{Li}_1(x) = \ln(1-x)$. The arguments necessary for computing the integrals are $\alpha_1 = \exp[\beta(e_- + \omega) - \eta_e]$ and $\alpha_2 = \exp(\beta e_- - \eta_e)$. Tables for computation of $\mathrm{Li}_n(y)$ and the I_is have been kindly provided by Sanjay Reddy.

Figure (B.1) shows the full scattering kernel for $\varepsilon_\nu = 20$ MeV and $\varepsilon'_\nu = 2$, 10, and 16 MeV as a function of the cosine of the scattering angle, $\cos\theta$. Note that although the absolute value of the energy transfer ($|\varepsilon_\nu - \varepsilon'_\nu|$) is the same for both $\varepsilon'_\nu = 16$ MeV and $\varepsilon'_\nu = 24$, the absolute value of $R^{\mathrm{out}}(20, 16, \cos\theta)$ is more than twice that of $R^{\mathrm{out}}(20, 24, \cos\theta)$, reflecting the fact that at this temperature the incoming neutrino is more likely to downscatter than upscatter. Figure (B.2) shows the scattering kernel for the same conditions as Fig. (B.1), but also includes both the first-order (short dashed lines) and second-order (long dashed lines) approximations to R^{out}. We employ the former. The latter is included to illustrate the improvement in including higher-order terms. In fact, the actual degree of expansion necessary to capture accurately the physics can only be ascertained by running full transport calculations. We have run dynamical simulations with only the zeroth-order and first-order terms in the Legendre expansion and find little or no difference between the emergent spectra and detailed thermodynamical evolution in the models we have studied. Smit (1998) and Smit & Cernohorsky (1996) have explored the importance of including the second-order term ($\propto \cos^2\theta$, shown here) and finds it negligible. The scattering-angle-averaged kernel, also the zeroth-order term in the Legendre series for R^{out}, is shown in Fig. (B.3) for ν_e-electron scattering for a matter temperature (T) of 6 MeV and with an electron degeneracy factor $\eta_e = \mu_e/T = 20$ as a function of ε'_ν for various incoming neutrino energies, ε_νs.

Even though we have made the simplifying assumption that the scattering kernel can be approximated by a Legendre series truncated at first order (eq. B.60), in a fully dynamical calculation it is numerically costly to compute the Legendre moments of the scattering kernel ($\Phi_0(\varepsilon_\nu, \varepsilon'_\nu)$ and $\Phi_1(\varepsilon_\nu, \varepsilon'_\nu)$) via eq. (B.59) at each point on the radial grid (at each temperature, density, and composition point) at each time step. In order to decrease the computation time, we tabulate $\Phi_0(\varepsilon_\nu, \varepsilon'_\nu)$ and $\Phi_1(\varepsilon_\nu, \varepsilon'_\nu)$ for each ε_ν and ε'_ν, for each neutrino species, on a grid in temperature and η_e. At each T-η_e point, we calculate both kernels for each ε_ν-ε'_ν point, given the energy grouping for the particular calculation. The angular integrals over $\cos\theta$ for $l = 0$ and $l = 1$ in eq. (B.59) are carried out using 16-point Gauss-Legendre quadratures. During an actual supernova calculation, we use simple trapezoidal rule quadrature to calculate the integral over ε'_ν for a given ε_ν. Each term in this integral contains the kernels, which must be evaluated for the each ε_ν-ε'_ν pair at the temperature/density/composition point currently being addressed by the code. η_e is calculated by the equation of state and we do a six-point bivariant interpolation in T-η_e space, for the given ε_ν-ε'_ν combination. In practice, we use 40 energy groups (n_f), 30 temperature points (N_T), and 30 η_e points (N_η). The tables are then $l \times n_f \times n'_f \times N_T \times N_\eta$ in size, with $l = 2$ (Φ_0 and Φ_1), or approximately 50 Megabytes. Since the vector and axial-vector couplings for electron scattering are different for each neutrino species, we compute tables for ν_e, $\bar{\nu}_e$, and ν_μ for each dynamical calculation. $\tilde{\eta}_\nu^{\rm scatt}$ and $\tilde{\chi}_\nu^{\rm scatt}$ are then included explicitly as a source and sink, respectively, in a manner analogous to any of the absorption and emission processes detailed in §B.1. Using this method, our calculations including neutrino-electron scattering, are just 10-15% slower than our calculations ignoring this important equilibration process.

Because we do not evaluate the scattering source and sink implicitly, we introduce an explicit timescale into the energy and electron fraction updates returned by our transport algorithm. In effect, if the scattering timescale $(c\tilde{\chi}_\nu^{\rm scatt})^{-1}$ is shorter than our timestep, we may encounter a numerical instability. For this reason, at high densities, where the neutrino phase-space distribution function is in local thermodynamic equilibrium, we divide the source and sink by a factor (typically 100 above $\rho = 10^{14}$ g cm^{-3}). This reduces the rate artificially, thus increasing the timescale for scattering. As this process is totally negligible in this regime, particularly considering the fact that $f_\nu = f_\nu^{\rm eq}$ at these high densities, we find this approximation acceptable.

B.3.2 Neutrino-Nucleon Scattering

The kernel for inelastic neutrino-nucleon scattering can be related to the non-relativistic structure function employed in the thermalization studies of Chapter 2 (see eqs. 2.12 & 2.13);

$$R^{\rm out}(\varepsilon_\nu, \varepsilon_\nu', \cos\theta) = G^2 S(q,\omega)[(1+\cos\theta)V^2 + (3-\cos\theta)A^2], \tag{B.80}$$

where $S(q,\omega)$ is given by eq. (2.14) in terms of the imaginary part of the polarization function, analogous to neutrino-electron scattering.

The neutrino-nucleon scattering kernels, while larger in absolute magnitude than the corresponding neutrino-electron scattering kernels are, at most points in energy space and thermodynamic space, much less broad. In fact, in thermodynamic regimes most relevant for the formation of the various species' spectra, the kernel is quite sharply peaked in energy. That is, for a given ε_ν the distribution of ε_ν''s is tightly centered on ε_ν because the ratio of the neutrino energy to the nucleon mass is small. $R^{\rm out}$ as a function of $\cos\theta$, for neutrino-neutron scattering, is shown in Fig. (B.4) at a representative thermodynamic point, a plot analogous to Fig. (B.1) for neutrino-electron scattering. By comparing the $\varepsilon_\nu' = 19$ MeV line with that for $\varepsilon_\nu' = 21$ MeV, one sees that the former is larger and, hence, downscattering is preferred. In addition, the overall magnitude is much larger than in the neutrino-electron scattering case. Figure (B.5) shows Φ_0 (eq. B.59) for neutrino-neutron scattering as a function of ε_ν' for several ε_ν's at the same thermodynamic point as used for Fig. (B.3), the corresponding figure for neutrino-electron scattering. Note that while downscatting is strong for the $\varepsilon_\nu = 35$ MeV kernel, there is almost equal upscattering at $\varepsilon_\nu = 5$ MeV.

The effect of this process on an actual neutrino distribution function was explored in Chapter 2. In order to explore the effect of this process on the emergent spectra in dynamical simulations we must first deal with a technical problem.

In a typical simulation, we employ 40 energy groups for all neutrino species with $1\,\mathrm{MeV} \leq \varepsilon_\nu \leq 320\,\mathrm{MeV}$ for electron-type neutrinos and $1\,\mathrm{MeV} \leq \varepsilon_\nu \leq 100\,\mathrm{MeV}$ for anti-electron and muon neutrinos. The grouping is generally logarithmic for the ν_es and linear for $\bar{\nu}_e$ and ν_μ. Neutrino-electron scattering and neutrino-nucleon scattering are most important as thermalization mechanisms at energies below ~ 60 MeV, where the phase space distribution of all neutrino species is largest. One can see clearly from Fig. (B.5) that a trapezoidal rule integration of Φ_0 over ε_ν' as it appears in eq. (B.65) and eq. (B.67) may grossly overestimate $\tilde{\eta}_\nu^{\mathrm{scatt}}$ and $\tilde{\chi}_\nu^{\mathrm{scatt}}$. In fact, with logarithmic energy grouping one may even calculate upscattering when there is none because the energy groups become larger with increasing energy.

For neutrino-electron scattering, we were able to employ a simple trapezoidal rule and adequately capture the qualities of the kernel. This implies that we use a linear interpolation for $\tilde{J}_\nu'$ and $\tilde{H}_\nu'$ in each energy bin. As Fig. (B.5) shows, however, in order to get an accurate integral over $\Phi_0(\varepsilon_\nu, \varepsilon_\nu')$, we must do better than simple trapezoidal rule with linear interpolation. In order to increase the accuracy of our scheme without compromising computational efficiency, for a given energy grouping, we pre-compute a grid of integrals over ε_ν'. We assume that during the dynamical calculation and the computation of $\tilde{\eta}_\nu^{\mathrm{scatt}}$ and $\tilde{\chi}_\nu^{\mathrm{scatt}}$, both $\tilde{J}_\nu'$ and $\tilde{H}_\nu'$ are proportional to $A\varepsilon_\nu' + B$ over an energy interval $\varepsilon_{\nu,i} \leq \varepsilon_\nu' \leq \varepsilon_{\nu,i+1}$. Given this assumption and both $\Phi_0(\varepsilon_\nu, \varepsilon_\nu')$ and $\Phi_1(\varepsilon_\nu, \varepsilon_\nu')$ at a given T and $\eta_{n,p}$, we tabulate the following integrals:

$$\int_{\varepsilon_{\nu,\,i}}^{\varepsilon_{\nu,\,i+1}} d\varepsilon_\nu' \varepsilon_\nu'^2 \Phi_l(\varepsilon_\nu, \varepsilon_\nu'),$$

$$\int_{\varepsilon_{\nu,\,i}}^{\varepsilon_{\nu,\,i+1}} d\varepsilon_\nu' \varepsilon_\nu'^2 \varepsilon_\nu' \Phi_l(\varepsilon_\nu, \varepsilon_\nu'),$$

$$\int_{\varepsilon_{\nu,\,i}}^{\varepsilon_{\nu,\,i+1}} d\varepsilon_\nu' \varepsilon_\nu'^2 e^{-\beta\omega} \Phi_l(\varepsilon_\nu, \varepsilon_\nu'),$$

and

$$\int_{\varepsilon_{\nu,\,i}}^{\varepsilon_{\nu,\,i+1}} d\varepsilon'_\nu \varepsilon'^2_\nu \varepsilon'_\nu \, e^{-\beta\omega} \Phi_l(\varepsilon_\nu, \varepsilon'_\nu),$$

where $l = 0, 1$ and each i is an individual energy group, set up at the beginning of the calculation. The integrals over ε'_ν are computed using 16-point Gauss-Legendre quadrature, each nested with another 16-point Gauss-Legendre quadrature for the integral over $\cos\theta$ necessary for each $\Phi_l(\varepsilon_\nu, \varepsilon'_\nu)$. These integrals are tabulated at 30 temperature and 30 $\eta_{n,p}$ points, analogous to the case with neutrino-electron scattering. For example, the integral

$$\begin{aligned}\int_0^\infty d\varepsilon'_\nu \varepsilon'^2_\nu \tilde{J}'_\nu \Phi_0(\varepsilon_\nu, \varepsilon'_\nu) &= \sum_{i=1}^{n_f} A_i \int_{\varepsilon_{\nu,\,i}}^{\varepsilon_{\nu,\,i+1}} d\varepsilon'_\nu \varepsilon'^2_\nu \varepsilon'_\nu \Phi_0(\varepsilon_\nu, \varepsilon'_\nu) \\ &+ \sum_{i=1}^{n_f} B_i \int_{\varepsilon_{\nu,\,i}}^{\varepsilon_{\nu,\,i+1}} d\varepsilon'_\nu \varepsilon'^2_\nu \Phi_0(\varepsilon_\nu, \varepsilon'_\nu), \qquad \text{(B.81)}\end{aligned}$$

where $A_i = (\tilde{J}^{i\,\prime}_\nu - \tilde{J}^{i+1\,\prime}_\nu)/(\varepsilon^{i\,\prime}_\nu - \varepsilon^{i+1\,\prime}_\nu)$ and $B_i = \tilde{J}^{i\,\prime}_\nu - A_i \varepsilon^{i\,\prime}_\nu$. The total source and sink are given by integrals analogous to eq. (B.81) with appropriate changes to A_i and B_i, depending on if the term in the source or sink is over $\tilde{J}'_\nu$ or $\tilde{H}'_\nu$. In practice, for a given temperature and density, we calculate the necessary integrals at the four nearest neighbor $T - \eta_{n,p}$ points saved in the table and then interpolate the solution using a four-point bivariant interpolation scheme. In this scheme, the energy integral over the kernel is reproduced extremely well and the primary uncertainty in calculating the total source and sink is due to the linear interpolation of $\tilde{J}'_\nu$ and $\tilde{H}'_\nu$ - the same as in the neutrino-electron scattering case. Also interesting is that because the neutrino-nucleon scattering kernel is so sharply peaked around ε_ν and drops off so quickly with ε'_ν, most terms in the sum in eq. (B.81) are zero. When we fill the table, we note the index i of the lowest and highest $\varepsilon'_{\nu,i}$ intervals that contribute significantly (to a part in 10^4) to the total ε'_ν integral over Φ_l. Typically, only four to five energy groups must be included in the final sum. This decreases both the size of the table and the amount of time needed to calculate $\tilde{\eta}^{\rm scatt}_\nu$ and $\tilde{\chi}^{\rm scatt}_\nu$. Although the vector and axial-vector couplings for neutrino-neutron scattering are independent of neutrino species, we calculate separate tables for ν_e, $\bar{\nu}_e$, and ν_μ so as to allow for arbitrary energy grouping for each species.

The Elastic Limit: With the inelastic formalism in hand, it is instructive to construct the elastic limit. Note that in the limit of zero energy transfer, $S(q,\omega) \rightarrow S(0) = Cn_{n,p}\,\delta(\omega)$, where C is a constant and $n_{n,p}$ is the neutron or proton number density. The scattering term can then be written as

$$\begin{aligned}\mathcal{L}_{(0)}^{\rm scatt}[f_\nu] &= (1-f_\nu)\frac{Cn_{n,p}}{c(2\pi\hbar c)^3}\int_0^\infty d\varepsilon_\nu'\varepsilon_\nu'^2 e^{-\beta\omega}\delta(\omega)\int_{-1}^{+1} d\mu' f_\nu' \int_0^{2\pi} d\phi'\, M \\ &- f_\nu\frac{Cn_{n,p}}{c(2\pi\hbar c)^3}\int_0^\infty d\varepsilon_\nu'\varepsilon_\nu'^2 \delta(\omega)\int_{-1}^{+1} d\mu' (1-f_\nu') \int_0^{2\pi} d\phi'\, M, \qquad \text{(B.82)}\end{aligned}$$

where $M = [(1+\cos\theta)V^2 + (3-\cos\theta)A^2]$. Using eqs. (B.57), (B.62), and (B.63) we find that

$$\mathcal{L}_{(0)}^{\rm scatt}[f_\nu] = (1-f_\nu)\frac{4\pi Cn_{n,p}}{c(2\pi\hbar c)^3}\int_0^\infty d\varepsilon_\nu'\varepsilon_\nu'^2 e^{-\beta\omega}\delta(\omega)[V^2(\tilde{J}_\nu' + \mu\tilde{H}_\nu') + 3A^2(\tilde{J}_\nu' - \mu\tilde{H}_\nu'/3)]$$

$$-f_\nu\frac{4\pi Cn_{n,p}}{c(2\pi\hbar c)^3}\int_0^\infty d\varepsilon_\nu'\varepsilon_\nu'^2 \delta(\omega)[V^2(1-\tilde{J}_\nu' - \mu\tilde{H}_\nu') + 3A^2(1-\tilde{J}_\nu' + \mu\tilde{H}_\nu'/3)]. \qquad \text{(B.83)}$$

Integrating over ε_ν' using the delta function, we have that

$$\begin{aligned}\mathcal{L}_{(0)}^{\rm scatt}[f_\nu] &= 4\pi C\varepsilon_\nu^2(V^2+3A^2)\left[(\tilde{J}_\nu - f_\nu) + \left(\frac{V^2-A^2}{V^2+3A^2}\right)\mu\tilde{H}_\nu\right] \\ &= \sigma_{n,p}n_{n,p}\left[(\tilde{J}_\nu - f_\nu) + \delta_{n,p}\mu\tilde{H}_\nu\right] \qquad \text{(B.84)}\end{aligned}$$

where $\sigma_{n,p} = (G^2/\pi c)\varepsilon_\nu^2(V^2+3A^2)$, $\delta_{n,p}$ is the scattering asymmetry for neutrino-neutron or neutrino-proton scattering, G is the weak coupling constant, and c is the speed of light. The result presented in eq. (B.84) is to be compared with the full scattering part of the collision term on the right-hand side of eq. (4.7):

$$-\kappa_s f_\nu + \frac{\kappa_s}{4\pi}\int \Phi(\mathbf{\Omega},\mathbf{\Omega}')\, f_\nu(\mathbf{\Omega}')\, d\Omega'. \qquad \text{(B.85)}$$

Approximating the integral elastic scattering source term as in eq. (4.8) we derive eq. (4.10). Combining the scattering sink, $-\kappa_s f_\nu$, with the scattering source, $\kappa_s\tilde{J}_\nu + \kappa_s\delta\mu\tilde{H}_\nu$, we obtain eq. (B.84) and an expression for $\delta_{n,p}$.

Note that taking the zeroth moment of $\mathcal{L}^{\rm scatt}_{(0)}[f_\nu]$ yields zero, as it should in the elastic scattering limit. Further, note that the first moment is non-zero:

$$\begin{aligned} \frac{1}{2}\int_{-1}^{+1} d\mu\mu\,\mathcal{L}^{\rm scatt}_{(0)}[f_\nu] &= \frac{1}{3}\frac{G^2}{\pi c}n_{n,p}\varepsilon_\nu^2\tilde{H}_\nu(V^2-A^2)-\frac{G^2}{\pi c}n_{n,p}\varepsilon_\nu^2\tilde{H}_\nu(V^2+3A^2) \\ &= -\frac{G^2}{\pi c}n_{n,p}\varepsilon_\nu^2\tilde{H}_\nu(V^2+3A^2)\left[1-\frac{1}{3}\delta_{n,p}\right] \\ &= -\sigma_{n,p}n_{n,p}\tilde{H}_\nu\left[1-\frac{1}{3}\delta_{n,p}\right] \end{aligned} \tag{B.86}$$

This expression is to be compared with the elastic scattering momentum source term on the right-hand side of the first moment of the transport equation, eq. (4.15). In fact, the quantity $\sigma_{n,p}n_{n,p}(1-\delta_{n,p}/3)$ defines the transport cross section in eqs. (4.15) and eqs. (4.18), which we use for elastic scattering in the models presented in Chapter 4.

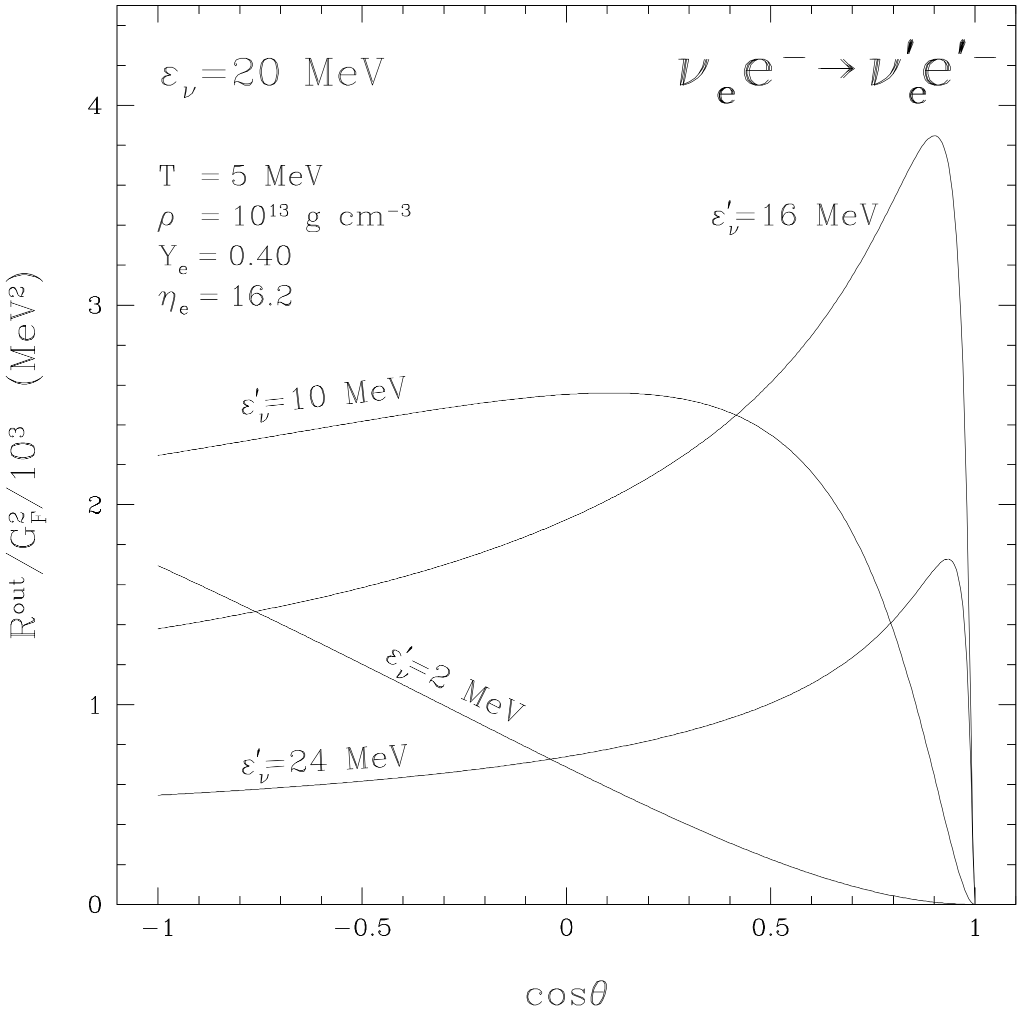

FIGURE B.1. The scattering kernel $R^{\rm out}(\varepsilon_\nu, \varepsilon'_\nu, \cos\theta)$ for ν_e−electron scattering as a function of $\cos\theta$ for $\varepsilon_\nu = 20$ MeV and $\varepsilon'_\nu = 2$, 10, 16, and 24 MeV, at a representative thermodynamic point ($T = 5$ MeV, $\rho = 10^{13}$ g cm^{-3}, $Y_e = 0.4$).

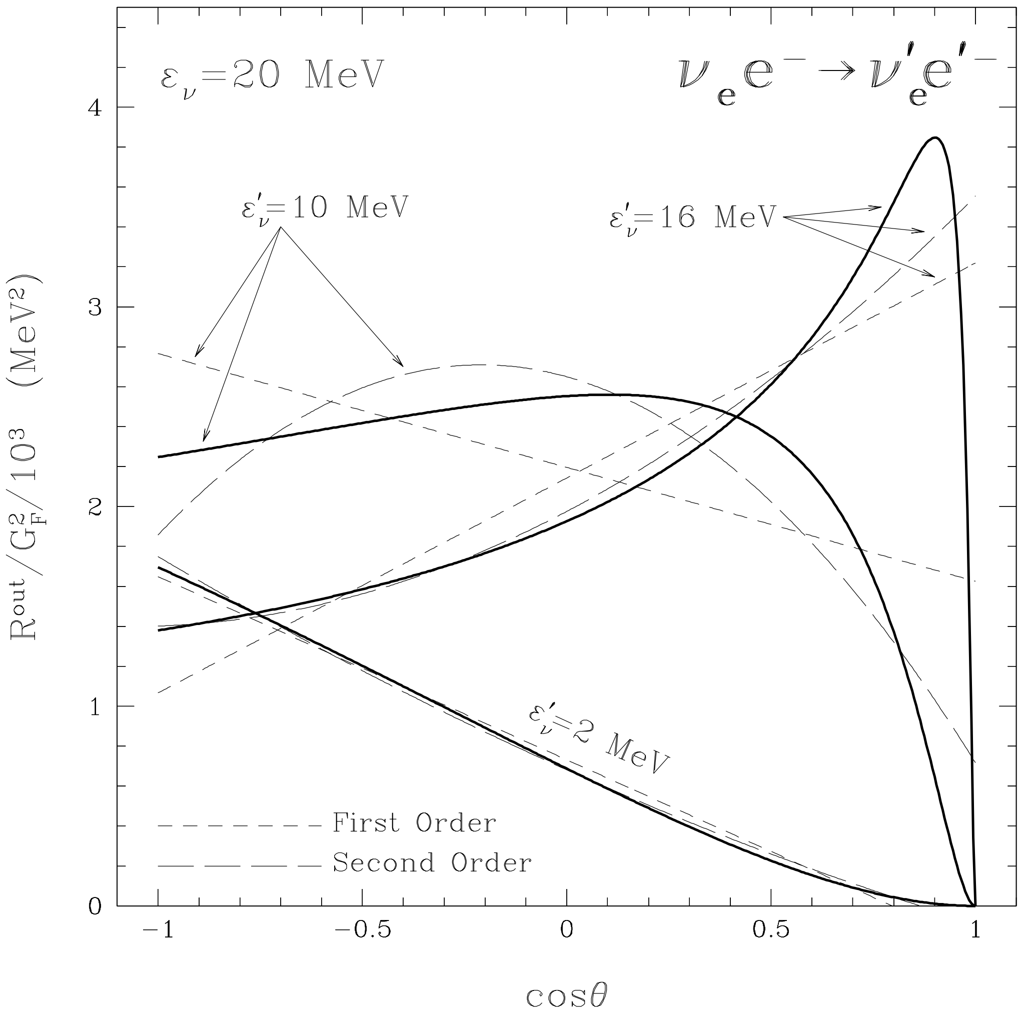

FIGURE B.2. For the same thermodynamic point as used for Fig. (B.1), the scattering kernel ($R^{\rm out}$, thick solid lines) for ν_e-electron scattering as a function of $\cos\theta$, for $\varepsilon_\nu =$ 20 MeV and $\varepsilon'_\nu = 2$, 10, and 16 MeV. Short dashed lines show the first-order Legendre series expansion approximation to $R^{\rm out}$, which is linear in $\cos\theta$; $R^{\rm out} \sim (1/2)\Phi_0 + (3/2)\Phi_1\cos\theta$. The long dashed line shows the improvement in going to second order in $\cos\theta$ by taking $R^{\rm out} \sim (1/2)\Phi_0 + (3/2)\Phi_1\cos\theta + (5/2)\Phi_2(1/2)(3\cos^2\theta - 1)$.

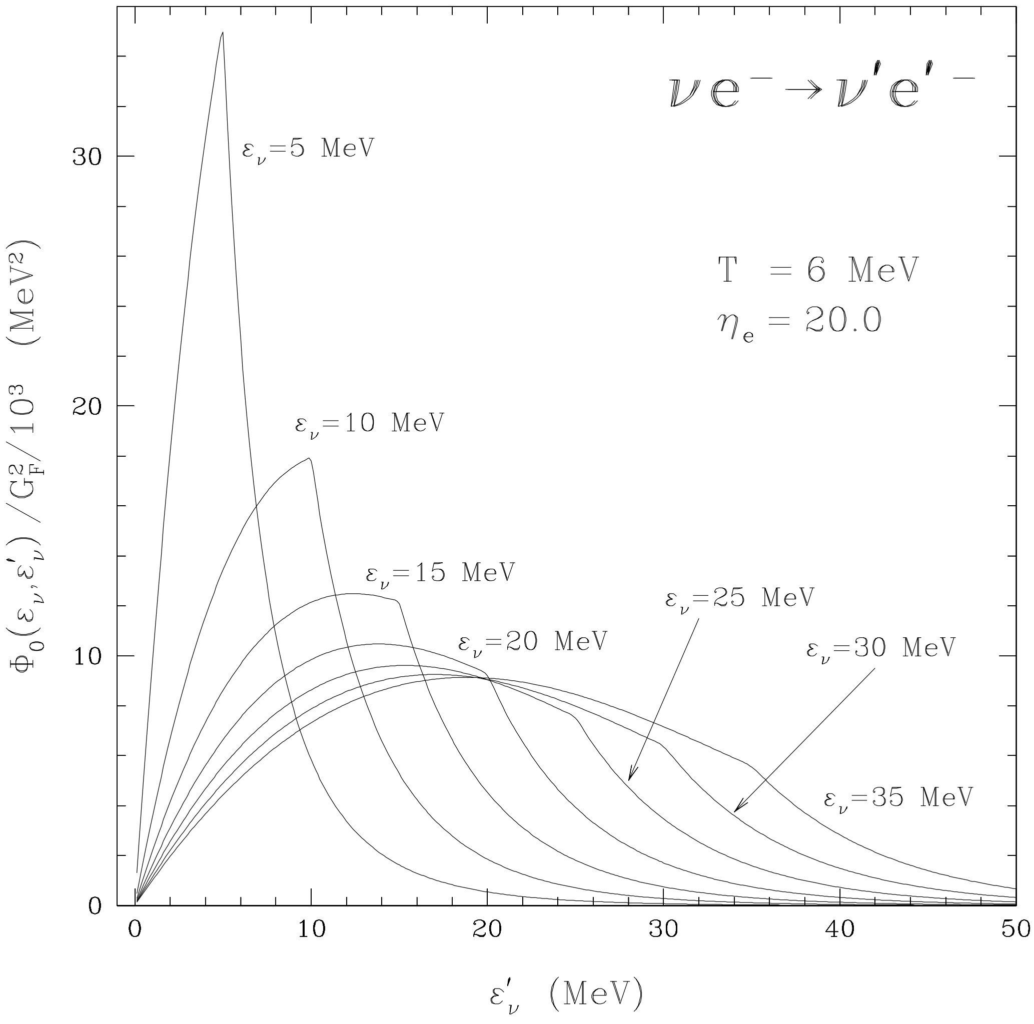

FIGURE B.3. The $l = 0$ term in the Legendre expansion of the ν_e−electron scattering kernel, $\Phi_0(\varepsilon_\nu, \varepsilon'_\nu)$ (eq. B.59), for $T = 6$ MeV and $\eta_e = 20$ as a function of ε'_ν for $\varepsilon_\nu = 5$, 10, 15, 20, 25, and 35 MeV. Note that for any ε_ν, the neutrino is predominantly downscattered. The magnitude of $\Phi_0(\varepsilon_\nu, \varepsilon'_\nu)$ and sign of $\langle\omega\rangle$ are to be compared with those in Fig. (B.5).

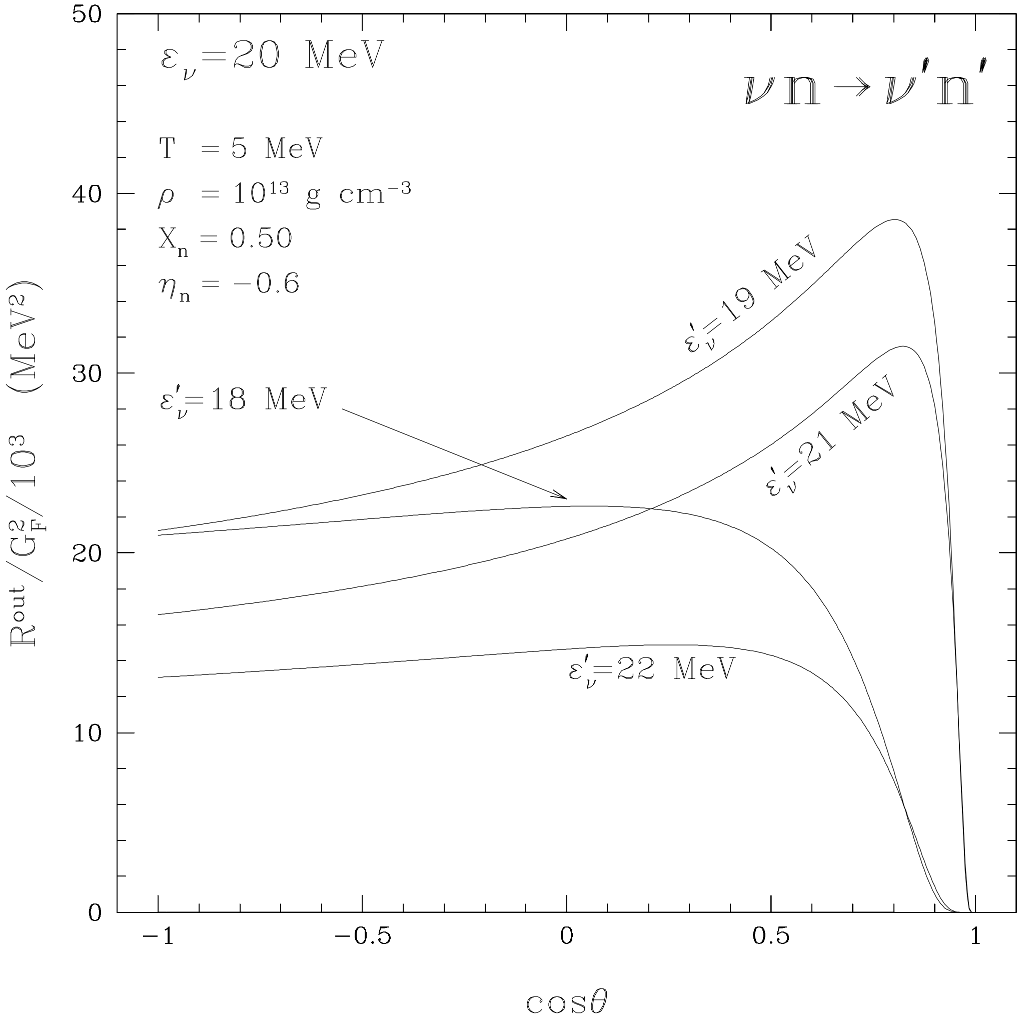

FIGURE B.4. The scattering kernel $R^{\rm out}(\varepsilon_\nu, \varepsilon'_\nu, \cos\theta)$ for ν_e−neutron scattering as a function of $\cos\theta$ for $\varepsilon_\nu = 20$ MeV and $\varepsilon'_\nu = 18$, 19, 21, and 22 MeV, at a representative thermodynamic point ($T = 5$ MeV, $\rho = 10^{13}$ g cm^{-3}, $X_n = 0.5$). Note that although the absolute value of the energy transfer ($|\varepsilon_\nu - \varepsilon'_\nu|$) is the same for both $\varepsilon'_\nu = 19$ MeV and $\varepsilon'_\nu = 21$, the absolute value of $R^{\rm out}(20, 19, \cos\theta)$ is greater than that of $R^{\rm out}(20, 21, \cos\theta)$, reflecting the fact that at this temperature the incoming neutrino is more likely to downscatter than upscatter.

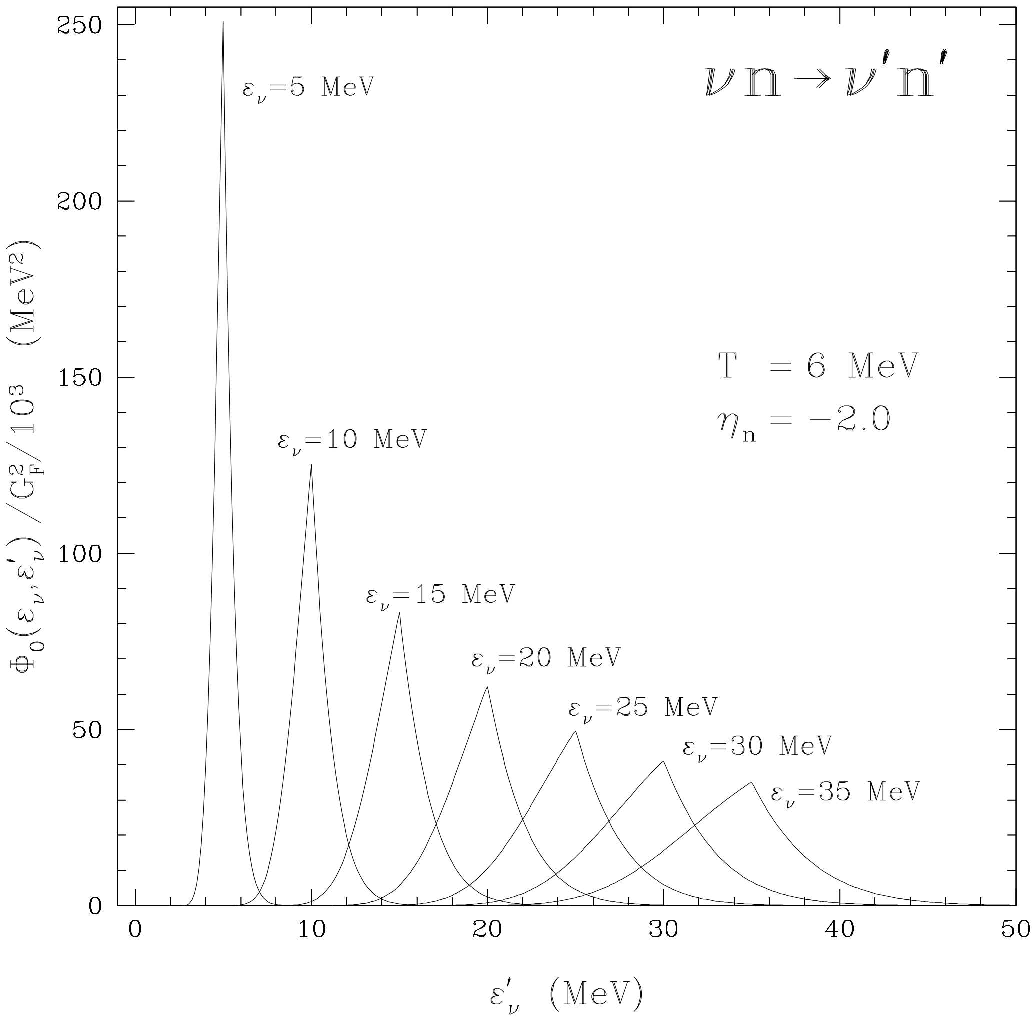

FIGURE B.5. The $l = 0$ term in the Legendre expansion of the neutrino-nucleon scattering kernel, $\Phi_0(\varepsilon_\nu, \varepsilon'_\nu)$ (eq. B.59), for $T = 6$ MeV and $\eta_n = -2$ as a function of ε'_ν for $\varepsilon_\nu = 5$, 10, 15, 20, 25, and 35 MeV. Note that for $\varepsilon_\nu = 5$ MeV the neutrino is predominantly upscattered, while for $\varepsilon_\nu = 35$ MeV the neutrino is predominantly downscattered. The magnitude of $\Phi_0(\varepsilon_\nu, \varepsilon'_\nu)$ and sign of $\langle\omega\rangle$ are to be compared with those in Fig. (B.3).

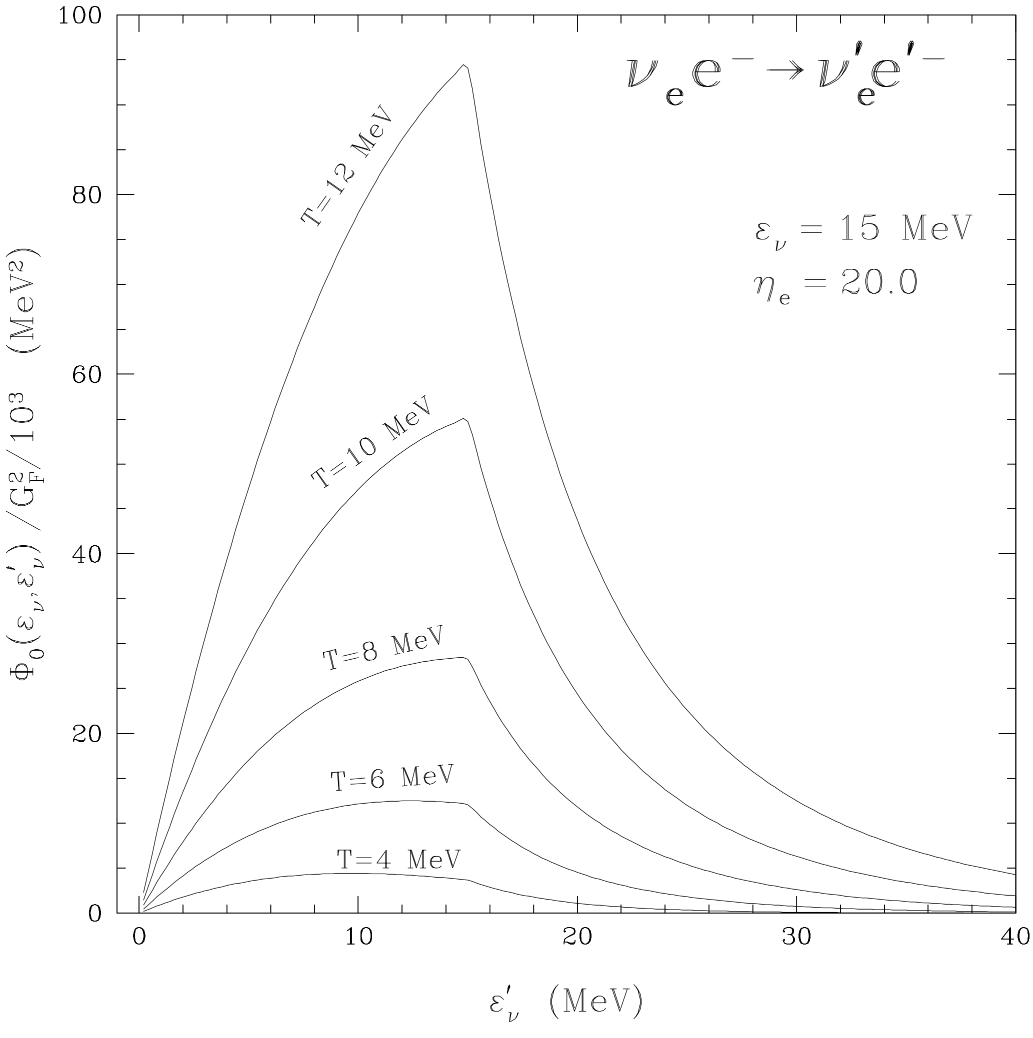

FIGURE B.6. $\Phi_0(\varepsilon_\nu, \varepsilon_\nu')$ for $\nu_e e^-$ scattering as a function of ε_ν' for $T = 4$, 6, 8, 10, and 12 MeV. Compare with Fig. (B.7) for νn scattering.

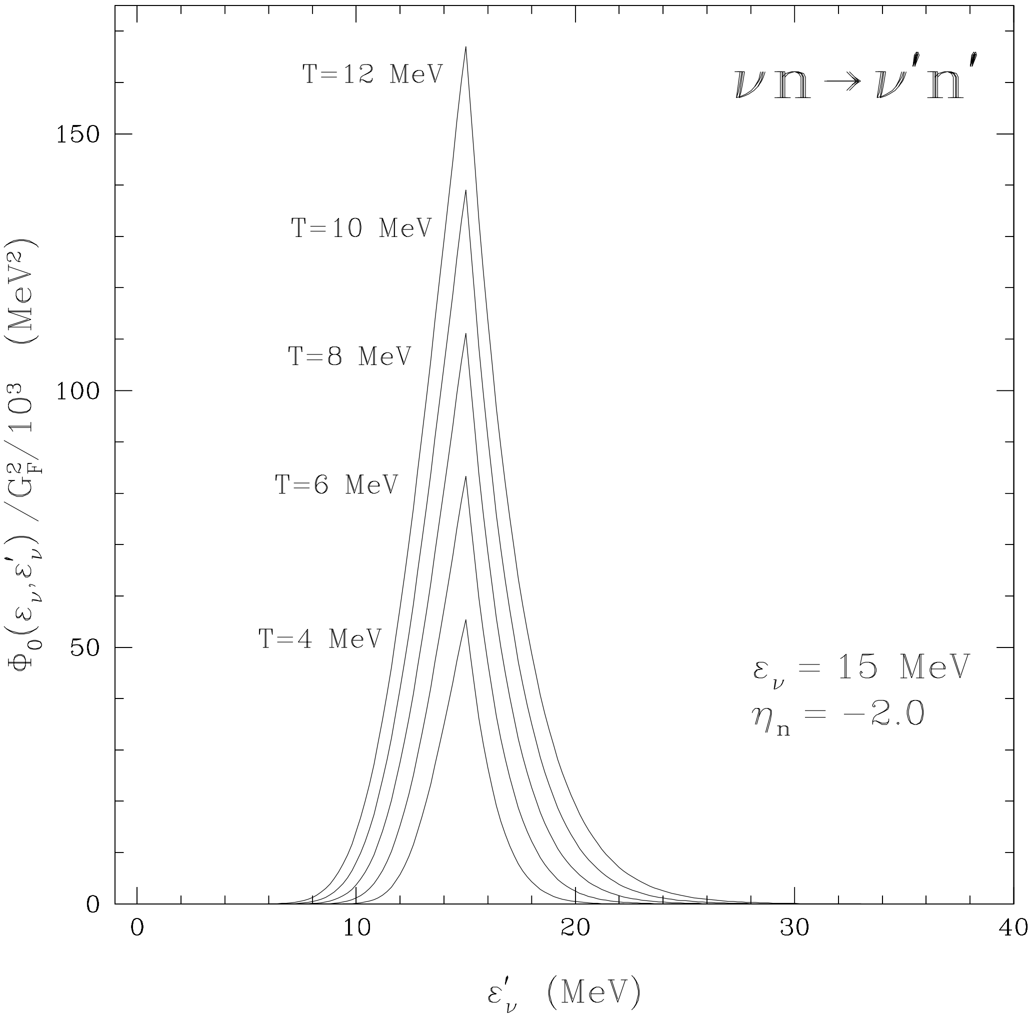

FIGURE B.7. $\Phi_0(\varepsilon_\nu, \varepsilon'_\nu)$ for νn scattering as a function of ε'_ν for $T = 4$, 6, 8, 10, and 12 MeV. Compare this figure with Fig. (B.6) for $\nu_e e^-$ scattering.

References

[1] Abromowitz, M. & Stegun, I. A., *Handbook of Mathematical Functions* (Dover Publications, Inc., New York, 1972)

[2] Ahmad et al. (2002), SNO collaboration, Phys. Rev. Lett., 89, 011301

[3] Arzoumanian, Z. 1995, Ph.D. Thesis, Princeton University

[4] Bahcall, J. N. 1964, Physical Review, 136, B1164

[5] Bahcall, J. N., Basu, S., & Pinsonneault, M. H. 1998, Phys. Lett. B, 433, 1

[6] Beacom, J. F., Boyd, R. N., & Vogel, P. 2000, Phys. Rev. Lett., 85, 3568

[7] Beacom, J. F. & Vogel, P. 1998, Phys. Rev. D, 58, 053010

[8] Bethe, H. & Wilson, J. R. 1985, ApJ, 295, 14

[9] Bhattacharya, M., Garcia, I., Kaloskamis, N. I., Adelberger, E. G., Swanson, H. E., Anne, R., Lewitowicz, M., Saint-Laurent, M. G., Donzaud, C., Guillemand-Mueller, D., Leenhardt, S., Mueller, A. C., Pougheon, F., Sorlin, O., Trinder, W. 1998, Phys. Rev. C, 58, 3677

[10] Bond, J. R., *Neutrino Production and Transport During Gravitational Collapse*, Ph. D. Thesis, Cal Tech, 1979

[11] Bowers, R. L. & Wilson, J. R. 1982, ApJS, 50, 115

[12] Brinkmann, R. P. & Turner, M. S. 1988, Phys. Rev. D, 38, 8, 2338

[13] Bruenn, S. W. 1985, ApJS, 58, 771

[14] Bruenn, S. W. & Mezzacappa, A. 1997, Phys. Rev. D, 56, no. 12

[15] Bruenn, S. W., De Nisco, K. R., & Mezzacappa, A. 2001, preprint (astro-ph/0101400)

[16] Burbidge, E. M., Burbidge, G. R., Fowler, W. A., & Hoyle, F. 1957, Rev. Mod. Phys., 29, 547

[17] Buras, R., Janka, H.-Th., Keil, M. Th., & Raffelt, G. G., Rampp, M. 2002, submitted to ApJ, (astro-ph/0205006)

[18] Burris, D. L., Pilachowski, C. A., Armandroff, T. E., Sneden, C., Cowan, J. J., & Roe, H. 2000, ApJ, 544, 302

[19] Burrows, A. & Goshy, J. 1993, ApJ, 416, L75

[20] Burrows, A., Klein, D., & Gandhi, R. 1992, Phys. Rev. D, 45, 10, 3361

[21] Burrows, A., Hayes, J., & Fryxell, B. A. 1995, ApJ, 450, 830

[22] Burrows, A., Young, T., Pinto, P., Eastman, R., & Thompson, T. A. 2000, ApJ, 539, 865

[23] Burrows, A. & Sawyer, R. 1998, Phys. Rev. C, 58, 554

[24] Burrows, A. & Sawyer, R. 1999, Phys. Rev. C, 59, 510

[25] Burrows, A. & Mazurek, T. J. 1982, ApJ, 259, 330

[26] Burrows, A. & Mazurek, T. J. 1983, Nature, 301, 315

[27] Burrows, A. & Lattimer, J. M. 1985, ApJ, 295, L15

[28] Burrows, A. & Lattimer, J. M. 1986, ApJ, 307, 178

[29] Burrows, A. 1988, ApJ, 334, 891

[30] Burrows, A. 1989, ApJL, 341, L63

[31] Burrows, A., Mazurek T. J., & Lattimer, J. M. 1981, ApJ, 251, 325

[32] Cardall, C. Y. & Fuller, G. M. 1997, ApJL, 486, 111

[33] Chandrasekhar, S., *An Introduction to the Study of Stellar Structure*, (Dover Publications, Inc., New York, 1967)

[34] Chevalier, R. 1989, ApJ, 346, 847

[35] Cayrel, R., Hill, V., Beers, T. C., Barbuy, B., Spite, M., Spite, F., Plez, B., Andersen, J., Bonifacio, P., Francois, P., Molaro, P., Nordström, B., & Primas, F. 2001, Nature, 409, 691

[36] Cernohorsky, J. 1994, ApJ, 433, 247

[37] Colella, P. & Woodward, P. 1984, J. Comp. Phys., 54, 174

[38] Cooperstein, J., van den Horn, L. J., & Baron, E. A., ApJ, 309, 653, 1986

[39] Cooperstein, J., van den Horn, L. J., & Baron, E. A. 1986, ApJ, 315, 729

[40] Cooperstein, J. & Baron, E. A. 1992, ApJ, 398, 531

[41] Cowan, J. J., Sneden, C., Truran, J. W., & Burris, D. L. 1996, ApJL, 460, 115

[42] Dicus, D. A. 1975, Phys. Rev. D, 6, 941

[43] Duncan, R. C., Shapiro, S. L., & Wasserman, I. 1986, ApJ, 309, 141

[44] Eggleton, P. P. 1971, MNRAS, 151, 351

[45] Eastman, R. & Pinto, P. 1993, ApJ, 412, 731

[46] Fetter, A. L. & Walecka, J. D., *Quantum Theory of Many Particle Systems* (McGraw-Hill, New York, 1971).

[47] Flammang, R. A. 1982, MNRAS, 199, 833

[48] Flowers, E. G. &Sutherland, P. S. 1976, ApJL, 208, L19

[49] Flowers, E. G., Sutherland, P. G., & Bond, J. R. 1975, Phys. Rev. D, 12, 2

[50] Freiburghaus, C., Rosswog, S., & Thielemann, F.-K. 1999, ApJL, 525, 121

[51] Freiburghaus, C., Rembges, J.-F., Rauscher, T., Kolbe, E., Thielemann, F.-K., Kratz, K.-L., Pfeiffer, B., & Cowan, J. J. 1999, ApJ, 516, 381

[52] Friman, B. L. & Maxwell, O. V. 1979, ApJ, 232, 541

[53] Fryer, C. L., Benz, W., Herant, M., & Colgate, S. 1999, ApJ, 516, 892

[54] Fryer, C. L., Burrows, A., & Benz, W. 1998, ApJ, 496, 333

[55] Fryer, C. L. & Heger, A. 2000, ApJ, 541, 1033

[56] Fryer, C. L. & Warren, M. 2002, accepted to ApJL, preprint (astro-ph/0206017)

[57] Fryxell, B. A., Müller, E. & Arnett, D. 1989,Max-Planck-Institut für Astrophysik Rep., 449

[58] Fuller, G. M. & Meyer, B. S. 1995, ApJ, 453, 792

[59] Fuller, G. M. & Qian, Y.-Z. 1996, Nuc. Phys. A, 606, 167

[60] Fuller, G. M., Fowler, W. A., & Newman, M. J. 1980, ApJS, 42, 447

[61] Fuller, G. M., Fowler, W. A., & Newman, M. J. 1982, ApJ, 252, 715

[62] Fuller, G. M. & Meyer, B. S. 1995, ApJ, 453, 792

[63] Hanhart, C., Phillips, D. & Reddy, S. 2001, Phys. Lett. B, 499, 9

[64] Hannestad, S. & Raffelt, G. 1998, ApJ, 507, 339

[65] Herant, M., Benz, W., Hix, W. R., Fryer, C. L., Colgate, S. A. 1994, ApJ, 435, 339

[66] Hill, V., Plez, B., Cayrel, R., & Beers, T. C. 2001, proceedings of Astrophysical Ages and Timescales, ASP Conference Series, preprint (astro-ph/0104172)

[67] Hoffman, R. D., Woosley, S. E., Fuller, G. M., & Meyer, B. S. 1996, ApJ, 460, 478

[68] Hoffman, R. D., Woosely, S. E., & Qian,Y.-Z. 1997, ApJ, 482, 951

[69] Horowitz, C. J. & Li, G. 2000, Proceedings of Intersections Conference, Qubec, preprint (astro-ph/0010042)

[70] Horowitz, C. J. 1997, Phys. Rev. D, 55, no. 8

[71] Horowitz, C. J. 2002, Phys Rev. D, 65, 043001

[72] ICARUS collaboration 2001, *The ICARUS Experiment*, Laboratory Nazionali del Gran Sasso, LNGS-P28, (hep-ex/0103008)

[73] Itoh, N., Hayashi, H., Nishikawa, A., & Kohyama, Y. 1996, ApJS, 102, 411

[74] Janka, H.-Th., Keil, W., Raffelt, G., & Seckel, D. 1996, Phys. Rev Lett., 76, 2621

[75] Janka, H.-Th. & Müller, E. 1996, A&A, 306, 167

[76] Janka, H.-Th. & Müller, E. 1995, ApJL, 448, 109

[77] Janka, H.-Th. 1991, A&A, 244, 378

[78] Janka, H.-Th. 2001, A&A, 368, 527

[79] Janka, H.-Th. & Hillebrandt, W. 1989, A&A, 224, 49

[80] Kajino, T., Otsuki, K., Wanajo, S., Orito, M., & Mathews, G. 2001, to appear in Few-Body Systems Suppl., preprint (astro-ph/0006079)

[81] Keil, W., Janka, H.-Th., & Raffelt, G. G. 1995, Phys. Rev. D, 51, 6635

[82] Kippenhahn, R., Weigert, A., & Hoffmeister, E. 1968, Meth. Comput. Phys., 7, 129

[83] Lamb, D. & Pethick, C. 1976, ApJL, 209, L77

[84] Lattimer, J. M., Pethick, C., Ravenhall, D., & Lamb, D. 1985, Nucl. Phys. A, 432, 646

[85] Lattimer, J. M. & Prakash, M. 2001, ApJ, 550, 426

[86] Lattimer, J. M. & Swesty, F. D. 1991, Nucl. Phys.A, 535, 331

[87] Leinson, L. B., Oraevsky, V. N., & Semikoz, V. B. 1988, Phys. Lett. B, 209, 1

[88] Liebendörfer, M. 2000, Ph.D. Thesis, Basel University, Basel, Switzerland

[89] Liebendörfer, M., Mezzacappa, A., Thielemann, F.-K., Messer, O. E. B., Hix, W. R., & Bruenn, S. W. 2001, PRD, 63, 103004

[90] Liebendörfer, M., Mezzacappa, A., Thielemann, F.-K. 2001, PRD, 63, 104003

[91] Liebendörfer, M., Messer, O. E. B., Mezzacappa, A., Hix, W. R., Thielemann, F.-K., & Langanke, K. 2002, *Proceedings of the 11th Workshop on Nuclear Astrophysics*, Hillebrandt, W. & Müller, E., eds., (astro-ph/0203260)

[92] Liebendörfer, M., Messer, O. E. B., Mezzacappa, A., Cardall, C. Y., & Thielemann, F.-K. 2002, submitted to ApJS, (astro-ph/0207036)

[93] London, R. A. & Flannery, B. P. 1982, ApJ, 258, 260

[94] MacFadyen, A. I. & Woosley, S. E. 1999, ApJ, 524, 262

[95] Mazurek, T. J. 1982, ApJ, 259, L13

[96] Mayle, R., Wilson, J. R., & Schramm, D. N. 1987, ApJ, 318, 288

[97] Mclaughlin, G., Fuller, G. M., & Wilson, J. R. 1996, ApJ, 472, 440

[98] McWilliam, A., Preston, G. W., Sneden, C., & Searle, L. 1995a, AJ, 109, 2757

[99] McWilliam, A., Preston, G. W., Sneden, C., & Shectman, S. 1995b, AJ, 109, 2757

[100] Mestel, L. 1968, MNRAS, 138, 359

[101] Meyer, B. S. & Brown, J. S. 1997, ApJS, 112, 199

[102] Meyer, B. S., Howard, W. M., Mathews, G. J., Woosley, S. E., & Hoffman, R. D. 1992, ApJ, 399, 656

[103] Mezzacappa, A. & Bruenn, S. W. 1993a, ApJ, 410, 637

[104] Mezzacappa, A. & Bruenn, S. W. 1993b, ApJ, 410, 669

[105] Mezzacappa, A. & Bruenn, S. W. 1993c, ApJ, 410, 740

[106] Mezzacappa, A., Liebendörfer, M., Messer, O. E. B., Hix, W. R., Thielemann, F.-K., & Bruenn, S. W. 2001, PRL, 86, 1935

[107] Mihalas, D. 1980, ApJ, 238, 1034,

[108] Mihalas, D. & Mihalas, B.,*Foundations of Radiation Hydrodynamics*, New York, Oxford University Press, 1984

[109] Myra, E. S. & Burrows, A. 1990, ApJ, 364, 222

[110] Nagataki, S. & Kohri, K. 2001, PASJ, 53, 547

[111] Nobili, L., Turolla, R., & Zampieri, L. 1991, ApJ, 383 250

[112] Ormand, W. E., Pizzochero, P. M., Bortignon, R. A., Broglia, R. A. 1995, Phys. Lett. B, 345, 343

[113] Otsuki, K., Tagoshi, H., Kajino, T., & Wanajo, S.-Y. 2000, ApJ, 533, 424

[114] Particle Data Group, *The European Physical Journal C*, 3, no. 1-4, 1998

[115] Pons, J. A., Miralles, J. A., Ibanez, J. M. 1998, A&A S., 129, 343

[116] Pons, J. A., Reddy, S., Prakash, M., Lattimer, J. M., & Miralles, J. A. 1999, ApJ, 513, 780

[117] Press, W. H., Teukolsky, S. A., Vetterling, W. T., & Flannery, B. P. 1992, Numerical Recipes in Fortran 77 (2d Ed.; New York, NY: Cambridge University Press)

[118] Qian, Y.-Z., Fuller, G. M., Mathews, G. J., Mayle, R. W., Wilson, J. R., Woosley, S. E. 1993, PRL, 71, 1965

[119] Qian, Y.-Z. 2000, ApJL, 534, 67

[120] Qian, Y.-Z. & Fuller, G. M. 1995a, PRD, 51, 14, 1479

[121] Qian, Y.-Z. & Fuller, G. M. 1995b, PRD, 52, 2, 656

[122] Qian, Y.-Z. & Wasserburg, G. J. 2000, Phys. Reps., 333, 77

[123] Qian, Y.-Z. & Woosley, S. E. 1996, ApJ, 471, 331

[124] Raffelt, G. & Seckel, D. 1998, Phys. Rev. Lett., 69, 2605

[125] Raffelt, G. 2001, ApJ, 561,890

[126] Raghavan, R. S. 1986, Phys. Rev. D, 34, 2088

[127] Rampp, M. 2000, Ph.D. Thesis, Max-Planck Institute for Astrophysics, Garching, Germany.

[128] Rampp, M. & Janka, H.-Th. 2000, ApJL, 539, 33

[129] Rampp, M., Buras, R., Janka, H.-Th., & Raffelt, G. G. 2002, *Proceedings of the 11th Workshop on Nuclear Astrophysics*, Hillebrandt, W. & Müller, E., eds., (astro-ph/0203493)

[130] Rampp, M. & Janka, H.-Th. 2002, submitted to A&A, (astro-ph/0203101)

[131] Reddy, S., Prakash, M., & Lattimer, J. M. 1998, PRD, 58, 013009

[132] Rosswog, S., Liebendörfer, M., Thielemann, F.-K., Davies, M., Benz, W., & Piran, T. 1999, A&A, 341, 499

[133] Salmonson, J. D. & Wilson, J. R. 1999, ApJ, 517, 859

[134] Schinder, P. J. 1990, ApJS, 74, 249

[135] Schinder, P. J., Schramm, D. N., Wiita, P. J., & Tubbs, D. L. 1987, ApJ, 313, 531

[136] Sehgal, I. 1974, Nucl.Phys., B70, 61

[137] Smit, J. M. 1998, Ph.D. Thesis, Universiteit van Amsterdam

[138] Smit, J. M. & Cernohorsky, J. 1996, A&A, 311, 347

[139] Smit, J. M., Cernohorsky, J., van den Horn, L. J., & van Weert, C. G. 1996, ApJ, 460, 895

[140] Sigl, G. 1997, Phys. Rev. D, 56, 3179

[141] SNO Collaboration, Phys. Rev. Lett., 89, 011301-1

[142] Sneden, C., McWilliam, A., Preston, G. W., Cowan, J. J., Burris, D. L., & Armosky, B. J. 1996, ApJ, 467, 819

[143] Sumiyoshi, K., Suzuki, H., Otsuki, K., Teresawa, M., & Yamada, S. 2000, PASJ, 52, 601

[144] Surman, R., Engel, J., Bennett, J. R., & Meyer, B. S. 1992, PRL, 79, 1809

[145] Suzuki, H. in *Frontiers of Neutrino Astrophysics*, ed. Suzuki, Y. & Nakamura, K. 1993, (Tokyo: Universal Academy Press), 219

[146] Swesty, F. D. 1996, J. Comp. Phys., 1, 118

[147] Takahashi, K., Witti, J., & Janka, H.-T. 1994, A&A, 286, 857

[148] Thompson, T. A., Burrows, A., & Horvath, J. E. 2000, PRC, 62, 035802

[149] Thompson, T. A., Burrows, A., & Meyer, B. S. 2001, ApJ, 562, 887

[150] Thorne, K. S., Flammang, R. A., & Zytkow, A. N. 1981, MNRAS, 194, 475

[151] Timmes, F. X. & Swesty, F. D. 2000, ApJS, 126, 501

[152] Timmes, F. X. & Arnett, D. 1999, ApJS, 125, 277

[153] Totani, T., Sato, K., Dalhed, H. E. & Wilson, J. R. 1998, ApJ, 496, 216

[154] Tubbs, D. L. & Schramm, D. N. 1975, ApJ, 201, 467

[155] Tubbs, D. L. 1979, ApJ, 231, 846

[156] Tubbs, D. L. 1978, ApJS, 37, 287

[157] Tubbs, D. L., Weaver, T. A., Bowers, R. L., Wilson, J. R., & Schramm, D. N. 1980, ApJ, 239, 271

[158] Vogel, P. 1984, Phys. Rev. D, 29, 1918

[159] Wallerstein, G., Iben, I., Parker, P., Boesgaard, A. M., Hale, G. M., Champagne, A. E., Barnes, C. A., Käppeler, F., Smith, V. V., Hoffman, R. D., Timmes, F. X., Sneden, C., Boyd, R. N., Meyer, B. S., & Lambert, D. L. 1997, Rev. Mod. Phys., 69, 995

[160] Wanajo, S., Kajino, T., Mathews, G. J., & Otsuki, K. 2001, ApJ, 554, 578

[161] Wasserburg, G. J. & Qian, Y.-Z. 2000, ApJL, 529, 21

[162] Weber, E. J. & Davis, L. 1967, ApJ, 148, 217

[163] Westin, J., Sneden, C., Gustafsson, B., & Cowan, J. J. 2000, ApJ, 530, 783

[164] Woosley, S. E. & Hoffman, R. D. 1992, ApJ, 395, 202

[165] Woosley, S. E., Wilson, J. R., Mathews G. J., Hoffman, R. D., & Meyer, B. S. 1994, ApJ, 433, 209

[166] Woosley, S. E. & Weaver, T. A. 1995, ApJS, 101, 181

[167] Yueh, W. R. & Buchler, J. R. 1976, Ap. Space Sci., 41, 221